MULTI-COMPONENT COMPLEX HYDRIDES FOR HYDROGEN STORAGE

Tobias Edward Cameron Price

Thesis submitted to the University of Nottingham

for the degree of Doctor of Philosophy

March 2010

Abstract

Hydrogen as an energy vector offers great potential for mobile energy generation through fuel cell technology, however this depends on safe, mobile and high density storage of hydrogen. The destabilised multi-component complex hydride system $LiBH_4$: MgH_2 was investigated in order to characterise the destabilisation reactions which enable reduction of operating temperatures for this high capacity system (*ca*. 9.8 wt.%). *In-situ* neutron diffraction showed that regardless of stoichiometry similar reaction paths were followed forming LiH and MgB_2 when decomposed under H_2 and Mg-Li alloys ($Mg_{0.816}Li_{0.184}$ and $Mg_{0.70}Li_{0.30}$) when under dynamic vacuum. Hydrogen isotherms of the $0.3LiBH_4$: MgH_2 showed a dual plateau behaviour with the lower plateau due to the destabilised $LiBH_4$ reaction. Thermodynamic data calculated from the isotherm results showed a significant reduction in the T(1bar) for $LiBH_4$ to 322 °C (*cf*. 459 °C for $LiBH_{4(l)}$).

Cycling behaviour of $0.3LiBH_4$: MgH_2 system decomposed under both reaction environments showed very fast kinetics on deuteriding at 400°C and 100 bar D_2, reaching 90 % conversion within 20 minutes. In contrast $2LiBH_4$: MgH_2 samples had kinetics an order of magnitude slower and after 4 hours conversions <50 %. These results demonstrate the strong influence of stoichiometry in the cycling kinetics compared to decomposition conditions.

Investigation of catalysts found dispersion of metal hydrides through long ball-milling times, or dispersion through reaction with metal halide additions provided the greatest degree of kinetic advantage, with pre-milled NbH providing the best kinetic improvement without reducing capacity due to Li-halide formation.

Finally, additions of $LiAlH_4$ to the system formed an Al dispersion through the sample during decomposition, which acted both as a catalyst and destabilising agent on the MgH_2 component, forming Mg-Al-Li alloys. Decomposition under H_2 also showed a destabilisation effect for the $LiBH_4$ component.

Publications

Price, T. E. C., D. M. Grant, I. Telepeni, X. B. Yu and G. S. Walker (2009). "The decomposition pathways for $LiBD_4$: MgD_2 multi-component systems investigated by in situ neutron diffraction." Journal of Alloys and Compounds **472**(1-2): 559-564.

Price, T. E. C., D. M. Grant, V. Legrand and G. S. Walker (2010)."Enhanced kinetics for the $LiBH_4$:MgH_2 multi-component hydrogen storage system - The effects of stoichiometry and decomposition environment on cycling behaviour." International Journal of Hydrogen Energy **35**(9): 4154-4161.

Price, T. E. C., D. M. Grant and G. S. Walker (2009). Synergistic Effect of $LiBH_4$ + MgH_2 as a Potential Reversible High Capacity Hydrogen Storage Material. Materials Innovations in an Emerging Hydrogen Economy. J. S. George G. Wicks: 97-104.

Walker, G. S., D. M. Grant, T. E. C. Price, V. Legrand and X. Yu (2009). "High capacity multi-component hydrogen storage materials investigation of the effect of stoichiometry and decomposition conditions on the cycling behavior of $LiBH_4$ - MgH_2." Journal of Power Sources **189**(2): 902-908.

Rechargeable Hydrogen Storage, G S Walker, D M Grant, T C Price, X Yu, UK Patent Application No. 0815899.0, Filing Date: 02 Sept 2008

Oral Presentations

Metal Hydrogen (2008), Reykjavik, Iceland (2008)

Materials Innovations in an Emerging Hydrogen Economy, Florida, USA (2008)

Acknowledgements

This thesis is dedicated to my father, John Cameron Price.

I would like to acknowledge the support and guidance of my supervisors Prof. Gavin Walker and Prof. David Grant, to whom I owe enormous thanks and many hours toiling in a nuclear bunker.

I would also like to thank all of the postgrads and technical staff who I have had the pleasure of working with. Special thanks to Irvin for his Neutron skills, Dave for his bucket skills and Tim for his desk sharing skills.

Special thanks to my family, for their love and support, all of whom I expect to read this thesis from cover to cover.

Finally, my thanks to Tasha for being there for me throughout the PhD.

The work carried out for this thesis was funded by the EPSRC as part of the UK Sustainable Hydrogen Energy Consortium (UK-SHEC) under the SUPERGEN initiative.

Contents

Glossary of terms

0.3:1 sample	$0.3LiBH_4 : MgH_2$ or $0.3LiBD_4 : MgD_2$
2:1 sample	$2LiBH_4 : MgH_2$ or $2LiBD_4 : MgD_2$
0.44:1 sample	$0.44LiBH_4 : MgH_2$ or $0.44LiBD_4 : MgD_2$
0.23:1 sample	$0.23LiBH_4 : MgH_2$ or $23LiBD_4 : MgD_2$
BCC	Body Centred Cubic
CCD	Charge-Coupled Device
DFT	Density Functional Theory
DOE	Department of Energy
DRIFT	Diffuse Reflectance Infrared Fourier Transform
DSC	Differential Scanning Calorimetry
DSMS	Dynamic Sampling Mass Spectrometer
EDX	Energy Dispersive Analysis of X-rays
HP	High Pressure
ICSD	Inorganic Crystal Structure Database
IEA	International Energy Agency
ICE	Internal Combustion Engine
ILL	Institut Laue-Langevin
INS	Inelastic Neutron Scattering
IPCC	Intergovernmental Panel on Climate Change
JCPDS-ICDD	Joint Committee on Powder Diffraction Standards-International Center for Diffraction Data
HCP	Hexagonal Close Packed
LAMP	Large Array Manipulation Program
MAD	Multi-Detector Acquisition of Data
MAS	Magic Angle Spinning

MOF	Metal-Organic Framework
MS	Mass Spectrometry
NMR	Nuclear Magnetic Resonance
NPD	Neutron Powder Diffraction
PCI	Pressure Composition Isotherm
PEMFC	Proton Exchange Membrane Fuel Cell
PPM	Parts Per Million
PTFE	Polytetraflouroethylene
PXD	Powder X-ray Diffraction
RMA	Reactive Mechanical Alloying
RPM	Revolutions per Minute
RT	Room Temperature
SEM	Scanning Electron Microscopy
SNL	Sandia National Laboratories
TEM	Transmission Electron Microscopy
TGA	Thermogravimetric Analysis
THF	Tetrahydrofuran
TPRS	Temperature Programmed Reaction Spectrometry
UNFCCC	United Nations Framework Committee on Climate Change
XRD	X-ray Diffraction

Nomenclature

Symbol	Definition	Unit
ΔG	Gibbs free energy	kJ
ΔH	Enthalpy	kJ mol^{-1}
ΔS	Entropy	J K^{-1}
d	d-spacing	Å
p	Pressure	bar
λ	Wavelength	Å
θ	Angle	°
T	Temperature	°C/K
R	Gas constant = 8.314	J K^{-1} mol^{-1}
ρ	density	g m^{-3}
λ_s or λ_l	Thermal conductivity (solid or liquid)	W m^{-1} K^{-1}
α_L	Coefficient of linear expansion	K^{-1}
E_{mass}	Mass density of energy	MJ Kg^{-1}
E_{vol}	Volumetric density of energy	kJ Kg^{-1}
M	Molar mass	g mol^{-1}

List of Figures

1. Introduction

1.1. Background

The reduction of human impact on the world has become increasingly important both politically and socially as our anthropogenic effects on the world climate have been realised. In 1988 the Intergovernmental Panel for Climate Change was founded, and its first assessment in 1990 reported a natural greenhouse warming effect and our impact upon it (Protocol 1990). The IPCC reported that the production of greenhouse gases CO_2, Nitrous Oxide, Methane and CFC's contributed to the greenhouse effect causing both oceanic and atmospheric temperature to increase (J. T. Houghton 2001). This report led to The United Nations Framework Committee on Climate Change (UN FCCC) to form in 1992 and in 1997 commitments were made to reduce emissions under the Kyoto Protocol. The UK is committed to a reduction in emission of greenhouse gasses of 12.5% from those of 1999 by 2012 (Nations 1997). Of particular importance is the reduction of CO_2 emissions due to its high radiative forcing which causes a net increase in atmospheric temperature (Tight *et al.*, 2005), potentially with catastrophic effect. The greatest challenge in reducing our output of CO_2 is the reduction of the use of fossil fuels, which when combusted in energy evolution produces 80% of anthropogenic CO_2 in the atmosphere (Quadrelli *et al.*, 2007). The reduction of fossil fuel use has provided an incentive for researching new energy technologies; these include alternatives to fossil fuelled power sources for our mobile energy needs.

1.2. Renewable Energy

Renewable energy refers to sources of energy which are naturally produced and replenished; these include wind, solar, geothermal and tidal energy. Their use

is of major importance in reducing the use of fossil fuels. Harnessing renewable sources of energy as mobile energy generators is problematic due to the low energy density of their input (*ie*. requiring large scale systems to achieve high energy output), their production is often intermittent (tidal, solar and wind) or fixed to a location (tidal and geothermal). A stable vector for renewable energy is therefore required to allow either mobile (*eg*. automotive) stationary (*eg*. back-up energy generators) or portable (*eg*. mobile phones) energy generation, thus reducing use of environmentally damaging fossil fuels. Electricity generated from renewable sources can be stored in batteries for mobile use, however due to their low capacity and high cost these systems have not superseded combustion engine systems and have either been integrated into combustion engine vehicles or used in short range transport. An alternative is the use of hydrogen, which could provide mobile energy generation without the associated emissions.

1.3. Hydrogen as an Energy Vector

Hydrogen is a very attractive energy vector because of its high mass density of energy, E_{mass}, of 141.8 MJ kg^{-1} (Lide 2007) and abundance in water and hydrocarbon forms. However extraction of hydrogen from water through electrolysis requires a very high energy process, needing 4.5–5 kWh m^{-3} H_2 for commercial electrolysers (Stojic *et al.,* 2003). Therefore this process would require a cheap non-fossil fuel energy source in order to make the process economically viable. Extraction from hydrocarbon breakdown releases CO_2 as a by-product and relies on supply of dwindling fossil fuels; it therefore does not offer a long term sustainable means of hydrogen production. The field of hydrogen storage is currently investigating a range of potential routes to

production of cheap hydrogen with minimum environmental impact (Farmer 2009).

Hydrogen use in energy production commonly relies on its reaction with oxygen to form water, this reaction can be utilised within a fuel cell to generate electricity whilst producing water as a waste product, the mode of operation of a fuel cell is shown in figure 1. Hydrogen could also be used analogously to petrol in internal combustion engines (ICE), however this process is only 25 % efficient, roughly half the efficiency of fuel cells (Schlapbach *et al.*, 2001).

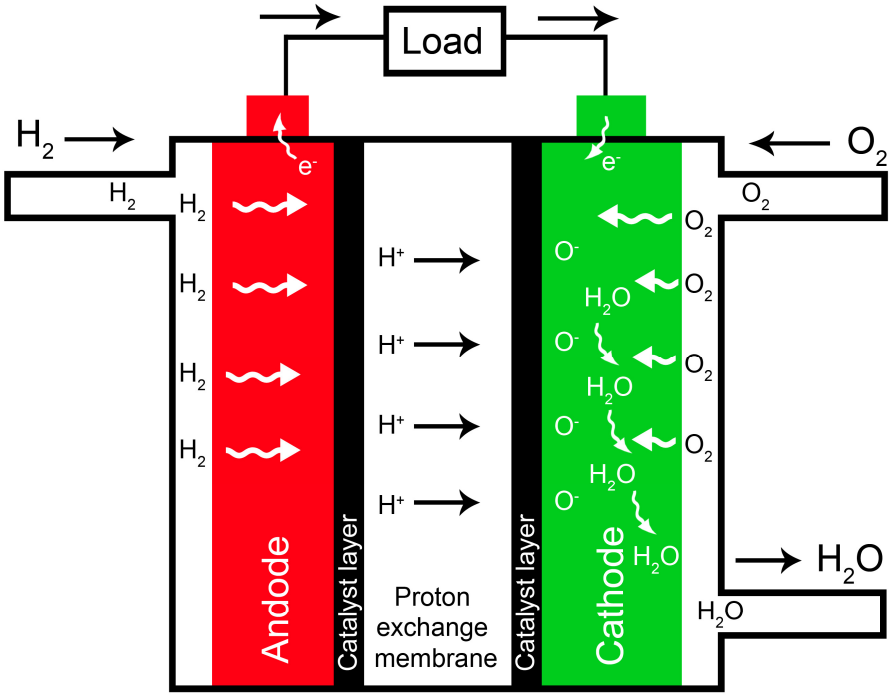

Figure 1. Proton Exchange Membrane Fuel Cell (PEMFC).

A major challenge in the use of hydrogen as an energy vector for mobile fuel cells is transport of the hydrogen. Hydrogen mass density of energy, E_{mass}, of 141.8 MJ kg^{-1} (Lide 2007) is greater than that of liquid hydrocarbons (*ca.* 47 MJ kg^{-1} (Schlapbach *et al.*, 2001)), however hydrogen volumetric density E_{vol} is very

poor, and at standard temperature and pressure only contains 12.74 kJ L^{-1} compared to hydrocarbons such as petrol which contain 32500 kJ L^{-1} (Ohlrogge *et al.,* 2001) thereby an equivalent hydrogen tank would need to be 2500 times bigger than an equivalent petrol tank. In order to make hydrogen fuel cells a viable option a safe high energy density hydrogen store is required. Automotive applications represent the largest market for use of hydrogen fuel cells, storage targets are therefore set with this market in mind. Discussion of hydrogen storage within this thesis is similarly aimed at this application.

1.4. Hydrogen Storage

In order to harness hydrogen as an energy vector a safe and economical mobile storage medium must be developed. Governmental bodies such as the US Department of Energy (DOE) have set targets for the storage of hydrogen,
table 1.1 displays the current (as of 2009) targets for mobile storage capacity of hydrogen for 2015 and ultimate targets, which represent an eventual goal with no date yet ascribed.

Year	**2015**	**Ultimate**
Gravimetric capacity	5.5 wt.%	7.5 wt.%
Volumetric capacity	40 g H_2 L^{-1}	70 g H_2 L^{-1}

Table 1.1. Key DOE technical targets for mobile hydrogen storage (Dilich 2009).

Meeting the storage constraints set by such targets, provides a significant scientific challenge and has been the focus of concerted research for several decades. Hydrogen storage fields can be broadly grouped into three categories; gas, liquid and solid storage.

1.4.1. Gas storage

Gaseous storage provides the simplest storage solution for H_2, and is currently the most favoured method. High pressure tanks have developed from steel or aluminium bottles which crippled total gravimetric storage capacity by their inherent weight. More recent designs utilise composite materials composed of metal liners wrapped in high strength carbon fibre. High pressures of hydrogen gas are required to approach DOE targets, if a composite bottle material of tensile strength 2000 MPa could be achieved, a bottle operating at 800 bar would achieve a total system storage capacity of 13 mass.% and 40 kg H_2 m^{-3}, achieving 2015 targets but falling short of ultimate targets. Current systems have reached H_2 densities of 36 kg H_2 m^{-3} at 80 MPa (Züttel *et al.*, 2003b), however this gravimetric capacity does not include the tank weight and still falls short of 2015 DOE targets. Increasing pressure requires heavier stronger tanks and a larger energy input for pressurising (*cf*. theoretical 2.21 kWh kg^{-1} H_2 for 80MPa under isothermal conditions (Züttel 2004)) which reduces system efficiency. Aside from volumetric issues with gaseous storage, other concerns relate to the safety of high pressure flammable gases and their use in populated places.

1.4.2. Liquid Storage

Liquid hydrogen systems allow increased densities without elevated pressures, cooled systems take hydrogen to liquid state at 33 K, achieving volumetric densities of 70.8 kg H_2 m^{-3} (Züttel *et al.*, 2003b), double that of 80 MPa gaseous hydrogen. However the liquefaction of H_2 presents a significant challenge in terms of creating an equilibrated para/ortho hydrogen liquid and in energy input; theoretically requiring 3.23 kWh kg^{-1} H_2 to cool to 33 K but in practise requiring 15.2 kWh kg^{-1} H_2 (Züttel 2004). Several safety concerns also make

liquid storage unfavourable; boil-off, the generated hydrogen caused by evaporating hydrogen from liquid stores causes H_2 pressure build up. Venting in enclosed spaces represents an explosion risk, whilst venting to the atmosphere poses an environmental risk. High infrastructure/heat management and energy costs of minimising boil off and maintaining a liquid store make liquid hydrogen currently unsuitable for mobile hydrogen storage. Development of insulated high pressure cryogenic tanks has shown storage of 5.2 wt.%, with a dormancy (period of inactivity before a vessel releases hydrogen to reduce pressure build up) of 5 days (Aceves *et al.,* 2006a; Aceves *et al.,* 2006b), further work into conformable tanks, lighter materials and longer dormancy periods is required to make these stores viable.

Solid hydrogen storage encompasses a range of storage materials, so it is best to further dissect this category into its main areas. Physisorption, Chemisorption and Hydrolytic systems.

1.4.3. Physisorption

Physisorption based systems such as carbon nanostructures (Benard *et al.,* 2008), zeolites (Weitkamp *et al.,* 1995) or metal-organic frameworks (Lin *et al.,* 2008) are porous materials that allow a non-dissociative physical adsorption of a H_2 molecule (adsorbate) on a solid surface (adsorbent) (Attard *et al.,* 1998). Their sorption properties are essentially determined by the surface area and the pore size (Panella *et al.,* 2005). Yan *et al.* show excess H_2 uptake (directly interacting with the surface) of 7.07 wt.% at 35 – 40 bar at 77 K with total H_2 uptake of 10.0 wt.% (including that not interacting with surface) at 77 bar and 77 K for a Cu (II) - framework (MOF NOTT-112) (Yan *et al.,* 2009). In general these materials suffer from poor volumetric properties (Benard *et al.,*

2008). Systems cycle well with fast kinetics and good reversibility, as no chemical reaction occurs during adsorption/desorption. However, the requirement for low operating temperatures (*ca.* 77 K) due to the low enthalpy of adsorption typically 4-10 $kJ.mol^{-1}$(Walker 2008) means that physisorbing materials require cryotank and heat management systems, adding weight and energy investment to maintain low temperatures, thereby reducing efficiency and gravimetric/volumetric capacity of a store. These issues currently make physisorption materials unsuitable for mobile hydrogen storage.

1.4.4. Hydrolysis reaction

Table 1.2. Hydride hydrolytic reactions and capacities (Schuth *et al.*, 2004)

Hydride	Reaction	Capacity / wt.%
LiH	$LiH + H_2O \rightarrow LiOH + H_2$	7.7
$LiBH_4$	$LiBH_4 + 4H_2O \rightarrow LiOH + H_3BO_3 + 4H_2$	8.6
$LiAlH_4$	$LiAlH_4 + 4H_2O \rightarrow LiOH + Al(OH)_3 + 4H_2$	7.3
NaH	$NaH + H_2O \rightarrow NaOH + H_2$	4.9
$NaBH_4$	$NaBH_4 + 4H_2O \rightarrow NaOH + H_3BO_3 + 4H_2$	7.3
$NaAlH_4$	$NaAlH_4 + 4H_2O \rightarrow NaOH + Al(OH)_3 + 4H_2$	6.4
MgH_2	$MgH_2 + 2H_2O \rightarrow MgH_2 + 2H_2O\ Mg(OH)_2 + 2H_2$	6.3
Al	$2Al + 6H_2O \rightarrow 2Al(OH)_3 + 3H_2$	3.7

Hydrolytic storage of hydrogen through metal or hydride water reaction has the potential to liberate large amounts of hydrogen, by releasing both hydrogen from water, but also that of the hydride (see section 2.2). The hydrolytic reactions result in either oxide or hydroxide formation along with hydrogen evolution (Aiello *et al.*, 1998). Metals which react to form oxides often generate passivating layers preventing complete hydrolysis, however some

hydrolytic reactions generate soluble hydroxides maintaining a reaction surface and may allow complete reaction; this makes hydroxide forming metals the most viable stores. Table 1.2 shows a range of potential hydrolytic hydride reactions, $NaBH_4$ is particularly promising as its reaction with water requires catalysis, it can therefore be transported in aqueous solution, with hydrolysis occurring on application of a ruthenium catalyst (Amendola *et al.,* 2000). The thermodynamic stability of end products would require very high energy processes to reform starting materials, ruling out onboard re-generation. Instead, large scale, highly energy intensive regeneration of reactants would be required; this reduces the attractiveness of hydrolysis based hydrogen stores.

1.4.5. Chemically Bound Hydrogen

Solid hydrogen in the form of chemically bound hydrides represents the most promising hydrogen storage medium, due to the high gravimetric and volumetric nature of these stores. Chemically bound hydrogen can be achieved by bonding hydrogen to carrier elements or storing the hydrogen interstitially within the lattice (Züttel *et al.,* 2003b). These systems theoretically offer very high storage capacity, e.g. 18.5 wt.% for $LiBH_4$ (Orimo *et al.,* 2005). However, the use of these materials is limited by the complexity of meeting operating conditions in terms of kinetics, capacity, operating conditions, safety and reversibility of stores. The development of solid hydrogen based storage systems is the focus of this report.

1.5. Aims and scope of the research

The aim of this research is to investigate destabilised multi-component complex hydride systems, in order to reduce system operating temperatures and improve cycling. Research will focus on lithium tetrahydridoborate ($LiBH_4$) destabilised by magnesium hydride (MgH_2). Effects of stoichiometry and reaction environment will be investigated through *in*-situ structural characterisation, allowing elucidation of the different reaction pathways of these systems through cycling. This research will determine optimal ratios and reaction conditions to be developed and explored. Catalysis and further destabilising additions will also be investigated in order to improve system kinetics and cycling behaviour.

Objectives

- Elucidate the reaction pathways for the decomposition of different stoichiometries of $LiBH_4$: MgH_2 under both hydrogen and dynamic vacuum.

- Investigate the effect of the different dehydrogenation routes upon the kinetics of hydrogenation.

- Identify catalysts for the $LiBH_4$: MgH_2 system.

- Determine the effect of additions of $LiAlH_4$ to the $LiBH_4$: MgH_2 system, with the aim of further reducing the decomposition temperature for the system.

1.6. Thesis overview

Chapter 2 will review critically the published literature into hydrogen storage hydride materials. The review will discuss hydrides, thermodynamic theory and destabilised systems before reviewing current multi-component systems, processing and catalysis.

Chapter 3 provides a detailed description of materials used in the research and the processing techniques to generate samples. The chapter will then detail the theory and experimental parameters for material characterisation used to generate results in chapter 4.

Chapter 4 presents results from the research into multi-component systems investigating decomposition pathways, cycling and catalysis.

Chapter 5 contains a detailed discussion of results presented in chapter 4 with discussion put into context through comparison to literature described in chapter 2. Conclusion from the work is presented in chapter 6 and the potential for further work into the topic in chapter 7.

2. Literature review

2.1. Hydrides

Solid state hydrogen storage can be achieved through hydride storage, where hydrogen is held in the solid state within a compound with other elements. Bonding of hydrides can take several forms, ionic, covalent, interstitial or complex. The simple equation for a simple reversible hydride is shown in equation 2.1. The forward reaction in equation 2.1 is an exothermic reaction, whilst the reverse decomposition reaction is an endothermic reaction. It is a reversible process of binding hydrogen and metal which hydride hydrogen storage seeks to harness.

$$2M_{(s)} + xH_{2(g)} \leftrightarrow 2MH_{x(s)}$$ **Equation 2.1**

Meeting the targets of institutions such as the DOE (see table 1.1) poses a significant challenge for the optimisation and generation of new hydride types. The development of hydride systems which meet these requirements has resulted in large amounts of research into a wide variety of different hydride types and catalysts. The most important characteristics of hydrides are their operation as a reversible system within a required pressure and temperature range. The temperatures and pressure at which a hydride store can operate are affected by the thermodynamics of the materials. Theoretical thermodynamics can be evaluated using Gibbs free energy, calculated through equation 2.2.

$$\Delta G = \Delta H - T\Delta S$$ **Equation 2.2**

The Gibbs free energy (ΔG) is directly linked to the enthalpy (ΔH) and entropy (ΔS) as it changes with temperature T. The free energy provides a quantification of the driving force to progress through the reaction (*ie*. Decompose from hydride to metal and hydrogen) equation 2.1. The Gibbs free energy is also related to the pressure and temperature through equation 2.3, where R is the gas constant (8.314 $J K^{-1} mol^{-1}$) T is temperature and *p* is pressure. The hydriding reaction is therefore related to both temperature and pressure.

$$\Delta G = -RT \ln p$$ **Equation 2.3**

The theoretical behaviour of these reactions can be observed experimentally using the Pressure-Composition-Isotherm relationship. An isothermal P-C-I plot shown in figure 2.1 shows the composition of a hydride as the pressure of hydrogen is changed at a fixed temperature.

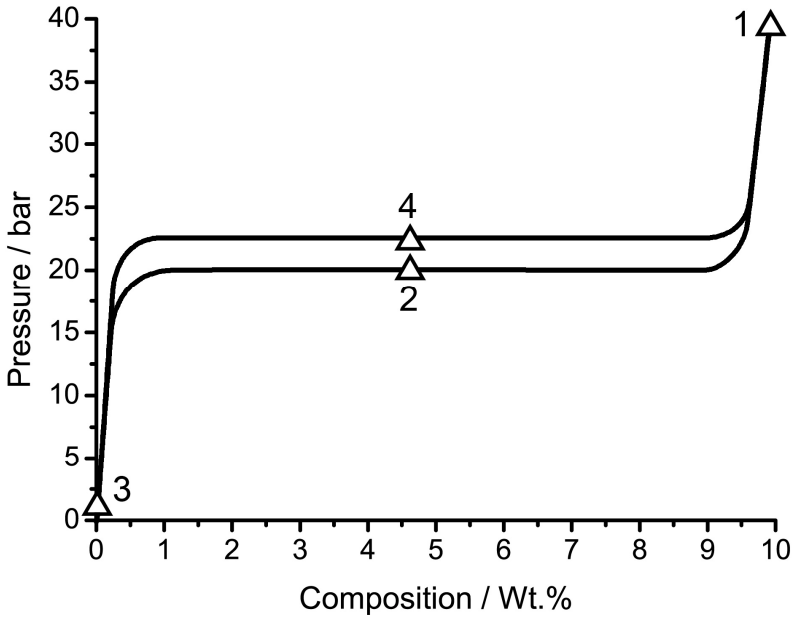

Figure 2.1. PCI plot for idealised hydride

The composition of the hydride will alter as the system pressure varies from its plateau pressure; this represents the equilibrium pressure to which a hydride will seek to evolve or uptake gas. For a hydride material with a plateau pressure of 20 bar at a given temperature, if the system is at 40 bar, the thermodynamic driving force is for the material to remain in the hydrided state (figure 2.1 point 1). By dropping the system pressure to below the plateau pressure, say 15 bar, the thermodynamic driving force will be for the hydride to evolve hydrogen. This process will continue until either the capacity of the hydride is exhausted (point 3), or the system pressure approaches the plateau pressure (point 2). Metal and hydrogen can be taken through both hydriding and decomposition reactions similarly by altering the pressure in the system. The plateau pressure of experimental systems is generally not flat but instead increases with increasing hydrogen content due in part to varying thermodynamic properties due to lattice expansion (Chandra 2008) but

primarily due to poor kinetics of systems. Most experimental PCI plots do not reach equilibrium on each aliquot yielding a sloping plateau, this effect also causes hysteresis where the decomposition plateau occurs lower than hydriding plateau.

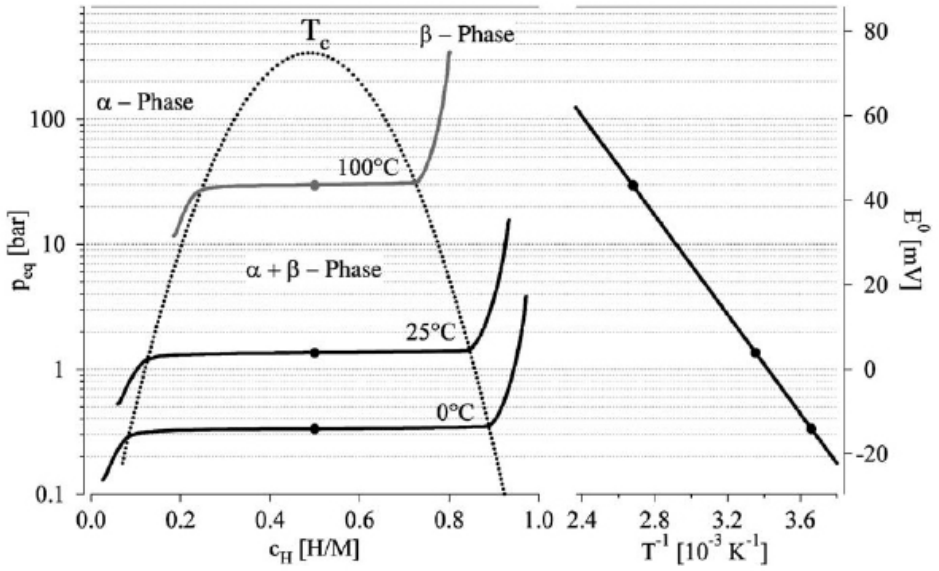

Figure 2.2. PCI Isotherms (left) Construction of a van't Hoff plot (right) (Züttel *et al.*, 2003b)

The role of pressure on metal hydrogen systems has been discussed, temperature similarly affects these dynamics. If temperature of a system is increased the thermodynamic drive to decompose a hydride increases (*ie*. ΔG becomes more negative according to equation 2.3) and therefore the plateau pressure for the hydride will rise; figure 2.2 (left) shows this effect.

Relating temperature and pressure to constants ΔH and ΔS for a specific hydride is achieved through the combination of equation 2.2 and equation 2.3, shown in equation 2.4. This forms the van't Hoff equation which can be directly linked to the experimental plateau pressures at different temperatures by

means of a van't Hoff plot, the construction of which is shown in figure 2.2 (right). Taking the plateau pressure at varying temperature, and plotting 1/T vs log*p* the gradient and intercept of the generated line can be related to ΔH and ΔS through the van't Hoff equation 2.4.

$$\ln P = -\frac{\Delta H}{RT} + \frac{\Delta S}{R}$$ **Equation 2.4**

The ΔH and ΔS now calculated, the Gibbs free energy at specific temperatures can be calculated and behaviour of a hydride predicted (with sufficient kinetics). The entropy component is due to the change from molecular gas to dissolved solid hydrogen which causes a reduction of the disorder within the system (Züttel *et al.,* 2003b), this value is therefore similar for binary metal hydrides (*ca.* 130 J mol^{-1} H_2 (Andreasen 2004)), but is generally lower for complex hydrides (*ca.* 97.3 J mol^{-1} H_2 for $LiBH_4$ (Chase 1998)). When the pressure in equation 2.3 equals one, the Gibbs free energy equals zero, this allows re-arrangement of equation 2.4 to give equation 2.5.

$$T(1\ bar) = \Delta H/\Delta S$$ **Equation 2.5**

This equation allows T(1bar) to be calculated, i.e. the temperature at which the hydride will show a plateau pressure of 1 bar. The T(1bar) provides a useful comparison of hydride material behaviour from its thermodynamic properties.

2.2. Basic Hydride types

2.2.1. Binary hydrides

Binary hydrides are formed from almost all metals in the periodic table. The reactivity of hydrogen with so many elements allows a huge variety of hydrides to be investigated. However most do not fall within the required pressure and temperature ranges of governmental targets, due to the requirement for high gravimetric storage only lighter elements are considered. Figure 2.3 shows the van't Hoff plot for the major binary hydrides which have been studied. Only VH_2 on this plot shows plateau pressures of 1-10 bar between 0-100 °C (viable operating temperature and pressure range shown by blue box in figure 2.3), however its poor gravimetric capacity (*ca.* 3.8 wt.%) and high cost rule it out for automotive targets (£20 per kg compared to £1 per kg for aluminium (InfoMine 2009)), but may offer application in niche applications or in the catalysis of bulk hydrides.

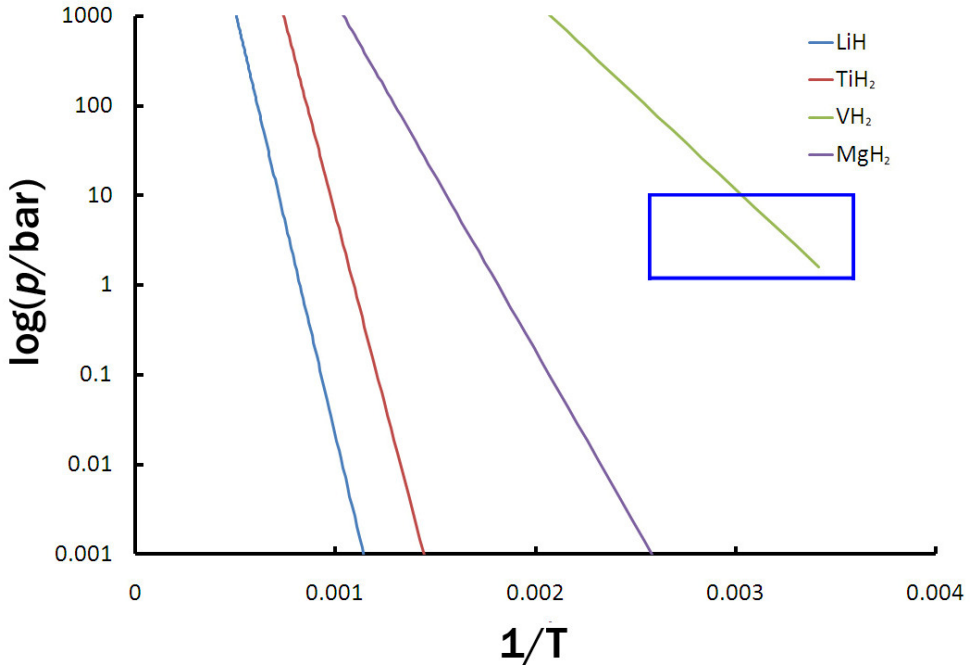

Figure 2.3. van't Hoff plot for a range of elemental hydrides.

2.2.1.1. MgH_2

Magnesium hydride has been one of the most studied elemental hydrides due to its high capacity (7.6 wt.%), however its large enthalpy of formation (ΔH_f = -75.3 kJ mol^{-1}) prevents it operating at a suitable temperature/pressure range. MgH_2 has a T(1bar) = 280 °C and even with sufficient kinetics this temperature is higher than required by DOE targets (<100 °C). MgH_2 forms a stable β- MgH_2 on saturation with hydrogen, occupying a tetragonal crystal structure, with space group *P42mnm* and lattice parameters a = 4.515 Å and b = 4.515 Å and c = 3.019 Å (Moriwaki *et al.*, 2006). The crystal structure for β - MgH_2 is shown in figure 2.4.

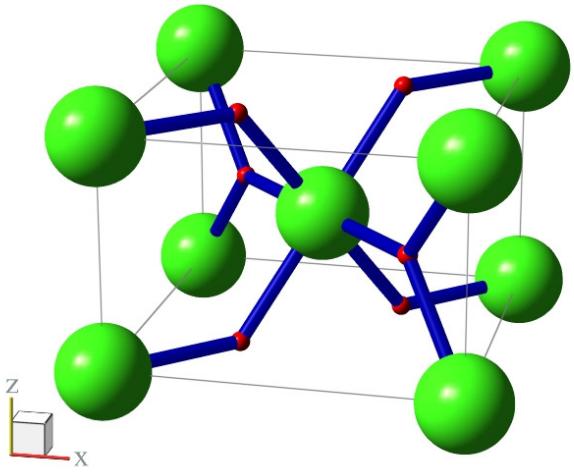

Figure 2.4. β- MgH_2 crystal structure using spacegroup and unit cell from Moriwaki *et al*. green, and red spheres represent Mg and H atoms respectively. (Moriwaki *et al.*, 2006).

The high gravimetric capacity of magnesium hydride has led to many studies into catalytic improvements of the hydride, an overview to this work is best provided by Huot *et al.*(Huot *et al.*, 2001) and Grant *et al.*(Grant 2008).

Further improvement of the hydride through thermodynamic destabilisation is discussed later in this review (see section 2.9).

2.3. Solid solution hydrides

Solid solution hydrides, can be classified as those which do not occupy stoichiometric compositions of metal/hydrogen. Instead hydrogen sits within the lattice in a disordered substitutional or interstitial form. Pd, Ti Zr, Nb and V all form solid solutions with hydrogen (Sandrock 1999). Solid solution hydrides offer the best properties when alloyed, particular focus has been drawn to BCC alloys, such as Ti–20Cr–12Mn–24V–5Fe showing 3.25 wt.% hydrogenation in 100 seconds (Yu *et al.,* 2004). Solid solution hydrides tend to exhibit poor capacity, but their fast kinetics allow them to be used as catalysts for higher capacity systems, MgH_2 (Yu *et al.,* 2009a; Yu *et al.,* 2009b) and with complex hydrides (Yu *et al.,* 2009c).

2.4. Inter-metallic Hydrides

Inter-metallic hydrides or alloy hydrides seek to combine the thermodynamic properties of different hydriding elements. Those which form strong hydrides are alloyed with elements which form weak hydrides in order to tailor the thermodynamic properties to fall within the required range. The most common example of an alloy hydride is $LaNi_5$ where stable hydride of La (LaH_2 ΔH = -208 kJ mol^{-1}) is combined with a weakly forming hydride of Ni (NiH, ΔH = -8.8 kJ mol^{-1}) (Sandrock 1999), this combination forms an inter-metallic hydride with an equilibrium pressure at room temperature of 1.62 bar and an enthalpy of formation of ΔH= -30.9 kJ mol^{-1}. The effect of this inter-metallic can be seen in figure 2.5 where calculated van't Hoff plot shows the elemental binary hydrides

as compared to the ternary inter-metallic. Inter-metallic hydrides generally form in the composition AB_5, AB_2, AB, A_2B where A is a lanthanide element and B is a transition metal, this generalised form allows for a huge range of possible hydrides. Generally, inter-metallics although exhibiting good thermodynamics and kinetics such systems generally show poor hydride capacity, i.e. under <2 wt.% (Sandrock 1999). The poor capacity makes them unsuitable for automotive application, however inter-metallic hydrides of nickel have found application as battery anodes.

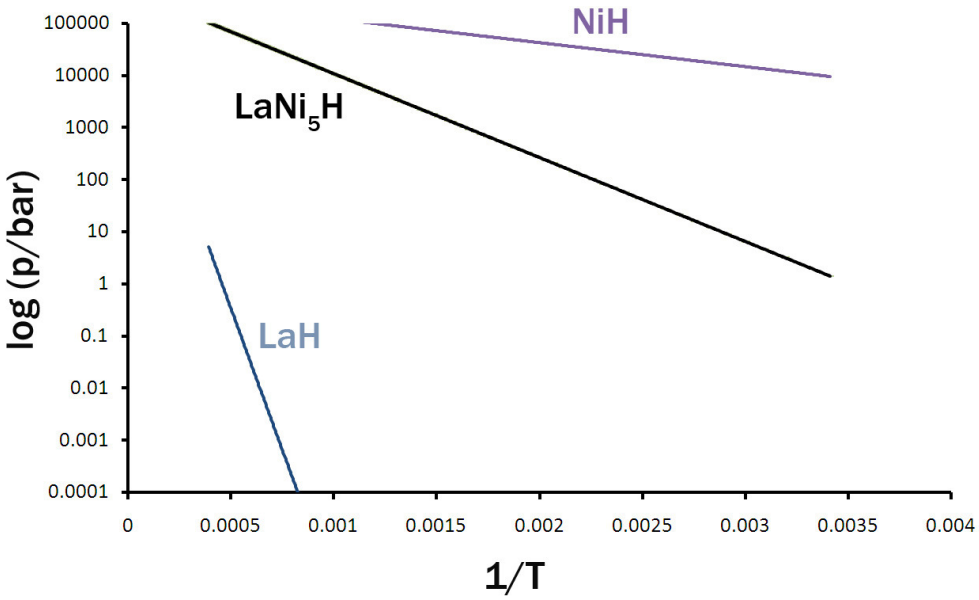

Figure 2.5. van't Hoff plots showing effects of inter-metallic hydrides compared to elemental hydrides, calculated using data from Sandrock *et al*.(Sandrock 1999) and Hypark hydride database (IEA/DOE/SNL).

2.5. Complex hydrides

Complex hydrides exhibit salt structures, with ionic bonding between the anion complex containing covalently bonded hydrogen, and a metal cation. The anion normally takes the form of a low valence aluminium or boron centre with hydrogen sitting at the corners of the tetrahedra. Alanates $[AlH_4]^-$, amides

$[NH_2]^-$, or borohydrides $[BH_4]^-$, are then combined with an electropositive element such as Li or Na to stabilise the system ($LiBH_4$, $NaAlH_4$). Complex hydrides were initially employed for single cycle storage (non-reversible) due to their high enthalpy of formation (*ca.* 116.27 kJ mol^{-1} for $NaAlH_4$ (Lee *et al.,* 2006)), until Bogdanovic and Schwickardi showed in 1997 that through doping with Ti, reversibility of $NaAlH_4$ could be achieved. They presented reversibility at 180°C and 211°C through PCI plots (Bogdanovic *et al.,* 1997) this ground breaking research led to complex hydrides becoming a key area of hydrogen storage research. Complex hydrides based on lithium have great potential as hydrogen storage materials, due to the light weight of lithium (*ca.* 6.94 g mol^{-1}) which allows high gravimetric hydrogen capacity. This review will focus on complex hydrides containing lithium, their processing (section 2.6), catalysis (section 2.7) and destabilisation (section 2.9).

2.5.1. Borohydrides of lithium

Various compositions of boron, hydrogen and metal classify as borohydrides, but the largest group is that of tetrahydridoborates $M(BH_4)_n$ composition. The low z boron provides a light anion tetrahedral structure ionically bonded to the metal (Liang *et al.,* 2004). Lithium tetrahydridoborate ($LiBH_4$), a pure metal anion complex hydride, was reported first in 1940 by Schlesinger and Brown (Schlesinger *et al.,* 1940); its synthesis is typically through the reaction of diborane (B_2H_6) with lithium dissolved in ethereal solvent (Schlesinger *et al.,* 1953). The complex hydride $LiBH_4$ has a very high gravimetric storage capacity of 18.5 wt.% (Schlesinger *et al.,* 1940) and a high volumetric capacity of 122.1 kg H_2 m^3 (Schlapbach *et al.,* 2001) it has therefore been the subject of significant research into its application as a hydrogen storage material (Züttel *et al.,* 2003b; Orimo *et al.,* 2005; Meisner *et al.,* 2006; Friedrichs *et al.,* 2008).

At room temperature $LiBH_4$ occupies a stable orthorhombic phase with what was initially thought to be Pcmn structure (Harris *et al.,* 1947) but has recently been shown to exhibit Pnma symmetry (Soulie *et al.,* 2002; Lodziana *et al.,* 2004) with a bulk density of 0.66 g cm^{-3} (Harris *et al.,* 1947) and unit cell *a*=7.179 Å, *b*=4.437 Å, c=6.803 Å (Soulie *et al.,* 2002), the orthorhombic phase structure is shown in figure 2.6 a. On heating $LiBH_4$ to 108-115 ºC (Lodziana *et al.,* 2004) a phase transformation occurs to a hexagonal structure with P63mc space group (Harris *et al.,* 1947), evolution of hydrogen has been shown during the phase change (*ca.* 0.3 mass.% (Züttel *et al.,* 2003a)), however these temperatures are below the theoretical T(1bar) for $LiBH_4$ (*ca.* 459 °C using thermodynamic data from Chase *et al.*(Chase 1998)) this therefore suggests weight loss due to H_2O or other impurities (Mosegaard *et al.,* 2007). A further high pressure phase change was first reported over 30 years ago, observed via a 6% density increase at 0.6 GPa at 298 K (Pistorius 1974) and since been refined on pressurising to 20 GPa showing three phase regions (Pistorius 1974; Talyzin *et al.,* 2007; Filinchuk *et al.,* 2008).

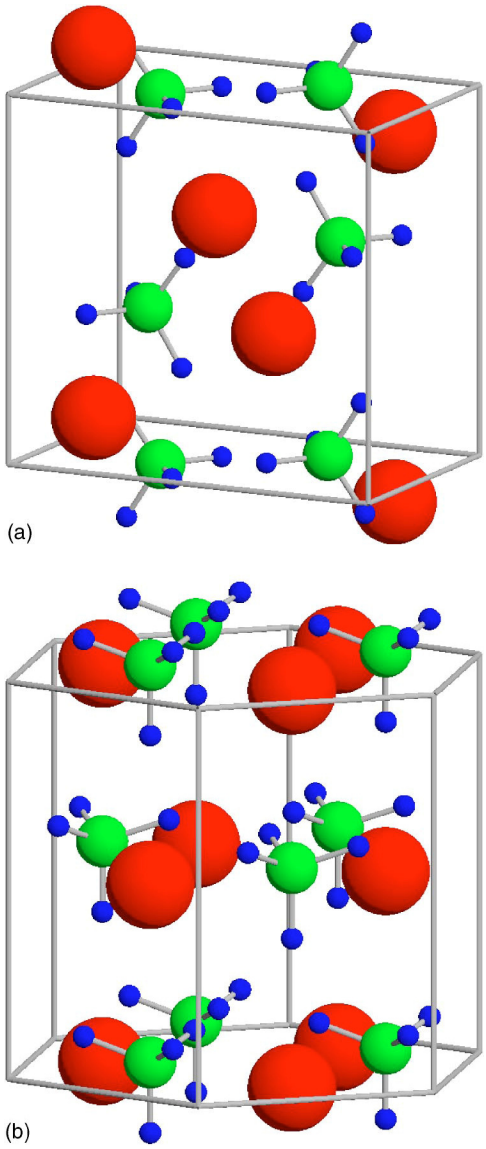

Figure 2.6. Crystal structures of LiBH4 in (a) orthorhombic phase at room temperature and (b) hexagonal phase at high temperature. Red, green, and blue spheres represent Li, B, and H atoms, respectively. (Miwa *et al.*, 2004)

Under atmospheric pressure, $LiBH_4$ melts at 268°C (Schlesinger *et al.*, 1940; Mosegaard *et al.*, 2007). Further heating of $LiBH_4$ causes the first decomposition stage of $LiBH_4$ as shown in equation 2.6.

$$LiBH_4 \rightarrow LiH + B + 1.5H_2$$ **Equation 2.6**

This reaction occurs at temperatures > 400ºC and theoretically liberates 13.8 wt.% of H_2 from the compound, the enthalpy of this reaction is ΔH = 66.9 kJ mol^{-1} H_2 (calculated from (Chase 1998) for decomposition from the liquid state $LiBH_{4)l)}$) whilst the entropy is 80.1 J K^{-1} mol^{-1} H_2. The remaining 4.5wt% hydrogen is retained as LiH, which is stable up to 900 ºC (Züttel *et al.,* 2003a). Experimental reports into the decomposition of $LiBH_4$ shows only 9 wt.% H_2 decomposed under 600 ºC (Züttel *et al.,* 2003a; Yu *et al.,* 2006b).

2.5.1.1. *Intermediate decomposition products of $LiBH_4$*

The first stage of decomposition of $LiBH_4$ shown in equation 2.6 has been reported to proceed through several intermediates. Several groups have investigated these possible phases, experimentally (Orimo *et al.,* 2005; Mosegaard *et al.,* 2007) and theoretically through density function theory (Lodziana *et al.,* 2004; Miwa *et al.,* 2004; Kang *et al.,* 2005; Ohba *et al.,* 2006). Orimo *et al.*, developed theoretical work by Ohba *at al*. with experimental results using *ex-situ* Raman and Nuclear Magnetic Resonance spectroscopy (NMR), showing an intermediate $Li_2B_{12}H_{12}$ progressing through equation 2.7 (Orimo *et al.,* 2005). Mosegaard *et al*. investigated $LiBH_4$ decomposition through *in-situ* synchrotron radiation powder x-ray diffraction (PXD) and through magic angle spinning NMR, finding two unidentified phases. The first appearing between 200-300 °C, occupying a hexagonal structure and the second between 300–400 °C occupying an orthorhombic structure (Mosegaard *et al.,* 2007), however no further details of these phases are reported. Several groups have utilised theoretical first principles calculations through DFT to suggest possible intermediate forms of $LiBH_4$, Kang *et al*. have suggested formation of other intermediate species such as Li_3BH_6 (Hexagonal R-3 space group) through

equation 2.8 and LiBH (Orthorhombic Pnma space group) through equation 2.9 (Kang *et al.*, 2005).

$12\ LiBH_4 \rightarrow Li_2B_{12}H_{12} + 10\ LiH + 13\ H_2$ **Equation 2.7**

$3\ LiBH_4 \rightarrow Li_3BH_6 + 2\ B + 3\ H_2$ **Equation 2.8**

$LiBH_4 \rightarrow LiBH + 3/2\ H_2$ **Equation 2.9**

Intermediate decomposition products are important in the full understanding of $LiBH_4$ behaviour; fully elucidating the intermediate stages of decomposition would allow reversibility of each transition to be investigated in-order to improve potential multi-component systems.

2.5.1.2. *Reversibility of $LiBH_4$*

Reversibility for the $LiBH_4$ decomposition requires elevated temperatures and pressures and has only been achieved from the elements using 35 MPa of H_2 at 564 °C for 12 h (Orimo *et al.*, 2005), or 15MPa of H_2 at 727 °C for 10h (Züttel *et al.*, 2007). Freidrichs *et al.* showed that by forming an Li_7B_6 compound under Ar at elevated temperatures, formation of $LiBH_4$ could be achieved at 15MPa of H_2 pressure at 700 °C after 40h (Friedrichs *et al.*, 2008).

The large enthalpy of the reaction yields a high T(1 bar) of 459 °C using thermodynamic data from Chase *et al.* (Chase 1998). The material is therefore stable up to 400ºC making pure $LiBH_4$ unsuitable for mobile hydrogen storage as required by DOE targets. However, its high capacity makes it an attractive component for a hydrogen store if its thermodynamics and kinetics can be improved.

2.5.2. Alanates of lithium

First characterised by Sylar *et al.* in 1967 by XRD (Sklar *et al.,* 1967), $LiAlH_4$ crystal structure is made up of $[AlH_4]^-$ tetrahedral complex anion surrounded by Li atoms. Decomposition of the alanate progresses through several stages, releasing 7.9 wt.% H_2. $LiAlH_4$ melting at 160-177 °C precedes intermediate decomposition forming solid reaction products through equation 2.10 (Block *et al.,* 1965).

$$LiAlH_4 \rightarrow 1/3\ Li_3AlH_6 + 2/3\ Al + H_2$$ **Equation 2.10**

This first decomposition is exothermic, with an enthalpy of ΔH=-10 kJ $mol^{-1}H_2$, this step is therefore non-reversible directly from the reaction products. This reaction has also been shown to occur during preparation of the hydride through ball milling (discussed in section 2.6) (Ares *et al.,* 2008). After intermediate decomposition from tetrahydridoalanate to hexahydridoalanate this phase then decomposes at *ca.* 228-282 °C through an endothermic step according to equation 2.11 with an experimentally calculated enthalpy of ΔH= 25 kJ $mol^{-1}H_2$.

$$Li_3AlH_6 \rightarrow 3LiH + Al + 3/2H_2$$ **Equation 2.11**

The LiH remains stable up to 370-483 °C when it decomposes, significantly below the T(1bar) for LiH (*cf.* 940 °C) this decomposition has been proposed to progress through equation 2.12 (Blanchard *et al.,* 2004) and represents a destabilisation reaction (see section 2.9). Various investigations into $LiAlH_4$ have been made to reduce decomposition temperatures, Ares *et al.* show 60 °C

decomposition temperature reduction through ball-milling (Ares *et al.,* 2008) (See 2.6), which also agrees with Corbo *et al.* who showed that the kinetics improved for the first stage of decomposition with smaller grain size (Corbo *et al.,* 2009). Chen *et al.* demonstrated that the reaction kinetics are improved by adding a $TiCl_3$ catalysts (Chen *et al.,* 2001).

$$3LiH + Al \rightarrow 3LiAl + 3/2H_2$$ **Equation 2.12**

The enthalpy for decomposition for equation 2.10 is exothermic, and has not been shown to be reversible even under elevated pressure and temperature, however Wang *et al.* have shown that decomposition products can be hydrogenated through formation of a solvent adduct.

$$LiH + Al + 3/2H_2 \rightarrow LiAlH_4$$ **Equation 2.13**

Their use of liquid complexing agent, Tetrahydrofuran (THF), allows hydrogenation through equation 2.13 of 4 wt.% at 100 °C at 4.5 - 97.5 bar H_2 using a Ti catalyst (Wang *et al.,* 2006). Liu *et al.* similarly showed reversibility of the $LiAlH_4$ using a Me_2O adduct at room temperature and 100 bar H_2 and decomposition at 120 °C (Liu *et al.,* 2009) they again showed use of a Ti catalyst.

2.6. Ball milling

Before discussing catalytic additions, ball milling should be discussed. The process involves grinding powders within a hardened steel or ceramic crucible through agitation with several stainless steel or ceramic ball bearings. This process can be carried out under various gas pressures (high pressure milling metals under H_2 is termed reactive mechanical alloying RMA) and at a variety of

revolution speeds and milling times. The effect of ball-milling are varied, primarily it allows the intimate mixing of the hydrides and additions which allows catalysts to be homogenously distributed through systems.

Ball-milling also causes an increase of surface area of powders by grinding them into smaller particles (Huot *et al.,* 1999), the effect of which not only increases the surface available for H_2 disassociation but also decreases the diffusion distances required for hydrogen to penetrate the particles, aiding kinetics. Smaller particles also reduce the effects of surface passivation caused by hydrided layers building up at the particle surface; which can hinder complete hydriding and thus reduce capacity (Puszkiel *et al.,* 2009). Other effects are to create surface and internal defects of the particles and decrease grain and crystal size (Ma *et al.,* 2007) which can lead to reduction in long range order of ball-milled materials causing amorphisation (Weeber *et al.,* 1988).

Particles after milling a frequently large ca. 10–100 μm but grain sizes down to 30 nm can be achieved (Zaluska *et al.,* 2001). Oxide layers on particles surface are also broken up when milled, which can further improve hydrogen diffusion (Mao *et al.,* 2007). Other notable effects are the creation of metastable phases through the high pressures generated through the milling process, the most widely reported of these is the γ-phase of MgH_2, shown to display different properties to that of β-MgH_2 (Gennari *et al.,* 2001). The high energy and high temperature (ca. 200 °C for planetary ball-mills (Takacs *et al.,* 2006)) can also cause reactions within samples, often prompting components to alloy or partially decompose, this process often accounts for reductions in experimental capacities below those calculated. Although the ball-milling process is not in itself a catalyst, it is the widely used preparatory route for hydride processing

and can improve system kinetics. Reported catalysts in this section have generally been ball milled under optimised parameters for the system.

2.7. Catalysis

In-spite of the poor thermodynamic properties of $LiBH_4$ the high gravimetric storage capacity of the material has led to many studies seeking to catalyse the decomposition of the compound (Züttel *et al.,* 2003a; Au *et al.,* 2006; Barkhordarian *et al.,* 2007; Fan *et al.,* 2008; Fang *et al.,* 2008a; Fang *et al.,* 2008b; Mosegaard *et al.,* 2008; Xia *et al.,* 2008; Yu *et al.,* 2009c). The decomposition of $LiBH_4$ and other complex hydrides does not simply rely on hydrogen diffusion as in binary hydrides; instead all elements diffuse in the decomposition of the material. Mass transport is therefore a major factor in the kinetics of hydrogenation and dehydrogenation (Vajo *et al.,* 2007a). Catalysts therefore need to be combined with other processes to reduce diffusion lengths in systems, such as those discussed in section 2.6.

2.7.1. Catalysis of binary hydrides

Much of the work into catalysis of metal hydrides involves the dispersion of metal particles over the bulk hydride surface; these studies have generally been investigated in the catalysis of binary metal hydrides, however they are also applied to borohydride catalysis. The effects of metal additions have been explored for a variety of elements including Ti, V, Mn, Ni, Fe (Liang *et al.,* 1999a) Nb (Huot *et al.,* 2003; Schimmel *et al.,* 2005) Pd (Krozer *et al.,* 1989; Zaluska *et al.,* 1999).

The main mechanism proposed is that metal particles act to aid disassociation of hydrogen H_2 at the hydride surface (Liang *et al.,* 1999b). This catalyses the transfer of hydrogen into the hydride phase through a process of spillover. Spill-over allows metals which readily disassociate hydrogen H_2 on their surface to allow hydrogen H to migrate to the host material, therefore improving kinetics by removing this disassociation barrier (Fleisch *et al.,* 1977; Zaluska *et al.,* 1999). Systems catalysed in this way therefore do not require an oxide/hydroxide free surface which is of great importance for practical hydride stores where maintaining entirely oxide free surfaces would be impossible. Schimmel *et al.* investigated similar effects due to additions of Nb and V, finding NbH or VH phases acting as a catalyst (Schimmel *et al.,* 2005). Additions of palladium metal have been explored as additives to MgH_2 (Krozer *et al.,* 1989; Zaluska *et al.,* 1999), they are shown to similarly aid disassociation, causing spill-over effect to the bulk metal.

Other work highlights the effects of oxides; Borgschulte *et al.* suggests all hydrides will form a surface oxide layer through most processing routes, which when heated will form vacancies which catalyse the dissociation of hydrogen and therefore improve kinetics of hydrogenation and dehydrogentation (Borgschulte *et al.,* 2008). However, if the thickness of an oxide layer is too great it will act as a barrier to hydrogen diffusion and hydrogenation/decomposition will cease. Additions of oxides have been widely explored, with Nb_2O_5 the most successful for MgH_2 catalysis. Barkhordarian *et* al. suggest that the effectiveness of Nb_2O_5 is because as an oxide it has the ability to occupy multiple valence states, improving the H_2 disassociation reaction at the surface (Barkhordarian *et al.,* 2003).

2.7.2. Catalysts for $LiBH_4$

Catalysts shown to improve kinetics for other complex hydrides have also been applied to $LiBH_4$. Titanium containing compounds such as $TiCl_x$ previously discussed in relation to $NaAlH_4$ was first shown by Bogdanovic *et al.* to act as a catalyst (Bogdanovic *et al.*, 1997). The reactivity of $LiBH_4$ allows additions of precursor compounds, which subsequently form more stable catalysts. Ti additions are often added through this route. Au *et al.* studied the effects of $TiCl_3$ on $LiBH_4$ decomposition, they looked at additions of 25% (yielding 8.2 wt.% experimental capacity with onset at 100 °C) and 10% (9.2 wt.% with onset at 250 °C) (Au *et al.*, 2006) they postulate cation exchange with $LiBH_4$ forms $Ti(BH_4)_3$ which subsequently decomposes to form TiB_2 but do not find evidence for this formation. Later work by Au *et al.* investigated LiCl formation through $0.1TiCl_3$ and $0.5TiCl_3$ additions, showing hydrogen build up during milling and formation of LiCl, with no $TiCl_3$ left after milling, again they propose formation of $Ti(BH_4)_3$ yet show no evidence for this phase, nor TiB_2 or TiH_2 on decomposition. Through NMR they locate two boron sources in milled materials, one matching $LiBH_4$ and the other they were unable to characterise, they propose Ti could form an amorphous phase with boron (Au *et al.*, 2008). From these results little evidence for $Ti(BH_4)_3$ has been shown, and seems more likely that a concerted reaction occurs between Ti salt and borohydride with formation of LiCl.

This would agree with Moseguaard *et al.* who investigated the effects of $TiCl_3$ in 2 mol% additions to $LiBH_4$; in-situ XRD showed LiCl formation for $LiBH_4$ and $TiCl_3$ after milling and on initial heating, they also showed dissolution of LiCl into $LiBH_4$ above *ca.* 100 °C, potentially altering its reaction behaviour (Mosegaard *et al.*, 2008). This agrees with other reports of dissolution of LiCl in $LiBH_4$, shown

to modify the unit cell of $LiBH_4$ and improve electrical conductivity (Motoaki *et al.,* 2009).

Despite the lack of specific knowledge of the role of metal and halide species $TiCl_3$ it is often added at the milling stage in numerous studies into $LiBH_4$ containing systems (Vajo *et al.,* 2005; Bosenberg *et al.,* 2007; Vajo *et al.,* 2007a).

Other halide additions widely investigated include titanium fluoride, TiF_3 (Bosenberg *et al.,* 2007; Kang *et al.,* 2007b; Wang *et al.,* 2009). Au *et al.* investigated TiF_3, in $0.1TiF_3$ and $0.5TiF_3$ additions, on milling they showed formation of LiF but with large amounts of unreacted TiF_3 and $LiBH_4$ suggesting the addition was less reactive than chloride equivalent. Decomposition yields a total weight loss for $LiBH_4 + 0.1TiF_3$ of 12 wt.%, with initial H_2 release occurring at 100 °C, this very low decomposition temperature is attributed to $Ti(BH_4)_3$ formation and decomposition analogous to the reaction postulated for chloride precursor additions, however they show no evidence for this formation and it appears more likely that the reaction occurs between lithium and fluoride. After the initial decomposition the sample did not decompose further until >300 °C, suggesting reaction of the precursor was complete at 100 °C (Au *et al.,* 2008). Effects >300 °C are likely to be due to a stable catalyst, which may be TiH_2 as this phase is shown in reaction products alongside LiF. Authors claim formation of unstable metal borohydrides ($Ti(BH_4)_3$) causes a reduction in reversibility, because on decomposition these phases tend to give off diborane B_2H_6, this depletion of boron has the effect of reducing reversibility. This seems unlikely as they are unable to show evidence for the cation exchange reaction, it is more likely that the high stability of formed chloride/fluoride species

limits system reversibility. This is analogous to work by Yu *et al* who showed reversibility of systems with additions of TiO_2 were limited by formation of stable lithium titanate phases (Yu *et al.,* 2008), this work is discussed in more detail in section 2.9.

Further effects of halide based additions may be due to the role of the halide anion, several studies have shown alteration of borohydride melting point due to halide additions. Au *et al*. showed additions of $TiCl_3$ caused a rise in $LiBH_4$ melting point, whilst TiF_3 additions reduced the melting point, they do not offer an explanation for this effect (Au *et al.,* 2008). This behaviour may be explained by an effect of LiCl reaction product on $LiBH_4$, Mosegaard *et al*. showed LiCl dissolution into $LiBH_4$ >100 °C (Mosegaard *et al.,* 2008), which may alter melting point, and potentially alter thermodynamics.

This work draws comparisons with investigations into alanate systems; Kang *et al*. investigated halide additives of TiF_3 and $TiCl_3$ into both $NaAlH_4$ and Na_3AlH_6, this work focused on the possible F^- substitution of H^- within the alanate leading to lattice strain and potential for alteration of thermodynamics for the system (Wang *et al.,* 2005a; Wang *et al.,* 2005b; Kang *et al.,* 2007a). Their work suggests fluoride additions show improvements over chloride additions due to this substitution. They suggest the lack of NaF in end products is due to fluoride doping, providing further evidence for a functional F^- ion. Their later work into $LiBH_4$ argues a similar effect, with F^- causing lattice substitution with H^-, they refer to alteration of the $LiBH_4$ melting point as further proof of this.

Au et al., investigated TiH_2 additions, $0.1TiH_2$ and $0.5TiH_2$ to $LiBH_4$ but found no reduction in onset temperature (Au *et al.,* 2008) suggesting little reaction of

TiH_2 with $LiBH_4$. As TiH_2 is often shown as an end product of halide additions it is possible that addition at milling stage does not allow good dispersion of the phase, thus limiting its effectiveness. Processing routes for addition of metal hydride catalysts to $LiBH_4$ requires further investigation.

It is clear that several effects are caused by metal halide additions. They certainly provide a route to dispersion of metal through reaction of the halide species with the borohydride, the potential catalytic effect of this dispersed metal has been discussed in section 2.7.1. The route to this dispersion has not been fully elucidated, whether it be through decomposition of an unstable borohydride formed by substitution of the metal cations, or through a direct reaction between Li and halide; however, the latter seems more likely. Finally, a secondary role of the halide may be to substitute with the H^- causing an alteration of borohydride thermodynamics, again, the role of varying halides has not been fully elucidated.

Moseguaard *et al*. investigated Au additions as catalysts, previously shown to catalytically enhance CO oxidation (Lopez *et al.,* 2004), 1.5 mol% additions were shown to cause some Li_xAu_{1-x} alloying, suggesting the effects were caused by destabilisation; catalytic aluminium additions have shown similar effects. Muller *et al*. added 10% Al additions to $LiBH_4$ allowing decomposition at 450 ºC evolving 12.4 wt.% in 12h, but they report a loss in cycling capacity on cycling. Again this is indicative of the reaction of Li with Al additions. (Muller *et al.,* 1980). Section 2.9 presents this work in relation to other destabilised systems.

Yu *et al*. have reported additions of hydride TiV alloys (BCC structure) have excellent catalytic properties when added to $LiBH_4$, with a reduction in the

main dehydrogenation peak of $LiBH_4$ to 380 °C (Yu *et al.,* 2009c). The $LiBH_4$ in this system also catalysed the decomposition of the BCC alloy, this mutual catalysis effect has also been noted in destabilised systems containing Mg (discussed in section 2.9). This work is interesting in that the end products show that the BCC alloy is retained, potentially providing a purely catalytic effect on $LiBH_4$. The authors postulate that the presence of the BCC alloy acts to improve hydrogen disassociation through increased surface vacancies.

Züttel *et al*. have looked at the effect of large quantities of SiO_2 (75%) yielding evolution of 9 mass.% of hydrogen from the $LiBH_4$ component starting at 380 °C, however taking the weight of the SiO_2 into account this equates to only 2.3 wt.% hydrogen release for the whole system. The system has not been shown to be reversible (Züttel *et al.,* 2003a) nor the exact nature of the catalytic effect discussed. The lack of reversibility could be explained by reaction of the catalyst and $LiBH_4$, Moseguaard *et al*. also investigated SiO_2 catalysts, with much lower additive quantity (*ca.* 5-20%), finding formation of orthosilicate Li_4SiO_4 in an irreversible process (Mosegaard *et al.,* 2008). Vajo *et al*. investigated the effect of Si with LiH, and found the formation of a Li_4Si decomposition product (Vajo *et al.,* 2004). Bowman *et al*. also investigated Li and Si reaction finding silicide intermetallics (Bowman *et al.,* 2005). These studies would suggest the effect of SiO_2/Si is not simply catalytic but a reaction with the Li component causing decomposition of the $LiBH_4$. The reactivity of additions with $LiBH_4$ sets a trend for other catalytic additions, many of which have problems with reaction with components of $LiBH_4$, however this reactivity can be harnessed in a process of destabilization. A more detailed discussion of this effect is presented in section 2.9.

This section has provided an overview of the routes to catalysis of $LiBH_4$, the difficulty of providing catalytic effect to such reactive compounds leads to many additions being made as precursors in order to reach more stable reacted products. However this leads to difficulty in elucidating the role of these catalysts, although many studies have shown effects of catalysts on behaviour of $LiBH_4$, the active phases and mechanisms involved in their catalysis are not fully understood.

2.8. Nanoscale and Encapsulated $LiBH_4$

Kinetic enhancement of $LiBH_4$ has also been investigated through addition of carbon structures, causing both encapsulation and reduction in particles to the nanoscale. Several reports have been made into combining nano-scale carbon structures with $LiBH_4$, with varying effects (Yu *et al.,* 2007; Fang *et al.,* 2008a; Fang *et al.,* 2008b; Gross *et al.,* 2008; Wellons *et al.,* 2009). Fang et al., investigated activated carbons chemically impregnated with $LiBH_4$, showing decomposition at 220 °C releasing 11.3 wt.% H_2 by 360 °C (Fang *et al.,* 2008b). They propose that the impregnated carbon yields a particle size for $LiBH_4$ of *ca.* 1.75 – 3.2 nm which reduces diffusion lengths aiding bulk diffusion; they also suggest the encapsulation prevents sintering of products and allows increased reversibility for the system.

Gross *et al*. also investigated confinement; their samples were synthesized through infiltration of molten $LiBH_4$ into carbon aerogel via capillary action. It was found that by confining $LiBH_4$ particles in carbon aerogel with tailored pore size (*ca.* 13 and 25 nm), particle size was limited. This effect was observed due to peak broadening in XRD patterns, this differs with the work of Fang *et al*. who observed no $LiBH_4$ component through XRD after chemical infiltration, this

is most likely due to the smaller pore sizes and infiltration mechanism reducing long range order. Gross *et al.* showed the main $LiBH_4$ decomposition temperature was lowered by 75°C to 380 °C, and kinetics at 300 °C were demonstrated to be 50 times faster than bulk $LiBH_4$. These effects were due to both a reduction in H-diffusion lengths, but also a reduction in the activation energy barrier for decomposition. An energetic destabilization from steric confinement was also postulated, but this effect is generally only applicable for solid systems, it was noted that the encapsulated material melted at a lower temperature than bulk $LiBH_4$ (*ca.* 30 °C lower) (Gross *et al.,* 2008) which was also observed by Fang *et al*.

2.9. Destabilisation

Catalysis has the potential to improve reaction kinetics and therefore reduce operating temperatures for a given hydride. However the thermodynamics for these reactions are not altered, it is through the process of destabilisation that this can be achieved.

Hydride destabilisation was first explored by Reilly *et al.* in their work into Mg/Cu and Mg/Ni systems (Reilly *et al.,* 1967; 1968) which showed that the addition of an alloying phase could reduce the enthalpy for decomposition of a hydride. The basis of destabilization is shown in figure 2.7; the left hand side shows the ΔH_a for decomposition of the system to constituent parts Y and Z, and ΔH_b for decomposition through formation of lower energy product YZ. This intermediary compound formation requires a smaller enthalpy of formation ($\Delta H_b < \Delta H_a$) and hence provides a route to full decomposition without the large energy input. In a hydride system (assuming similar entropy for reaction) this equates to a smaller required temperature for decomposition, a lower T(1 bar),

and a higher plateau pressure at a given temperature. $2MgH_2$ + Si provides a good example of single phase destabilisation (Vajo *et al.*, 2004; Bowman *et al.*, 2005). Vajo *et al.* investigated this system in 2004, showing reversible reaction according to equation 2.14

$$2MgH_2 + Si \rightarrow Mg_2Si + 2H_2$$ **Equation 2.14**

The stability of Mg_2Si (*ca.* ΔH= -77.8 kJ mol^{-1}) reduces the enthalpy for MgH_2 dehydrogenation from 75.3 kJ mol^{-1} H_2 for pure MgH_2 to 36.4 kJ mol^{-1} H_2 for MgH_2 + ½ Si. This has the effect of reducing T(1 bar) from 296 °C for MgH_2 to 20 °C for the destabilized system (Vajo *et al.*, 2004).

The right hand side of figure 2.7 shows the same effect but for a complex or intermetallic hydride comprising XYH_2. In this case the destabilising addition Z forms a lower energy product with one of the constituents X or Y, forming two resultant products X + YZ (or Y + XZ). This destabilisation mechanism can be expanded to include any number of additions, in complex, alloy or elemental hydride form.

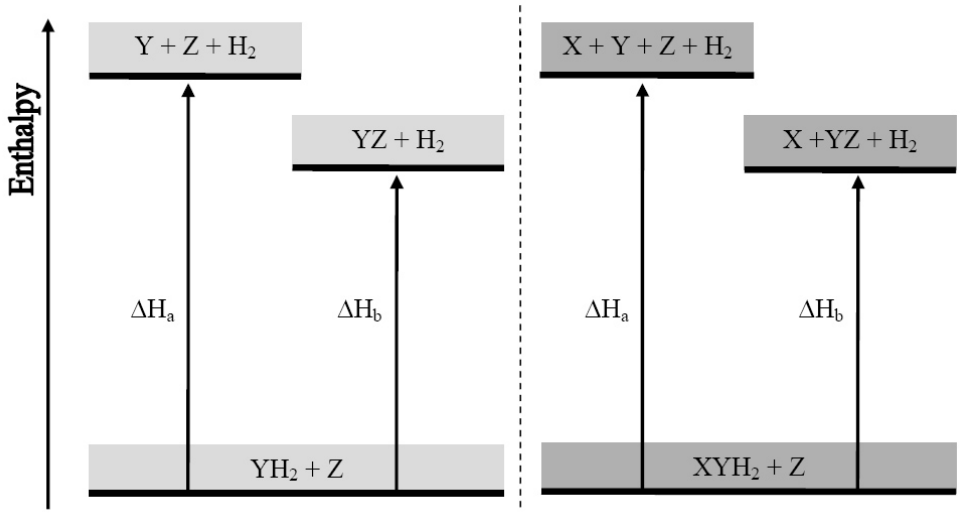

Figure 2.7. Destabilisation schematic showing lower enthalpy products with single evolved phase (left) and dual evolved phases (right).

The most significant breakthrough in this field came in 2005 when Vajo *et al.* reported work into a novel destabilised system of $2LiBH_4 : MgH_2$, the system was shown to progress reversibly through equation 2.15 with a theoretical capacity of 11.5 wt.%. Destabilisation occurs through the exothermic formation of MgB_2 which lowers the endothermic energy barrier for $LiBH_{4(l)}$ decomposition from ΔH= 58.6 kJ mol^{-1} H_2 and ΔS= 80.1 J K^{-1} mol^{-1} H_2, to values of ΔH=39.8 kJ mol^{-1} H_2 and ΔS= 91.0 J K^{-1} mol^{-1} H_2 with a consequent theoretical T(1bar)= 225 °C (Vajo *et al.*, 2004).

$$2LiBH_4 + MgH_2 \leftrightarrows 2LiH + MgB_2 + 4H_2$$ **Equation 2.15**

This system offers a unique advantage in that by destabilising through a hydride phase the system capacity is not reduced as much as for a pure metal addition.

Vajo *et al.* investigated the $2LiBH_4 : MgH_2$ system through ball-milling $LiH + 1/2MgB_2 + 0.03TiCl_3$ under Ar for 1h, the $TiCl_3$ added as a catalyst and milling

aid (see section 2.7). Hydriding behaviour of samples was evaluated at 100 bar H_2 generating >9 wt.% on heating to 350 °C over 6h. On subsequent cycles, the reaction took place significantly faster, achieving >9 wt.% capacity in 2h at 300 °C. Samples were decomposed on heating in a sealed vessel under an initial vacuum, hydrogen evolution began at *ca.* 270 °C close to the expected melting point of $LiBH_4$, the sample then evolved 8 wt.% over two stages 270-340 °C and 380-440 °C, by 450 °C the sample had evolved 5-6 bar of H_2. XRD of milled materials of $LiBH_4$ + 1/2MgH_2 + 0.03$TiCl_3$ show LiCl lines alongside $LiBH_4$ and MgH_2, whilst decomposed material showed LiCl, LiH and MgB_2, finally rehydrided materials show $LiBH_4$ and MgH_2 but no LiCl (Vajo *et al.,* 2005). They suggest possible solubility of LiCl in $LiBH_4$ which agrees with experiments by Moseguaard *et al.* discussed in section 2.7 (Mosegaard *et al.,* 2008) showing evidence of LiCl solubility in $LiBH_4$.

Experiments were repeated for materials decomposed under dynamic vacuum, with results showing no MgB_2 decomposition product, instead XRD results showed formation of metallic Mg and LiH.

The investigation by Vajo *et al.* into destabilised multi-component hydride system 2$LiBH_4$: MgH_2 (referred to as 2:1) generated many further studies into the system, its cycling and kinetics. Barkhordarian *et al.* also investigated the stochiometric system, confirming the reaction mechanism shown by Vajo *et al.*, they found the MgB_2 provided an effective precursor for borohydride formation. Further work showed formation of $NaBH_4$, and $Ca(BH_4)_2$ using MgB_2 as a boron source, an example of this formation is presented in equation 2.16. They propose that the crystalline boron form allows improved nucleation of the anion borohydide complex (Barkhordarian *et al.,* 2007).

$2NaH + MgB_2 + 4H_2 \rightarrow 2NaBH_4 + MgH_2$ **Equation 2.16**

Further work in to stoichiometric $2LiBH_4 : MgH_2$ by Bosenberg *et al*. elucidated the reaction pathway for decomposition through *in-situ* X-ray diffraction during decomposition in hydrogen. They found evidence of MgB_2 and LiH formation (Bosenberg *et al.,* 2007) which further supports the reaction mechanism investigated by Vajo *et al*. However, it does show the decomposition reaction is not concerted, with MgH_2 decomposing before $LiBH_4$. Vajo *et al*. have shown that under equilibrium conditions, ie. through a PCI experiment, that destabilisation does occur concomitantly (Vajo *et al.,* 2005), but the kinetics of this reaction seems to prevent this occurring during temperature ramps. Investigation by Pinkerton *et al*. into the cycling behaviour of $LiBH_4$ showed that samples decomposed under hydrogen pressure (*ca*. 4.6 bar) were rehydrided much faster than samples decomposed under 0.55 bar H_2. The uptake for the sample decomposed into 0.55 bar only reached 3.3 wt.% after 8 h at 100 bar which suggests re-hydrogenation of only the Mg component.

They therefore propose that reversibility can only occur when the system decomposes forming MgB_2 (Pinkerton *et al.,* 2007). However their reaction conditions do not include dynamic vacuum, which does not allow comparison with investigation of the system by Yu *et al*. into destabilisation under vacuum.

Yu *et al*. explored a non-stoichiometric ratio of $0.3LiBH_4 : MgH_2$ with decomposition into dynamic vacuum, their results conflict with other studies into the system under vacuum. Yu *et al*. Show that under vacuum conditions MgH_2 decomposes to Mg and H_2; it is suggested that the presence of Mg catalyses decomposition of $LiBH_4$ and the resultant LiH is destabilised by the

presence of Mg. *Ex-situ* XRD shows evidence of the formation of an HCP α-alloy $Mg_{0.816}Li_{0.184}$ (on heating > 440 °C) and α-alloy + cubic β-alloy $Mg_{0.30}Li_{0.70}$ on heating to 600 °C: the total reaction progresses through equation 2.17.

$$MgH_2 + 0.3\ LiBH_4 \rightarrow 0.37\ Mg_{0.816}Li_{0.184} + 0.15\ MgB_2 + 0.78\ Mg_{0.70}\ Li_{0.30} + 1.60\ H_2$$

Equation 2.17

Alloy formation can be looked at in more detail through the Mg-Li phase diagram, shown in figure 2.8, starting at the Mg rich end of the phase diagram (left) as Li diffuses into the Mg the formation of α-alloy occurs, continuing until saturation of this alloy in a composition $Mg_{0.816}Li_{0.184}$, at this point a β-alloy $Mg_{0.30}Li_{0.70}$ forms and the system exhibits a dual phase structure.

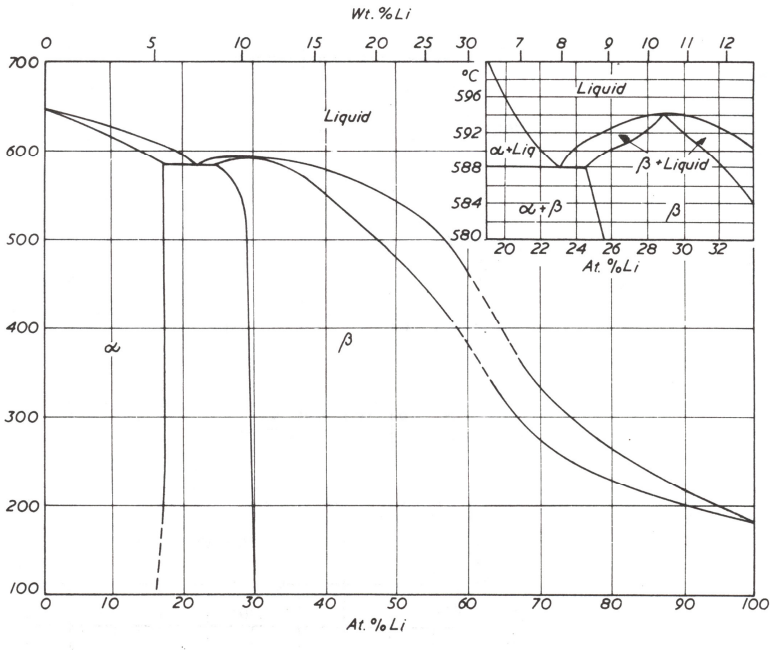

Figure 2.8. Mg-Li phase diagram. (Butts *et al.*, 2004a)

Yu *et al.* show formation of MgB_2 occurs on heating to >500 °C depleting the Mg composition of the alloy, forming a greater β-component. Re-hydrogenation of

the sample was achieved at 100 bar H_2 and 400 °C for 24 h, yielding $LiBH_4$ reformation as shown by XRD analysis. They suggest decomposition products formed under vacuum, (*viz.* α-alloy and β-alloy) allow reversibility of the system (Yu *et al.,* 2006b). Mg-Li alloy formation has subsequently been shown to form during inert dehydrogenation of other Mg/Li containing hydride systems (Fang *et al.,* 2009).

Alloy formation conflicts with other groups who show formation of Mg on decomposition under dynamic vacuum (Vajo *et al.,* 2005; Nakagawa *et al.,* 2007; Pinkerton *et al.,* 2007). Nakagawa *et al.* explored the stochiometric ratio $2LiBH_4$: MgH_2 catalysed by $TiCl_3$, and they also showed that decomposing under a sealed 5 bar H_2 pressure the system decomposes to form MgB_2 and under flowing Ar the formation of Mg metal (Nakagawa *et al.,* 2007). However they do not mention the significant shift in Mg XRD lines within their data, which suggests Mg alloys with Li through the reaction shown for the 0.3:1 system and reported by Yu *et al.*

A key advantage of the mechanism proposed by Yu *et al.* is the increased capacity over an equivalent boride forming system, as the destabilisation of LiH which remains stable on MgB_2 formation provides increased H_2 capacity through the formation of the Mg-Li alloys. However, in the 0.3:1 system, the capacity of 9.8 wt.% is still lower than the 11.5 wt.% for the stochiometric ratio explored by Vajo *et al.* Investigation into Li rich compositions of $LiBH_4$: MgH_2 decomposing through the proposed alloy forming destabilisation route has not been explored.

The conflicting results between groups investigating $LiBH_4$: MgH_2 show a disparity in terms of reaction environment, system ratio and added catalysts. This makes comparison of systems difficult and full elucidation of the reaction pathway impossible.

Other investigations into the multi-component $LiBH_4$: MgH_2 system was made through increased milling times, Wan *et al*. investigated milling LiH : MgB_2 for up to 120 h (over the 1-3 h used by other groups), they suggest processing of LiH:MgB_2 to the nano-scale allows improved kinetics for the system hydrogenation. They demonstrate that 120h of milling generates a structure with ultrafine particle size, large surface area, high defect concentration and nanoscale grain sizes (Wan *et al.*, 2008). They demonstrate at 265 °C and 90 bar H_2 uptake of 8.3 wt.%. However they only show uptake for the second cycle of approximately 2 wt.%, with remnant MgB_2 shown in ex-situ XRD. This could be indicative of Li depletion, potentially from oxidation, as there were many unidentified peaks shown in their XRD data. Wan *et al*. only investigate the impact of processing the whole system, rather than focusing on specific additions; $LiBH_4$ is generally milled for short times, whilst MgH_2 has been investigated with milling times up to 400 h (Ares *et al.*, 2007).

An interesting alternative investigation into the $LiBH_4$: MgH_2 system came through investigation of MgH_2 catalysis through additions of $LiBH_4$. Johnson *et al*. demonstrated a significant improvement in kinetics for the MgH_2 : 0.1$LiBH_4$ system, which showed improved kinetics over milled MgH_2. However, their results show no change in MgH_2 thermodynamics, instead they propose that the presence of Li^+ could create hydride anion vacancies, which improves diffusion. Their equivalent investigation of $NaBH_4$ additions did not show the same

improvements, suggesting the Li rather than B, plays a significant role. This work agrees with reports by Yu *et al*. who show mutual catalysis of MgH_2 : $LiBH_4$ systems (Yu *et al.,* 2009c) however they are unable to fully elucidate the catalytic effect of these additions.

Mao *et al*. further explored the catalytic effects of $LiBH_4$ in mass ratio $4MgH_2$: $LiBH_4$ which showed 6.7wt.% H_2 uptake in 1h at 250 °C and 3 MPa H_2 pressure (Mao *et al.,* 2007). They also explored $10MgH_2$: $LiBH_4$ cycling, presenting PCI plots at 350 °C, they do not report a destabilisation effect as the main plateau is at the expected MgH_2 pressure. They do not comment on an apparent small plateau at 0.5 bar shown as a shoulder on the data, which could indicate $LiBH_4$ also decomposes, however this would indicate $LiBH_4$ plateau pressure is increased (*ca.* 0.19 bar at 350 °C). This plateau is not shown on hydriding cycle which could be due to a concomitant reaction for hydriding between reaction products; however this possibility is not explored in the paper. They also show a smaller shoulder for the MgH_2 sample, which could suggest the effect is due to contamination from another hydriding material, however with the limited information this is difficult to elucidate. Their work also found no evidence for Li-Mg alloy formation, which is most likely due to their decomposition temperature *ca.* 350 °C, significantly lower than observed experimental temperatures of Li-Mg alloy formation (ca. 490 °C (Yu *et al.,* 2006b; Walker *et al.,* 2009)).

Puszkiel *et al*. explore small $LiBH_4$ additions to MgH_2 in their work into hydrogenation of Mg alloys $Mg_{50}Ni$ and $Mg_{15}Fe$ with 10 mol% additions of $LiBH_4$ (Puszkiel *et al.,* 2009). The Ni additions were shown to form an irreversible $MgNi_3B_2$ with the $LiBH_4$ component, this stable boride phase they suggest acts to

improve H diffusion. Hydriding kinetics were shown to improve through the additions, at 250 °C they achieve 6.0 wt.% H_2 (Ni) and 4.0 wt.% H_2 (Fe) in 600 seconds at 2.5 MPa H_2 pressure (Puszkiel *et al.*, 2009). However, their study does not explore the exact role of $LiBH_4$ in this system.

The potential for destabilised systems, containing any number of components of varying type, offers a vast range of possible systems. This has led to increased use of techniques to guide research to the systems offering the greatest potential. Modelling the reactions has therefore become a key tool in this search. Density functional theory (DFT) is one such technique, simply calculating the ground state (*viz.* the lowest energy end products) for a given reaction. Alapati *et al.* used DFT in order to theorise over 100 possible destabilised systems, although only 10 of these offer the thermodynamics suitable for fuel cell applications ($30 \leq \Delta H \leq 60$ kJ mol^{-1} H_2). Wolverton *et al.* also utilised DFT studies to identify a range of possible systems (Wolverton *et al.*, 2008), their work was subsequently investigated experimentally by Yang *et al.* who covered nine systems of the generalised form $M(H_2)$-$LiBH_4$ compositions, where $M(H_2)$ = Al, Mg, Ti, Sc, V, Cr.

Both DFT studies highlighted CaH_2 : $LiBH_4$ as a potential system with a theoretical enthalpy of 60.3 kJ mol^{-1} H_2. They both proposed destabilisation according to equation 2.18.

$$CaH_2 + 6LiBH_4 \leftrightarrow CaB_6 + 6LiH + 10H_2$$ **Equation 2.18**

The CaH : LiBH4 system was subsequently investigated by Ibikunle *et al.* who found reversibility was poor and decomposition temperatures were high (*ca.*

>400 °C) however their evidence of CaB_6 formation demonstrates the role of DFT in predicating potential systems (Ibikunle *et al.,* 2009). This system has recently been investigated further by both Pinkerton et al. and Lim *et al*. Pinkerton *et al*. added 0.25 mol.% $TiCl_3$ which reduced the decomposition characteristics to 9 wt.% hydrogen evolution by 400 °C *(Pinkerton et al., 2008)* and cycled to approx 90 % under 8.3 MPa at 400 °C . Lim *et al*. added 0.2 mol.% NbF_5 and similarly achieved 9.1 wt.% hydrogen evolution by 400 °C. The experimental enthalpy for the reaction is 56.5 kJ mol^{-1} H_2, *(Lim et al., 2008)* which is close to that calculated through DFT by Alapati *et al*. (*ca*. 60.3 kJ mol^{-1} H_2). These results demonstrate the importance of DFT as a tool to highlight possible systems, however reaction conditions, catalysts and processing parameters should also be investigated when developing an optimized system.

Other destabilising additions to $LiBH_4$ include Ni, explored by Xia *et al.*, who showed $2LiBH_4$: Ni releases 5.61 wt.% over 300-500 °C, followed by a subsequent reaction releasing 1.76 wt.% over temperature range 500-600 °C (*ca*. 7.4 wt.% total). Their end products characterised through XRD show formation of $Li_{3.59}Ni_{7.52}B_6$. They propose two reactions, firstly a destabilisation reaction through equation 2.19 occurring <500 °C, followed by a reaction between LiH and BNi to form $Li_{3.59}Ni_{7.52}B_6$ and several unidentified phases (Xia *et al.,* 2008). They did not explore the ratio $LiBH_4$: 2Ni which could progress to fully BNi_2 but the low theoretical capacity (*ca*. 5.79 wt.%) makes it less attractive as a storage material.

$$2LiBH_4 + Ni \rightarrow (1/2)BNi_2 + 2LiH + (3/2)B + 3H_2$$ **Equation 2.19**

Hydrogenation to a capacity of 5.27 wt.% was achieved at 600 °C under 10 MPa hydrogen pressure for 30 h, with some un-reacted Ni_2B retained. From van't Hoff equation applied to PCI results, an enthalpy and entropy of ΔH =-60.76 kJ mol^{-1} H_2 and ΔS =91.21 J K^{-1} mol^{-1} H_2 were calculated. They compare these values to literature values for ΔH and ΔS for $LiBH_4$ decomposing through equation 2.6 (*ca.* ΔH= 66.6 kJ mol^{-1} H_2, ΔS= 97.4 J K^{-1} mol^{-1} H_2). They suggest these values are too similar to those of pure $LiBH_4$ for any significant destabilization effect to be attributed to Ni. Whilst this is true if the reaction progressed through equation 2.19, if the reaction continued to formation of $Li_{3.59}Ni_{7.52}B_6$, the LiH component would also be decomposed and the experimental enthalpy should be compared to full $LiBH_4$ decomposition to elements ($LiBH_{4(l)}$ ΔH = 89.2 kJ mol^{-1} H_2 calculated from (Lide 2007)) this would equate to a 22.6 kJ mol^{-1} H_2 reduction in enthalpy. However, without structural characterisation of the decomposition products from PCI experiments the reaction pathway and hence the degree of destabilisation is not known.

Additions of Al, have also been proposed by several groups (Au *et al.,* 2006; Cho *et al.,* 2006; Kang *et al.,* 2007b; Remhof *et al.,* 2009). Cho *et al.* proposed the reaction through DFT calculations, suggesting the reaction route in equation 2.20, other groups experimentally show that stoichiometric ratio $2LiBH_4$: Al does progress through the proposed reaction. (Cho *et al.,* 2006; Kang *et al.,* 2007b; Remhof *et al.,* 2009). However DFT calculations by van Setten *et al.* suggest AlB_2 formation enthalpy may be as low as 16 kJ mol^{-1} H_2, thereby reducing the effect of AlB_2 formation on the destabilisation of $LiBH_4$ (van Setten *et al.,* 2009).

$$2LiBH_4 + Al \leftrightarrow AlB_2 + 2LiH + 3H_2$$ **Equation 2.20**

Kang *et al*. explored the 2:1 system with TiF_3 catalyst, decomposition at 450 °C occurred over 4h and subsequent cycles show decomposition within an hour, hydriding kinetics under 10 MPa gave uptake of approximately 5 wt.% within 2h. However, they also showed a large drop in capacity on cycling (*ca*. 7 wt.% first decomposition, to 3 wt.% on fourth decomposition) (Kang *et al.,* 2007b) they propose that diborane vaporization is to blame for the loss of capacity and also suggest incomplete AlB_2 formation could reduce capacity. This is supported by the un-reacted Al shown in *ex-situ* XRD and supports the possibility that AlB_2 is not stable enough to effect a destabilization. Remhof *et al*. investigated cycling of $2LiBD_4 : MgD_2$ system through *in-situ* neutron diffraction, showing deuteriding at 450 °C in 2h under 50 bar D_2. However they also show capacity loss when cycling with decomposition under D_2 backpressure, which they claim promotes formation of AlB_2 (rather than Li-Al alloys) (Remhof *et al.,* 2009). They suggest the separation of B and Al phases results in the capacity loss. This work agrees with Kim *et al*. who show segregation of these phases, with Al forming large grains thereby requiring long range diffusion for AlB_2 formation, this causes incomplete cycling and reduces capacity (Kim *et al.,* 2009) this could explain the presence of the large un-reacted Al component in work by Kang *et al* and further supports the low stability for the compound calculated by van Setten *et al*. (van Setten *et al.,* 2009).

Yang *et al*. also investigated destabilisation of $LiBH_4$ through Al additions, showing the material cycles through AlB_2 formation with decomposition under 1 bar H_2, however they found capacity dropped to 6.3 to 3.8 wt.% by the third cycle. On cycling with decomposition into a higher H_2 pressure of 3 bar they found much improved cycling (Yang *et al.,* 2007). They suggest, similarly to Remhof *et al*. that H_2 promotes AlB_2 formation, preventing Li-Al alloying.

Friedrichs *et al.* explored un-catalysed $2LiBH_4$: Al starting with hydrogenation of LiH and AlB_2. At 150 bar and 450°C they showed uptake of 7.6 wt.% in 20h. They agree with the theoretical DFT investigations (van Setten *et al.,* 2009) finding little destabilising effect through AlB_2 formation, but instead propose the AlB_2 source of boron promotes kinetics of hydrogenation of the borohydride phase formation (Friedrichs *et al.,* 2009). These results agree with the investigation of MgB_2 as a precursor to borohydride formation by Barkhordarian *et al.* (Barkhordarian *et al.,* 2007).

Another interesting aspect of their study is their identification of LiAl within reaction products after PCI cycling, which they suggest is due to vacuum conditions allowing LiH destabilisation by Al. However, their experiments are optimised for AlB_2 formation and the LiAl formation is noted as a possible cause in eventual reduction in hydrogen capacity (its initial formation increases capacity due to the decomposition of LiH, but prevents AlB_2 formation). They also cite the difficulty of AlB_2 formation on the long range diffusion of B required for its formation (Friedrichs *et al.,* 2009), but it seems more likely LiAl formation is more thermodynamically favourable under low partial pressure of H_2.

The range of investigations into Al destabilisation of $LiBH_4$ suggests AlB_2 formation has a low enthalpy (van Setten *et al.,* 2009) and therefore yields a small destabilising effect. However, cycling of the system seems to be improved by the AlB_2 form of B for $LiBH_4$ formation. Secondarily a LiAl phase has been identified under low partial pressure of H_2 in several studies (Friedrichs *et al.,* 2009; Remhof *et al.,* 2009), which may offer an analogous system to that proposed by Yu *et al.* into $0.3LiBH_4$: MgH_2 (Yu *et al.,* 2006b).

The phase diagram for Li-Al is presented in figure 2.9, providing several potential alloy formations such as LiAl through equation 2.21 which would yield 8.28 wt.%.

$$LiBH_4 + Al \rightarrow LiAl + B + 2H_2$$ **Equation 2.21**

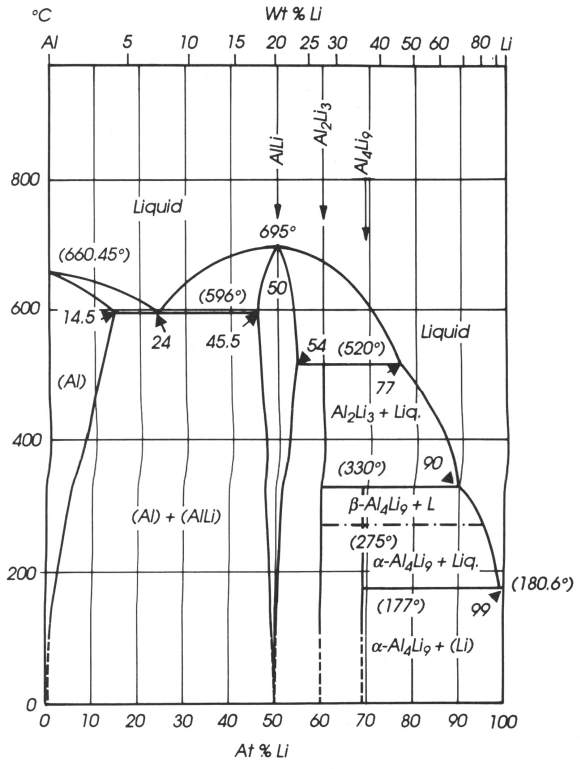

Figure 2.9. Li-Al phase diagram (Butts *et al.*, 2004a).

The use of oxides for destabilisation of $LiBH_4$ was first discussed with regard to Zuttle *et al., who* reported catalysis of $LiBH_4$ by addition of SiO_2 (*cf.* Section 2.7). The effect of SiO_2 is postulated to be due to formation of lithium silicides (Mosegaard *et al.,* 2008) (Vajo *et al.,* 2004), in a destabilisation rather than catalytic reaction. Other oxides such as TiO_2, ZrO_2, SnO_2, V_2O_3 (Au *et al.,* 2006; Yu *et al.,* 2008) have been investigated as destabilising additions for $LiBH_4$.

TiO_2 additions have been explored by Yu *et al*. who report decomposition starting at 150 °C for 1:4 mass ratio $LiBH_4$: TiO_2, with the majority of hydrogen evolved by 220 °C. Kinetics for the system are also improved, with 80% of hydrogen evolved <60 min at 220 °C. *In-situ* neutron diffraction was used to follow the phase progression through decomposition of this system. It was shown to progress through equation 2.22.

$$LiBH_4 + TiO_2 \rightarrow LiTiO_2 + B + 2H_2$$ **Equation 2.22**

The *in-situ* neutron diffraction showed $LiTiO_2$ formation beginning at 220 °C, supporting TG measurements. Unfortunately formed lithium titanates were very stable and reversibility was not achieved under 10 MPa H_2 and 400 °C (Yu *et al.*, 2008). The low capacity of this system in 4:1 mass ratio (*ca.* 3.7 wt.%) highlights the advantages of hydride additions for destabilisation in maintaining capacity of systems over oxide or chloride additions.

Hydrogen storage through destabilised complex hydrides presents a promising mechanism for reducing operating conditions of high capacity hydrides. The $LiBH_4$: MgH_2 system is one of the most exciting of these systems as it offers proven cyclability without the loss of capacity inherent in oxide and chloride additions. However, knowledge of the role of the Mg within the system and the reaction pathways of the components of the system is vital in order to optimize the system.

2.9.1. Alanate destabilising additions

Multi-component system $LiBH_4$: MgH_2 has been discussed in detail, both of its component hydride phases have been shown to be destabilized by Al, both through Al addition, or as $LiAlH_4$.

Exploration of multi-component hydride systems of MgH_2 with Al additions has been explored by Zalusaka *et al.* showing formation of $Al_{12}Mg_{17}$ alloy on decomposition (Zaluska *et al.,* 2001; Glage *et al.,* 2009). The potential for Al : Mg systems was extended to complex hydrides by Léon *et al.* who explored MgH_2 : $LiAlH_4$ and Mg : LiH : Al with processing through long ball-milling times of 48 h under 100bar H_2. They found formation of Li_3AlH_6 and an unidentified phase through ball-milling, which is most likely to be due to an iron based impurity from extended high energy milling. Subsequent decomposition under 5 bar H_2 resulted in Mg_2Al and $Al_{12}Mg_{17}$ alloys as indentified in *ex-situ* XRD (Léon *et al.,* 2009). Their exploration of $LiAlH_4$: MgH_2 does not show structural characterisation of decomposition products, however DSC experiments show a eutectic melting point at 450 °C suggesting a similar destabilisation reaction through alloy formation. Destabilization through alloy formation draws comparison to the destabilized $LiBH_4$: MgH_2 system, yet formation was shown with decomposition under 5 bar H_2, ie. Conditions under which $LiBH_4$: MgH_2 shows LiH/MgB_2 formation.

Zhang et al. also explored $LiAlH_4$: MgH_2 showing a significant destabilization effect of the system on heating under inert conditions. Samples in molar ratios of MgH_2:$LiAlH_4$ 1:1, 2:1 and 4:1 were milled for 1h and yielded enthalpies calculated through DSC measurements of 45, 48.6 and 61 kJ mol^{-1} H_2 for decomposition (NB. MgH_2= 76 kJ mol^{-1} H_2), decomposition of MgH_2 was shown to

occur at 250 °C (Zhang *et al.*, 2008) with decomposition forming $Mg_{0.816}Li_{0.184}$ and $Al_{12}Mg_{17}$ between 250-500 °C through equation 2.23 and equation 2.24.

$$4.08MgH_2 + 0.92LiH \rightarrow 5Mg_{0.816}Li_{0.184} + 4.54H_2$$ **Equation 2.23**

$$17MgH_2 + 12Al \rightarrow Al_{12}Mg_{17} + 17H_2$$ **Equation 2.24**

As the destabilising additions were the products of $LiAlH_4$ rather than the alanate phase they also explored LiH : MgH_2, Al : MgH_2 and LiH : Al : MgH_2 systems. The Al : MgH_2 decomposed to form $Al_{12}Mg_{17}$ which they suggest is very stable and hard to reverse. LiH : MgH_2 sample decomposed to form dual alloys $Mg_{0.816}Li_{0.184}$ and $Mg_{0.70}Li_{0.30}$, this result agrees well with destabilization reactions shown by Yu *et al.* through alloy formation for $LiBH_4$: MgH_2 (Yu *et al.*, 2006b). Their results for MgH_2 : Li : Al yielded the same reaction products as the $LiAlH_4$ additions, forming $Al_{12}Mg_{17}$ and $Mg_{0.816}Li_{0.184}$. However none of these reactions showed as low decomposition temperatures as for $LiAlH_4$ additions, they therefore suggest dispersion of LiH and Al is responsible for the improved reactions.

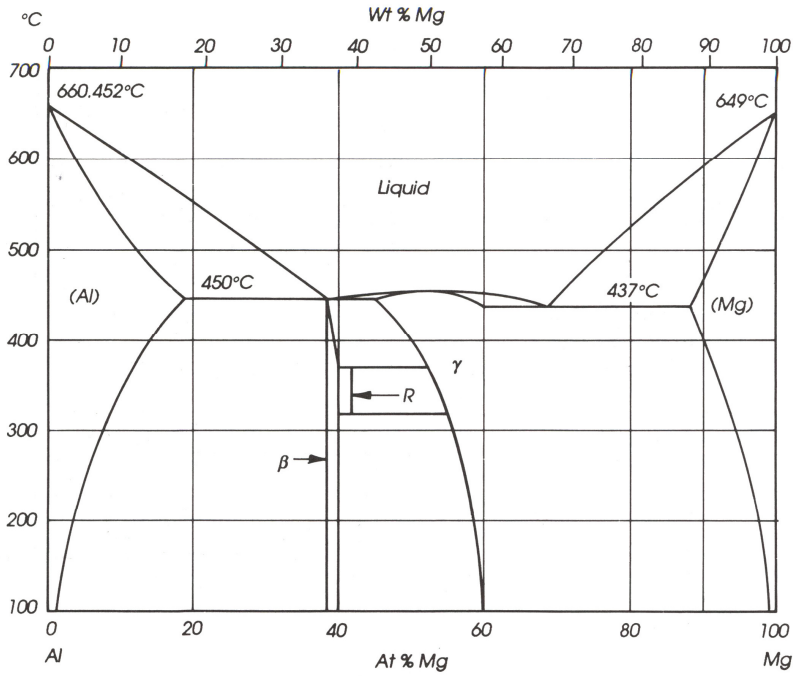

Figure 2.10. Mg-Al phase diagram (Butts *et al.*, 2004a).

The results from these three groups investigating $LiAlH_4$: MgH_2 systems demonstrates the variability of results, according to the reaction conditions, cycling parameters, ratios and any added catalysts. Léon *et al.* ball milled 1:1 ratio samples for 48h at 600 rpm under 100 bar of H_2, compared with Zhang *et al.* who milled for just 1h at 450 rpm under Ar. Both groups found components forming alloys, but Zhang *et al.* showed both Li-Al and Mg-Al alloys (under inert conditions), and Léon *et al.* showed just Mg-Al alloys (under 5 bar H_2 pressure) this is most likely that H_2 stabilized the LiH component in work by Léon *et al.*

The investigation of Al additions to MgH_2 to enable destabilised Al formation, and the addition of Al to $LiBH_4$ yielding LiAl alloys suggests that under inert conditions formation of a ternary phase hydride system could be investigated into $LiBH_4$: MgH_2 : $LiAlH_4$, no such study has been undertaken in the literature.. It also presents possibilities for other additions to the $LiBH_4$: MgH_2 system

designed to form alloys, as their use as light engineering alloys is widespread, with many other constituent elements investigated (Kellington *et al.,* 1969; Aiello *et al.,* 1998; Holzkamp *et al.,* 2000; Agnew *et al.,* 2001; Kevorkov *et al.,* 2001; Grobner *et al.,* 2002; Song *et al.,* 2005).

2.9.2. Catalysis of multi-component destabilised systems

Catalysts for multi-component systems become more complicated than for single component systems, this is particularly true for systems containing borohydrides due to the reactivity of the components. Many catalysts applied to multi-component systems have been discussed in section 2.7, with investigation being made into catalysts shown to improve both phases.

Additions of $TiCl_3$ have been widely investigated as additions to $2LiBH_4 : MgH_2$ at the ball-milling stage (Vajo *et al.,* 2004; Vajo *et al.,* 2005; Bosenberg *et al.,* 2007; Vajo *et al.,* 2007b). The advantages of other catalysts are discussed by Bosenberg *et al.,* investigating $2LiBH_4 : MgH_2$ heated to 400 °C under 5 bar H_2 pressure they show kinetics can be improved for samples decomposed at 400 °C from 20h for un-catalysed material, to 2.5h for samples with 5 at.% titaniumisopropoxide added. Worth noting is the two stage decomposition of samples during isothermal decomposition, suggesting even with a catalyst the reaction is not concomitant, but instead that an incubation period exists before $LiBH_4$ decomposition: Bosenberg *et al.* attribute this to slow diffusion combined with large grain sizes and poor reactivity of complex hydrides. They do not discuss improvements of catalytic additions to milling effectiveness. Hydriding was shown through *in-situ* XRD to occur after approximately 2h at 250 °C and 150 bar H_2 (Bosenberg *et al.,* 2007). After holding for 5h they show some small $LiBH_4$ peaks in *ex-situ* XRD.

Fan *et al.* investigated additions of 16 wt.% Nb_2O_5 to 1:1, 2:1 and 1:4 ratios of $LiBH_4$: MgH_2. They demonstrated through TG experiments a capacity of 6-8 wt.% for samples decomposed below 400 °C, with 5-6 wt.% re-hydrided at 1.9 MPa in 4 h at 400 °C (Fan *et al.,* 2008). They suggest the role of Nb_2O_5 is to form NbH_2, which forms a porous layered microstructure thus aiding hydrogen mobility within the system. However, the oxygen additions are unaccounted for, with the presence of large MgO peaks in decomposition product XRD not commented upon, they do not explore other niobium additions which do not contain oxygen.

2.10. Summary

This review of the field of hydrogen storage has focused on solid state hydride storage with particular emphasis on complex hydrides and specifically lithium tetrahydridoborate. Through this review the relevant routes to improvement of these systems toward the goals of mobile hydrogen storage have been discussed. Clearly hydrogen storage systems have great complexity, a balance of processing parameters, chemistry and reaction conditions must be carefully tailored to specific systems. The most exciting research has been into destabilised systems, with $LiBH_4$: MgH_2 system showing the most promising properties. The lack of full understanding of this system has been described in the review, highlighting the importance of understanding the reaction pathways under varying reaction conditions. System catalysis has been discussed, with catalysis results for multi-component and single phase hydrides presented. However, clearly the variety of reported effects for the same additions highlights the importance of processing and reaction environment on system behaviour. Finally, the development of systems to include further additions tailored for specific reaction pathways has been discussed.

3. Experimental Methods

3.1. Introduction

This chapter details the preparation methods and handling procedures for the samples investigated, followed by the characterisation techniques. Where equipment varies from that available commercially, any modifications, or bespoke designs are detailed.

3.2. Powder Preparation/ Ball milling

All investigated hydride samples are highly sensitive to oxygen and moisture. Therefore all handling and transfer procedures were designed to avoid any exposure to air. All samples were handled and stored in an MBRAUN Unilab glove box under Ar gas allowing O_2 < 0.1 ppm and H_2O < 0.1 ppm conditions to be maintained. Samples of 1.1 g were weighed using a Sartorius CP225D-OCE micro-balance (accuracy 0.01 mg). Samples were transferred to stainless steel ball milling pots (vol = 80 cm^3) within the glove box, loose pot lids were placed on a compression sealing PTFE ring, tape was applied to the rim of pots in order to prevent leakage during sample transfer to the mill, where pots were clamped shut. Samples were milled in a 20:1 ball to powder ratio with stainless steel ball bearings (∅ = 10 mm) for 1h (or 30h for pre-milled catalysts), at a speed of 300 rpm in a Fritsch P5 planetary ball-mill. Samples were milled in 10 minute periods, followed by 10 minute rests, preventing temperature build-up within the milling pots.

3.3. Materials

The materials purchased, including hydrides and catalysts are detailed in table 3.1. Hydride catalysts synthesised from materials presented in table 3.1 are detailed in section 3.4.6.2. Catalysts of Pd supported on nanocones were synthesised by Paolo Matelloni at The University of Nottingham using nanocone substrates supplied by SCATEC, achieving an average 3.13 nm particle size of Pd.

Material	Supplier	Purity / %
$LiBH_4$	Acros Organics	95
$LiBD_4$	Katchem	95
$^{7}Li^{11}BD_4$	Katchem	^{11}B >99,8, ^{2}D >98, ^{7}Li >98
MgH_2	Sigma Aldrich	98
$LiAlH_4$	Acros Organics	>95
$LiAlD_4$	Sigma Aldrich	90
Nanocones + 10 a.% Pd	SCATEC	-
Nb* (<45 μm)	Sigma Aldrich	99.8
NbF_5	Sigma Aldrich	98
TiH_2	Acros Organics	98
$TiCl_3$	Sigma Aldrich	99.995

Table 3.1. Materials suppliers and purity.

3.4. Material Characterisation techniques

3.4.1. Powder X-ray diffraction (XRD)

Structural analysis of samples was performed on all synthesised materials and for *ex-situ* samples from thermal analysis. X-ray diffraction offers a convenient and quick characterisation technique, providing structural analysis by probing samples with X-rays. The technique is based on the fulfilment of Bragg's law, shown in equation 3.1 where n represents the order of diffraction, λ the X-ray wavelength, d the inter-planar spacing and θ the angle of incident X-rays.

$$n\lambda = 2d\sin\theta$$ **Equation 3.1**

By probing samples with an X-ray beam through a varying angle, elastic electron scattering from separate planes within the crystallite lattice will constructively interfere when the angle fulfils Bragg's law. At such angles scattered X-rays are picked up by the detector. The polycrystalline nature of powder diffraction samples causes diffracted X-rays to be emitted in rings, which for a point detector yields a single peak for each diffraction angle fulfilling Bragg's law. The peak position from the beam axis 2θ can be used to calculate the lattice spacing, d of the phase through equation 3.1. Phase identification is performed through indexing XRD patterns to reference diffraction data for phases, accessible through the ICSD (Fluck 1996) and JCPDS-ICDD (Jcpds-Icdd 1996) databases. The shape of peaks can provide more detailed information of particle sizes and strain within the lattice using further equations based on Bragg's law. However, data presented here is used purely for characterising phases generated through hydride processing, crystallite size and strain is not reported.

X-ray diffraction experiments were performed using a Bruker D8 Advance operating with a CuK_α (λ = 1.5406 Å) source at 40 kV and 40 mA emitting through a 0.6 mm exit slit. Diffracted X-rays were collected using a Sol-X detector over a 2θ range of 20 ° - 80 °, step size of 2 ° = 0.02 ° with a one second dwell time.

Samples were mounted on a single crystal silicon wafer, providing negligible background and allowing samples as small as 1 mg to be investigated. Samples were analysed on a spinning stub, to improve homogeneity of sample crystallite alignment, unfortunately for several experiments the spin function did not engage until partway through scans, this resulted in a background shift to higher intensities at low 2θ in several XRD figures in chapter 4. In order to protect air sensitive samples all powders were prepared in an Ar glove-box and covered with an amorphous polymer tape which limits diffusion of oxygen and moisture to the hydride surface. All scans took < 4 h to complete, yielding only small oxide peaks if any.

3.4.2. Synchrotron X-ray diffraction

Synchrotron X-ray diffraction provides higher flux than that of the D8 advance used for standard XRD experiments. This allows high resolution data to be collected over significantly shorter times (30s scans rather than 2h scans) which suits dynamic temperature and pressure experiments where structural changes can occur quickly. Synchrotron experiments also provide the increased flux required for transmission based diffraction, where the beam passes through both the sample and the sample holder. *In-situ* experiments were performed by researchers from the Centre for Energy Materials at the University of Aarhus under the supervision of Associate Professor Torben R Jensen. Samples were

prepared at The University of Nottingham along with temperature and pressure profiles for *in*-situ experiments. Synchrotron data was collected at the synchrotron MAX II, Lund, Sweden MAX-Lab beamline I711 with a MAR165 CCD detector system. The selected wavelength was 1.09719 Å. The sample cell was specially developed for studies of gas/solid reactions and allows high pressure and temperature to be applied. The samples were mounted in a sapphire single crystal tube (1.09 mm o.d., 0.79 mm i.d., Al_2O_3) in an argon filled glove box $p(O_2, H_2O) < 0.1$ ppm. The temperature was controlled with a thermocouple placed in the sapphire tube next to the sample. A gas supply system was attached to the sample cell, which allows change of gas and pressure via an oil pump during X-ray data acquisition (achieving a dynamic vacuum of 10^{-2} bar). The system was flushed with N_2 or He and evacuated three times before the valve to the sample was opened prior to the X-ray experiment. The X-ray exposure time was 20 s or 30 s per powder diffraction pattern for the *in situ* experiments. The FIT2D program was used to remove diffraction spots from the sapphire sample holder and to transform raw data to powder patterns (transformation from .tiff to .chi). An excel spreadsheet macro was used to calculate peak area and was also used for calculation of Neutron Powder Diffraction peak areas.

3.4.3. Neutron Powder Diffraction (NPD)

Neutron powder diffraction shares similarities with X-ray diffraction in that it utilises elastic scattering of an incident beam, relying on the Bragg equation to provide structural analysis of the sample. NPD has advantages when studying light elements due to its increased sensitivity of the technique to low-Z elements. This is due to the interaction of the beam with the material; in X-ray diffraction the beam interacts with the electrons surrounding the nuclei and is

therefore influenced to a greater extent by high-Z elements. In neutron diffraction the beam probes the nucleus itself and scattering length is not related to atomic number, this means many low-Z elements can be detected more easily and makes it an ideal technique for tracing boron and lithium within $LiBH_4$ systems. The large incoherent scattering length of hydrogen, causes high background levels for hydride samples, this can be negated by using deuterium D_2 instead of H_2. Deuterided hydrides $LiBD_4$ and MgD_2 were therefore used for all experiments (synthesis of MgD_2 is detailed in section 3.4.6.1). Reducing incoherent scattering can be further achieved by the use of specific isotopes of elements; experiments were performed on isotopically enriched $^7Li^{11}BD_4$ which allowed improved detection of boron containing phases in diffraction data. The NPD experiments were carried out at the Institute Laue-Langevin (ILL) in Grenoble, France. The D20 neutron diffractometer at the facility was used for all experiments (Hansen *et al.*, 2008).

Experimental parameters used for all experiments were a wavelength of λ = 2.42 Å, with a flux of 4.2 $x10^7$ ns^{-1} cm^{-2}. Data was analysed using Large Array Manipulation Program (LAMP) version 6. Samples of 1 g mass (approx 1 cm^3 for optimum resolution) were loaded into stainless steel 316L vessels of 7 mm diameter bore and 10mm O.D., with a length of 500 mm and sealed under Argon gas with a Swagelok 10 mm ball valve for transportation and connection to the manifold. A gas manifold system was designed for experiment 5-25-145, before addition of automated valves and increased manifold capacity for experiment 5-125-171. The latest iteration of the design is shown in figure 3.1, the system included connections via air operated bellows valve, AV2, to deuterium supply at 100 bar, and a vacuum pump (multi-stage roots pump) via air operated bellow valve AV3. AV4 is also air actuated and allows opening of

the manifold to sample during data acquisition for monitoring of fast kinetic reactions. Manual ball valve V5 was used to isolate samples under Ar for transportation and the tubing between AV4 and V5 was evacuated before opening up the sample. Pressure was monitored with an MKS 890B Baratron. A 75 cm^3 calibrated volume integral to the manifold allowed a large volume of gas to be supplied to the sample during deuteriding, helping to minimise pressure drop of the system during deuteriding. Bellows valves were operated using 6 bar of N_2 gas, from outside the experimental area.

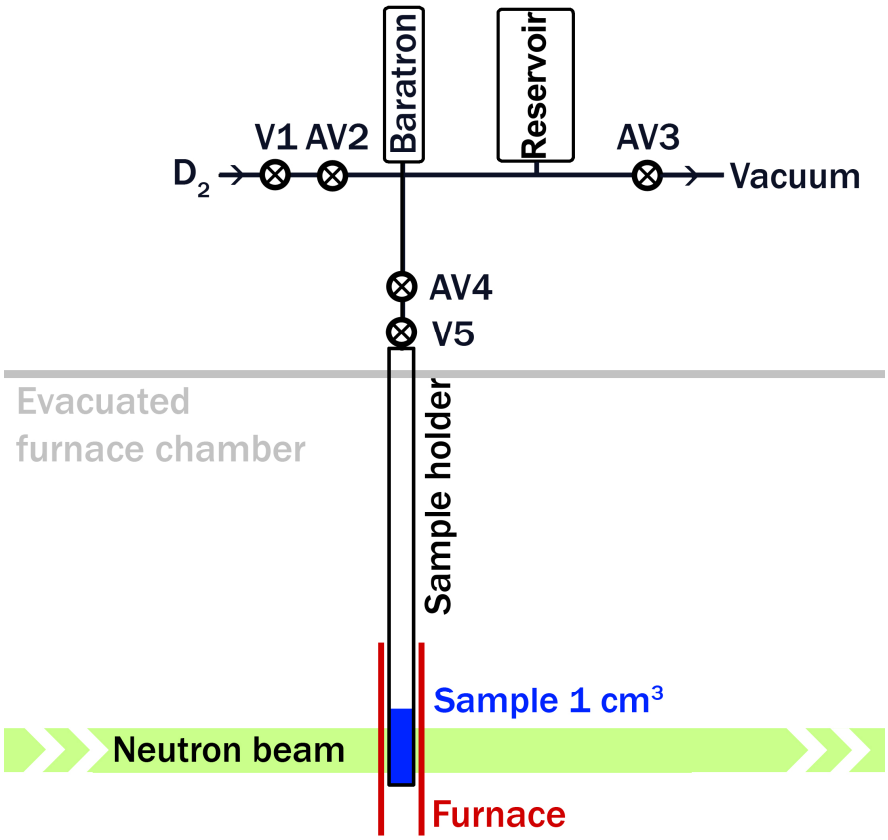

Figure 3.1. NPD gas manifold and sample holder schematic.

The baratron output was logged through use of a labVIEW program (program written for purpose using National Instruments labVIEW 8.2) to monitor pressure changes. An internal temperature calibration of a blank sample vessel

was used to calibrate any variance from the *in-situ* sample temperatures measured on the outside of the vessel during the neutron diffraction experiments, the temperature profiles were subsequently calculated and programmed using ILL software Multi-detector Acquisition of Data (MAD).

3.4.4. Differential Scanning Calorimetry (DSC)

Differential Scanning Calorimetry was performed on samples to measure the heat flow into and out of the sample. This allows detailed information on the endothermic and exothermic reactions which characterise the events during sample decomposition. DSC works through a differential system where the heat flow is measured relative to an empty sample holder. This allows variations in heat flow due to reactions within the sample to be monitored. DSC was performed using a Netzsch 204 HP Phoenix, samples were routinely run through a temperature ramp of 20-585 °C at a ramp rate of 10 °C min^{-1}. Samples were loaded in the glove-box into hermetically sealed Al pans, the sample itself was contained in a smaller Al_2O_3 crucible, this prevented sample contact with Al and therefore the potential for reaction. Before placing the sample within the DSC the Al pan was pierced using a needle, allowing gas flow into the sample during the run. The sample was quickly placed into the DSC chamber (which was under Ar) reducing any exposure time to air to <10 seconds. It should be noted that this period includes time within the Ar filled chamber, the density of which should prevent it being displaced by air (Ar = 1.633 g L^{-1} over air = 1.204 g L^{-1} (Lide 2007)). After clamping the lid closed, the sealed chamber was then flushed with argon gas three times. For samples run under inert conditions the sample received a continuous flow of argon gas (BOC, purity N6.0) at 100 ml min^{-1} at 1 bar absolute pressure for the duration of the test. Samples were also run under flowing H_2 (Air Products, purity N6.0 supplied through liquid

nitrogen trap) at 4 bar absolute pressure at 100 ml min^{-1}. The HP Phoenix also allows high pressure application of H_2 in order to hydride samples *in-situ*, parameters for these experiments are detailed for the relevant data in chapter 4.

3.4.5. Thermogravimetry (TG)

Thermogravimetry was performed using the Netzsch 209 F1 Iris, which had been modified to allow use of hydrogen gas. Thermogravimetry allows the weight loss/gain of a sample to be measured through a temperature profile. For the F1 Iris sample weight could be measured to 0.1 µg. Samples were run under the same conditions as the DSC measurements, in order to allow direct comparison of thermodynamic effects from DSC with the weight changes from TG. An empty sample pan/crucible was run for buoyancy correction before each test (or after changing gas type/flow). This standard run comprised of an initial evacuation followed by an hour isothermal at 30°C under flowing Ar/H_2 gas at 100 ml min^{-1} to allow the balance to settle. The F1 Iris did not allow high pressure environments to be achieved, therefore only experiments under atmospheric pressure could be compared to equivalent DSC runs.

3.4.6. Sieverts Apparatus

Hydride catalyst synthesis and deuteriding was performed using an in-house manufactured sieverts apparatus. A schematic of the system is shown in figure 3.2 and comprises of a calibrated manifold volume connected to a sample volume via a ball valve V2. The manifold is kept at a steady 35 °C ±0.5 °C temperature within a Perspex box surrounding the manifold, using circulation fans and heater. A Druck PMP 4010, (accuracy 0.04 % FS) pressure transducer

allows monitoring of the pressure within the sample, which was logged using a Labview program (Labview 8.2). The sample volume was heated using a eurotherm ring heater, providing temperature control from 25-650°C. Calibration and experimental gases He (BOC, purity N5.0) and H_2 (Air Products, purity N6.0) were supplied via a liquid nitrogen trap to prevent any contamination of the sample. A Pfeiffer turbomolecular drag pump also allowed 10^{-5} mbar vacuum to be achieved for decomposition of samples under vacuum and for ensuring complete removal of moisture and oxygen from system during sample changes.

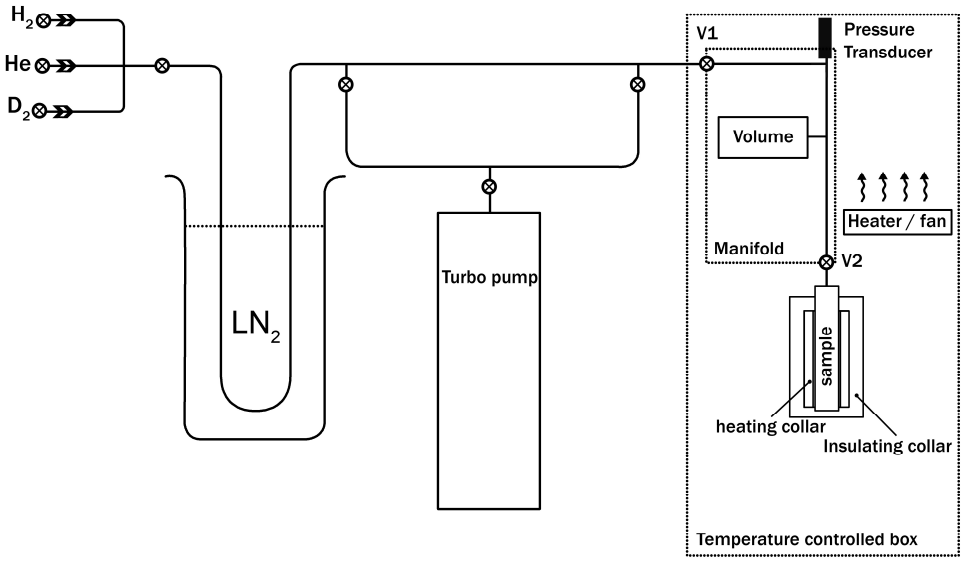

Figure 3.2. Schematic of sieverts apparatus.

3.4.6.1. *Deuteriding*

For preparation of deuterided samples for NPD, MgD_2 samples were prepared using the sieverts equipment. Samples of 2.5g MgH_2 were pre-milled for 1h to improve sample kinetics using milling conditions detailed in section 3.2. Samples were loaded in the glovebox into the sample vessel and sealed with valve V2. The sample vessel was attached via a VCR fitting to sieverts

apparatus and manifold was put under vacuum before flushing with He gas. The sample was then opened to a turbo pump with sample temperature increased to 350 °C for 10 h or until the logged pressure remained stable on closure of V1. Samples were then deuterided by applying 70 bar of D_2 (CK gas, purity D= 99.8 %, D_2= 99.6 % + HD 0.4 % supplied through liquid nitrogen trap) at 300 °C until pressure equilibrated (above plateau pressure for MgD_2 at 300 °C (*ca.* 1.8 bar)). The sample was cycled through a further decomposition and deuteriding cycle to improve the D_2:H_2 ratio. Synthesised MgD_2 was subsequently analysed through temperature controlled reaction spectrometry experiments to measure the isotope ratio of mass 4 to mass 2, structural analysis was performed through XRD.

3.4.6.2. *Hydriding*

Catalysts including VH and NbH were synthesised using sieverts apparatus. V was hydrogenated by applying 11 bar H_2 pressure at 450 °C for 24h, Nb was hydrogenated by applying 50 bar H_2 pressure at 450 °C for 24h. These materials were subsequently characterised by XRD to confirm hydrogenation.

3.4.7. PCTPro

A standard commercial sieverts apparatus (Seteram PCTPro 2000) was used for PCI cycling experiments. Samples were transferred from the glove box via a detachable sample holder, sealed with a ball valve. Samples of 100 mg were placed within an Al_2O_3 crucible acting as a barrier to the stainless steel sample holder, preventing cross contamination between samples. The PCTPro automated software took samples through required pressure profiles, whilst logging data. Effective volume calculations were performed through helium

pressure drops at experimental temperatures in order to account for temperature effects on volumetric measurements. Specific sample conditions are detailed in results chapter 4. Error for experiments was calculated for potential temperature inaccuracy of ± 5 °C and a pressure inaccuracy (shown by variability of vacuum value for pump) of ±0.1 bar, error bars are only presented for temperature variation as the potential pressure error is within the range given by data point symbols.

3.4.8. Temperature programmed reaction spectrometry (TPRS)

Mass spectrometry for evolved gases was characterised using a TPRS system shown in figure 3.3. Sample loading was performed within the glove box, samples were loaded into an alumina crucible held within a stainless steel sample holder. Quick release Swagelok connections (V1 and V2) maintained inert environment on removal from glove box and attachment to the TPRS system. An Ar flow of 100 ml min^{-1} was passed over sample during experiments, maintained via a MKS mass flow controller controlled through a MKS PR4000 control unit. The sample vessel sat within a eurotherm ring heater, controlled via a eurotherm 2416 controller. The flowing Ar gas passed through the sample vessel and exhaust gases were monitored via a capillary line to a mass spectrometer (Hiden Analytical, Dynamic Sampling Mass Spectrometer (DSMS)). Samples were heated to 500 °C at 10 °C min^{-1} with mass 1,2,3,4 logged for characterisation of evolved gases.

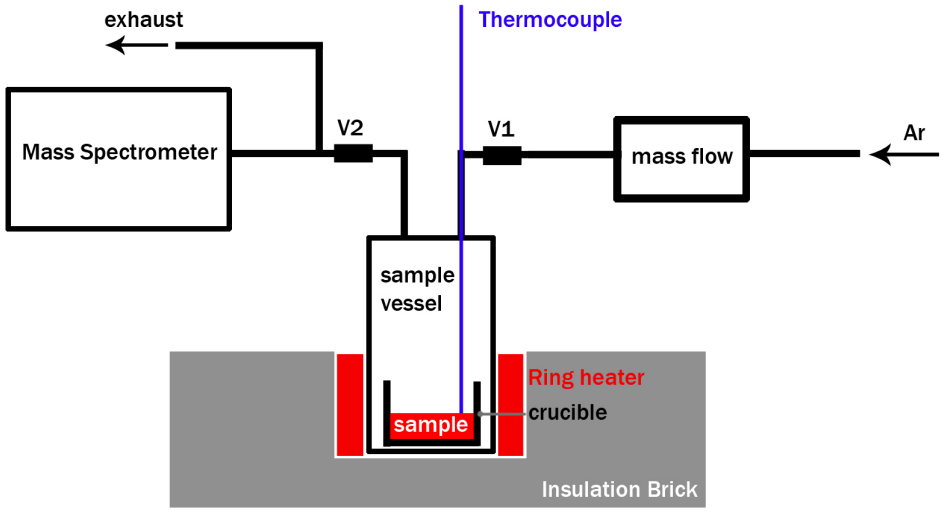

Figure 3.3. Schematic of TPRS equipment.

4. Results

4.1. Introduction

Results presented in this chapter focus on gaps in the literature discussed in chapter 2. These results will firstly present an investigation into the reaction pathways for the multi-component system $LiBH_4$: MgH_2. Investigation of single component hydrides will be presented first in section 4.2, in order to better understand their behaviour within multi-component systems. *Ex-situ* structural characterisation and DSC experiments (section 4.3.1) will then probe the behaviour of multi-component systems to compare directly with results reported in the literature. Results for *In-situ* structural characterisation (section 4.3.2) will then allow the intermediate phases and reaction pathways for $0.3LiBD_4$: MgD_2 and $2LiBD_4$: MgD_2 ratios under both hydrogen pressure and dynamic vacuum to be followed. *In-situ* structural characterisation during cycling will then be compared to PCI experiments in order to characterise the role of decomposition pathway on cycling behaviour in section 4.3.4. This broad investigation will allow the most promising system to be further investigated through addition of catalysis in order to highlight the most effective additions in section 4.4. Finally, in section 4.5, further destabilising additions of Al, are incorporated into the system in order to investigate the potential of ternary phase destabilised systems.

4.2. Single component characterization

4.2.1. $LiBH_4$ and MgH_2

Presented here are the milled and as received structural characterisation for the individual components of the explored multi-component system $LiBH_4$: MgH_2.

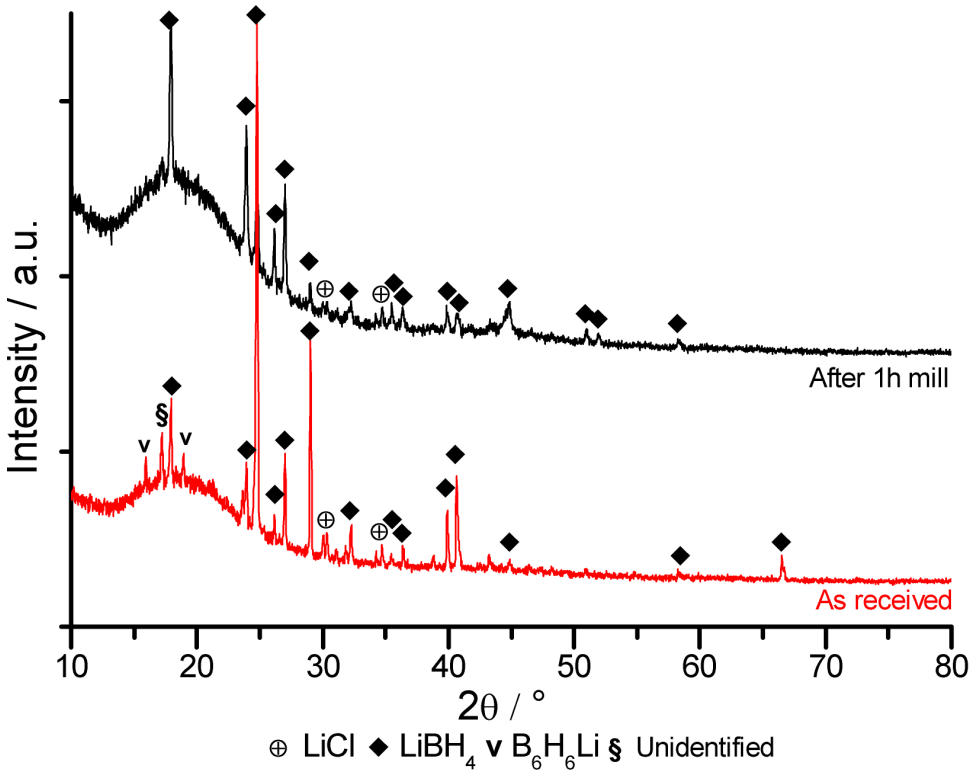

Figure 4.1. XRD data of $LiBH_4$ as received and after 1h mill.

Figure 4.1 shows XRD data for $LiBH_4$, both as received and after ball-milling for 1h. As received data shows lines matching those of the low temperature orthorhombic phase of $LiBH_{4(ortho)}$ and some evidence of trace impurities LiCl and B_6H_6Li alongside an unidentified diffraction line. Ball-milled $LiBH_4$ again shows $LiBH_4$ orthorhombic phase but all intensities are reduced, with some line intensities reduced more than others.

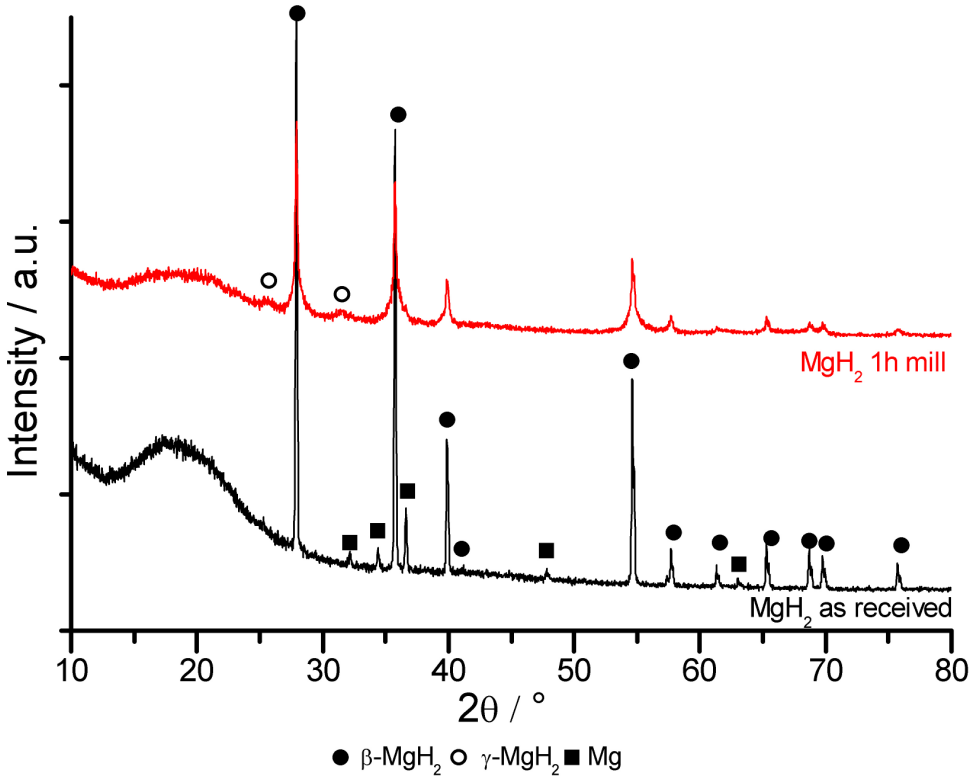

Figure 4.2. XRD data of MgH_2 as received and after 1h mill.

Figure 4.2 shows XRD data for MgH_2, for both as received and after ball-milling for 1h. The as received material had a sharp β-MgH_2 diffraction pattern and evidence of Mg metal. The ball-milled sample did not show Mg metal, instead there was broadening of the β-MgH_2 diffraction lines and a very weak γ-MgH_2 pattern.

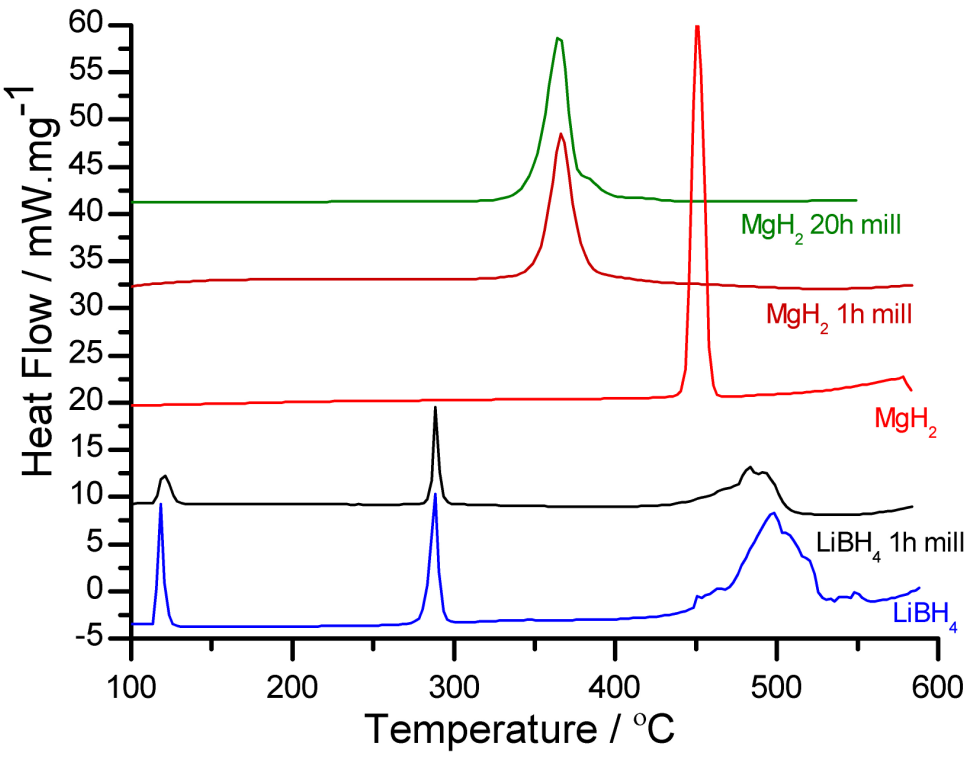

Figure 4.3. DSC plots of as received and milled samples of MgH_2 and $LiBH_4$ on heating to 585 °C under flowing Ar at 10 °C min^{-1}.

DSC plots for the single phase hydrides are shown in figure 4.3. The MgH_2 data had a large endothermic event at 450 °C, while the 1h and 20h milled samples showed similar large peaks at reduced temperature (*ca.* 366 °C and 365 °C respectively). As received $LiBH_4$ data shows three major events, two small endotherms with peaks at 118 °C and 289 °C and a broad endothermic event between 450 °C and 547 °C peaking at 497 °C. Milled $LiBH_4$ shows similar peaks, with the high temperature event, beginning at a similar temperature but ending at 500 °C, lower than for the as received sample.

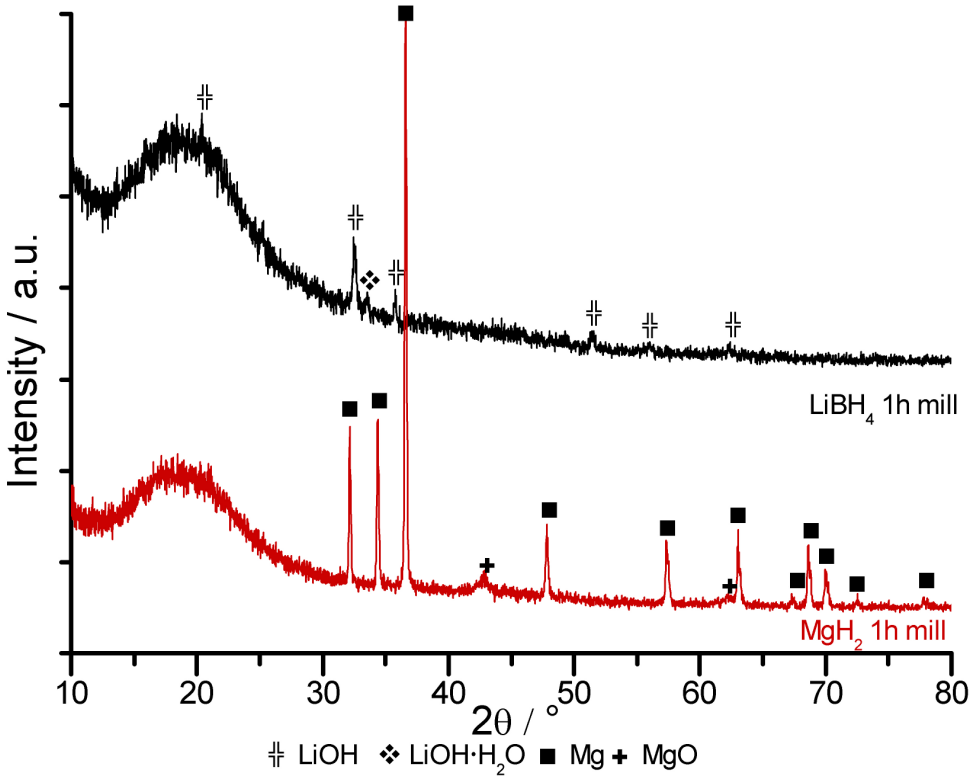

Figure 4.4. XRD data for the DSC end products of single component hydride samples, DSC experiments presented in figure 4.3

End products for single phase hydrides, $LiBH_4$ and MgH_2, characterised through *ex-situ* XRD are shown in figure 4.4. End products of MgH_2 sample contain a strong Mg pattern and MgO. $LiBH_4$ shows LiOH and $LiOH{\cdot}H_2O$ patterns.

4.2.2. MgD_2 synthesis

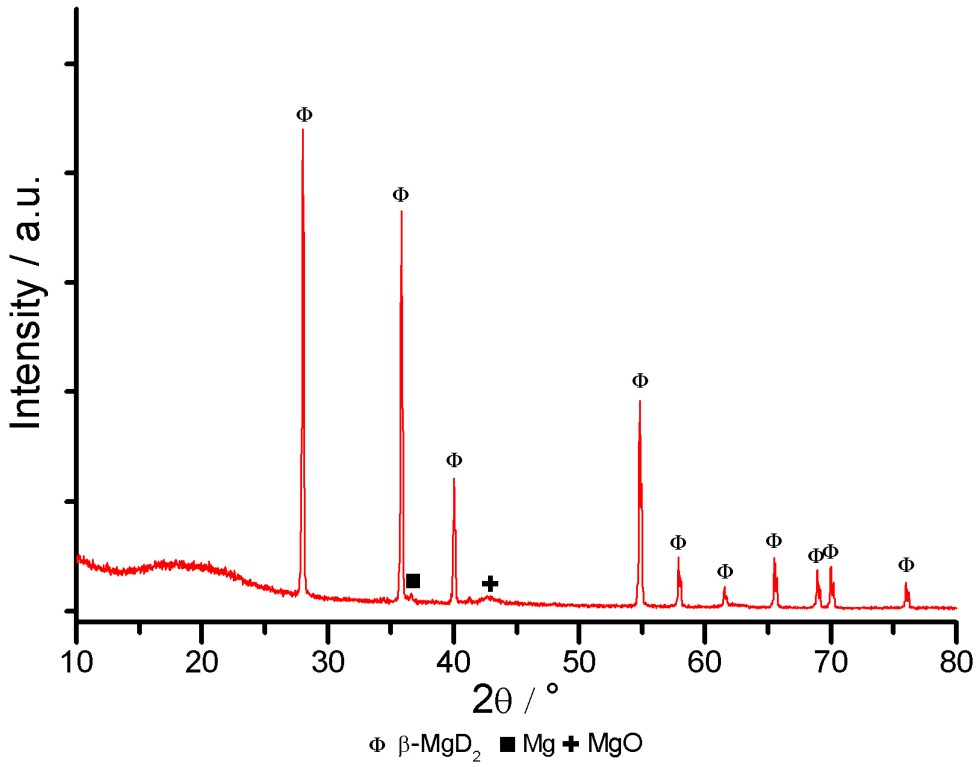

Figure 4.5. XRD data of MgD_2 synthesised.

XRD for synthesised MgD_2 prepared as detailed in section 3.4.6.1, is presented in figure 4.5. The sample gave a strong β-MgD_2 pattern, with a small MgO and Mg component.

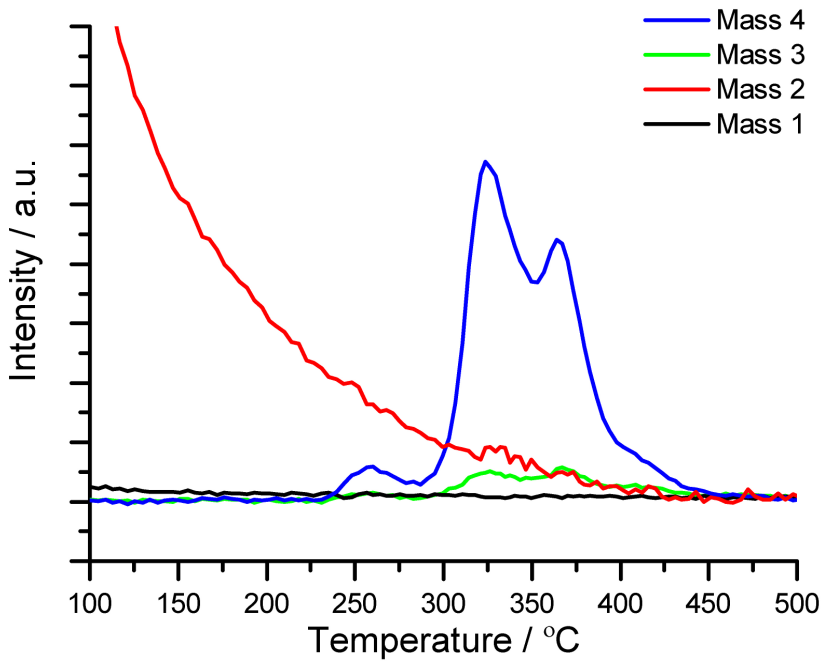

Figure 4.6. MS data for synthesised MgD_2 sample during ramp to 500 °C.

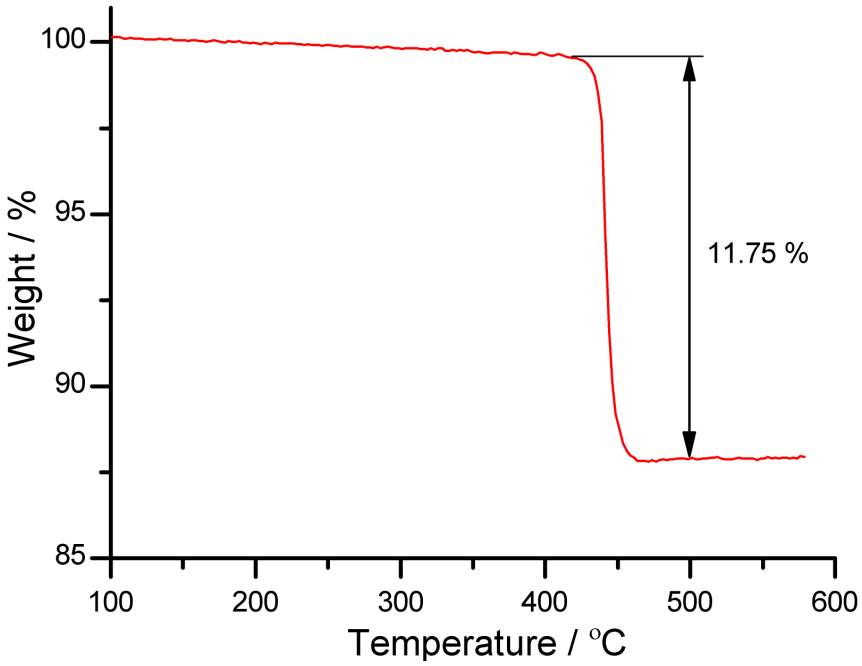

Figure 4.7. TG data for synthesised MgD_2 sample, on heating to585 °C at 10 °C min^{-1} under flowing Ar.

TG and MS data for synthesised MgD_2 through temperature ramp under flowing Ar are shown in figure 4.6 and figure 4.7. Sample weight loss begins at 410 °C,

yielding 11.75 wt.% by 500 °C. MS data shows three overlapping peaks with evolution of mass 4 and a small mass 3 peak, mass 2 peak background drops throughout the experiment showing a small peak aligned with that of mass 4.

4.3. Multi-component systems

4.3.1. Ex-situ structural and DSC results

Results presented in this section characterise the $LiBH_4$: MgH_2 multi-component system through DSC and *ex-situ* XRD techniques. Samples are referred to by their molar ratio relative to magnesium, ie. 0.3:1 refers to $0.3LiBH_4$: MgH_2. Samples of 0.3:1 and 2:1 were characterised through *ex-situ* XRD and DSC under Ar and H_2. Samples of Mg rich compositions, 0.23:1 and 0.44:1, were characterised through decomposition under just Ar.

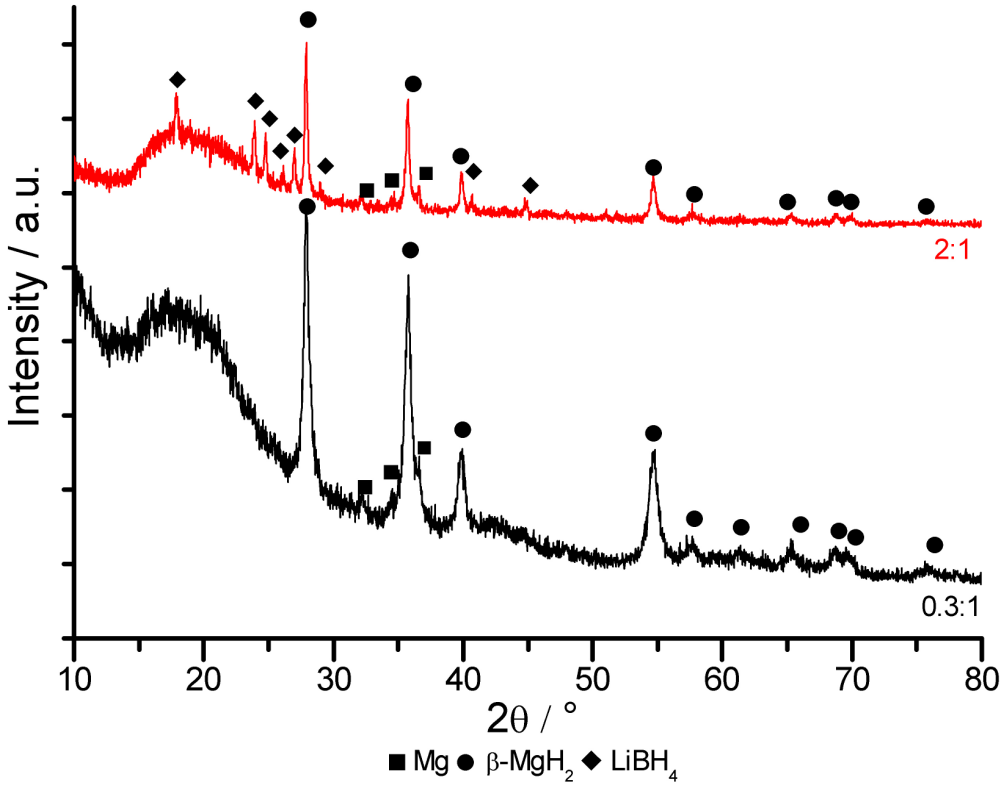

Figure 4.8. XRD data of as prepared $LiBH_4$: MgH_2 ratios.

Figure 4.8 shows the XRD for as prepared $LiBH_4$:MgH_2 ratios 0.3:1 and 2:1. The 0.3:1 data shows principally β-MgH_2 lines, with a small Mg content and no evidence of $LiBH_4$. The 2:1 sample showed β-MgH_2, Mg and $LiBH_4$ patterns.

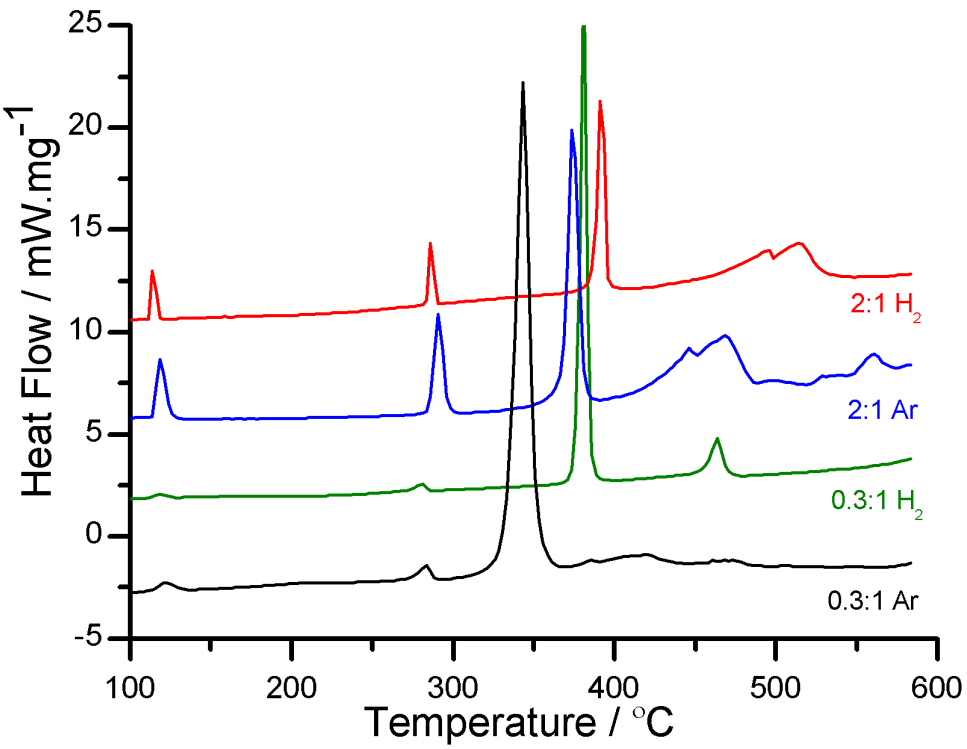

Figure 4.9. DSC plots of $LiBH_4$: MgH_2 samples on heating to 585 °C under flowing gas (1 bar Ar or 4 bar H_2) at 10 °C min^{-1}.

Figure 4.9 shows DSC data for decomposition of 0.3:1 and 2:1 samples decomposed under flowing gas (either Ar or H_2). 0.3:1 sample decomposed under Ar had small endothermic events at 122 °C and 283 °C followed by a large endothermic event at 344 °C, followed a main peak at 417 °C. 0.3:1 sample decomposed under H_2 displayed similar endotherms below 300 °C to those under Ar, however the large third endotherm is shifted to a higher temperature than under Ar to 381 °C, a final endotherm occurs at 464 °C. The 2:1 sample decomposed under Ar showed a fourfold intensity increase in endotherms at 119 °C and 292 °C compared to the 0.3:1 sample. The sample showed a large endotherm at 374 °C, which was a quarter of the area of the equivalent 0.3:1 peak, at higher temperatures a further endothermic event occurred with peaks at 469 °C and 447 °C. The 2:1 sample decomposed under H_2 had similar events

at 114 °C and 287 °C than that under Ar, before a large endotherm at 392 °C followed by an endothermic event with peaks at 497 °C and 514 °C. It is interesting to note all peaks above 300 °C appear at higher temperatures under H_2 than under Ar.

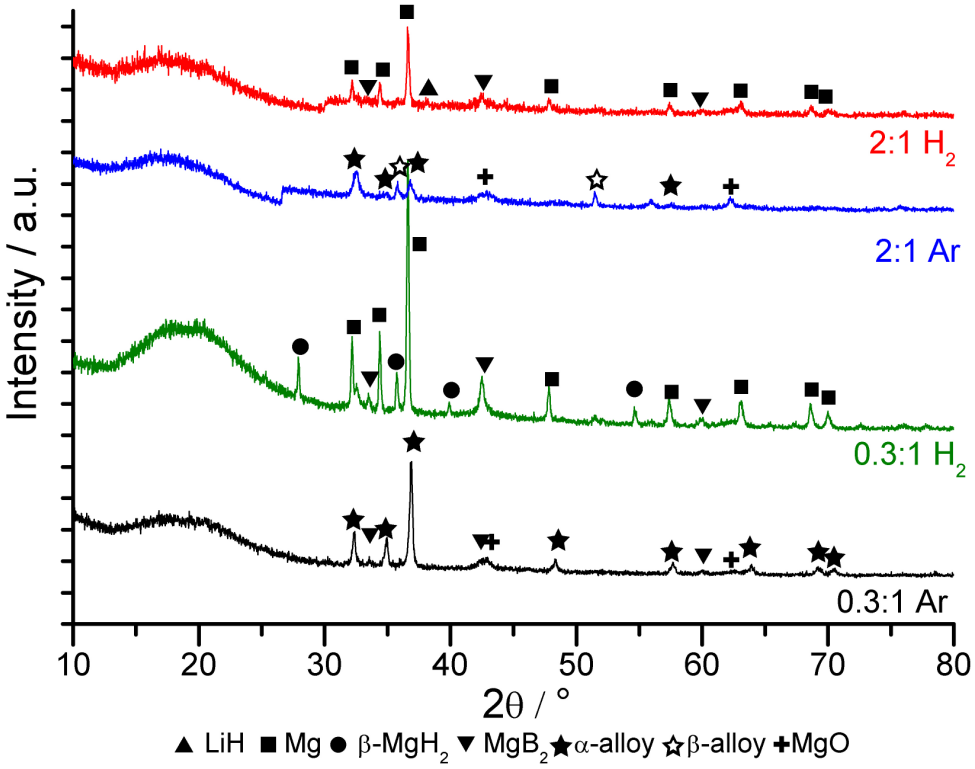

Figure 4.10. XRD data of the end products after the DSC experiments presented in figure 4.9.

Figure 4.10 shows XRD data for the DSC end products of experiments presented in figure 4.9. The 0.3:1 sample decomposed under Ar contained principally reflections matching those for $Mg_{0.816}Li_{0.184}$ (Herbstein *et al.*, 1956)(which will be referred to as the α-alloy), also detected were lines for MgB_2 and MgO. The end products for 0.3:1 sample decomposed under H_2 were a Mg phase, with a significant amount of β-MgH_2 and some MgB_2/MgO phases. Interestingly the 2:1 sample decomposed under Ar contained α-alloy and a secondary alloy

$Mg_{0.70}Li_{0.30}$ (Herbstein *et al.*, 1956)(which will be referred to as β-alloy) alongside some MgO. The 2:1 sample after DSC under H_2 showed presence of Mg, MgO, LiH and MgB_2 phases.

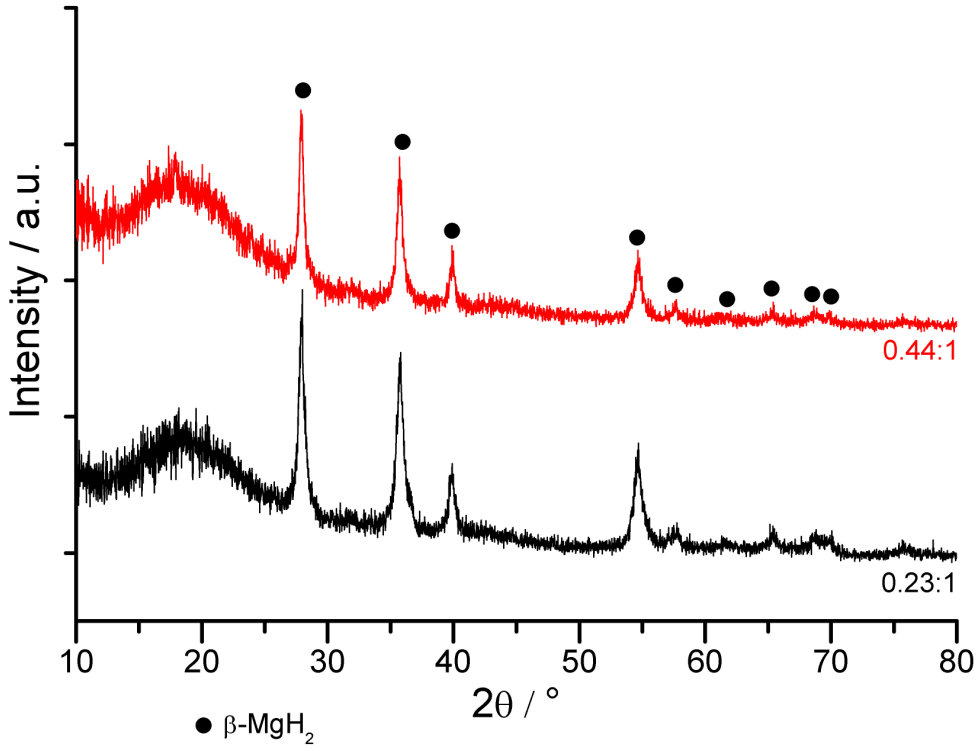

Figure 4.11. XRD data of as milled Mg-rich $LiBH_4$: MgH_2 samples.

Figure 4.11 shows XRD data for as milled Mg rich ratios $0.44LiBH_4$: MgH_2 and $0.23LiBH_4$: MgH_2, data presented shows only β-MgH_2 patterns in both samples.

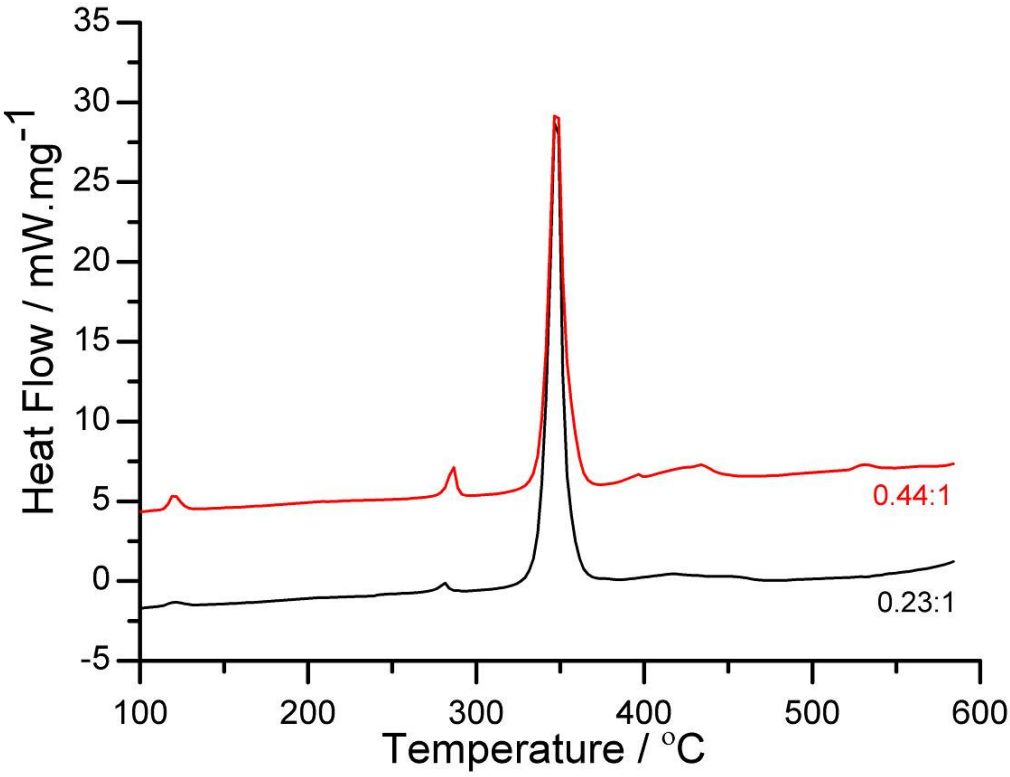

Figure 4.12. DSC plots of Mg rich ratios 0.44$LiBH_4$: MgH_2 and 0.23$LiBH_4$: MgH_2 run under flowing Ar at 10 °C min^{-1}.

Figure 4.12 shows the DSC plots of the ratios on decomposition under Ar. Both samples displayed similar endothermic events to that of 0.3:1 ratio at similar temperatures, however the 0.23:1 ratio showed a more intense third peak, whilst the first, second and fourth events were comparably less intense. The 0.44:1 sample by contrast showed more intense first second and fourth peaks, and a reduced third peak.

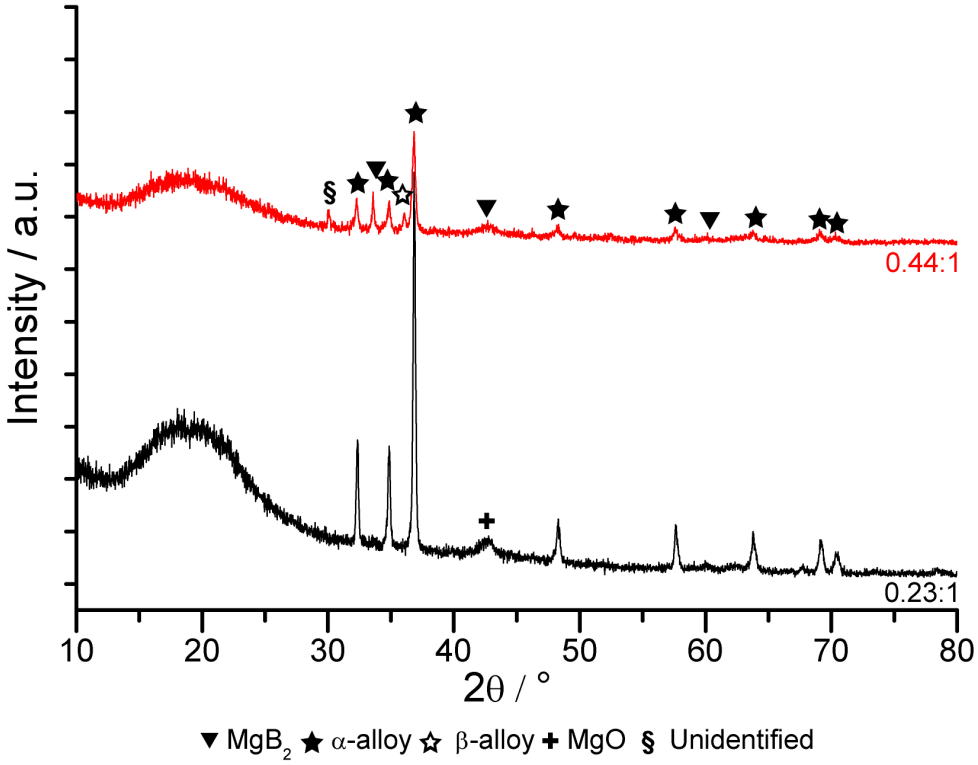

Figure 4.13. XRD data of end products after DSC experiments presented in figure 4.12.

Figure 4.13 shows XRD data for the decomposition products of DSC experiments under Ar shown in figure 4.12. The 0.23:1 sample decomposed under Ar had principally an α-alloy pattern, whilst 0.44:1 sample shows patterns for α-alloy and the Li rich β-alloy. Also detected were MgB_2 and MgO phases, and one unidentified diffraction line.

4.3.2. Neutron diffraction results

NPD results presented in this section provide *in-situ* structural analysis of varying ratios of $LiBD_4$: MgD_2. Presented plots are combined datasets taken over 5 minute periods during the temperature ramp at 1 °C min^{-1} to 560 °C (under either sealed 1 bar D_2 or dynamic vacuum) before cooling to an isothermal at 400 °C and application of 100 bar D_2 for deuteriding, samples were then cooled to 200 °C. Note that for purposes of clarity temperatures below 200 °C are not displayed in figure 4.14 avoiding the orthorhombic to hexagonal phase change. However this transition can be seen in illustrative single temperature plots in figures 4.15 to 4.18.

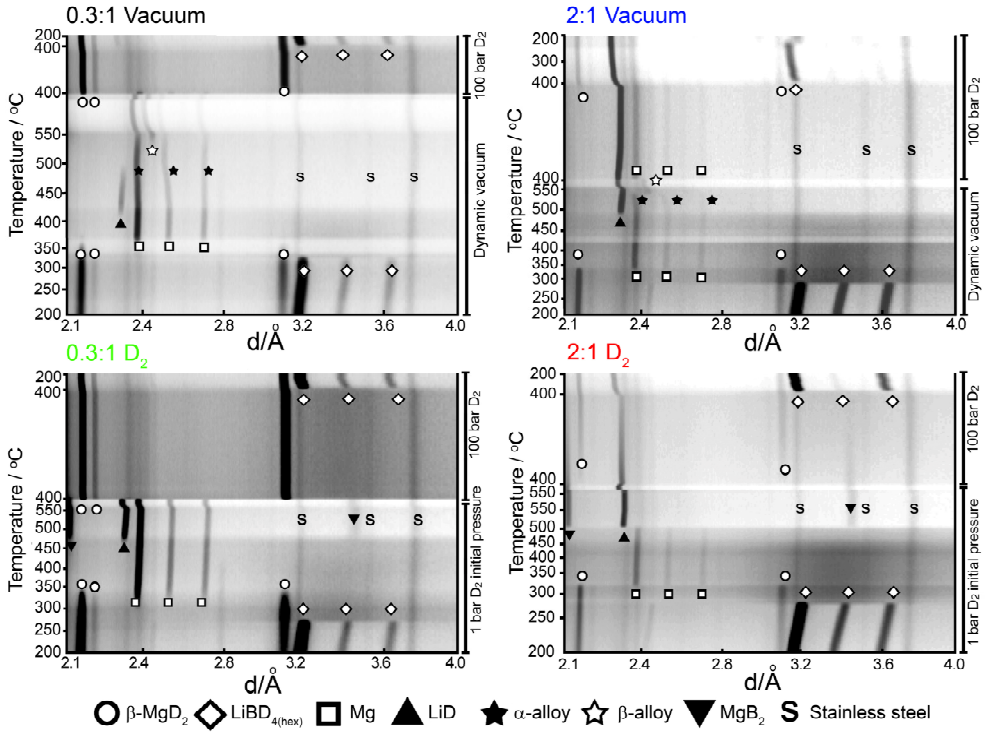

Figure 4.14. NPD data for $LiBD_4$: MgD_2 samples through temperature ramps under dynamic vacuum and D_2 pressure followed by deuteriding at 400 °C under 100 bar D_2.

In-situ NPD data for the 0.3:1 sample run under dynamic vacuum and its re-deuteriding is shown in figure 4.14, individual patterns at specific temperatures

are reproduced in figure 4.15. On heating from 200 °C the first major event was the loss of $LiBH_{4(hex)}$ phase coinciding with formation of an amorphous hump in the NPD patterns by 330 °C (visible as a darkened region centred around a d-spacing of 3.4 Å, in figure 4.14, and as a hump in figure 4.15). At 330 °C the β-MgD_2 began to drop coinciding with the formation of a Mg phase. Heating to 400 °C the amorphous hump disappeared and a LiD phase appeared. At this point there was a shift to smaller d-spacing in the Mg diffraction lines, signifying the formation of the α-alloy and at 530 °C a β-alloy phase appeared. At 560 °C the sample retained dual α-alloy / β-alloy composition. The decomposed sample was then cooled to 250 °C (sample retained α / β composition) before ramping to 400 °C and 100 bar D_2 was applied. On deuteriding, α-alloy and β-alloy phases were lost with a concomitant formation of the amorphous hump and β-MgD_2. After 1h deuteriding the sample was cooled to 200 °C whereupon a $LiBD_{4(hex)}$ phase formed alongside a β-MgD_2 and residual LiD phase.

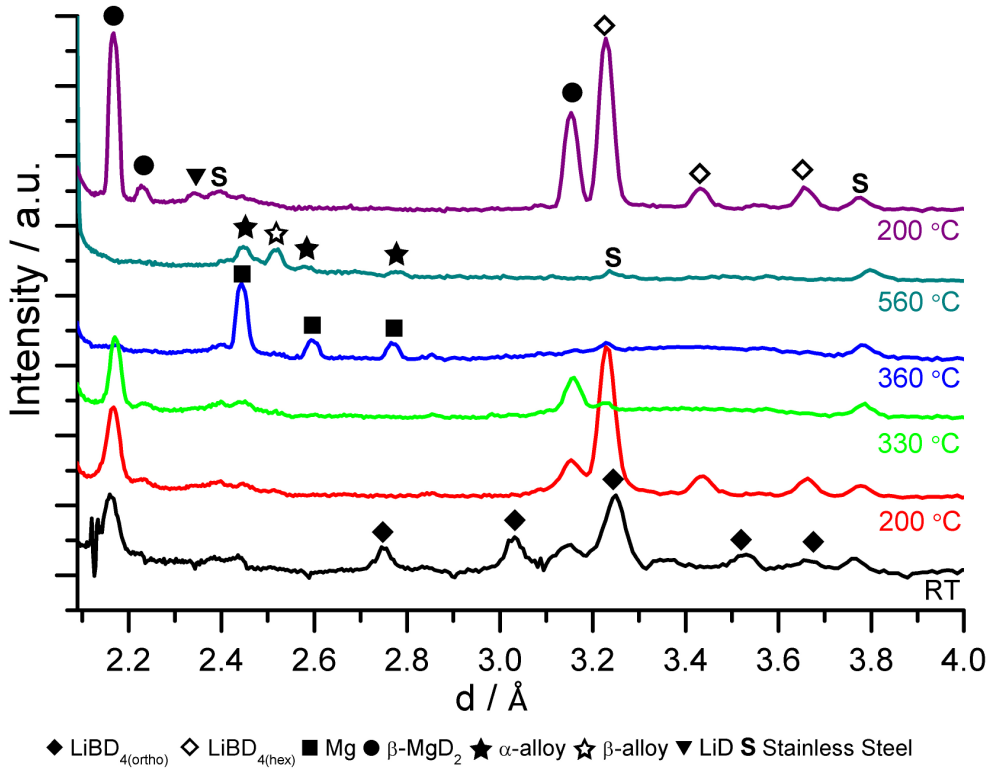

Figure 4.15. Single temperature NPD plots for 0.3$LiBD_4$: MgD_2 sample decomposed under dynamic vacuum and deuterided under 100 bar D_2 at 400 °C for 4h.

NPD data for a 0.3:1 sample decomposed under deuterium is shown in figure 4.14 and figure 4.16, the data displays a similar phase progression to that under dynamic vacuum up until loss of β-MgD_2 phase at 320 °C. At 470 °C the amorphous hump disappeared and LiD and MgB_2 patterns appeared alongside the Mg, this structure was kept on heating to 560 °C and on cooling to 400 °C. On application of 100 bars D_2 at 400 °C the LiD and MgB_2 patterns reduced quickly with a concomitant formation of the amorphous hump and β-MgD_2 phase. The cooled sample gave a $LiBD_{4(hex)}$ pattern alongside β-MgD_2 and a small residual LiD phase.

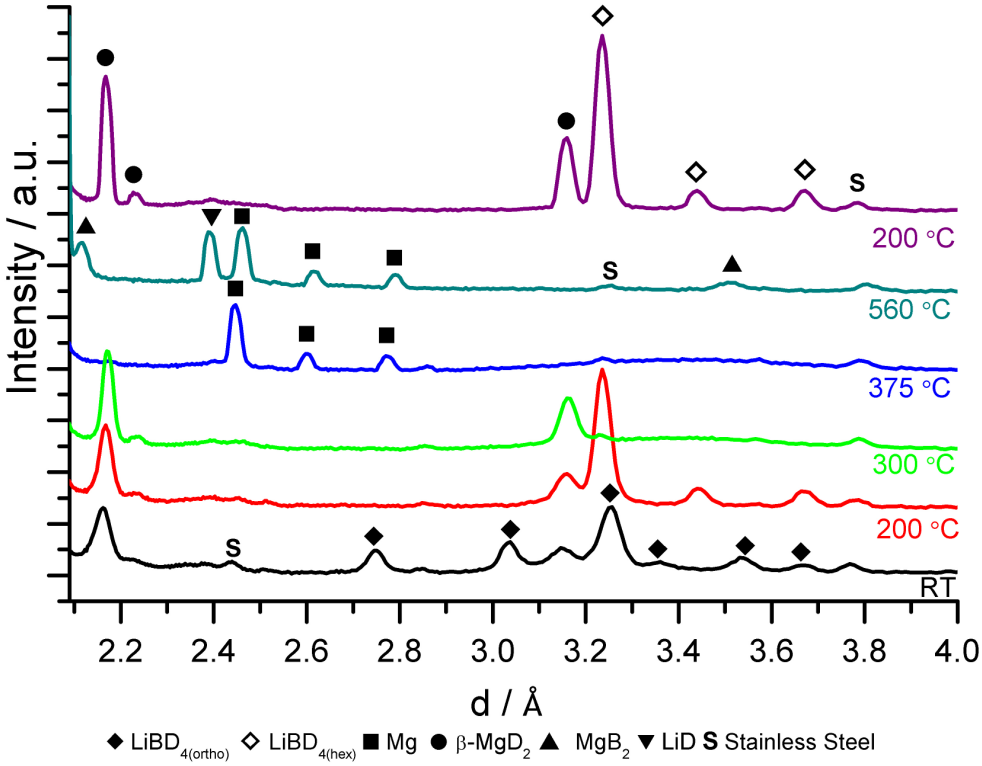

Figure 4.16. Single temperature NPD plots for $0.3LiBD_4 : MgD_2$ sample decomposed into an initial 1 bar D_2 and deuterided under 100 bar D_2 at 400 °C for 4h.

NPD results for a 2:1 sample decomposed under dynamic vacuum is shown in figure 4.14 and figure 4.17. The materials at RT had, as expected, a lower intensity β-MgD_2 pattern (a quarter of the peak area of 0.3:1), and a more intense $LiBD_4$ pattern (twice the peak area of 0.3:1). Interestingly, on heating the phase progression was similar to that for the 0.3:1 sample run under vacuum, progressing through formation of alloys. After LiD formation at *ca.* 480 °C a shift to smaller d-spacing occurred in Mg diffraction lines as α-alloy formed. At 540 °C the β-alloy phase appeared, this alloy formation continued until only β-alloy existed alongside LiD by 560 °C. The sample was then cooled to 400 °C and 100 bar of D_2 was applied, on deuteriding β-alloy was quickly lost and a Mg phase appeared. In stark contrast to 0.3:1 sample under vacuum, instead of β-MgD_2 formation within 10 minutes, no formation of β-MgD_2 was

observed until 200 minutes of deuteriding. On cooling under deuterium the β-MgD_2 pattern significantly increased in intensity, with a weak $LiBD_{4(hex)}$ pattern also observed. However, large patterns of LiD and Mg were retained.

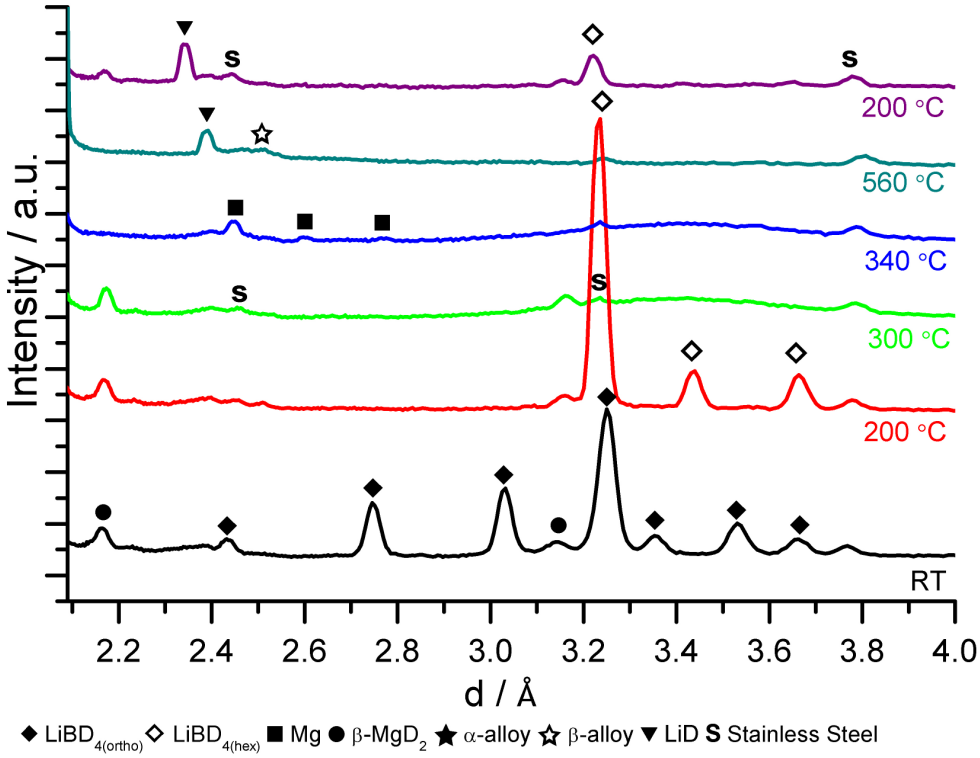

Figure 4.17. Single temperature NPD plots for $2LiBD_4 : MgD_2$ sample decomposed under dynamic vacuum and deuterided under 100 bar D_2 at 400 °C for 4h.

NPD results for the 2:1 sample decomposed under deuterium are shown in figure 4.14 and figure 4.18. Starting materials are similar to those of 2:1 under vacuum, with events up to loss of the amorphous hump progressing through the same transitions. Heating to 440 °C the amorphous hump begins to reduce and towards the end of the hump loss, at 510 °C, LiD and MgB_2 patterns appeared, this structure was maintained on heating to 560 °C. The sample was then cooled to 400 °C and 100 bar D_2 was applied, resulting in the steady decrease in intensity of the LiD and MgB_2 patterns and a corresponding increase in intensity

of the β-MgD_2 pattern and amorphous hump. $LiBD_{4(hex)}$, β-MgD_2 and LiD were observed on cooling to 200 °C.

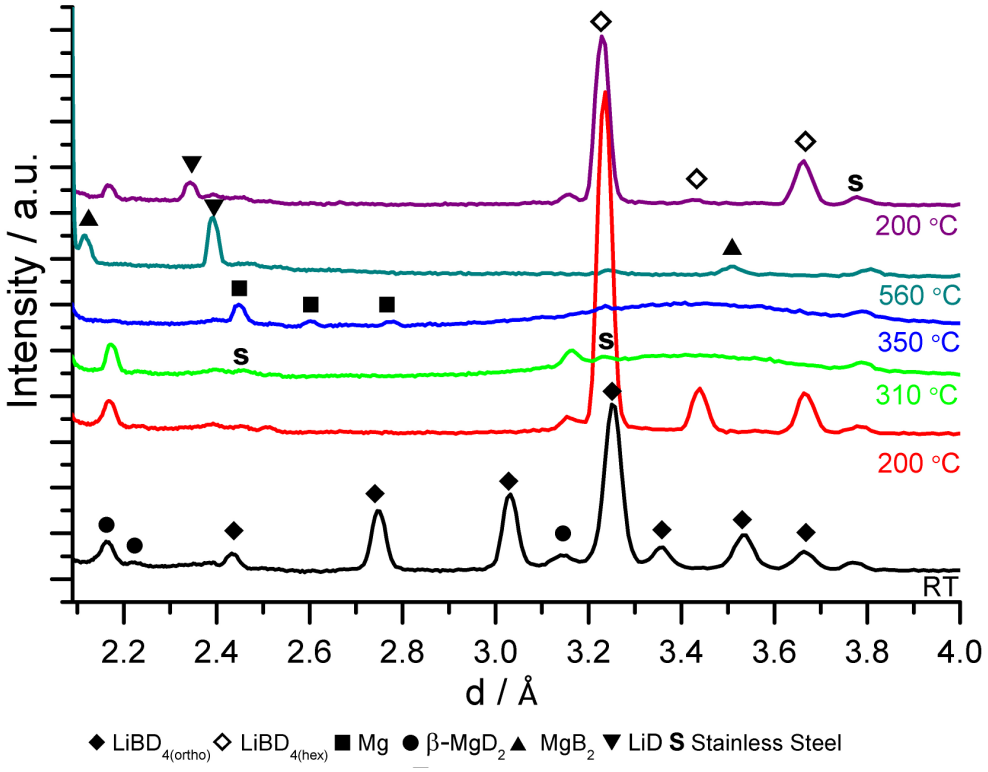

Figure 4.18 Single temperature NPD plots for $2LiBD_4 : MgD_2$ sample decomposed into an initial 1 bar D_2 pressure and deuterided under 100 bar D_2 at 400 °C for 4h.

4.3.2.1. *Magnesium rich systems*

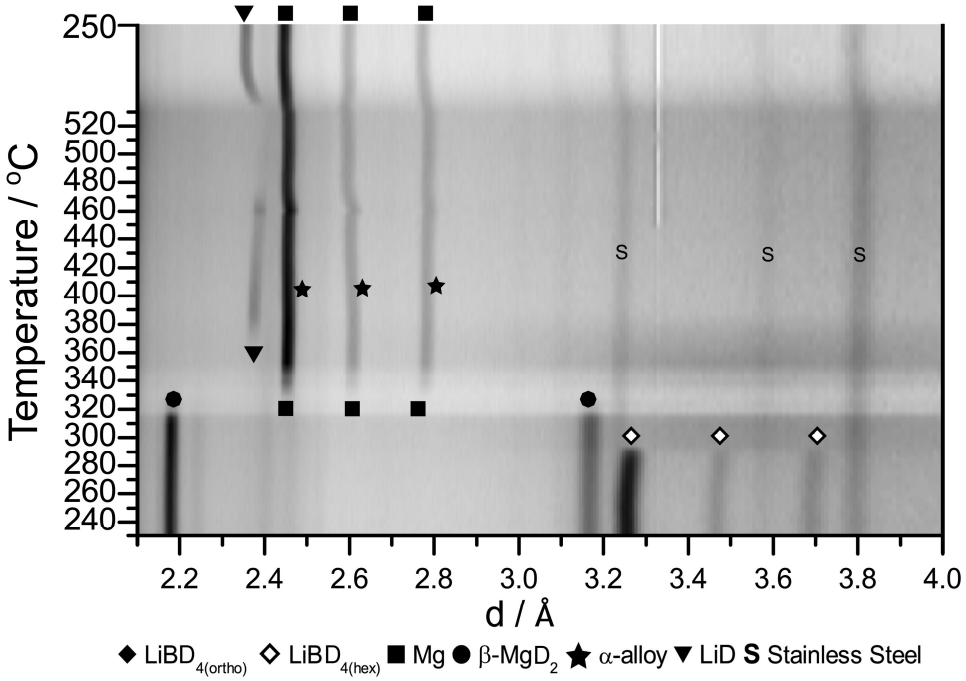

Figure 4.19. NPD data for 0.23$LiBD_4$: MgD_2 through temperature ramp and cool under dynamic vacuum.

In-situ NPD for a Mg-rich 0.23:1 sample run under dynamic vacuum is shown in figure 4.19 and figure 4.20. Unfortunately there is a blip in the baseline at d = 3.35 Å running throughout the data set, which was due to an instrument data processing error. Phase progression followed that of 0.3:1 sample under vacuum; through alloy formation, however there were several interesting differences between the samples. Formation of α-alloy began at *ca.* 390 °C, however on heating to 477 °C there occurred an increase in LiD intensity coinciding with a rapid shift in α-alloy peaks to larger d-spacing, on further heating peaks returned to smaller d-spacing and LiD lines reduced, before being lost at 496 °C. At the end of the temperature ramp, 533 °C, the sample contained only α-alloy pattern, this compares to 0.3:1 sample which showed both α and β-alloy. Interestingly, unlike other presented NPD data, these phases do not remain stable on cooling, instead there appears to be an increase

in d-spacing for the α-alloy lines, seen most clearly in (002) plane (this is acting against the effects of cooling), LiD phase also appears at *ca.* 400 °C. At 260 °C the cooled sample contained LiD and Mg phases.

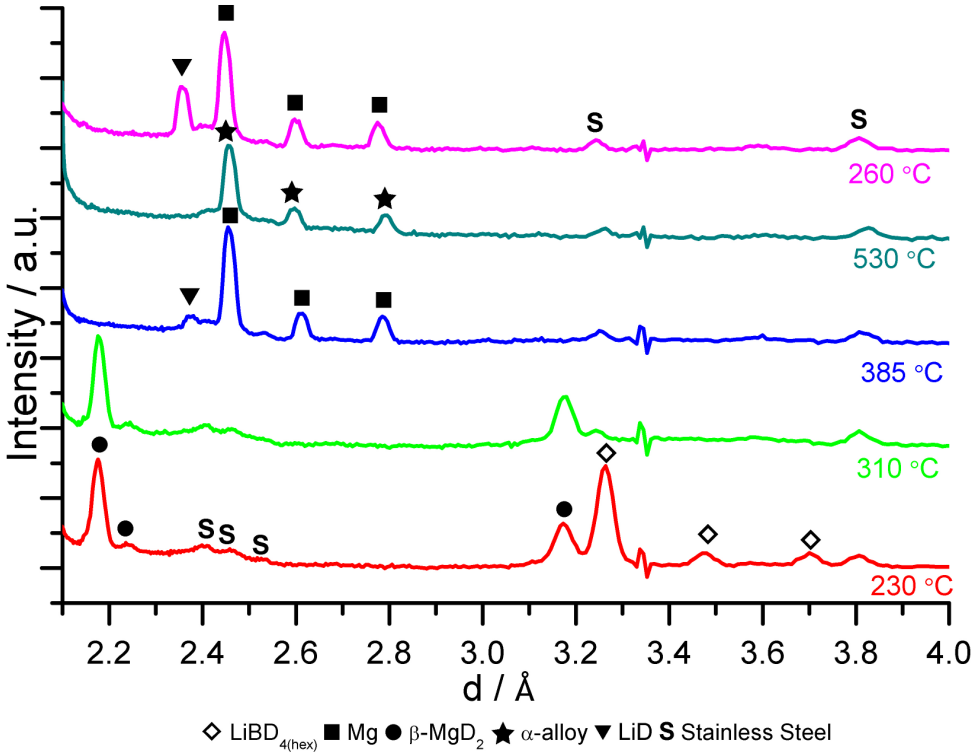

Figure 4.20. Single temperature NPD plots for $0.23LiBD_4 : MgD_2$ sample decomposed into a dynamic vacuum through temperature ramp to 530 °C and cool.

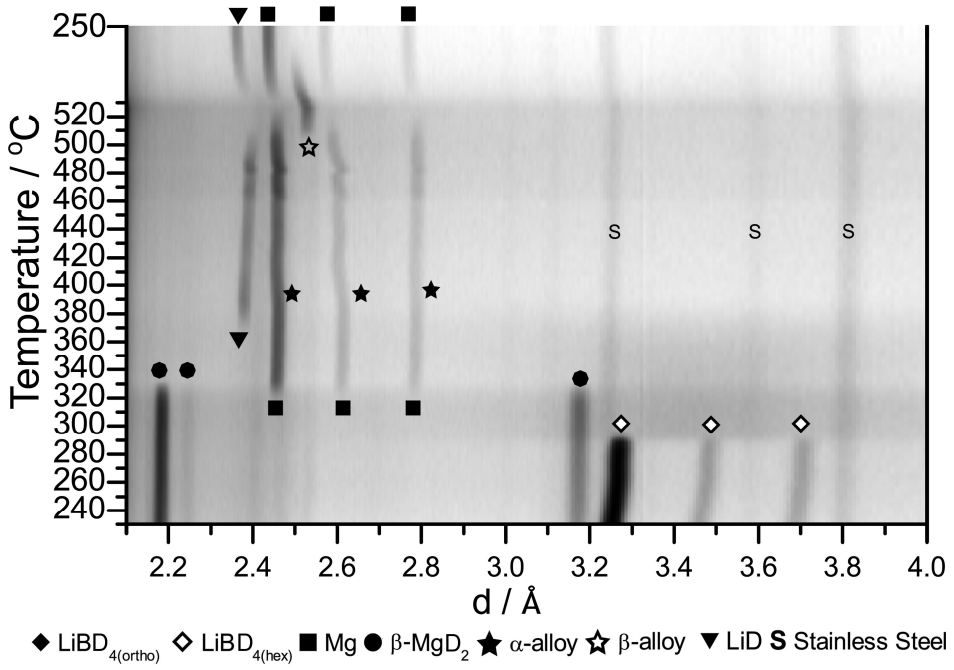

Figure 4.21. NPD data for 0.44LiBD$_4$: MgD$_2$ through temperature ramp and cool under dynamic vacuum.

In-situ NPD for a Mg rich 0.44:1 sample run under dynamic vacuum is shown in figure 4.21 and figure 4.22. Starting materials and phase progression are similar to those of 0.3:1 and 0.23:1 under vacuum, up until alloy formation. Formation of α-alloy began at *ca.* 380 °C, however on heating to 490 °C and then again at 500 °C LiD lines spiked in intensity, with a concomitant shift in α-alloy to larger d-spacing, each time the LiD was quickly reduced on further heating and α-alloy lines return to smaller d-spacing. In contrast to the 0.23:1 sample, β-alloy appeared at 535 °C. The temperature ramp ended at 535 °C with an isothermal for 25 minutes, LiD lines were lost after 10 minutes and α-alloy lines lost after 20 minutes leaving only a β-alloy pattern. Similarly to 0.23:1 sample, and in contrast to other presented NPD data, this phase does not remain stable on cooling to 250°C, instead LiD and α-alloy phases were re-formed at 400 °C and at 280 °C β-alloy phase was lost. At 260 °C sample showed LiD and α-alloy lines.

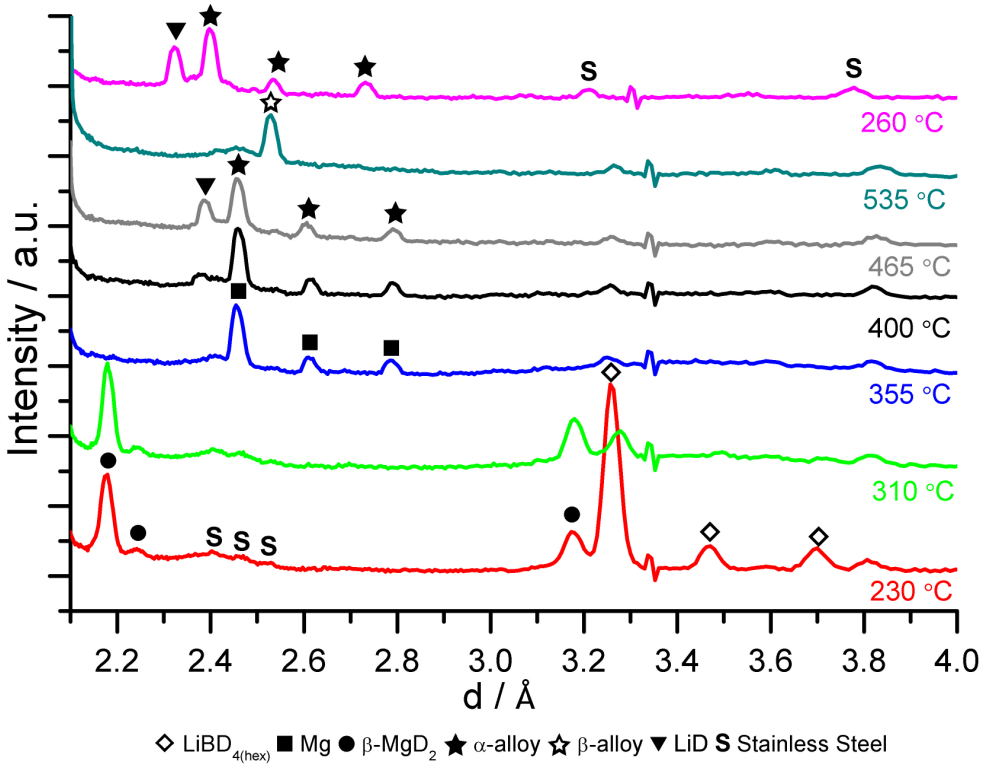

Figure 4.22. Single temperature NPD plots for $0.44LiBD_4 : MgD_2$ sample decomposed into a dynamic vacuum through temperature ramp to 530 °C and cool.

4.3.3. In-situ XRD

Results presented in this section show *in-situ* synchrotron XRD experiments undertaken on a 0.3:1 sample, allowing phase progressions for Mg containing phases to be further elucidated owing to the techniques improved sensitivity to these phases. However sensitivity to Li containing phases is much poorer than NPD. The sample was taken through a temperature ramp under vacuum to 520 °C at 5 °C min^{-1} followed by cooling to 215 °C at 20 °C min^{-1} before re-heating to 315 °C min^{-1} at 5 °C min^{-1} for an isothermal hydrogenation over 3.5 h under 100 bar H_2, finally cooling the sample to 215 °C.

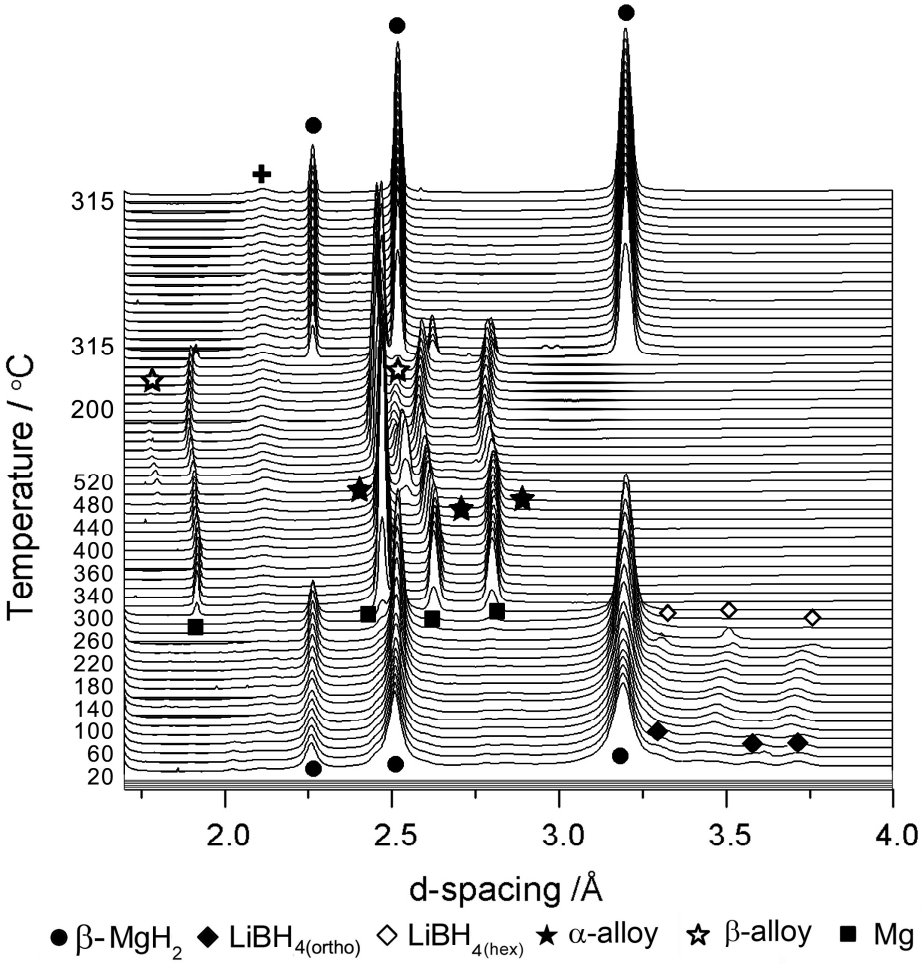

Figure 4.23. Synchrotron XRD data for *in-situ* experiments on a 0.3$LiBH_4$: MgH_2 sample, decomposed under dynamic vacuum to 520 °C followed by hydriding at 315 °C at 100 bar H_2.

In-situ XRD data for a 0.3:1 sample run under dynamic vacuum is shown in figure 4.23 and figure 4.24. Three inset graphs within figure 4.24 show single patterns containing low intensity lines within key d-spacing ranges. The RT materials contained expected $LiBH_{4(ortho)}$ and β-MgH_2 patterns alongside MgO and Mg not observed in NPD. MgO was retained throughout the experiment, with a sharp rise in intensity on formation of Mg at *ca*. 340 °C. As expected the sample displayed a similar phase progression during heating to that presented in NPD data in figure 4.14 (for a 0.3:1 sample decomposed under vacuum). However the increased sensitivity to Mg phases allowed significant phase formations to be elucidated. The most interesting of these occurred at 490 °C, after the expected α-alloy formation. Alongside the β-alloy formation a small MgB_2 pattern forms (shown inset middle, figure 4.24) with the sample showing at 520 °C, MgB_2 and MgO alongside the expected α-alloy and β-alloy. Similarly to the Mg-rich samples in figure 4.19 and figure 4.21, this structure was not retained on cooling, instead β-alloy pattern reduces in intensity whilst α-alloy pattern increases and a small LiH phase appears. On application of 100 bar H_2 at 315 °C the α-alloy d-spacing shifts to larger values before the both alloys are lost with a concomitant rise in β-MgH_2 pattern, the LiH component also increases in intensity (shown in inset graph, left, in figure 4.24). After hydriding for 3.5 h the sample was cooled to 215 °C and contained a strong β-MgH_2 pattern, a small $LiBH4_{(hex)}$ phase and small MgO and LiH patterns.

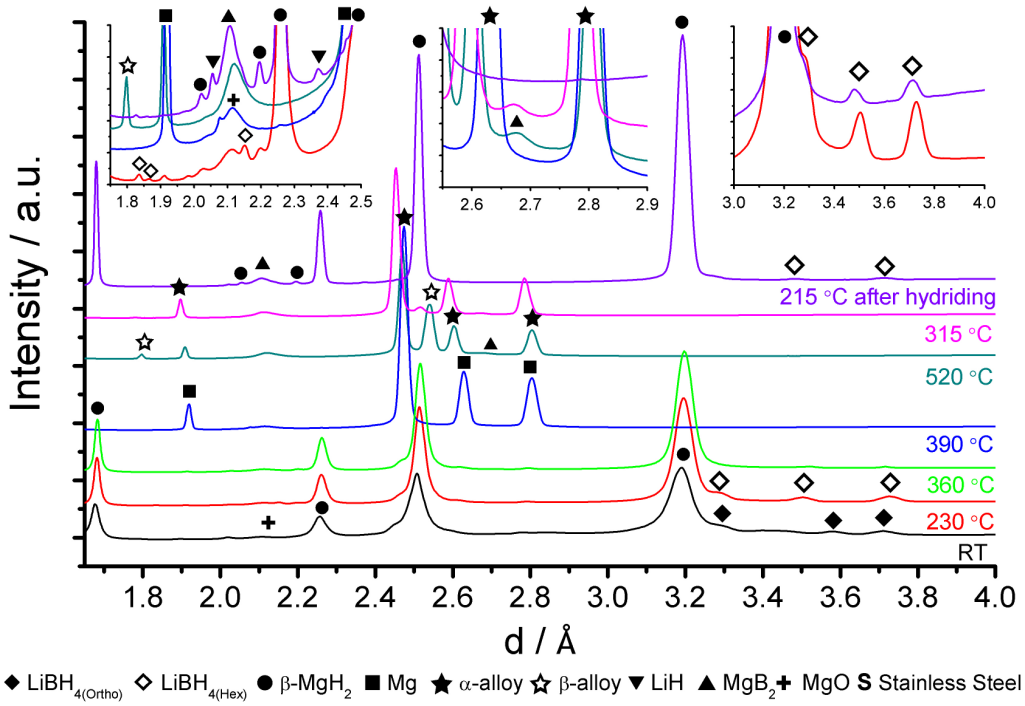

Figure 4.24. Single temperature synchrotron XRD data for *in-situ* experiments for a 0.3$LiBH_4$: MgH_2 sample decomposed under dynamic vacuum to 520 °C followed by hydriding at 315 °C at 100 bar H_2.

4.3.4. PCI experiments

PCI experiments were conducted into the cycling behaviour of 0.3:1 at varying temperatures.

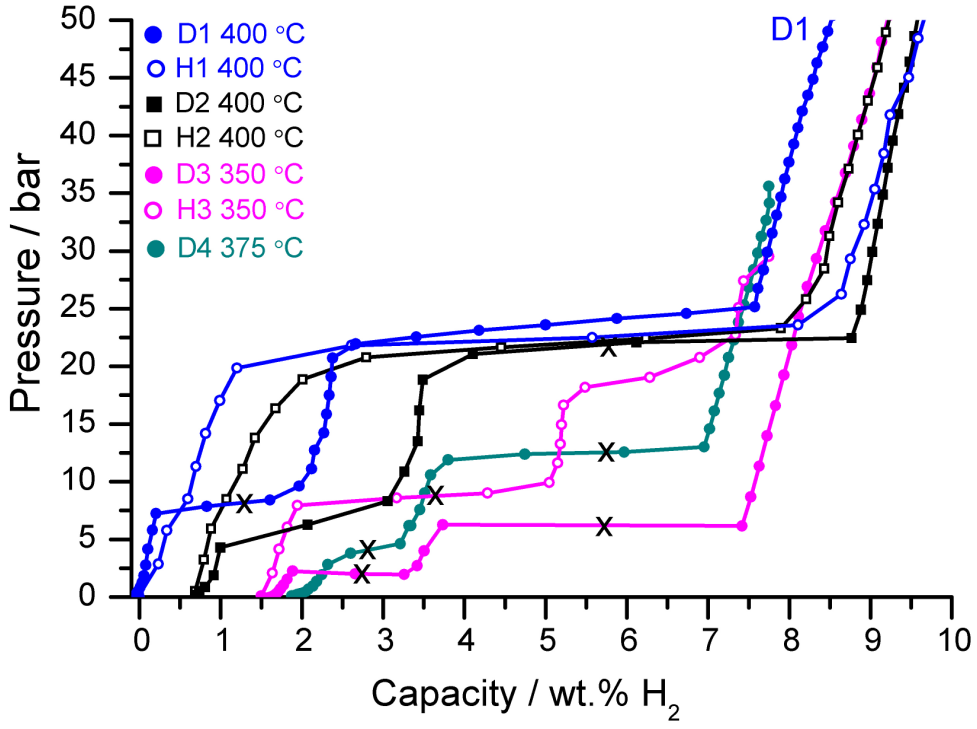

Figure 4.25. PCI data for $0.3LiBH_4 : MgH_2$ through two isothermal cycles at 400 °C, one cycle at 350 °C and a single decomposition isotherm at 375 °C.

A cycled 0.3:1 sample, decomposed under an initial 4 bar H_2 pressure at 400 °C for 2 h, followed by hydriding at 66 bar H_2 for 2 h at 400 °C, was taken through several isotherms as shown in figure 4.25 (starting from a capacity of 8.5 wt.%). The sample was taken through two cycles at 400 °C followed by one full cycle at 350 °C and finally a dehydrogenation isotherm at 375 °C. The first dehydrogenation isotherm, D1, started at 50 bar and reducing the pressure to 25 bar caused the sample to show a plateau centred at 23.90 bar, yielding a weight loss of 6.22 wt.%. Reducing the pressure further caused another plateau

centred at 8.18 bar, showing a reduction in capacity by a further 2.27 wt.%, further aliquots reduced the pressure to zero, yielding a total weight loss of 8.48 wt.%. On hydrogenation, H1, the sample displayed just one plateau centred at 22.49 bar, giving a total capacity of 9.62 wt.% by 50 bar. The second dehydrogenation, D2, again displayed two plateaus, at 21.84 bar (6.21 wt.%) and 6.43 bar (2.73 wt.%), yielding a total capacity of 8.94 wt.%. The sample was then hydrogenated, H2, with the isotherm having a single plateau centred at 21.5 bar, with total uptake reaching 8.52 wt.% by 50 bar.

The sample was then cooled to 350 °C, for the dehydrogenation isotherm, D4, which displayed two plateaus, the first centred at 6.27 bar (5.76 wt.%) and the second at 2.14 bar (1.95 wt.%), the total capacity was 7.70 wt.%. Hydrogenation at 350 °C, H4, gave a plateau at 8.80 bar (3.69 wt.%) and surprisingly a second plateau at 19.15 bar (2.59 wt.%), taking total uptake of 6.28 wt.% by 50 bar. The sample was then heated to 375 °C and taken through a single dehydrogenation isotherm, D5, which had plateaus centred at 12.46 bar (4.33 wt.%) and 4.20 bar (1.59 wt.%) yielding a total hydrogen content of 5.92 wt.%.

4.4. Catalysts for the $0.3LiBH_4 : MgH_2$ multi-component system

4.4.1. Pre-milling

A variety of catalysts and catalyst precursors were investigated either as additions during ball milling of the multi-component materials, or by pre-milling with MgH_2 for 30 h before milling with $LiBH_4$ for 1h. Additions of VH, NbH and TiH_2 were pre-milled with MgH_2 in 5 mol.% additions in order to improve dispersion without increasing milling time for $LiBH_4$. XRD results for as prepared hydrides and pre-mills are presented in figure 4.26 and figure 4.27 respectively.

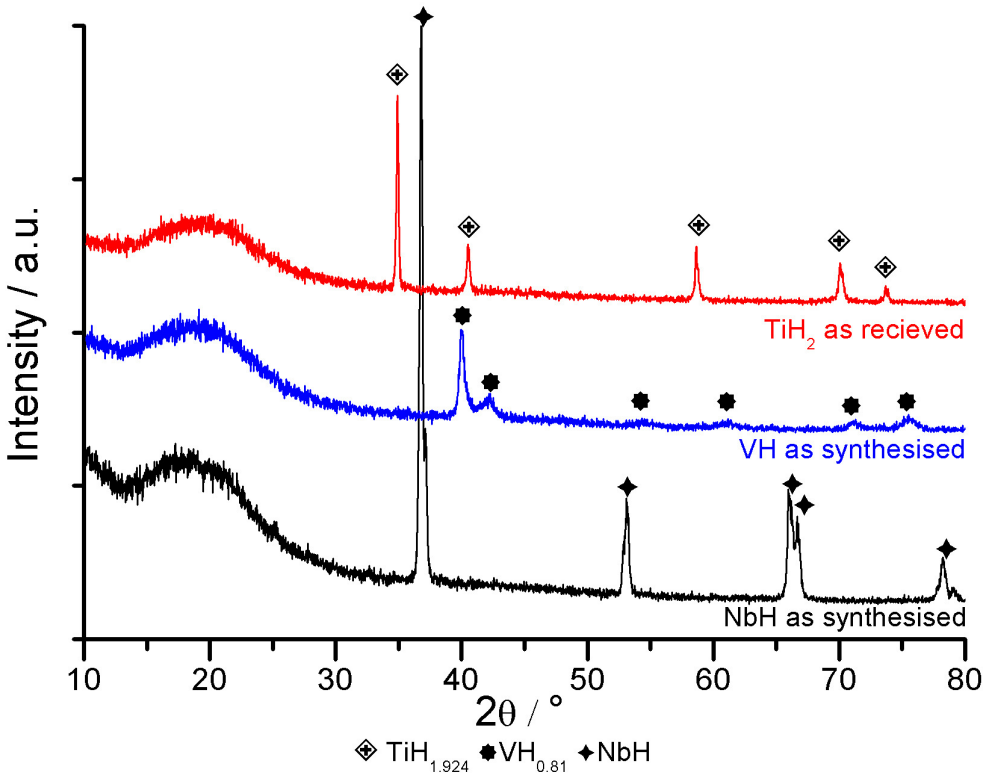

Figure 4.26. XRD data for synthesised and as received hydride materials.

XRD data for synthesised NbH, showed a clear NbH pattern with no detected impurities. The XRD for VH as synthesised matched that for a $VH_{0.81}$ phase. XRD

for the as received TiH_2 showed a clear pattern of $TiH_{1.924}$ with no detected impurities.

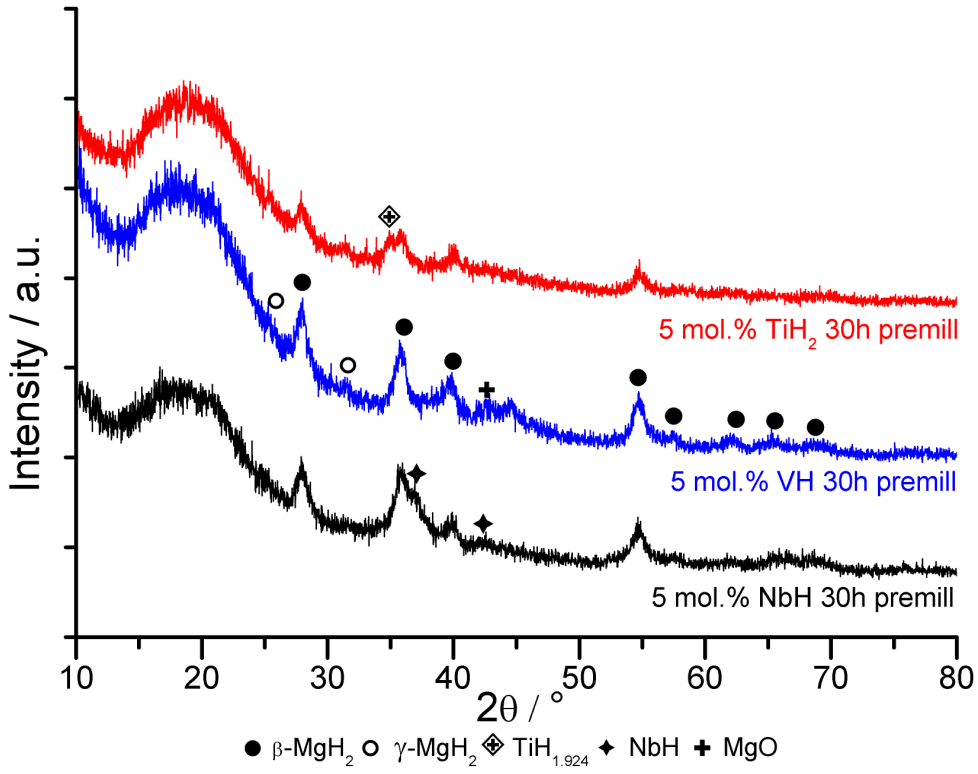

Figure 4.27. XRD data for pre-milled samples of MgH_2 with 5 mol.% catalyst precursor.

The XRD results for the pre-milled samples (30 h milling) of MgH_2 with 5 mol.% additions of NbH, VH and TiH_2 are shown in figure 4.27. All samples showed the presence of β-MgH_2 and γ-MgH_2 phases, a small presence of MgO and the metal hydride addition (NbH, $VH_{0.81}$ and $TiH_{1.924}$ respectively).

4.4.1. Titanium based catalysts

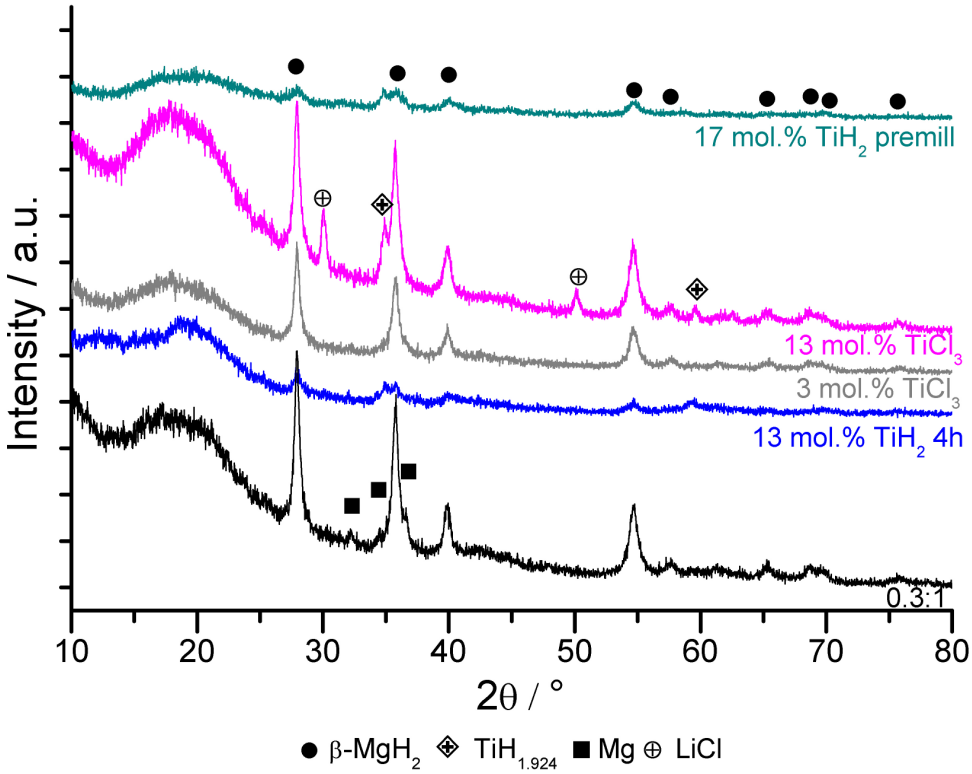

Figure 4.28. XRD data of as prepared Ti based catalysts with 0.3$LiBH_4$: MgH_2.

Figure 4.28 shows the XRD data for as prepared Ti based catalyst additions to 0.3:1. Additions of 13 mol.% TiH_2 milled for 4h to 0.3:1 showed β-MgH_2 and $TiH_{1.924}$ pattern and a weak Mg pattern in the milled products. 3 mol.% $TiCl_3$ additions to 0.3:1 only had evident a β-MgH_2 pattern in the as milled products, whilst higher $TiCl_3$ content sample 13 mol.% $TiCl_3$ showed significant LiCl, and $TiH_{1.924}$ patterns alongside β-MgH_2. Milled products for 17 mol.% TiH_2 pre-milled additions to 0.3:1 showed β-MgH_2 and $TiH_{1.924}$ patterns.

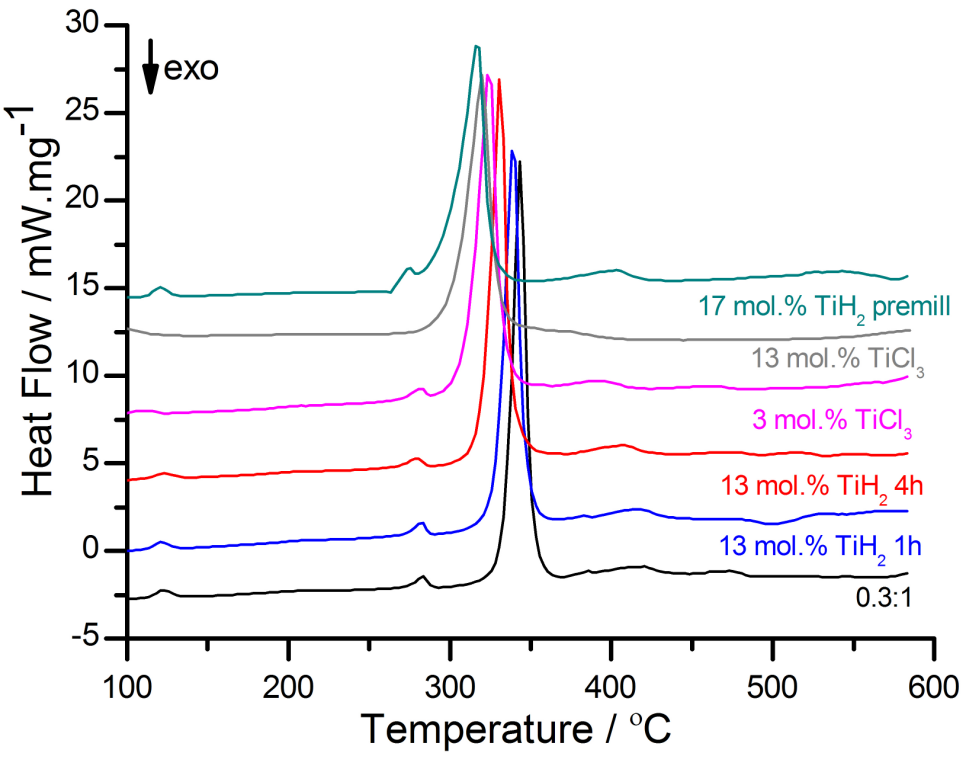

Figure 4.29. DSC plots of Ti based catalysts milled with 0.3LiBH$_4$: MgH$_2$ heating under flowing Ar at 10 °C min^{-1}.

Figure 4.29 shows DSC data for the decomposition under Ar of 0.3:1 samples with Ti-based additions. 0.3:1 with 13 mol.% additions of TiH_2 milled for 1h showed small endothermic events at 121 °C and 282 °C followed by a large endotherm starting at 340 °C, and finally an endothermic event at 415 °C. The sample with 13 mol.% TiH_2 but milled for 4h showed comparable endotherms at 123 °C and 280 °C but a slight drop in temperature for the subsequent peaks, at 331 °C and 408 °C. The sample milled with 3 mol.% $TiCl_3$ showed a similar series of endothermic events with the third and fourth peaks occurring at lower temperatures, 326 °C and 392 °C respectively. Samples milled with 13 mol.% $TiCl_3$ interestingly did not show the first two small endotherms, instead only the third event is present, at the lower temperature of 320 °C with two shoulders at 348 °C and 370 °C. Sample with 17 mol.% TiH_2 pre-milled does

show the first two small endotherms, with the third and fourth events occurring at lower temperatures, 319 °C and 404 °C respectively.

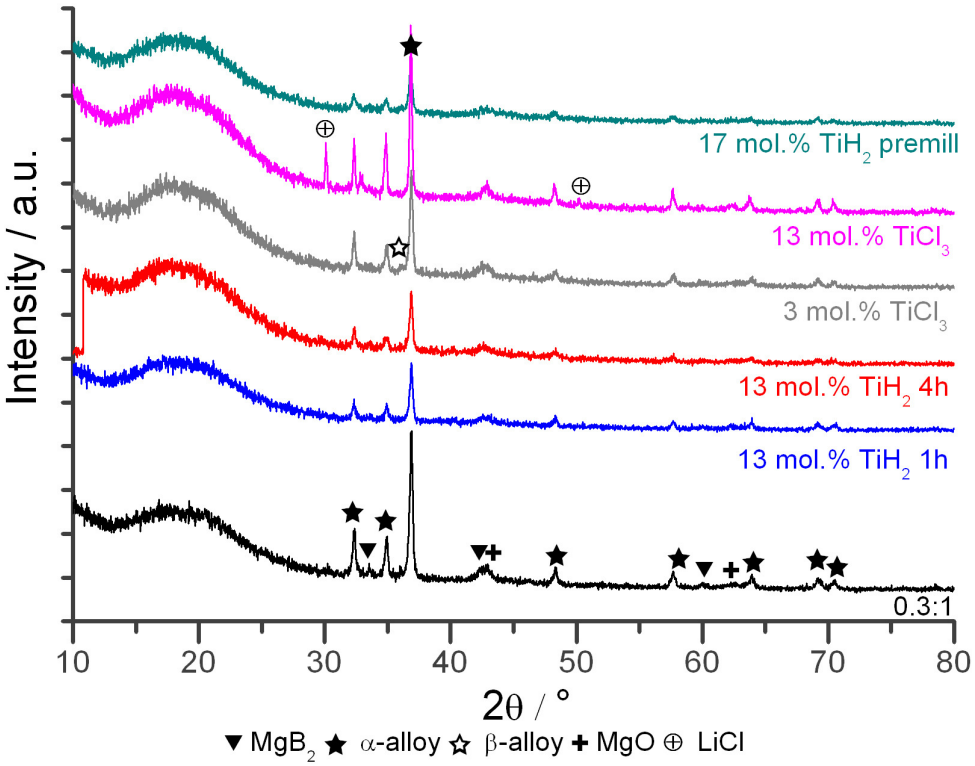

Figure 4.30. XRD data for the DSC end products of $0.3LiBH_4 : MgH_2$ samples with Ti-based catalyst additions, DSC experiments presented in figure 4.29.

The end products from the DSC experiments presented in figure 4.29 were analysed by XRD, figure 4.30. It was found that the 0.3:1 with 13 mol.% TiH_2 samples milled for 1 h and 4 h both consisted of α-alloy, MgB_2 and MgO phases. The decomposition products for the 0.3:1 sample milled with 3 mol.% $TiCl_3$ had in addition to the phases found for the TiH_2 sample a weak β-alloy pattern. Decomposition products for 13 mol.% $TiCl_3$ additions showed LiCl alongside α-alloy and MgO lines. Decomposition products for samples with pre-milled additions of 17 mol.% TiH_2 showed α-alloy pattern, with MgB_2 and MgO patterns.

4.4.2. Niobium based catalysts

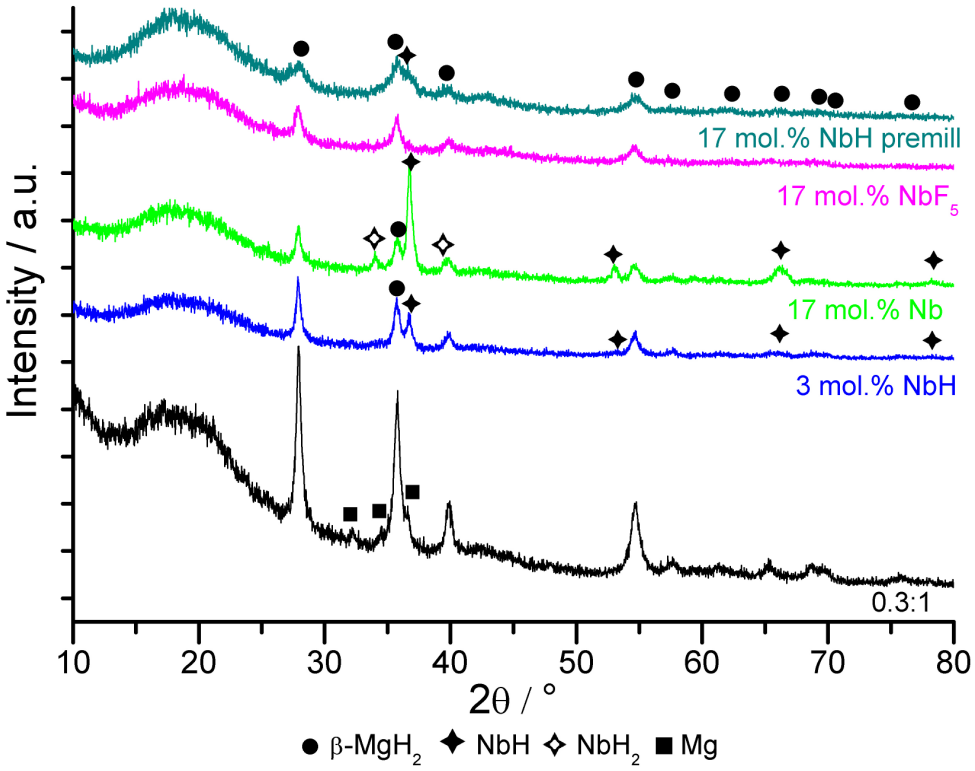

Figure 4.31. XRD data of as prepared Nb-based catalysts with 0.3$LiBH_4$: MgH_2.

Figure 4.31 shows the XRD data for as prepared samples with Nb-based catalysts, milling additions of 3 mol.% NbH yielded weak β-MgH_2 and NbH patterns. The 17 mol.% additions of Nb had similar products to those of NbH, but alongside β-MgH_2 lines there was a stronger NbH pattern and a NbH_2 phase. XRD of the 17 mol.% NbF_5 sample showed only a β-MgH_2 pattern. Pre-milled MgH_2 plus 5 mol.% NbH additions, had a β-MgH_2 pattern and small NbH diffraction line.

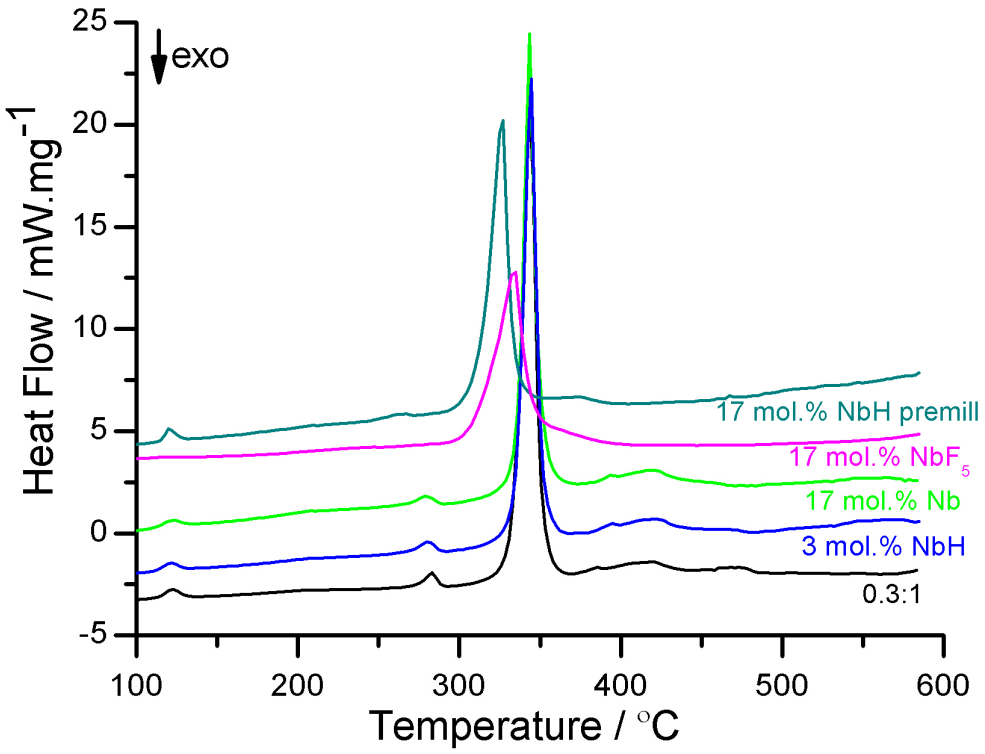

Figure 4.32. DSC plots of Nb-based catalysts with 0.3$LiBH_4$: MgH_2, heating under flowing Ar at 10 °C min^{-1}.

Figure 4.32 shows DSC data for decomposition of 0.3:1 samples with Nb-based additions, decomposed under Ar. Addition of 3 mol.% NbH and 17 mol.% Nb both had a series of endotherms very similar to that of the un-catalysted sample with peaks at 122 °C, 281 °C, 344 °C and 417 °C. The sample with 17 mol.% NbF_5 behaved very differently, only exhibiting a broad endotherm at 334 °C, with a shoulder visible at 360 °C. The pre-milled 17 mol.% addition of NbH had small endotherms at 120 °C and 267 °C, the third and fourth endotherms occurred at lower temperatures compared to the other NbH samples, with peaks at 327 °C and 374 °C.

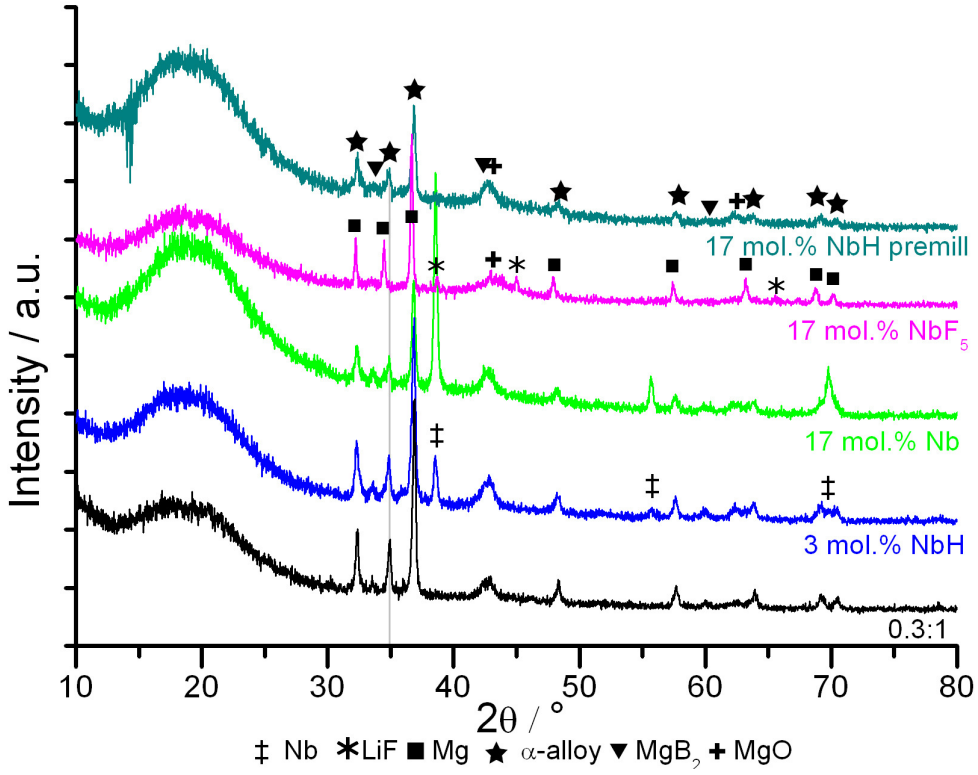

Figure 4.33. XRD data for the DSC end products of $0.3LiBH_4 : MgH_2$ samples with Nb-based catalyst additions, DSC experiments presented in figure 4.32.

XRD of the decomposition products after the DSC experiments (figure 4.32) are shown in figure 4.33. The 0.3:1 sample with 3 mol.% NbH addition showed on decomposition XRD patterns for α-alloy, MgB_2, MgO lines and Nb lines. Additions of 17 mol.% of Nb metal, showed the same phases but Nb pattern was more intense in comparison. The decomposition products for the sample containing NbF_5 were very different, consisting of Mg (*cf.* α-alloy for the other samples), LiF, MgO and MgB_2 phases. Decomposition products for samples with pre-milled additions of 17 mol.% NbH showed α-alloy pattern, with MgB_2 and MgO patterns.

4.4.3. Vanadium based catalysts

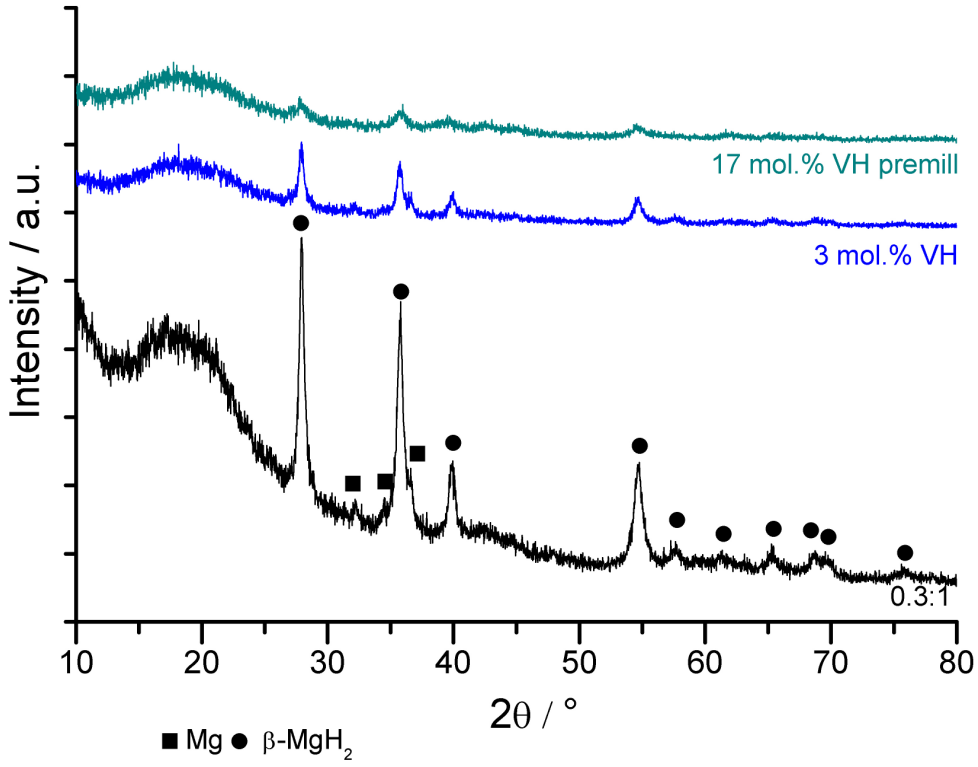

Figure 4.34. XRD data of as prepared V-based catalysts with 0.3$LiBH_4$: MgH_2.

Figure 4.34 shows the XRD data for as prepared 0.3:1 samples with V-based catalyst precursor additions. Sample of 0.3:1 with a 3 mol.% VH addition had a β-MgH_2 pattern and a very weak Mg pattern in the milled products. For the sample using the pre-milled MgH_2 with 17 mol.% VH the as-milled products gave only a very weak β-MgH_2 diffraction pattern.

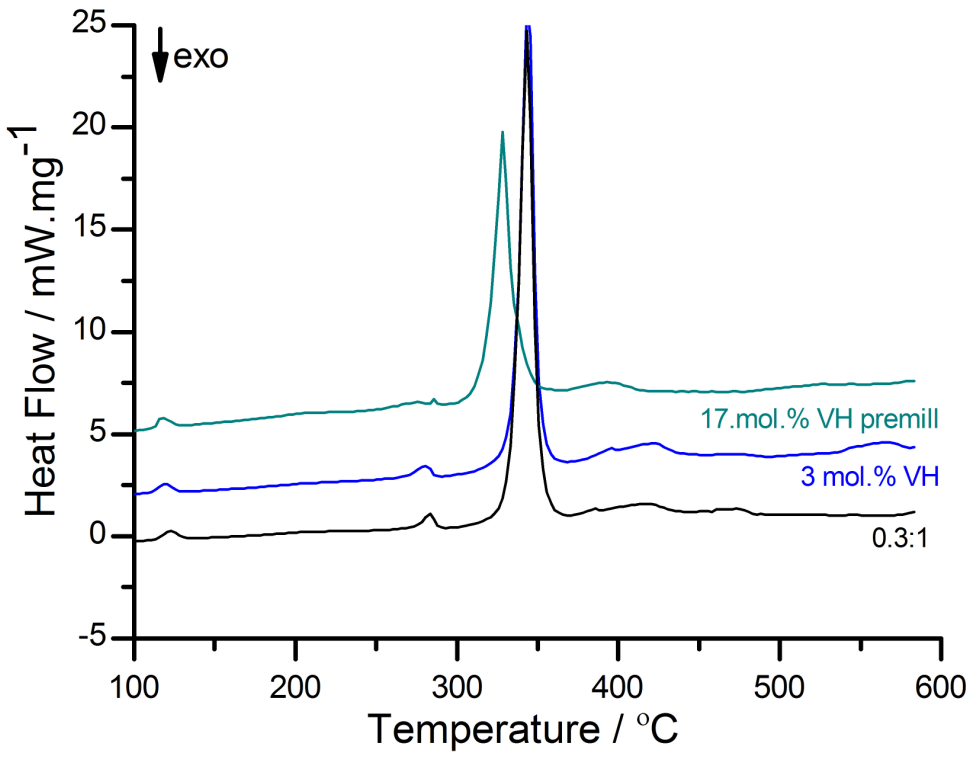

Figure 4.35. DSC plots of V-based catalysts with $0.3LiBH_4 : MgH_2$, heating under flowing Ar at 10 °C min^{-1}.

Figure 4.35 shows DSC data (under Ar) for 0.3:1 samples with V-based additions. The 0.3:1 sample with 3 mol.% additions of VH had a very similar series of endotherms to the uncatalysed sample. In contrast the pre-milled sample showed a significant reduction in the temperature of the third and fourth peaks, to 330 °C and 395 °C (*cf.* 344 °C and 417 °C for 0.3:1).

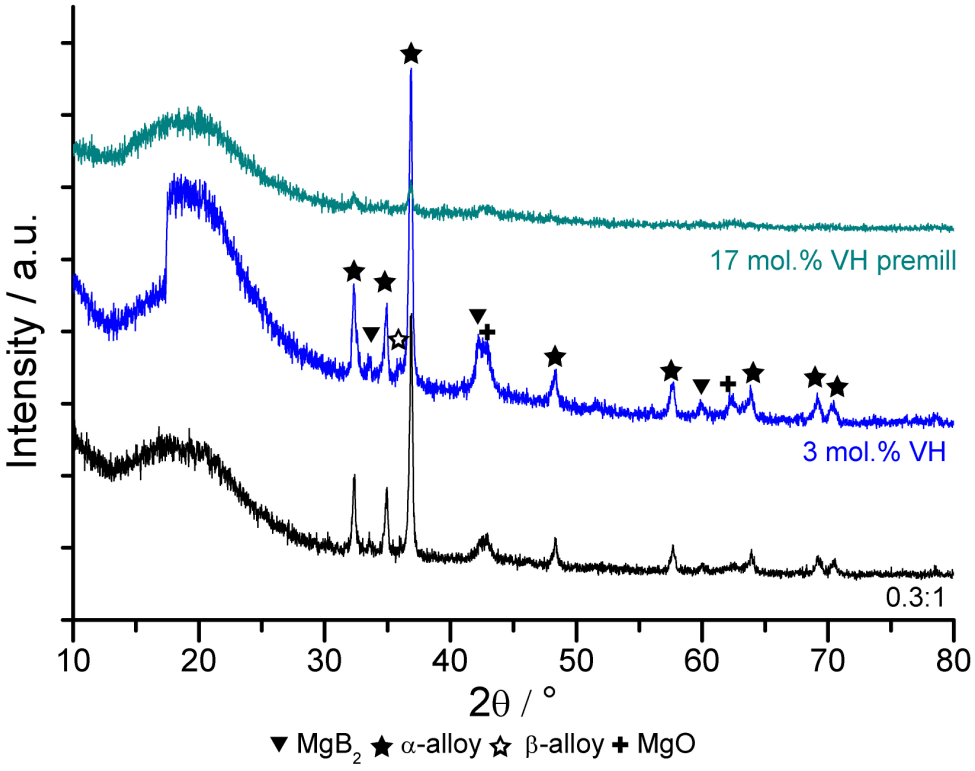

Figure 4.36. XRD data for the DSC end products of $0.3LiBH_4 : MgH_2$ samples with V-based catalyst additions, DSC experiments presented in figure 4.35.

Figure 4.36 shows XRD data for the end products after DSC experiments run under Ar (as presented in figure 4.35). The 0.3:1 sample with 3 mol.% VH additions had patterns corresponding to α-alloy, β-alloy, MgB_2 and MgO, but the pre-milled sample only had a very weak and diffuse pattern corresponding to the α-alloy and MgO.

4.4.4. Nano Pd additions

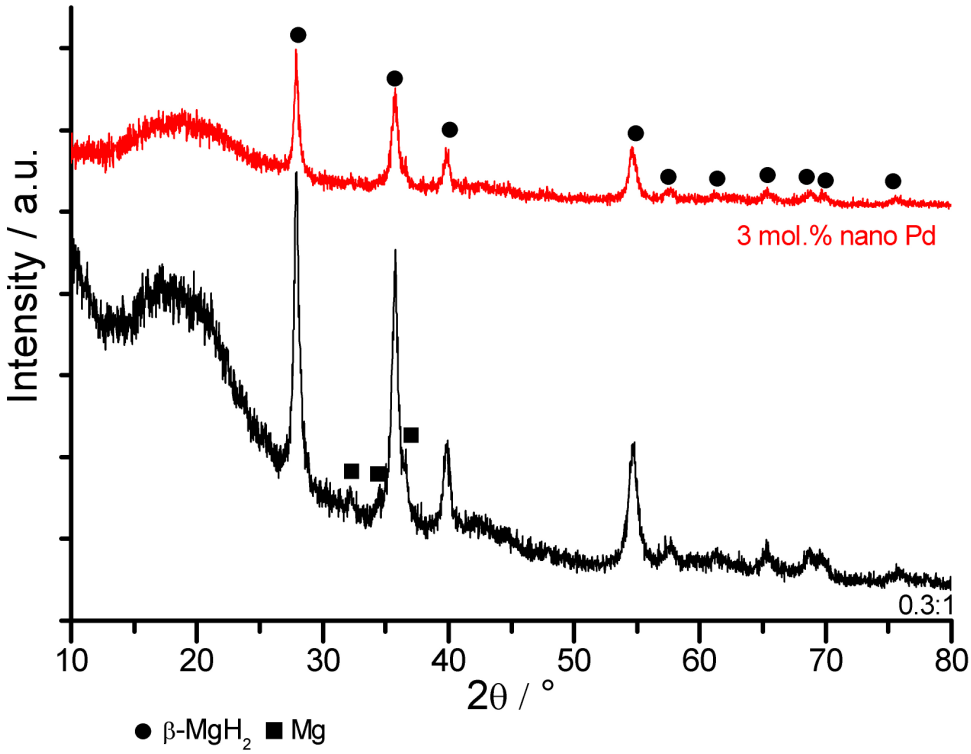

Figure 4.37. XRD data of as prepared $0.3LiBH_4 : MgH_2$ with a nano Pd catalyst.

Figure 4.37 shows XRD data for as prepared sample of 0.3:1 mixture with 3 mol.% nano Pd catalyst, nano scale Pd supported on carbon cone structure (90% C, 10% Pd). The catalysed sample had a similar pattern to that of uncatalysed 0.3:1, consisting of β-MgH_2 and trace Mg.

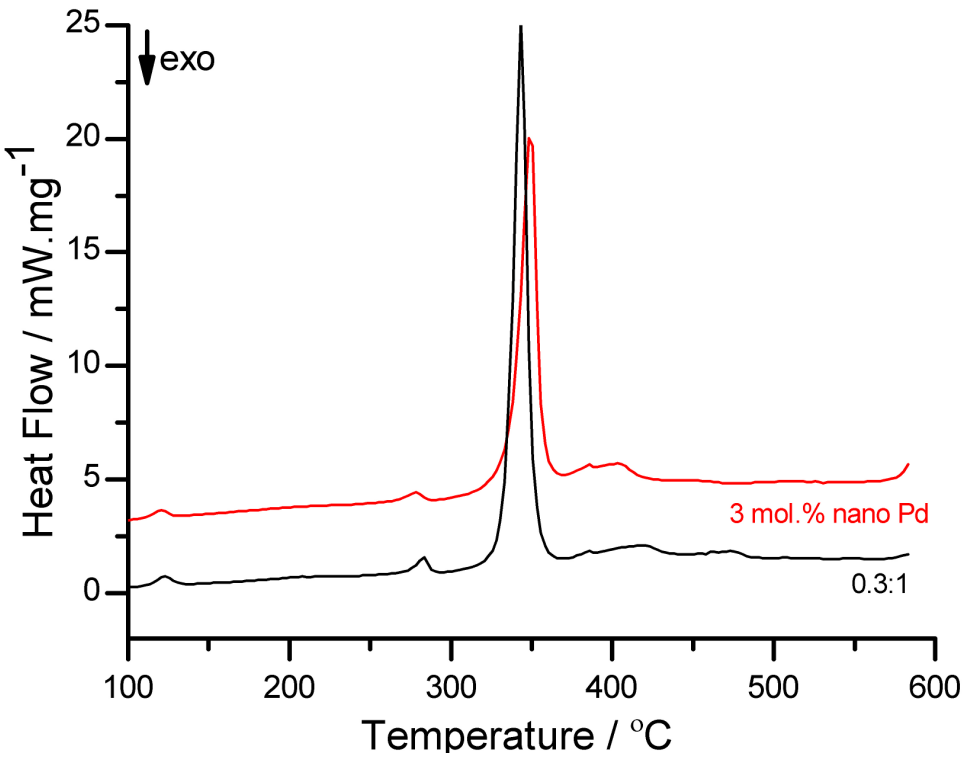

Figure 4.38. DSC plots of nano Pd catalyst with $0.3LiBH_4 : MgH_2$, heating under flowing Ar at 10 °C min^{-1}.

Figure 4.38 shows DSC data for the 0.3:1 + 3 mol.% nano Pd sample run under Ar. There were small endotherms at 122 °C and 280 °C, followed by a large endotherm peaking at 351 °C, slightly higher than for standard 0.3:1 sample (*cf*. 344 °C). Finally an extended endotherm occurred at 403 °C, lower than for the equivalent 0.3:1 endotherm (*cf*. 417 °C).

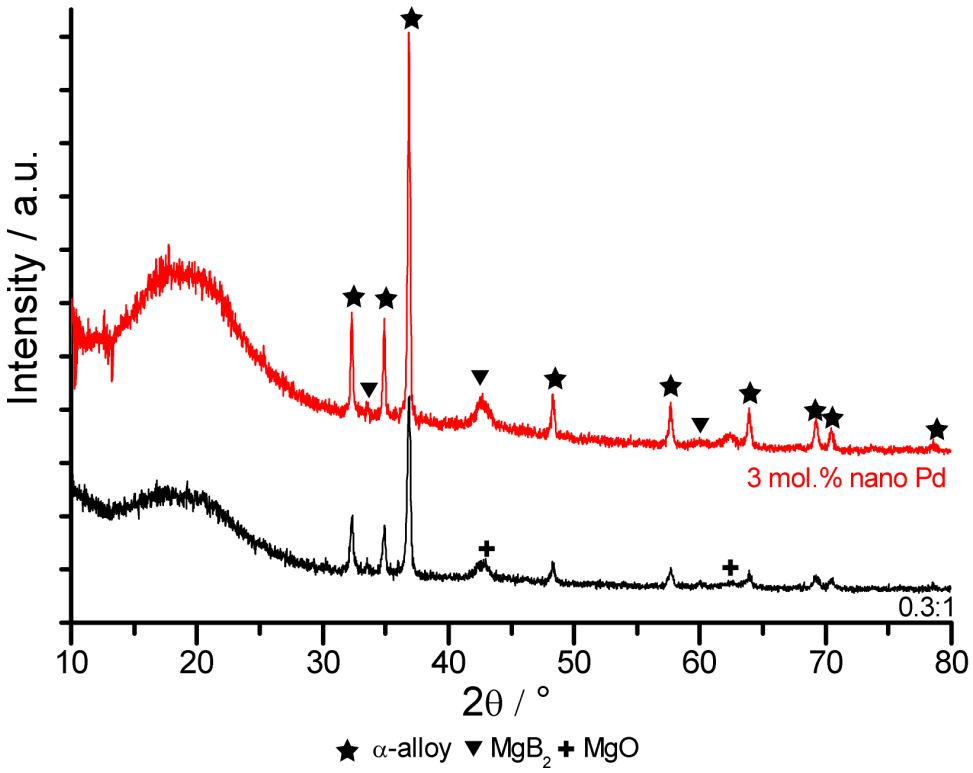

Figure 4.39. XRD data for the DSC end products of $0.3LiBH_4 : MgH_2$ samples with nano Pd catalyst additions, DSC experiments presented in figure 4.38.

The 0.3:1 + 3 mol.% nano Pd sample after DSC under Ar, was found to have similar XRD patterns to that for the 0.3:1 sample. *viz*. α-alloy, MgB_2 and MgO patterns.

4.5. Ternary phase systems

4.5.1. Characterisation for the $LiAlH_4$ component

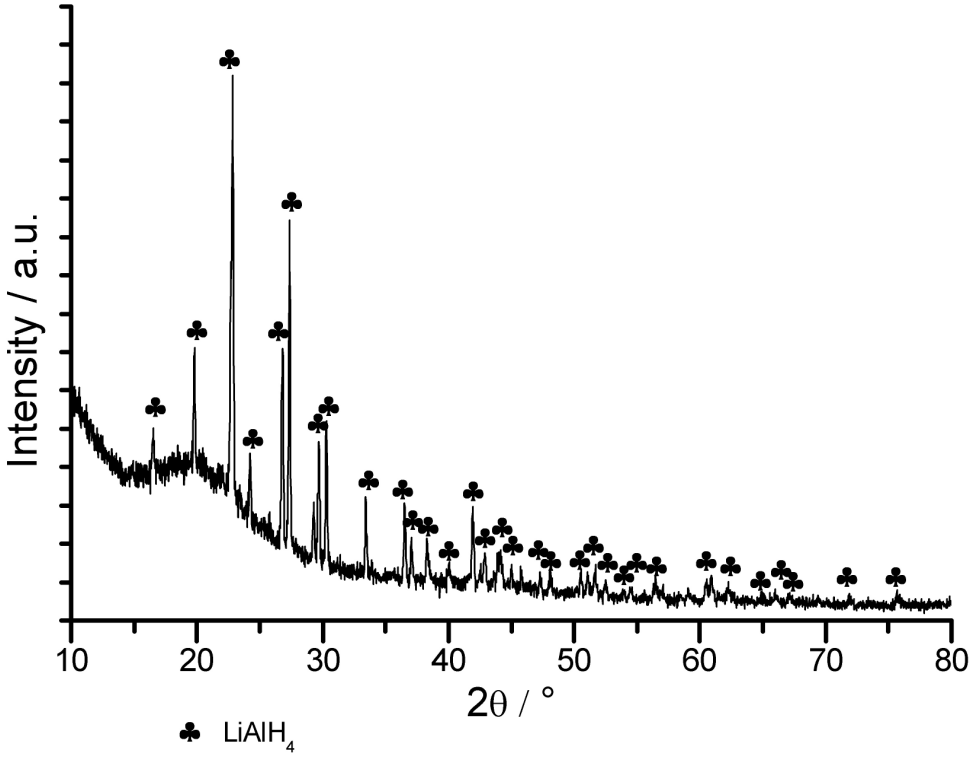

Figure 4.40. XRD data of the as received $LiAlH_4$.

Before presenting the results for the $LiAlH_4$: $LiBH_4$: MgH_2 ternary phase system, characterisation results for the additional alanate component and for binary phase mixtures will be presented first. Figure 4.40 shows the XRD data for the as received $LiAlH_4$, the pattern matches well that for the $LiAlH_4$ phase, with no impurities detectable.

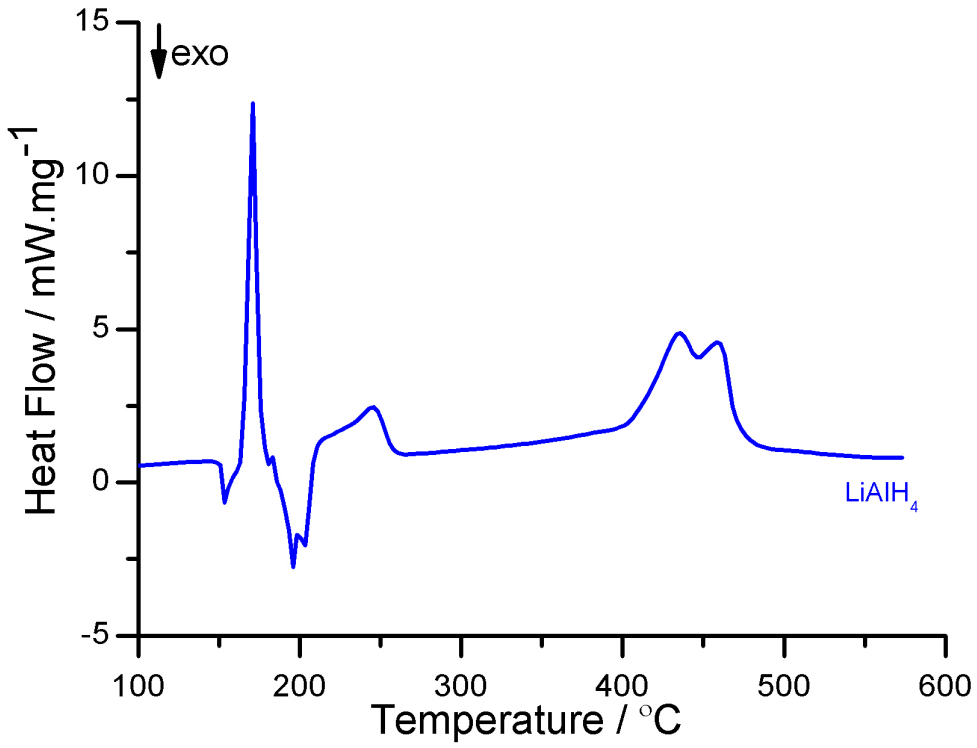

Figure 4.41. DSC plot for as received $LiAlH_4$ heating at 10 °C min^{-1} under flowing Ar.

Figure 4.41 shows DSC data collected for the as received $LiAlH_4$. The plot shows several heat flow events, the first was a small exotherm at 153 °C, followed by a large endotherm at 171 °C before a second exotherm at 197 °C. These combined events are likely to be an endotherm superimposed on an exothermic event. There was a second endotherm at 246 °C and at higher temperatures the sample presented two overlapping endotherms, at 436 °C and 461 °C.

4.5.2. *Binary phase systems including $LiAlH_4$*

4.5.2.1. *MgH_2 : $LiAlH_4$ and $LiBH_4$: $LiAlH_4$*

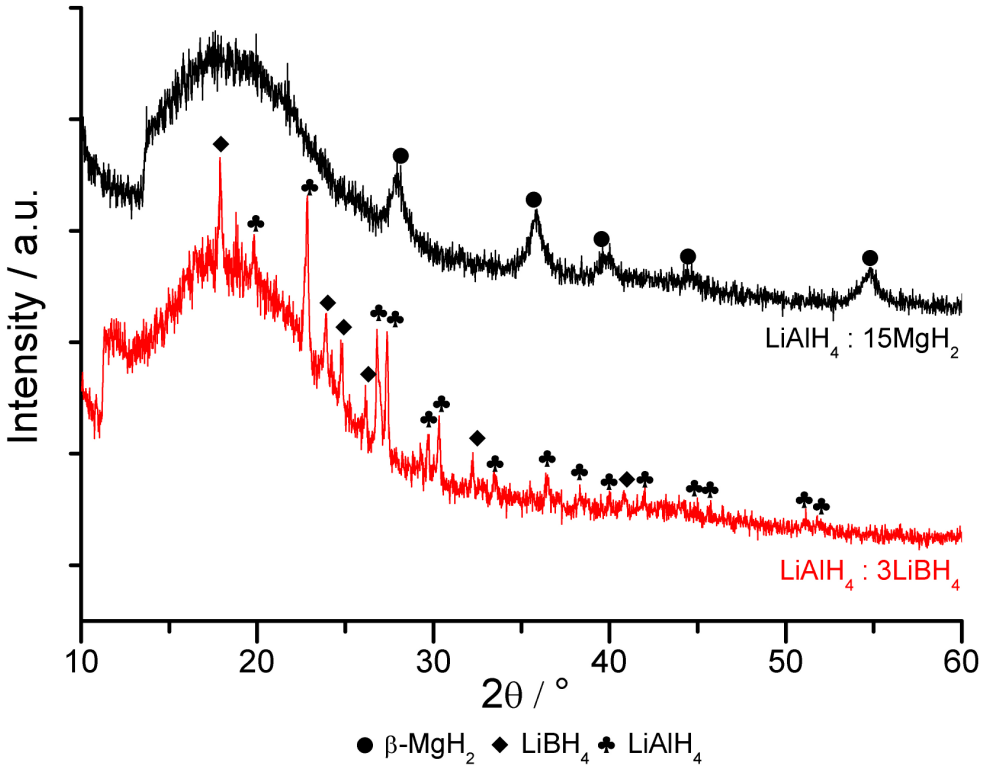

Figure 4.42. XRD data for as prepared binary phase systems.

Figure 4.42 shows XRD data for as prepared $LiAlH_4$: $3LiBH_4$, and $LiAlH_4$: $15MgH_2$ samples after ball milling (these ratios were chosen as they reflect the ratios to be used in the ternary phase samples). The $LiAlH_4$: $3LiBH_4$ sample had strong $LiBH_4$ and $LiAlH_4$ patterns and the $LiAlH_4$: $15MgH_2$ sample only contained a β-MgH_2 pattern.

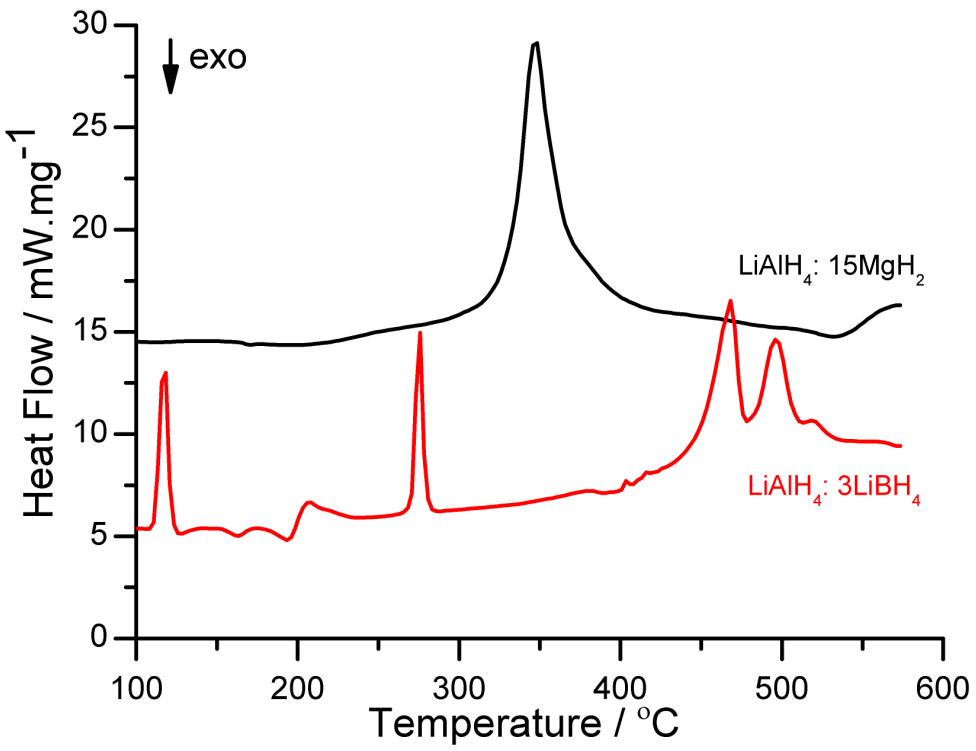

Figure 4.43. DSC plots for binary phase systems heating at 10 °C min^{-1} under flowing Ar.

Figure 4.43 shows DSC plots for binary phase systems of $LiAlH_4$: $15MgH_2$ and $LiAlH_4$: $3LiBH_4$ heated under flowing Ar. The $LiAlH_4$: $3LiBH_4$ sample displayed large endothermic events at 118 °C and 276 °C, between these temperatures a multistage heatflow event occurred with exothermic peaks at 163 °C and 195 °C and an endothermic peak at 207 °C. Between 400 °C and 420 °C there were some small fluctuations in the baseline, before several overlapping endotherms, at 468 °C, 469 °C and 513 °C. The $LiAlH_4$: $15MgH_2$ sample showed only a small exotherm at 170 °C before a large endotherm at 347 °C, which had a shoulder at 347 °C.

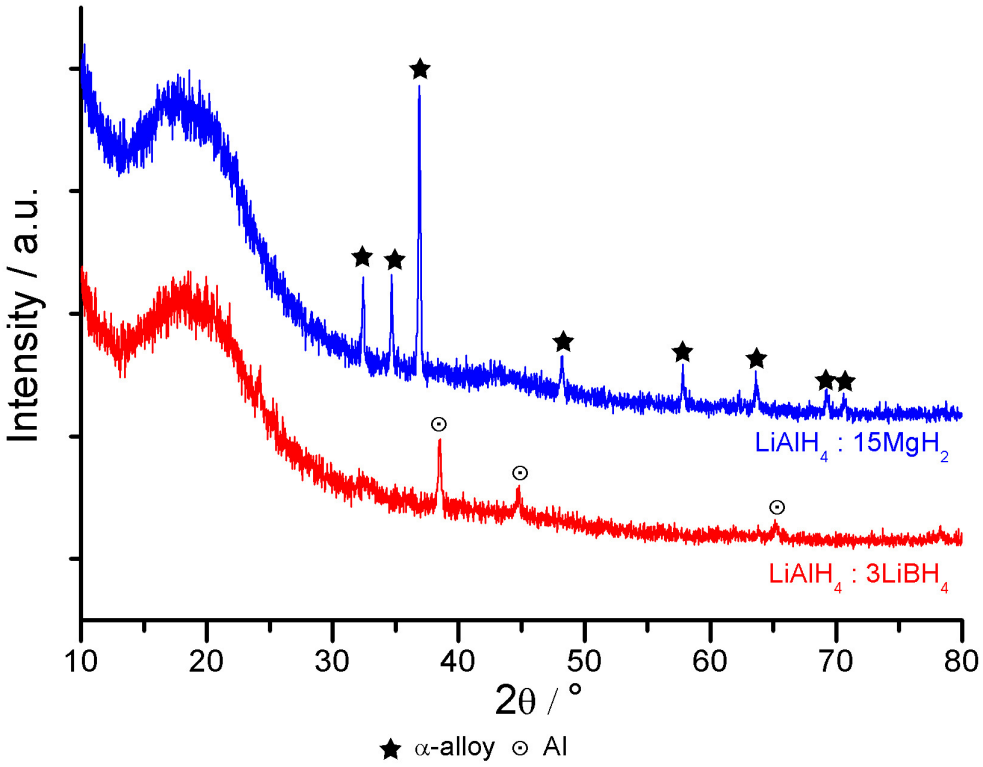

Figure 4.44. XRD data for the end products after DSC for experiments shown in figure 4.43.

Figure 4.44 shows XRD data for the end products after DSC experiments run under Ar (as presented in figure 4.43). The $LiAlH_4$: $3LiBH_4$ sample showed an Al pattern, whilst $LiAlH_4$: MgH_2 sample displayed an α-alloy pattern.

4.5.3. Ternary phase system

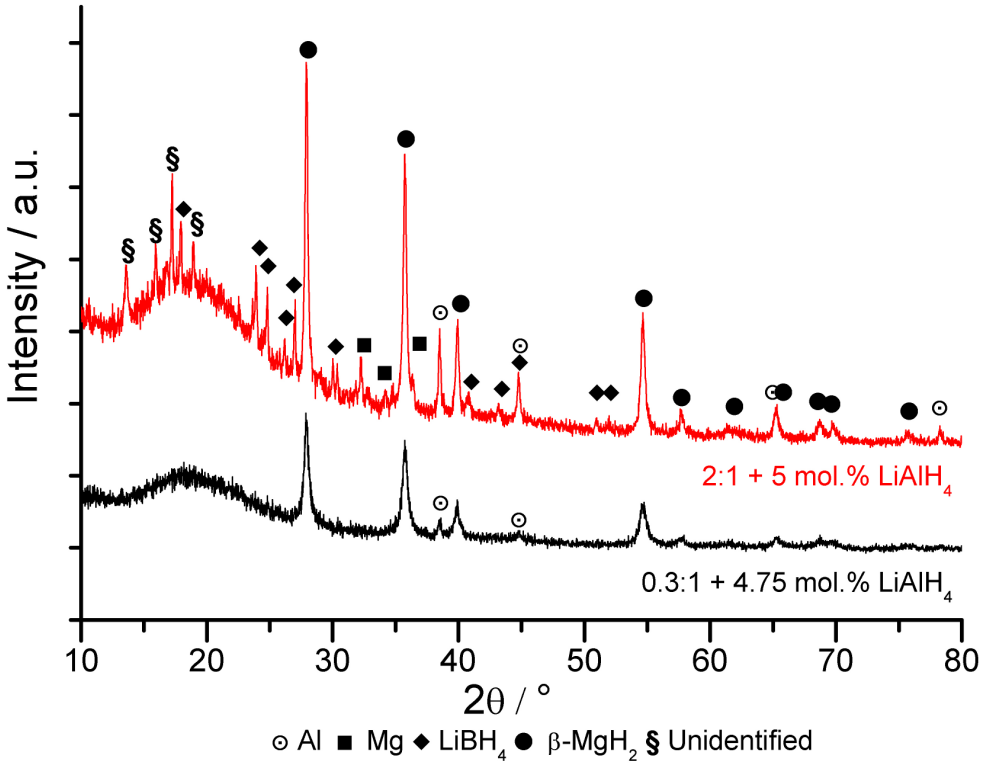

Figure 4.45. XRD data for as prepared ternary phase systems.

Figure 4.45 shows XRD data for as prepared ternary phase systems, the 0.3:1 ratio + 4.75 mol.% $LiAlH_4$ (77MgH_2 : 18 $LiBH_4$: 5 $LiAlH_4$) and 2:1 + 5 mol.% $LiAlH_4$ (31.7MgH_2 : 58.3 $LiBH_4$: 5 $LiAlH_4$). The XRD for 0.3:1 + 4.75 mol.% $LiAlH_4$ had a clear β-MgH_2 pattern and Al pattern. The 2:1 + 5 mol.% $LiAlH_4$ had patterns for β-MgH_2, Al and $LiBH_4$, alongside an unidentified phase.

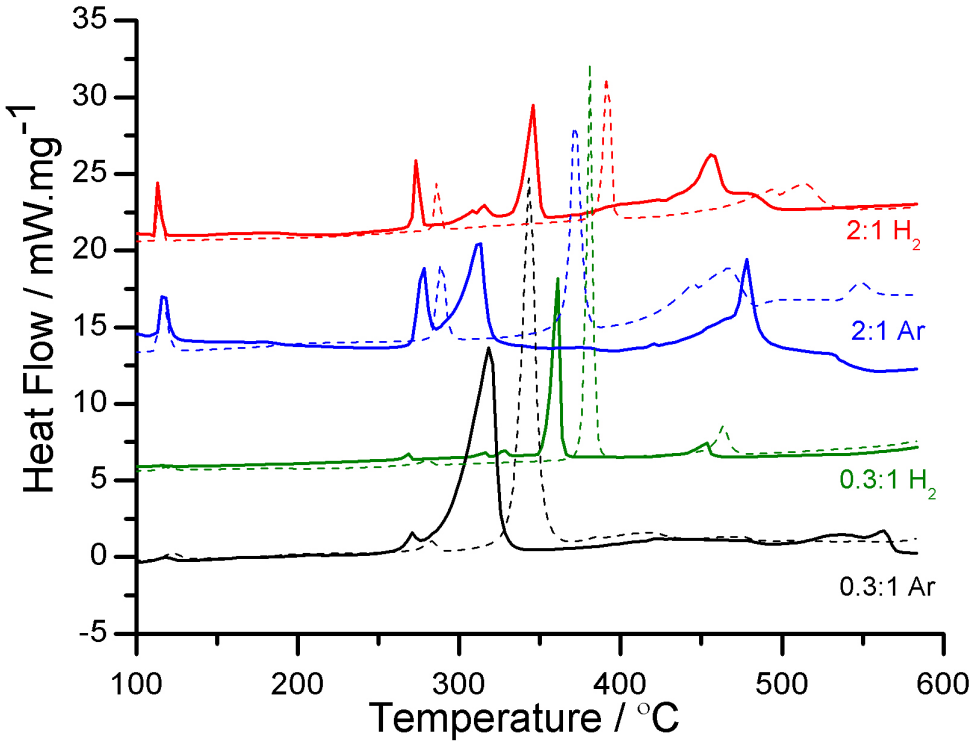

Figure 4.46. DSC data for ternary phase systems (solid) compared to standard $0.3LiBH_4 : MgH_2$ and $2LiBH_4 : MgH_2$ ratios (dotted lines), heated at 10 °C min^{-1} under flowing gas (1 bar Ar, 4 bar H_2).

Figure 4.46 shows DSC data, under flowing gas (either 1 bar Ar or 4 bar H_2), for ternary phase systems 0.3:1 + 4.75 mol.% $LiAlH_4$ and 2:1 + 5 mol.% $LiAlH_4$. To aid comparison the results for the standard 0.3:1 and 2:1 equivalents are reproduced (dotted lines). Ternary 0.3:1 + 4.75 mol.% $LiAlH_4$ sample run under flowing Ar showed similar endothermic events to its 0.3:1 equivalent, with the second, third and fourth peaks shifted, to 271 °C (*cf*. 283 °C), 319 °C (*cf*. 344 °C) and 431 °C (*cf*. 417 °C) respectively. A sample from the same batch was decomposed under 3 bar H_2 and displayed similar shifts in the second, third and fourth peaks relative to 0.3:1 under H_2, to 269 °C (*cf*. 283 °C), 361 °C (*cf*. 381 °C) and 453 °C (*cf*. 464°C) respectively, the sample also gave two small endotherms at 317°C and 328 °C.

Ternary 2:1 + 5 mol.% $LiAlH_4$ sample showed similar events when run under Ar to that of the equivalent 2:1, however the second, third and fourth peaks were shifted, to 278 °C (*cf*. 292 °C), 312 °C (*cf*. 374 °C) and 478 °C (*cf*. 469 °C) respectively. A sample from the same mill was run under 4 bar H_2 and similar events to the equivalent 2:1 sample under H_2. Again, the events were shifted, with the second third and fourth shifted to 274 °C (*cf*. 287 °C), 346 °C (*cf*. 392 °C) and 456 °C (*cf*. 283 °C) respectively. Between the second and third peaks two small endotherms occurred at 308 °C and 316 °C.

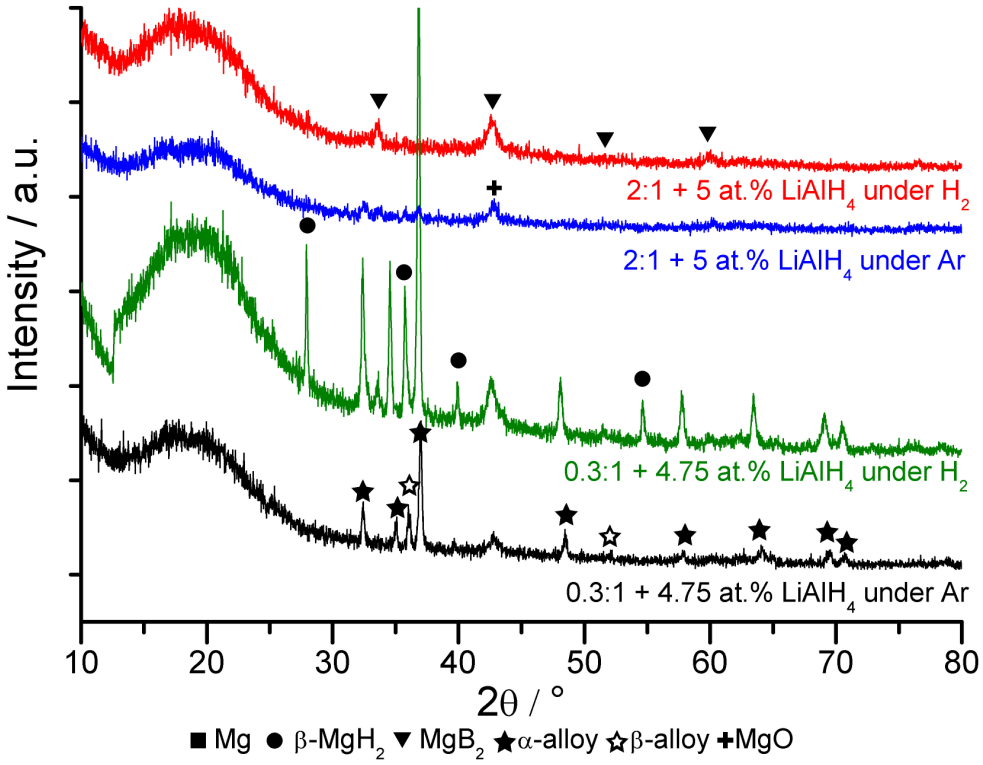

Figure 4.47. XRD data for end products after DSC for experiments shown in figure 4.46.

Figure 4.47 shows XRD data for the products after DSC of the ternary phase samples. The end products of 0.3:1 + 4.75 mol.% $LiAlH_4$ decomposed under Ar had α-alloy, β-alloy and MgO phases. End products of 0.3:1 + 4.75 mol.% $LiAlH_4$

decomposed under H_2 surprisingly contained a Mg-alloy pattern and a strong β-MgH_2 pattern alongside MgB_2 and MgO phases. The DSC end products for 2:1 + 5 mol.% $LiAlH_4$ decomposed under Ar, showed only MgO lines and weak α-alloy. The end products of 2:1 + 5 mol.% $LiAlH_4$ decomposed under H_2 gave only a MgB_2 phase.

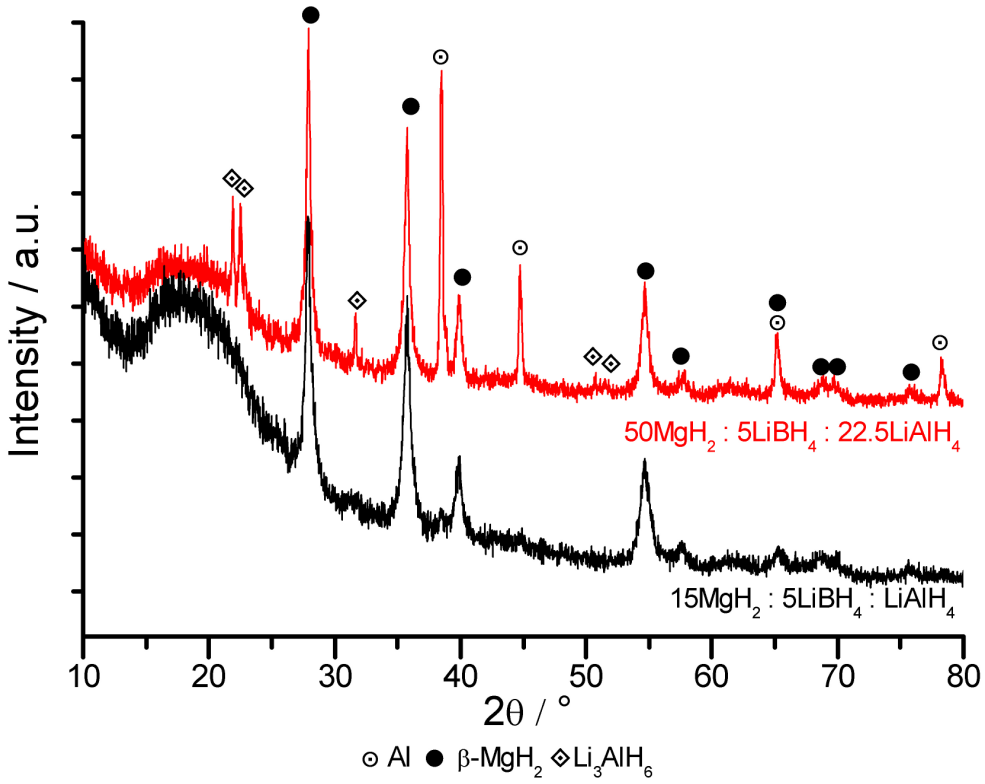

Figure 4.48. XRD data for ternary phase systems as prepared.

Figure 4.48 shows XRD data for as prepared ternary phase systems. Sample $15MgH_2$: $5LiBH_4$: $LiAlH_4$ showed a strong β-MgH_2 pattern alongside a small Al content. The sample $50MgH_2$: $5LiBH_4$: $22.5LiAlH_4$ also showed a β-MgH_2 pattern, alongside strong Al and Li_3AlH_6 patterns.

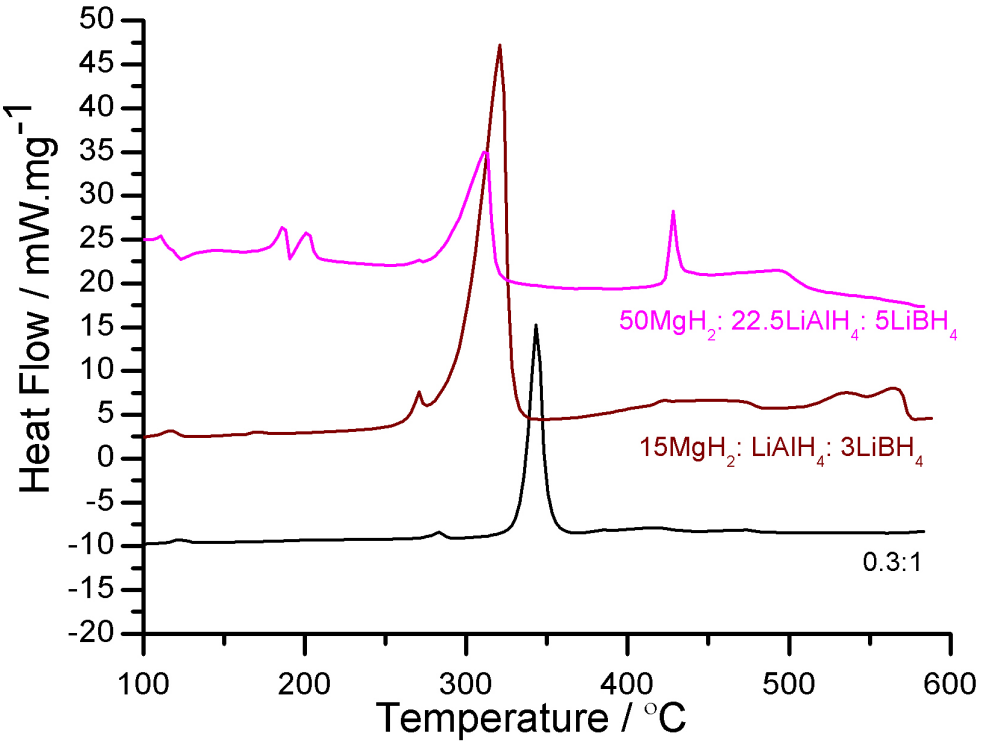

Figure 4.49. DSC data for ternary phase systems heated at 10 °C min^{-1} under flowing Ar gas.

Figure 4.49 shows DSC data for ternary phase systems decomposed into flowing Ar. The sample $15MgH_2$: $3LiBH_4$: $LiAlH_4$ shows small endothermic events at 117 °C, 169 °C and 271 °C before a large endotherm at 321 °C (lower than the 0.3:1 equivalent *cf.* 344 °C). At higher temperatures several events occur, with endotherms at 422 °C, 534 °C and 564 °C. Sample $50MgH_2$: $5LiBH_4$: $22.5LiAlH_4$ showed small peaks at 111 °C, and 270 °C lower than their 0.3:1 equivalents (122 °C and 283 °C). Between these small endotherms a multistage event occurs, with exotherms at 123 °C and 190 °C and endotherms at 187 °C and 202 °C. The sample then gave a large endotherm at 312 °C (significantly lower than the 0.3:1 equivalent 344 °C), followed by a very sharp peak at 428 °C overlapping with a wider endothermic event, peaking at 494 °C.

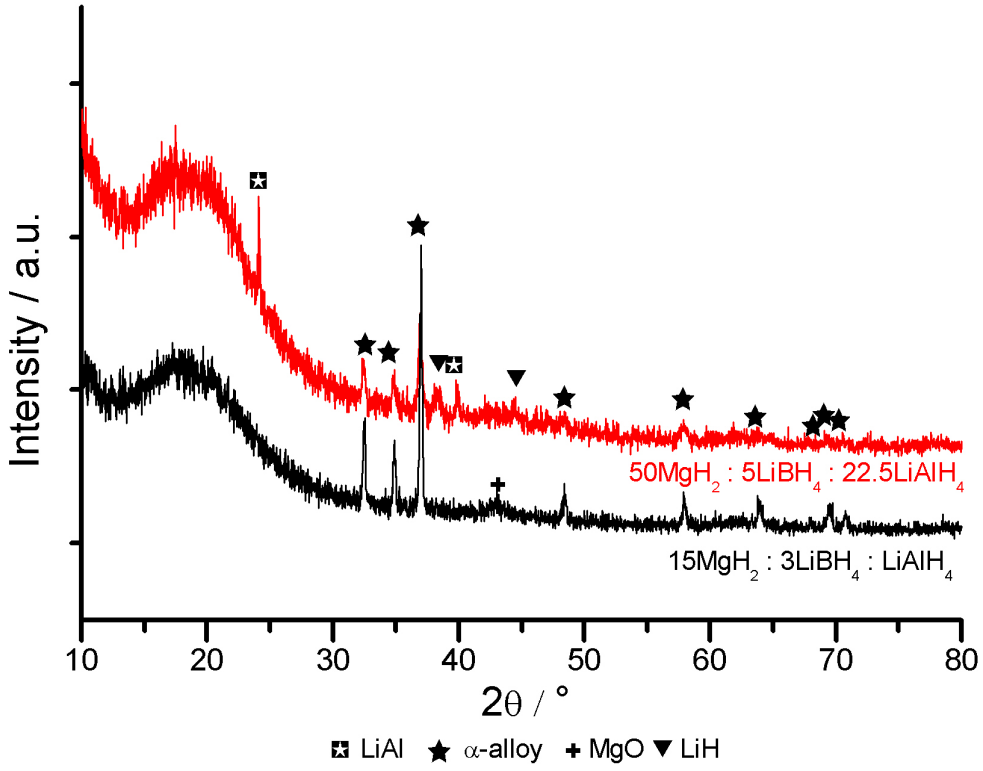

Figure 4.50. XRD data for DSC end products after experiments shown in figure 4.49.

Figure 4.50 shows XRD data for end products of ternary phase system DSC experiments shown in figure 4.49. End products of $15MgH_2$: $3LiBH_4$: $LiAlH_4$ showed evidence of α-alloy and MgO. End products of $50MgH_2$: $5LiBH_4$: $22.5LiAlH_4$ showed an α-alloy pattern alongside LiAl alloy, LiH and MgO phases.

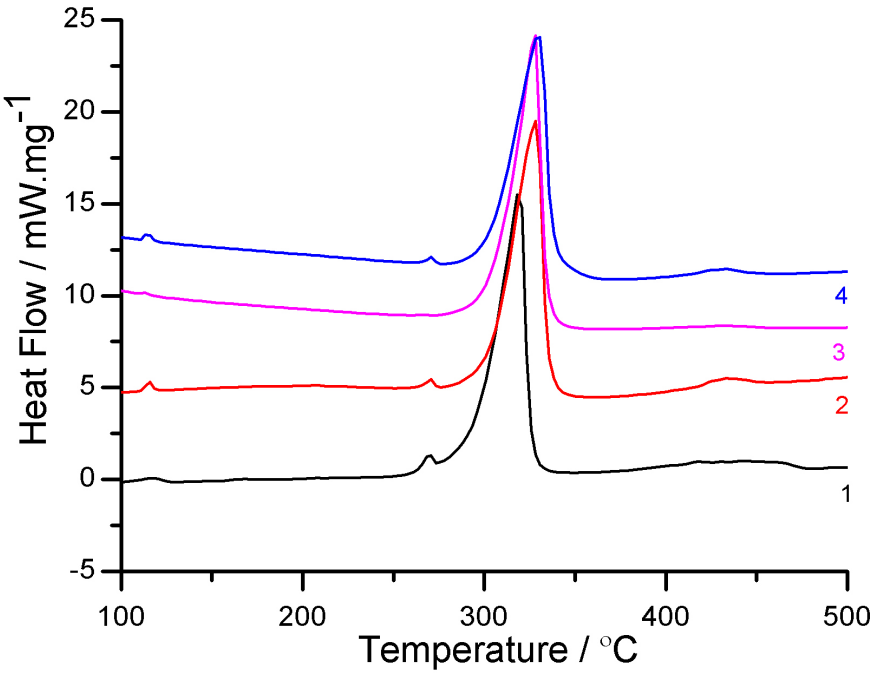

Figure 4.51. DSC data for decomposition stage for cycling $15MgH_2 : 5LiBH_4 : LiAlH_4$ through 4 cycles, decomposition into flowing Ar, hydrogenation at 400 °C and 50 bar for 1h.

Figure 4.51 shows DSC data for cycling experiments of $15MgH_2 : 5LiBH_4 : LiAlH_4$, the data presented is for the decomposition stage only, with hydriding stage being performed at 400 °C under 50 bar H_2 for 1h (1 minute in hydriding cycle before decomposition 3). Cycles show similar heat flow events but with temperature shifts, the peak temperatures are presented for each cycle in table 4.1 .

Table 4.1. Peak temperatures for DSC data presented in figure 4.51

Cycle	1st endotherm / °C	2nd endotherm / °C	Large endotherm / °C	First multi-stage endotherm / °C
1	117	271	321	422
2	115	270	328	433
3	112	-	328	-
4	115	271	330	432

5. Discussion

5.1. Introduction

The destabilised system $LiBH_4$: MgH_2 has been widely reported in the literature, principally in the stoichiometric ratio $2LiBH_4$: MgH_2 (Vajo *et al.*, 2005; Barkhordarian *et al.*, 2007; Bosenberg *et al.*, 2007; Pinkerton *et al.*, 2007). However experiments into the Mg rich system 0.3:1 (Yu *et al.*, 2006b; Mao *et al.*, 2007), and 0.1:1 (Johnson *et al.*, 2005), suggest the larger magnesium component may offer both improved kinetics and potentially an alternative reaction pathway when decomposed under inert conditions. These studies are discussed in section 2.9 and illustrate the lack of understanding of the system, its behaviour under varying reaction conditions and in different stoichiometries. Chapter 4 presented results of experiments into this system and the discussion in this chapter will seek to explain the apparent disparities in the literature as well as exploring new combinations of stoichiometry and reaction condition.

In chapter 5, discussion first focuses on single component hydrides, through XRD and DSC experiments. The discussion then draws on *ex-situ* XRD and DSC results into the $LiBH_4$: MgH_2 system, to allow direct comparison with the literature for varying reaction environment and stoichiometry.

Discussion then interprets *in-situ* structural characterisation to identify decomposition pathways for samples. This data also allows discussion of the effect of partial pressure of H_2 on cooled decomposition products and the potential for $LiBH_4$ intermediate phases. System cycling is then evaluated, drawing on *in-situ* NPD results and PCI experiments.

Discussion is then made of these systems in the broader context of commercial application, highlighting the routes to development of the system. Catalysis of multi-component systems is discussed in relation to a range of investigated additions in order to identify the role and effect of these additions. Finally discussion will focus on addition of $LiAlH_4$ and its effects within the ternary phase multi-component system.

5.2. Single component characterisation

Characterisation of single component hydrides used through this research is vital in order to fully understand the effects of processing parameters on hydrides and to allow comparison with multi-component systems. Results presented in section 4.2 showed the XRD data for as received materials of MgH_2 and $LiBH_4$ in their as received and milled states. Structural data for $LiBH_4$ (figure 4.1) contained low temperature orthorhombic phase of $LiBH_{4(ortho)}$, however some reflections were more intense than the reference data (Jcpds-Icdd 1996) suggesting preferential alignment within the as received material. Also detected within the as received material were evidence of impurities LiCl and B_6H_6Li (the as received material had a purity of 95 %). After milling the sample structural data showed some peaks associated with $LiBH_{4(ortho)}$ were less intense, this was due to reduction in preferential alignment of the sample during milling, as the process is more likely to cleave crystals perpendicular to a preferential growth direction.

The XRD of as received MgH_2 (figure 4.2) showed an Mg component alongside the β-MgH_2 pattern, which is due to the purity of the as received sample (*ca.* 98 %, with the main impurity being Mg). On milling, the sample contained no detectable Mg, due to reduction in the long range order of the Mg phase during

milling. The β-MgH_2 component lines are also broader after milling, this was due to a reduction in grain size and increase in lattice strain as a consequence of milling, as shown in the literature (Zaluska *et al.,* 2001). Alongside the β-MgH_2 XRD lines are lines for γ-MgH_2 phase which has been shown to form during the milling of MgH_2 in planetary ball mills (Danaie *et al.,* 2009). This meta-stable phase is formed through high energy milling of MgH_2 and is not reversible so would not provide a practical advantage in a cycled store. The phase was not detected in milled samples containing $LiBH_4$.

Decomposition of as received and ball-milled single component samples characterised through DSC is shown in figure 4.3, the as received MgH_2 sample displayed only one large endothermic event at 450 °C, this was due to the decomposition of MgH_2 to form Mg and H_2, equation 5.1.

$$MgH_2 \rightarrow Mg + H_2$$ **Equation 5.1**

The 1h milled sample showed a significant reduction in the MgH_2 decomposition temperature, to 366 °C, which agrees with decomposition temperatures reported for 1h ball-milled MgH_2 (*ca.* 372 °C (Schulz *et al.,* 1999)) however milling for 20h only reduces the peak a further 1 °C suggesting a limited effect for further milling under the explored conditions. Ball-milling effects on reduction of crystal and particle size (Ma *et al.,* 2007) and consequent increase in defects have been shown to improve diffusion and kinetics, thus reducing MgH_2 decomposition temperatures through a temperature ramp.

The DSC data for the as received and 1h milled $LiBH_4$ shows multiple decomposition events; firstly a small endotherm at 118 °C corresponding with

the orthorhombic to hexagonal phase change (Gomes *et al.,* 2002; Soulie *et al.,* 2002) the temperature of which agrees with literature values (*ca.* 108–112 °C (Züttel *et al.,* 2003b)), this feature was followed at 289 °C by a second endotherm, corresponding with the expected melting point of $LiBH_4$ (*ca.* 268–286 °C (Schlesinger *et al.,* 1940; Mosegaard *et al.,* 2007)) but seems slightly higher than literature values, this may be due to impurities, possibilities for this effect are discussed with relevance to catalysts in section 5.8. Finally a broad endotherm occurred at 497 °C due to the partial decomposition of $LiBH_4$ and corresponding well with the expected decomposition temperatures (*ca.* 400 °C– 600 °C (Züttel *et al.,* 2003b)) progressing through equation 2.6. The 1h milled sample differed only slightly from the as received material, suggesting a minimal effect of ball milling under the experimental parameters investigated. This is to be expected as $LiBH_4$ decomposes in the molten state and hence reduction of grain size above melting point is clearly not an important consideration.

The decomposition products after DSC experiments into $LiBH_4$ and MgH_2 were investigated through XRD experiments (figure 4.4), for MgH_2 these products contained an expected Mg phase alongside a small MgO content most likely due to oxidation with air during transfer of the sample between DSC and glove-box. Visual inspection of $LiBH_4$ end products after DSC showed evidence of foaming from the DSC pan, yielding very small samples for subsequent XRD experiments. The DSC products only contain LiOH and $LiOH{\cdot}H_2O$ suggesting samples were oxidised, this is most likely due to the reactive nature of $LiBH_4$ at high temperatures; DSC for this sample was run at 1°C min^{-1} rather than 10 °C min^{-1} (in order to reduce sample foaming on evolution of gas in the liquid state) the increased time at elevated temperatures may have caused contamination of

the sample from any oxygen impurity in the gas supply line, this effect will be significantly larger for the 1 °C min^{-1} run sample than for 10 °C min^{-1} run samples.

5.3. *Ex-situ* characterisation of $LiBH_4$: MgH_2

XRD data for the as prepared 0.3:1 sample (figure 4.8) showed a Mg pattern alongside β-MgH_2. The presence of Mg differs from as milled MgH_2 presented in figure 4.2, its presence suggests milling with $LiBH_4$ causes some decomposition of MgH_2, potentially due to a catalytic effect from $LiBH_4$ reported by several groups (Johnson *et al.,* 2005; Mao *et al.,* 2007; Puszkiel *et al.,* 2009). No evidence of $LiBH_4$ was detected in XRD for this sample, most likely due to the combined effects of low content in the 0.3:1 ratio and the effects of milling on $LiBH_4$ decreasing long range order of the material. The XRD data for the 2:1 sample shows β-MgH_2 and Mg peaks, again potentially due to partial decomposition, the sample also shows a $LiBH_{4(ortho)}$ pattern, which is likely due to its larger component in the sample over 0.3:1.

The DSC results for the 0.3:1 sample decomposed under Ar (figure 4.9) showed small endothermic peaks at 122 °C and 283 °C, corresponding with phase change and melting of $LiBH_4$ respectively (section 5.2). The melting point of 283 °C was slightly lower than that for as received $LiBH_4$ (*ca.* 289 °C) which is probably due to the improved thermal conductivity of the MgH_2 component (MgH_2= 2 W m^{-1} K^{-1} at 250 °C (Kapischke *et al.,* 1998) $LiBH_4$= 1.23 W m^{-1} K^{-1} at 27 °C (Sundqvist *et al.,* 2009)). The large endothermic event at 344 °C corresponds with MgH_2 decomposition, this peak temperature is 106 °C lower than that for the as received MgH_2 decomposition temperature (*ca.* 450 °C) and 22 °C lower

than 1h milled MgH_2 (*ca.* 366 °C). This suggests $LiBH_4$ has a large catalytic effect on decomposition of this phase, which agrees with investigation by Yu *et al.* into the ratio showing decomposition at 354 °C for MgH_2 (Yu *et al.,* 2006b), and reports of catalytic effect of $LiBH_4$ on MgH_2 by Johnson *et al.* (Johnson *et al.,* 2005). Decomposition of $LiBH_4$ occurred with the main peak at 417 °C significantly lower than for $LiBH_4$ (*cf.* 497 °C), again this matches results by Yu *et al.* into 0.3:1 showing decomposition of this phase at *cf.* 405 °C. If the reaction proceeds through equation 2.17 proposed by Yu *et al.* this would be a significant reduction in the LiH decomposition temperature (T(1 bar) = 940 °C (Lide 2007)). These results also compare well with investigations by Fan *et al.* into 0.3:1 and 0.6 :1 ratios under equivalent conditions, showing a similar MgH_2 decomposition temperatures (*cf.* 344-352 °C) and a similar $LiBH_4$ decomposition *cf.* 431 °C (Fan *et al.,* 2008).

The 0.3:1 sample decomposed under H_2 displayed similar thermal events to those under Ar, however the MgH_2 decomposed at 381 °C, 37 °C higher than when under Ar, $LiBH_4$ also decomposed at the higher temperature of 464 °C, 44 °C higher than under Ar. The rise in decomposition temperatures is most likely to be due to H_2 pressure; taking the start temperatures for MgH_2 decomposition under Ar, and 4 bar H_2 (327 °C and 374 °C) these equate to plateau pressures of 3.7 bar and 10.9 bar of H_2 respectively (IEA/DOE/SNL), this suggests that decomposition of MgH_2 was kinetically limited by overpressure rather than being under direct thermodynamic control. The $LiBH_4$ theoretical decomposition temperature through equation 2.7 would not be reached until 585 °C under 4 bar H_2 (Chase 1998), therefore the component is not behaving as pure $LiBH_4$ (see section 5.6.2) however the H_2 pressure is effecting kinetics of

dehydrogenation, as under-pressure will be smaller for sample under 4 bar H_2 than under Ar.

The 2:1 samples had similar DSC features, but the peaks attributed to $LiBH_4$ were greater in intensity and the MgH_2 related peaks were smaller than those for 0.3:1, merely reflecting the higher $LiBH_4$ content of the ratio. The 2:1 sample decomposed under Ar showed phase changes at 119 °C and melting at 292 °C, similar to those of as milled $LiBH_4$. The MgH_2 decomposition occurred at 374 °C which was 8 °C higher than as milled MgH_2 and 30 °C higher than the equivalent 0.3:1 sample. This is most likely due to the larger $LiBH_4$ component, which may yield poorer milling than Mg-rich composition samples (or as-milled MgH_2), which would agree with investigation by Fan *et al*. which also showed higher MgH_2 decomposition temperatures with more Li-rich samples (Fan *et al.*, 2008). The $LiBH_4$ component then decomposed at 447 °C, these temperatures are higher than for 0.3:1 decomposition (*ca.* 420 °C) but are still lower than as-milled $LiBH_4$ (*ca.* 500 °C) which suggests MgH_2 presence reduces $LiBH_4$ decomposition, but either poorer milling or smaller Mg composition may yield a lesser effect than the 0.3:1 ratio. These results agree with investigation by Bosenberg *et al*. who showed MgH_2 decomposition at 350 °C and $LiBH_4$ at 450 °C, for the 2:1 sample under Ar, the slower heating rate (DSC ramp rate of 5 °C min^{-1} used in their experiments explains the slight reduction in temperature from those presented here (Bosenberg *et al.*, 2007)).

The 2:1 sample decomposed under H_2 showed similar endothermic events to those under Ar, however MgH_2 decomposition occurred at 397 °C, which was 11 °C higher than for 0.3:1, and 18 °C higher than this ratio gave under Ar, this suggests a combined effect of kinetic limitation due to H_2 pressure and reduced

milling efficiency by the larger $LiBH_4$ component increased decomposition temperature. Finally the $LiBH_4$ component decomposed peaking at 497 °C and 514 °C, higher than those of 0.3:1 under H_2 which may again be due to the lower Mg component and poorer milling. The decomposition temperatures agree with those reported in the literature for the 2:1 ratio under H_2, *cf*. 385 °C for MgH_2 decomposition, and *cf*. >470 °C for $LiBH_4$ decomposition (under 3 bar H_2 at 5 °C min) (Bosenberg *et al.*, 2007).

The XRD data for DSC end products of the 0.3:1 sample decomposed under Ar (figure 4.10) contained mainly reflections for α-alloy, this phase has been shown to form on decomposition to 500 °C for the 0.3:1 ratio under Ar (Yu *et al.*, 2006b) and can be seen by the shift in d-spacing for the (002) Mg reflection from d= 2.606 Å for Mg in MgH_2 decomposition products (*cf*. figure 4.2) to d= 2.568 Å in 0.3:1 products (theoretical Mg, d= 2.605 Å (Busk 1952) and α-alloy, d= 2.566 Å (Fluck 1996)). On decomposition to 600 °C 0.3:1 has been shown to form a β-alloy alongside the α-alloy but was not detected for this sample, this discrepancy is discussed later with the *in-situ* results, section 5.4.1.1.

End products for 0.3:1 sample decomposed under H_2 did not show alloy formation, instead Mg metal, significant amounts of β-MgH_2 and MgB_2 were formed, which suggests the H_2 environment inhibits alloy formation. The presence of MgH_2 will be due to hydrogenation of free Mg on cooling, i.e. at temperatures where the plateau pressure is <4 bar (*ca*. T <330 °C (IEA/DOE/SNL)).

The 2:1 sample decomposed under Ar, showed formation of α-alloy and β-alloy phases in the end products. The presence of alloys conflicts with reported

decomposition pathways in the literature for the stoichiometric ratio, reporting that the decomposition of 2:1 into a dynamic vacuum yields free Mg alongside decomposition products of $LiBH_4$ (LiH, B and H_2)(Vajo *et al.,* 2005; Pinkerton *et al.,* 2007). However these results suggest an alternative destabilisation effect similar to that shown by 0.3:1 samples under inert conditions. The presence of α-alloy however is surprising, as a 2:1 Li/Mg ratio puts the sample entirely in the β-alloy phase (*cf.* Mg-Li phase diagram shown in figure 2.8) and will be revisited in the *in-situ* structural analysis, section 5.4.3.

The end products for 2:1 under H_2 were found to be Mg, LiH and MgB_2 which agrees with the expected phases from the literature (Vajo *et al.,* 2005), however there remains an unreacted Mg content, this is most likely due to the sluggish kinetics of MgB_2 formation during the experiment.

The discussion of DSC and XRD data presented here allows the decomposition pathways for samples to be postulated, however without *in-situ* structural analysis, the precise progression of these pathways cannot be elucidated.

5.4. Reaction pathways

5.4.1. $0.3LiBD_4 : MgD_2$ under vacuum

In-situ NPD for sample 0.3:1 run under dynamic vacuum is shown in figure 4.14, room temperature milled material (figure 4.15) contained $LiBD_{4(ortho)}$ and β-MgD_2, the lack of Mg in comparison to XRD results (figure 4.11) is likely due to the lower sensitivity of NPD to this phase. Heating from 200 °C the starting materials contain high temperature hexagonal $LiBD_{4(hex)}$ phase alongside β-MgD_2. On heating, the first major event was the hexagonal $LiBD_{4(hex)}$ phase melting

causing formation of a wide hump centred at a d-spacing of 3.2 Å in the ND data by 330 °C due to diffuse diffraction of the amorphous $LiBD_{4(l)}$. At 330 °C the β-MgD_2 decomposed, forming Mg, which roughly agrees with the peak from DSC (*ca.* 344 °C). This first stage of decomposition is shown in reaction equation 5.2.

$$0.30\ LiBD_4 + MgD_2 \rightarrow\ 0.3\ LiBD_4 + Mg + D_2$$ **Equation 5.2**

Heating to 400 °C the intensity of the $LiBD_4$ amorphous hump begins to drop as the phase decomposes, during this decomposition a LiD phase appears. This first stage of $LiBD_4$ decomposition agrees with DSC temperature (*cf.* Peak at 417 °C). On formation of LiD a further reaction begins to take place, the decomposition of the LiD and alloying of Mg and Li. Alloy formation can be followed by observation of the Mg pattern d-spacing, as lithium diffuses into the Mg the smaller lithium atoms distort the Mg lattice shifting the d-spacing to smaller values. This can be seen by a shift in the three Mg lines in figure 4.14 (100) (002) (101) to smaller d-spacing. Figure 5.1 shows the change in these lines in more detail, the (002) line can be seen to shift the most, from d= 2.600 Å to d= 2.575 Å, this expansion acts against thermal expansion due to increasing temperature which can be seen for the LiD phase in figure 5.1, as the lattice expands on heating from 425 °C to 500 °C the diffraction line shifts from 2.366 Å to 2.380 Å. The Li content continued to increase until the α-alloy saturation limit, $Mg_{0.816}Li_{0.184}$, was reached (equation 5.3) at this point (*ca.* 530 °C) a β-alloy phase appeared ($Mg_{0.70}Li_{0.30}$) alongside the α-alloy. At 560 °C the sample retained the dual α-alloy/β-alloy composition, figure 4.15, the reaction having progressed according to equation 5.4. The full decomposition reaction is shown in equation 5.5.

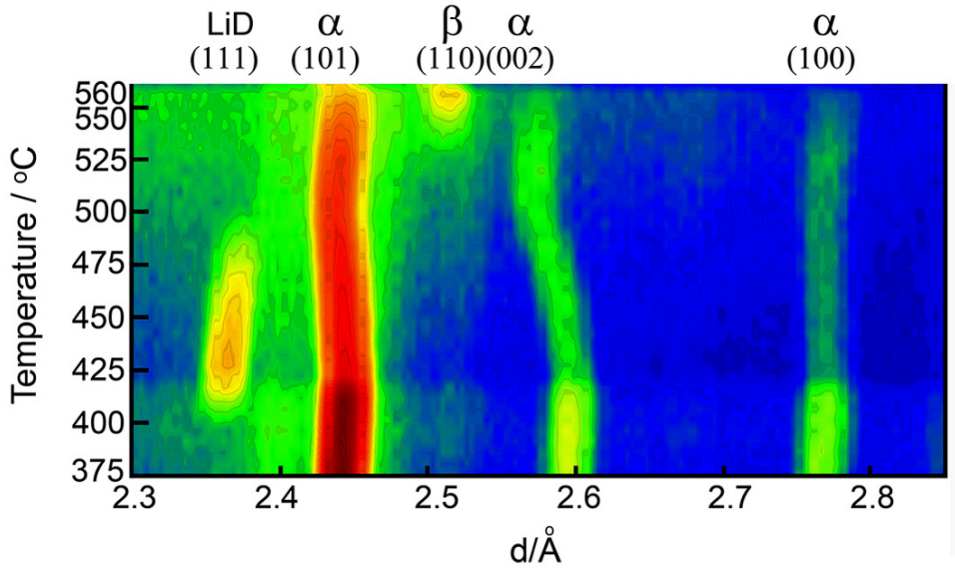

Figure 5.1. d-spacing for Mg containing phases and LiD through alloying, investigated through NPD, figure 4.14.

$$0.3\ LiBD_4 + Mg + D_2 \rightarrow 0.77\ LiD + 1.23\ Mg_{0.816}Li_{0.184} + 0.3\ B + 0.215\ D_2$$

Equation 5.3

$$0.77\ LiD + 1.23\ Mg_{0.816}Li_{0.184} \rightarrow 0.78\ Mg_{0.816}Li_{0.184} + 0.52\ Mg_{0.70}Li_{0.30} + 0.385\ D_2$$

Equation 5.4

$$0.30\ LiBD_4 + MgD_2 \rightarrow 0.78\ Mg_{0.816}Li_{0.184} + 0.52\ Mg_{0.70}Li_{0.30} + 0.3\ B + 1.60\ D_2$$

Equation 5.5

5.4.1.1. *Effect of DSC conditions on reaction progression*

The lack of a MgB_2 phase in the NPD results suggests this phase does not form under inert conditions until temperatures >570 °C, *ex-situ* XRD (figure 4.10) for a 0.3:1 sample decomposed through DSC under Ar to 585 °C (figure 4.9) showed formation of MgB_2 but no β-alloy. These results suggest that the increased decomposition temperature of 585 °C allowed significant MgB_2 formation, however the fast ramp rate (*ca.* 10 °C min^{-1}) may not have allowed sufficient time for the β-alloy to form. The alloys reported by Yu *et al.*, were observed when samples were taken above alloy melting temperature (*ca.* 588 °C (Butts *et al.*, 2004a)) allowing mass transport issues and consequent slow kinetics of the β-alloy to be overcome, this would yield end products closer to equilibrium than the DSC experiments (samples heated to 585 °C). The postulated reaction equation for DSC is shown in equation 5.6, with the assumption that all the boron forms MgB_2.

$$0.30\ LiBH_4 + MgH_2 \rightarrow\ \ 1.042\ Mg_{0.816}Li_{0.184} + 0.15\ MgB_2 + 0.108\ LiH + 1.546\ H_2$$

Equation 5.6

5.4.1.2. Phase progressions for in-situ synchrotron XRD experiments

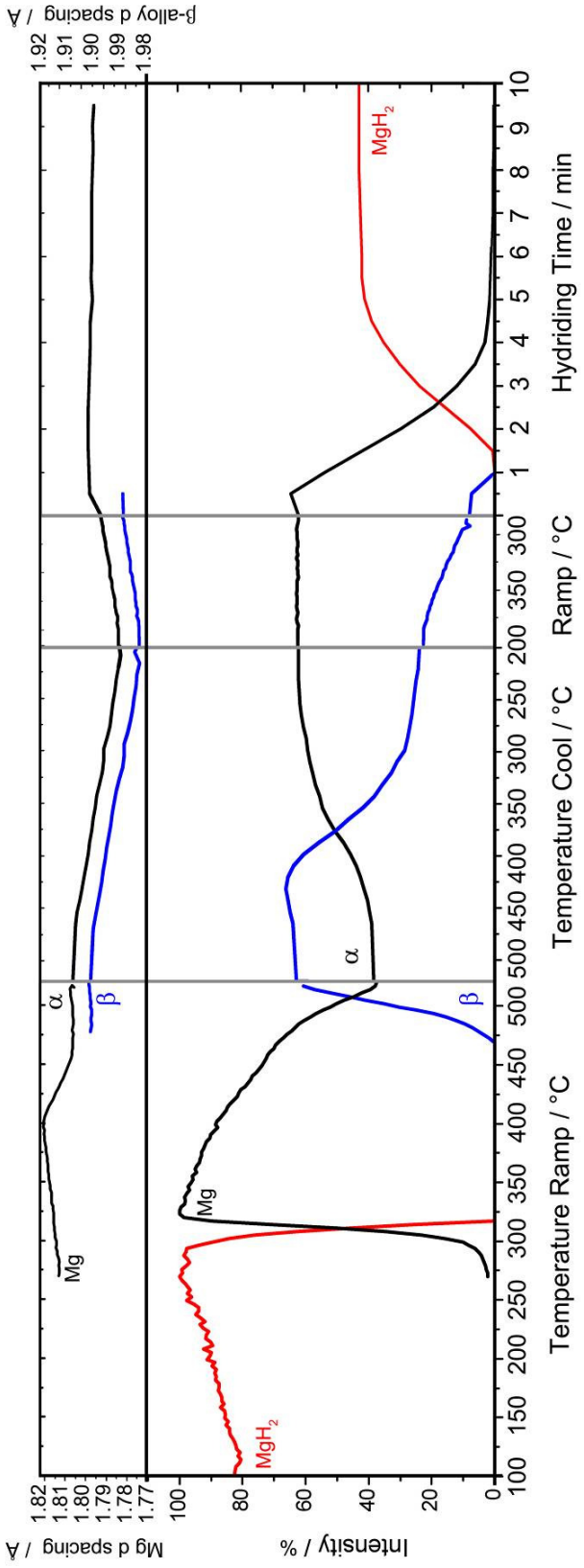

Figure 5.2 Intensity and d-spacing data for synchrotron XRD data collected through experiment presented in figure 4.23.

In-situ synchrotron XRD experiments allow comparison with *ex-situ* XRD and *in-situ* NPD by virtue of their increased resolution and ability to resolve Mg phases, however sensitivity to Li is reduced, they therefore provide complimentary data to other techniques.

Figure 5.2 shows peak area calculations (detailed in section 3.4.2) for key phases through decomposition of 0.3:1 under 10^{-2} bar vacuum conditions. Single pattern datasets are shown in figure 4.24, allowing low intensity phases and structure at key temperatures to be compared. Intensities are scaled to 100 % of their maximum intensity (combined alloys are scaled to a total of 100 % at 520 °C), observation of peak intensity between phases is therefore best made from figure 4.24.

On heating of the sample from 100 °C a rise in β-MgH_2 intensity was observed, this is due to crystallisation of the as milled materials and is similarly shown in NPD data. Between 265 °C and 315 °C β-MgH_2 decomposes, concomitant with the appearance of Mg and a rise in MgO intensity, this oxidation will be due to exposure of fresh Mg surface on β-MgH_2 decomposition, allowing further oxidation with an oxygen impurity either from a small leak or by back diffusion from the pump. Oxidation causes a reduction in Mg intensity from 315 °C to 390 °C, at this point $LiBH_4$ decomposes as evidenced by LiH formation (*cf.* inset top right in figure 4.24 at 390 °C) this also agrees with the decomposition observed during NPD for 0.3:1 under vacuum (*cf.* 400 °C). After LiH reaches max intensity (*ca.* 415 °C) α-alloy formation begins, as shown by a drop in Mg intensity and d-spacing shift to smaller values (shown in figure 5.2 top). At 465 °C a β-alloy is formed and Mg d-spacing stops reducing as this phase reaches saturation limit of Li for this phase. Alongside β-alloy, a small MgB_2 component also forms

(shown in figure 4.24 inset middle) this phase was not detected in NPD experiments into the 0.3:1 sample under vacuum, it is likely that this was due to poorer sensitivity of NPD to boron and magnesium. These results suggest that the MgB_2 reaction will progress at high temperatures alongside alloy formation, this agrees with reports from the literature observing this phase above 500 °C (Yu *et al.,* 2006b) under inert conditions. These results also explain the presence of this phase detected through *ex-situ* XRD data discussed in section 5.3, where samples have been heated to >500 °C. The reaction therefore proceeded through that proposed by Yu *et al* in equation 2.17.

Cooling of the decomposition products and subsequent hydrogenation will be discussed in relation to reaction environment in section 5.5 and cycling in section 5.6.1.

5.4.2. $0.3LiBD_4 : MgD_2$ decomposed under D_2

NPD data for the 0.3:1 showed that this ratio under D_2 decomposes through the same initial stages as under vacuum, with phase change and melting proceeding at the expected temperatures, followed by the decomposition of the β-MgD_2 to form Mg (following equation 5.2). The first significant difference occurred during the $LiBD_{4(l)}$ decomposition (*ca.* 470 °C), instead of forming an alloy the $LiBH_4$ decomposed to form LiD and MgB_2 phases. A reduced Mg phase was retained on formation of MgB_2 and LiD, due to the excess Mg content (compared to the stoichiometric 2:1 ratio). No further changes were detected on heating to 550 °C. This reaction pathway appears to follow that proposed by Vajo *et al*. shown in equation 5.7.

$0.3\ LiBD_4 + MgD_2 \rightarrow 0.3\ LiD + 0.15\ MgB_2 + 0.85\ Mg + 1.45\ D_2$ **Equation 5.7**

Ex-situ experiments discussed in section 5.3 showed similar end products for 0.3:1 decomposed under 4 bar H_2, with some β-MgH_2 phase formed on cooling (due to hydrogenation of unreacted Mg), therefore the reaction equation on decomposition before cooling can be assumed to similarly follow equation 5.7.

5.4.3. $2LiBD_4 : MgD_2$ decomposed under vacuum

NPD for the stoichiometric 2:1 sample heated under vacuum (figure 4.14) was found to initially decompose in a similar manner to the 0.3:1 samples. After melting of the $LiBD_{4(hex)}$ phase and decomposition of the β-MgD_2, further heating to 450 °C showed the $LiBD_{4(hex)}$ amorphous hump begin to disappear and at 480 °C LiD appeared. In an analogous reaction to the 0.3:1 sample decomposed under vacuum the sample showed alloy formation. Firstly a α-alloy at 480 °C then at 540 °C a β-alloy phase appeared. Unlike the 0.3:1 sample, the greater Li-content meant that by 560 °C the sample no longer contained any α-alloy, just β-alloy and LiD phases, (equation 5.8) which would suggest that the reaction was incomplete by 560 °C. This agrees with the sluggish formation of β-alloy shown in the *ex-situ* XRD work. Further destabilisation of LiD would appear to progress at a much reduced rate, as evidenced by the rate of LiD reduction.

$2\ LiBD_4 + MgD_2 \rightarrow 1.57\ LiD + 1.43\ Mg_{0.70}Li_{0.30} + 2\ B + 4.22\ D_2$ **Equation 5.8**

Ex-situ XRD experiments discussed in section 5.3 also showed alloying, however cooled reaction products display α-alloy as well as β-alloy. From *in-situ*

experiments we know system decomposes to form β-alloy and LiD under slow ramp rate (1 °C min^{-1}) we also know that the formation of β-alloy has poor kinetics, as shown by lack of formation in *ex-situ* XRD into 0.3:1 ratio. Therefore is it likely that the reaction did not fully progress according to equation 5.8 during the faster DSC experiment ramp (*ca.* 10 C min^{-1}) thereby showing α-alloy/β-alloy composition on cooling.

5.4.4. $2LiBD_4 : MgD_2$ under D_2

NPD data for the stoichiometric 2:1 sample heated under D_2 (figure 4.14) presents a similar decomposition progression to other NPD samples, only after decomposition of $LiBD_4$ are any differences in phase progression shown. Heating to 440 °C the amorphous hump begins to reduce indicating $LiBD_4$ decomposition, toward the end of the hump loss at 510 °C LiD and MgB_2 phases are formed and are retained on heating to 560 °C, following equation 5.9, this progression differs from the 0.3:1 sample decomposed under D_2 in that all Mg forms MgB_2.

$$2\ LiBD_4 + MgD_2 \rightarrow 2\ LiD + MgB_2 + 4\ D_2$$ **Equation 5.9**

Comparing NPD end products with those after DSC experiments discussed in section 5.3 it would appear the DSC sample had not fully progressed through equation 5.9 due to kinetics. However, these results show progression through the reported destabilisation mechanism proposed by Vajo *et al*. (Vajo *et al.*, 2005).

5.4.5. *Phase Orders and Intermediate Phases*

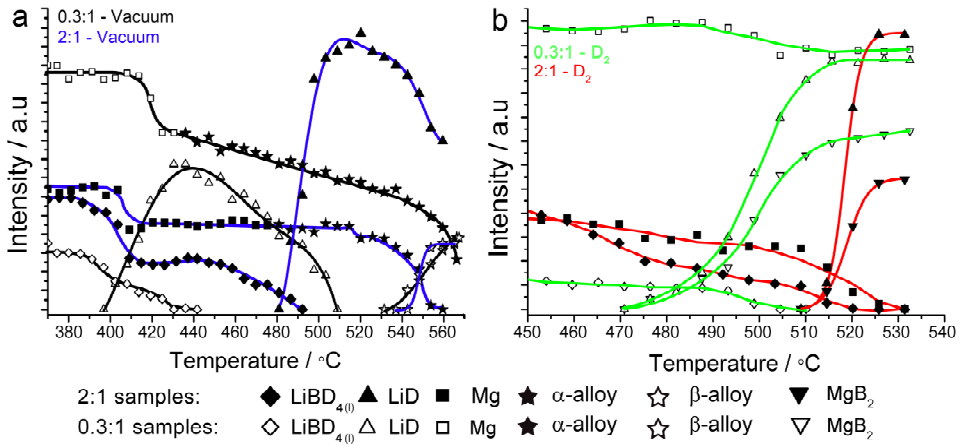

Figure 5.3. NPD Peak areas for key phases through decomposition of samples shown in figure 4.14.

Figure 5.3a shows in more detail the changes in NPD phase intensity for the 2:1 and 0.3:1 samples decomposing under a dynamic vacuum (a) and D_2 (b). These intensities were calculated using a statistical fit macro detailed in section 3.4.3. The phase progressions through these ramps has been discussed in each case, however the key difference between samples is that whilst both ratios exhibited similar phase changes under the same decomposition environment, the phase order varies. The amorphous $LiBD_{4(l)}$ phase loss for 0.3:1 samples demonstrates a concomitant formation of the decomposition products (LiD and MgB_2) or (LiD and α-alloy), but the 2:1 sample only started to form these decomposition products when the intensity for the $LiBD_4$ phase had almost reached zero. It is interesting to note that the initial loss in intensity of the $LiBD_{4(l)}$ phase for the 2:1 sample occurred at a similar temperature to the 0.3:1 sample under both decomposition environments. This suggests that the $LiBD_4$ species has become thermally unstable, but for the 0.3:1 sample this results in complete decomposition and formation of reaction products whereas for the 2:1 sample it results in the formation of an amorphous intermediate phase.

Orimo *et al.* have shown formation of an intermediate when $LiBH_4$ is decomposed on its own; from Raman results and comparing with the calculated phonon density of states, they suggested the intermediate was $Li_2B_{12}H_{12}$ (Orimo *et al.,* 2006) forming during the decomposition according to equation 2.7. However this decomposition relies on the formation of LiD which was not evident during the loss of the $LiBD_4$ phase for the 2:1 samples, suggesting this is unlikely to be the intermediate. Kang *et al.* have suggested, from DFT results, the potential formation of other intermediate species such as Li_3BH_6 and LiBH as in equation 2.8 and equation 2.9 (Kang *et al.,* 2005). Formation of these intermediates does not lead to the formation of LiH and are therefore potential candidates to explain the intermediates formed. However, Li_3BH_6 is unrealistic as B does not favour 6-coordinate (Kang *et al.* also found a higher activation energy barrier to the formation of this species), thus LiBH is more likely. However, there is no experimental evidence to show that this species can be formed and it would be a surprising species as this would leave the B in a less favourable electronic configuration. The difficulty of investigating amorphous phases through diffraction techniques makes it unsuitable for further investigation. The possibilities for future investigation are discussed in section 7.

5.4.6. Mg-rich systems $0.23LiBH_4 : MgH_2$ and $0.44LiBH_4 : MgH_2$

The 0.23:1 and 0.44:1 ratios were selected to explore the alloy formation for samples run under dynamic vacuum. The 0.23:1 system contains a ratio of 0.186 Li : 0.814 Mg i.e the maximum Li-content for the α-alloy and the 0.44:1 system contains 0.305 Li : 0.69 Mg which is close to the minimum Li content for the β-alloy phase.

In-situ NPD for ramped decomposition of the 0.23:1 sample (figure 4.19) and 0.44:1 sample (figure 4.21) under vacuum, show similar initial phase progression to that shown for the 0.3:1 ratio under vacuum. However, subsequent to α-alloy formation both the samples show a sudden increase in LiD intensity and a shift in α-alloy peaks to larger d-spacing (toward that of Mg), shortly after this event the LiD lines reduce in intensity and α-alloy peak positions return to smaller d-spacing. These effects, at 477 °C for 0.23:1, and twice for 0.44:1 (490 °C and 500 °C) suggest a temporary loss in pumping efficiency occurs, with consequent increase in D_2 partial pressure causing deuteriding of Li and reduction in Li composition of α-alloy. Once pumping efficiency is regained the alloy reforms, decomposing LiD. The high rate of formation of α-alloy during these events suggests the formation of the α-alloy is a highly facile reaction.

For the 0.23:1 sample, heating to 535 °C gave decomposition products of α-alloy only, agreeing with the expected products for the ratio. The reaction therefore progressed through equation 5.10.

$$0.23\ LiBD_4 + MgD_2 \rightarrow\ 1.23\ Mg_{0.816}Li_{0.184} + 0.23\ B + 1.46\ D_2$$ **Equation 5.10**

For the 0.44:1 sample, heating to 535 °C the sample contained only β-alloy lines, with complete loss of α-alloy. Again, these end products agree with those expected for the Mg/Li ratio. The sample therefore decomposes through equation 5.11.

$$0.44\ LiBD_4 + MgD_2 \rightarrow\ 1.467\ Mg_{0.7}Li_{0.3} + 0.44\ B + 1.88\ D_2$$ **Equation 5.11**

The DSC end products for these ratios investigated through XRD (figure 4.13) showed similar phases to NPD for the 0.23:1 sample, however the 0.44:1 end products show α-alloy, β-alloy and MgB_2 lines. These end products conflict with the fully β-alloy shown from NPD, this is likely to be due to the fast ramp rate not providing sufficient time for equilibrated end products to form. This suggests that the α-alloy formation is a more facile reaction than that for the β-alloy.

5.5. Reaction environment and the role of partial pressure

It had been a puzzle why the early paper from Vajo *et al*. did not find the formation of alloys for decomposition under dynamic vacuum, finding instead LiD and Mg metal phases remaining. This is in marked contrast to *ex-situ* and *in-situ* data discussed so far. The potential cause of this disparity can be made by considering the partial pressure of H_2 under dynamic vacuum conditions.

Interesting observations can be made into the cooling of decomposition products during *in-situ* NPD and XRD experiments. The key variation between experiments was the vacuum pump used. For experiments into 2:1 and 0.3:1 ratios, the pump used was a scroll vacuum pump (Varian SH-110) connected directly to the sample vessel, the specification for this pump gives an ultimate pressure of $6.6x10^{-5}$ bar, however experiments into achievable H_2 pumping pressure have shown achievable pressure is two orders of magnitude poorer, *cf*. 10^{-3} bar H_2 (In 2009) for scroll pumps. NPD experiments into Mg-rich 0.23:1 and 0.44:1 sample used a multi-stage roots pump (Adixen ACP-28) connected through an automated gas system (figure 3.1), the specification for this pump states a $3x10^{-5}$ bar ultimate pressure, however the achievable pressure for H_2 is not specified and will be higher than that for heavier gases. The pump was also

situated further from the sample, the partial pressure of H_2 is therefore likely to be higher than that achieved by the scroll pump i.e. > 10^{-3} bar H_2. Finally, *in-situ* XRD experiments used a rotary oil sealed pump, providing 10^{-2} bar vacuum, again the associated hydrogen pressure is likely to be higher than this value and achieve a poorer vacuum than the scroll pump.

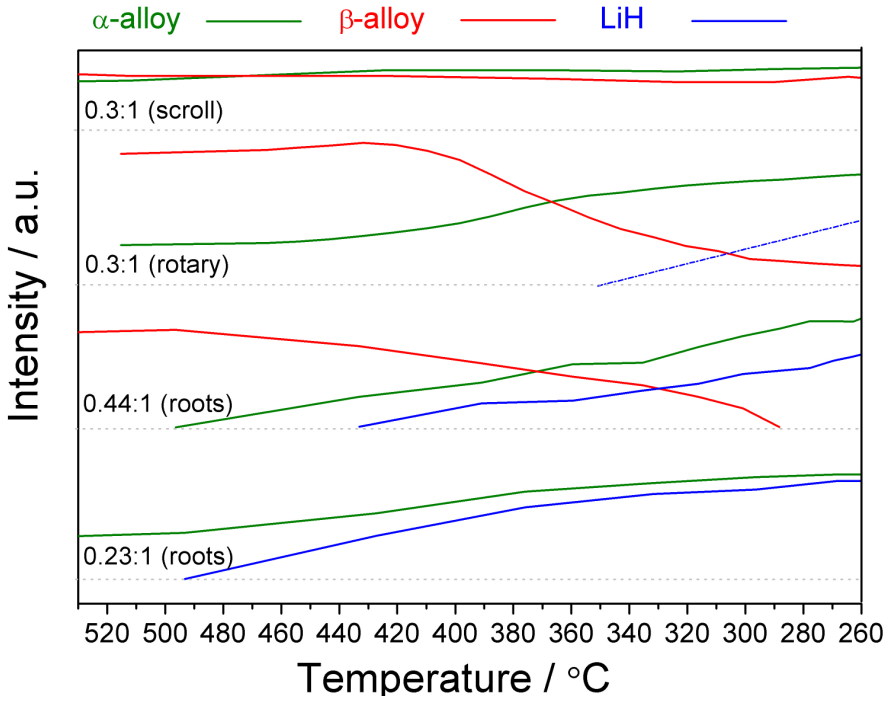

Figure 5.4. Sample composition as characterised by peak intensity analysis during cooling under various partial pressures of D_2/H_2 for $0.3LiBD_4 : MgD_2$ scroll-pump (figure 4.14) and $0.3LiBH_4 : MgH_2$ rotary (figure 5.2) $0.44\ LiBD_4 : MgD_2$ roots-pump (figure 4.22) and $0.23LiBD_4 : MgD_2$ roots-pump (figure 4.20).

Comparison of the NPD/XRD peak areas for decomposition products through cooling is made in figure 5.4. A 0.3:1 sample cooled under a high quality vacuum (scroll pump), is compared to a 0.3:1 sample cooled under a poorer vacuum (rotary pump) and with other Mg-rich compositions 0.23:1 and 0.44:1 ratios cooled under a poor vacuum (roots pump). On cooling the 0.3:1 sample under vacuum (scroll) the α-alloy and β-alloy phases remain stable from 520 °C

to 260 °C, with no evolution of LiD. Direct comparison can be made with 0.3:1 cooled under poor vacuum (rotary pump), the decomposition products at 520 °C contain a predominantly β-alloy composition of α-alloy and β-alloy, on cooling the β-alloy intensity drops at *ca.* 430 °C with concomitant rise in α-alloy, this shift in composition is due to hydriding of Li under a low partial pressure of H_2, LiH lines are too low in intensity for peak area measurement but a straight line estimating intensity of this phase has been added to the plot. The decomposition products of Mg rich compositions 0.23:1 and 0.44:1 cooled under a poor vacuum (roots pump) are also presented, showing the LiD formation more clearly. For the 0.44:1 sample the decomposition product at 535 °C, β-alloy, reduces on cooling with appearance of α-alloy at 500 °C and LiD at 430 °C, by 260 °C all β-alloy is lost, leaving α-alloy and LiD phases. The 0.23:1 sample decomposition product at 535 °C, α-alloy, on cooling shows an increase in intensity as Li diffuses out forming LiD at *ca.* 490 °C, rising in intensity on cooling as more Li diffuses out of the alloy.

These transitions allow evaluation of destabilisation of LiH, for pure LiH a temperature of 500 °C yields a plateau pressure of $3x10^{-5}$ bar H_2 (Lide 2007), experimental pressures would need to be below this pressure for LiH decomposition below 500 °C. None of the investigated pumps are likely to achieve such a low partial pressure of hydrogen, presence of alloys therefore shows a destabilisation reaction between LiH and Mg which would raise the plateau pressure above experimental partial pressure of H_2 at these temperatures (ca. > 470 °C for NPD experiments in figure 4.19 and figure 4.21) allowing decomposition of the phase. Cooling into a partial pressure then drops equilibrium pressure through the experimental partial pressure and hydrogenation occurs, further experiments into Mg and LiH exchange through

PCI experiments would be required to elucidate this interaction, and quantify the thermodynamics of the reaction.

A rough calculation of the thermodynamics can be made from re-arrangement of equation 2.2 and equation 2.3 to give equation 5.12

$$\Delta H = \Delta ST - RT \ln p$$

Equation 5.12

Assuming LiH entropy is the same for the destabilised system and assuming a minimum H_2 pressure for the scroll pump of 10^{-3} bar H_2 this would equate to a reduction in ΔH from 181 kJ mol^{-1} H_2 to 105 kJ mol^{-1} H_2 to allow destabilisation at above >400 °C.

These results help us to understand the apparent disparity within the literature for reported decomposition products under vacuum conditions. Observation of Mg and LiH end products for samples decomposed under vacuum (Vajo *et al.*, 2005; Pinkerton *et al.*, 2007) suggests dynamic vacuum conditions may have had a partial pressure of H_2 high enough to cause hydrogenation of the Li component of the alloys. Experiments by Yu *et al.* were run under flowing Ar, which will give a partial pressure of H_2 close to zero, thus retaining the alloys formed. These findings highlight the role of *in-situ* structural characterisation when following phase progressions, particularly when evolved phases may be dependent on partial pressures of H_2 and changing temperature.

5.6. Cycling

5.6.1. In-situ structural cycling characterisation

NPD results presented in section 4.3.2 have been discussed with regard to decomposition in section 5.4. Samples were also deuterided *in-situ* in order to

assess the behaviour of different reaction products. Figure 5.5 shows peak area analysis for key phases through deuteriding at 100 bars D_2 at 400 °C.

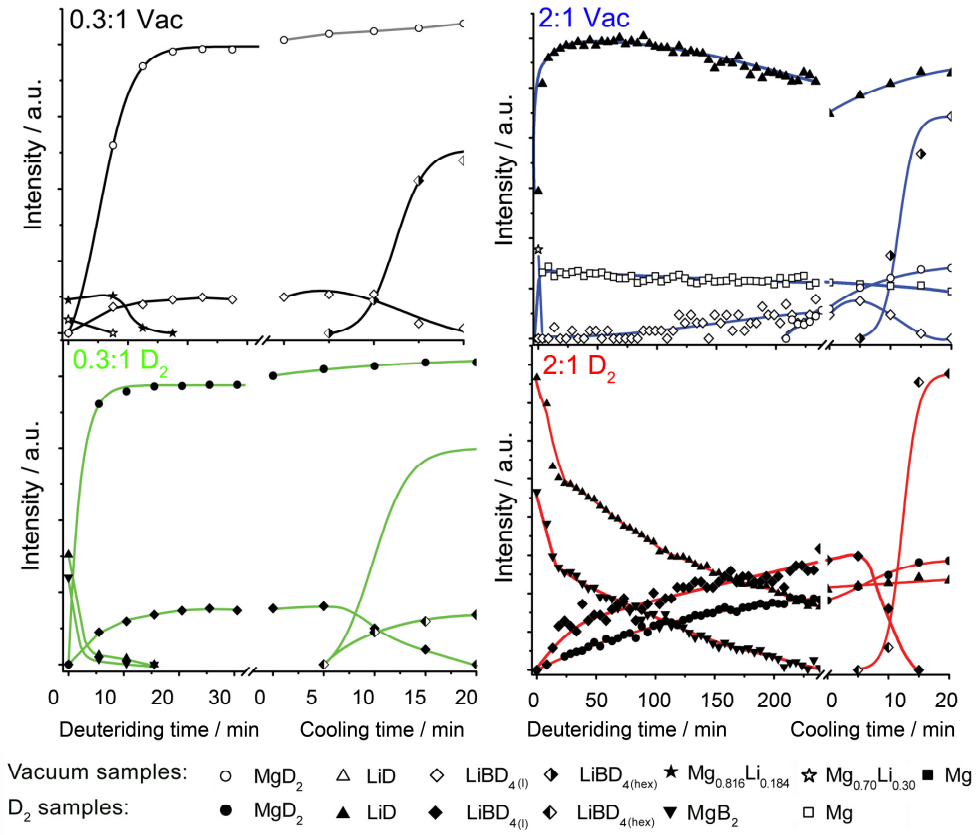

Figure 5.5. NPD peak areas for key phases through deuteriding of samples shown in figure 4.14.

On deuteriding the vacuum decomposed 0.3:1 sample the alloy phases were lost rapidly (β-alloy first followed by α-alloy) due to the removal of Li from the alloys forming $LiBD_{4(l)}$ and a concomitant formation of β-MgD_2, both the phases reached 90% conversion within 15 minutes. Under these deuteriding conditions any available Mg would be deuterided quickly; hence it would appear that the reaction of the lithium bound in the alloys was controlling the rate at which β-MgD_2 formed. It is unclear whether LiD is an intermediate in the formation of $LiBD_4$ as no LiD phase was identified, hence if this phase was involved it reacted

quickly and did not form in detectable amounts. After deuteriding for 1h (only 30 minutes shown in figure 5.5, the sample was cooled to 250 °C and a strong $LiBD_{4(hex)}$ pattern appeared as this solid phase crystallised out. Determining the final % conversion was difficult as the intensity of the $LiBD_4$ and β-MgD_2 patterns was greater than those for the as prepared materials. Weaker diffraction patterns for milled starting materials is likely due to reduction in long range order on milling, whilst the stronger diffraction pattern on deuteriding is due to improved crystalline nature of evolved hydrides.

Deuteriding also occurred very rapidly for the 0.3:1 sample which had been decomposed under deuterium, in figure 5.5 (bottom left), forming β-MgD_2 reaching 90% conversion within 15 minutes and $LiBD_4$ phases deuteriding slightly slower, reaching 90% within 20 minutes. Concomitant with $LiBD_{4(l)}$/β-MgD_2 formation was loss of the Mg, MgB_2 and LiD phases. Upon cooling to 250 °C a $LiBD_{4(hex)}$ phase crystallised out.

Figure 5.5 (top right) shows the progression of deuteriding for the 2:1 sample decomposed under vacuum and under a D_2 pressure. It is immediately obvious that the rate of deuteriding was over an order of magnitude slower than for the 0.3:1 sample. For the 2:1 sample decomposed under vacuum, a sharp increase in the LiD intensity was detected as the β-alloy reverted to a magnesium phase (as corroborated by the d-spacing for the (002) reflection). This indicated that the lithium in the alloy was preferentially deuterided (reflecting the higher reactivity of Li) forming LiD and Mg. However, after this initial reaction there was only a very slow drop in LiD intensity concomitant with slow formation of $LiBD_{4(l)}$. It is only toward the end of deuteriding that MgD_2 peaks can be seen,

this is surprising as Mg should deuteride more quickly. It is also surprising LiD forms instead of $LiBH_4$ (as shown for 0.3:1 sample).

The slow kinetics for Mg deuteriding may be due to the diffusion of lithium out of β-alloy forming a passivating layer of LiD around the magnesium, hindering the formation of β-MgD_2. A schematic of the potential microstructural effects on a single particle of β-alloy, is shown in figure 5.6. The particle at 1, shows β-alloy before deuteriding, 2 shows application of D_2 and consequent migration and LiD formation on the particle surface. On cooling (3) contraction of the passivating LiD layer tend to crack due to the comparatively large difference in the coefficient of thermal expansion between the two phases (Mg = $25x10^{-6}$ K^{-1}, LiD = $46x10^{-6}$ K^{-1} (Lide 2007)). These cracks would expose the Mg core enabling deuteriding of the metal forming MgD_2 (4). This process would also be accelerated by the subsequent expansion of the magnesium containing core leading to further cracking and potentially delamination of the LiD layer (formation of magnesium hydride results in a 33 % volume expansion (Zlotea *et al.*, 2006)) (5). From the NPD data cooling to 250 °C shows formation of a small $LiBD_{4(hex)}$ component, suggesting at least partial reversibility (approximately 10% $LiBD_4$ and 30% MgD_2 completion of reaction as calculated from peak area analysis of main peaks at 150°C before and after cycling) which is consistent with a very slow reaction between the LiH surface and B. The poor reversibility of the 2:1 multi-component system when decomposed under vacuum agrees with reports from other groups under similar conditions (Vajo *et al.*, 2005).

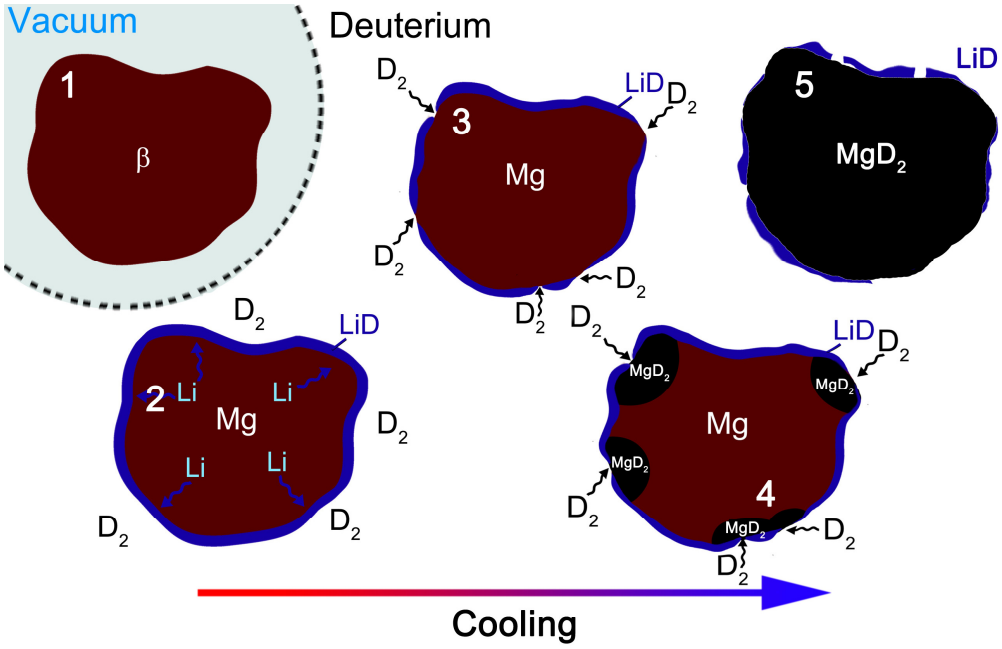

Figure 5.6. Schematic of effects of deuteriding on single particle of β-alloy, on application of D_2 at 400 °C followed by cooling.

For the 2:1 sample decomposed under deuterium (figure 5.5 bottom right) the decomposition products of LiD and MgB_2 showed initially a rapid drop in both phases over the first 11 minutes, with concomitant rise in $LiBH_{4(l)}$/β-MgD_2 as the sample deuterided. Following the initial fast kinetics the reaction slowed, showing a steady drop in intensity for the decomposition products and a concomitant rise in MgD_2 and $LiBH_{4(l)}$ phases over the 4 hours of deuteriding. The fast kinetics during the start of deuteriding is likely to be associated with the fast reaction of particles of solid LiD and MgB_2 in contact, however, on formation of a significant liquid $LiBH_{4(l)}$ component the particles will no longer be in direct contact. This would change the rate limiting factor to diffusion through the liquid phase, slowing the reaction. This effect was not shown for the 0.3:1 sample, which is likely to be due to the far smaller liquid component within the sample. On cooling the 2:1 sample after deuteriding, $LiBD_{4(hex)}$ was

formed, but there was still some LiD present, with approximately 50% $LiBD_4$ and 43% MgD_2 re-formed after cycling.

Interesting comparison can be made with *in-situ* XRD hydrogenation presented in section 4.3.3, figure 5.2 shows the intensities for phases during the first 30 minutes of hydrogenation of 0.3:1 at 315 °C and 100 bar H_2. During the first minute β-alloy is lost forming a small LiH line (visible inset left of figure 4.24) d-spacing of α-alloy peak shifts to Mg values and β-MgH_2 starts to form. After 5 minutes β-MgH_2 reaches >95 % of maximum intensity. Over the following 30 minutes MgB_2 component (as discussed this is a very small composition) reduces linearly. After 3.5 h the sample was cooled and figure 4.24 (inset top right) shows formation of $LiBH_4$ after sample is cooled below melting point of this phase. These results allow us to see the stability of MgB_2 over α/β alloys, as it is only after 3.5 h of hydrogenation that MgB_2 is lost (compared to 5 minutes for Mg-alloys). The retained LiH component throughout hydriding seems to be the source of poor reversibility of $LiBH_4$, which is likely due to the low hydriding temperature for the experiment (*ca.* 315 °C). These results would suggest that only at 400 °C has the evolved Li from alloys formed $LiBH_4$ without progressing through LiH (or detectable amounts thereof).

5.6.2. PCI cycling

Cycling of the 0.3:1 ratio was performed through two isothermal cycles at 400 °C followed by one at 350 °C and finally a single dehydrogenation at 375 °C (section 4.3.4). It is assumed that the reaction for decomposition and hydrogenation followed a similar reaction path to that of the NPD work for 0.3:1 under D_2 (equation 5.7), as the decomposition reaction progresses toward equilibrium, the pressure of H_2 will cause MgB_2/LiH reaction products rather than alloys.

Cycles for 0.3:1 sample showed two plateaus on decomposition, one at high pressure (upper) and one at lower pressure (lower), whilst the hydrogenation reactions showed a single plateau (at a similar pressure to the upper plateau for decomposition). Weight changes associated with the upper and lower plateaus for each isotherm are shown in table 5.1. The upper plateaus on dehydrogenation are close to the theoretical weight loss expected for the MgH_2 component (*ca.* 6.13 wt.%) whilst the lower plateau is similar to that expected for the $LiBH_4$ component (*ca.* 2.76 wt.%) and the single upper plateau on hydrogenation is similar to the theoretical full capacity for the system through equation 5.7 (*ca.* 8.89 wt.%).

The first hydrogenation H1, surprisingly showed a larger capacity than on the first decomposition, this was due to decomposition D1 being made from partially hydrided products (ie. through a low overpressure kinetic experiment *cf.* section 4.3.4), yielding a smaller decomposition capacity than expected, which was fully hydrogenated on the following cycle. On further cycling the sample showed a capacity drop for both phases due to oxidation of the sample. Unfortunately this was caused by a system leak which was detected in

subsequent investigation and confirmed by large oxide contamination in sample end products.

Table 5.1. PCI plateau capacity changes for isotherms of 0.3:1 sample presented in figure 4.25.

Cycle	Upper plateau Capacity change / wt.%	Lower plateau Capacity change / wt.%	Total / wt.%
D1 400 °C	6.22	2.27	8.49
A1 400 °C	9.62		9.62
D2 400 °C	6.21	2.73	8.94
A2 400 °C	8.52		8.52
D3 350 °C	5.76	1.95	7.71
A3 350 °C	3.69 / 2.59		6.28
D4 375 °C	4.32	1.59	5.92

All cycles showed the same single plateau behaviour on hydrogenation, however for the 350 °C cycle the sample unexpectedly showed two plateaus, one matching the upper plateau from decomposition and the other at a higher pressure (*ca.* 19.1 bar). This plateau may be due to phase segregation during the decomposition cycle, generating a new phase with a higher plateau pressure. However, as only one cycle was completed at 350 °C further work would be required to elucidate the source of this plateau.

PCI results can be further compared to the literature through presentation in the form of a van't Hoff plot, allowing the thermodynamics for the destabilised reactions to be calculated. Figure 5.7 shows constructed lines using experimental plateau pressures from upper and lower plateaus from the decomposition isotherms (second cycle at 400 °C was used due to its flatter plateau), also included for comparison are experimental values for the 2:1 ratio from Vajo *et al.* (Vajo *et al.,* 2005), alongside lines for $LiBH_{4(l)}$ (for partial decomposition to LiH) and MgH_2 calculated from the literature ΔH and ΔS values (IEA/DOE/SNL; Chase 1998; Lide 2007).

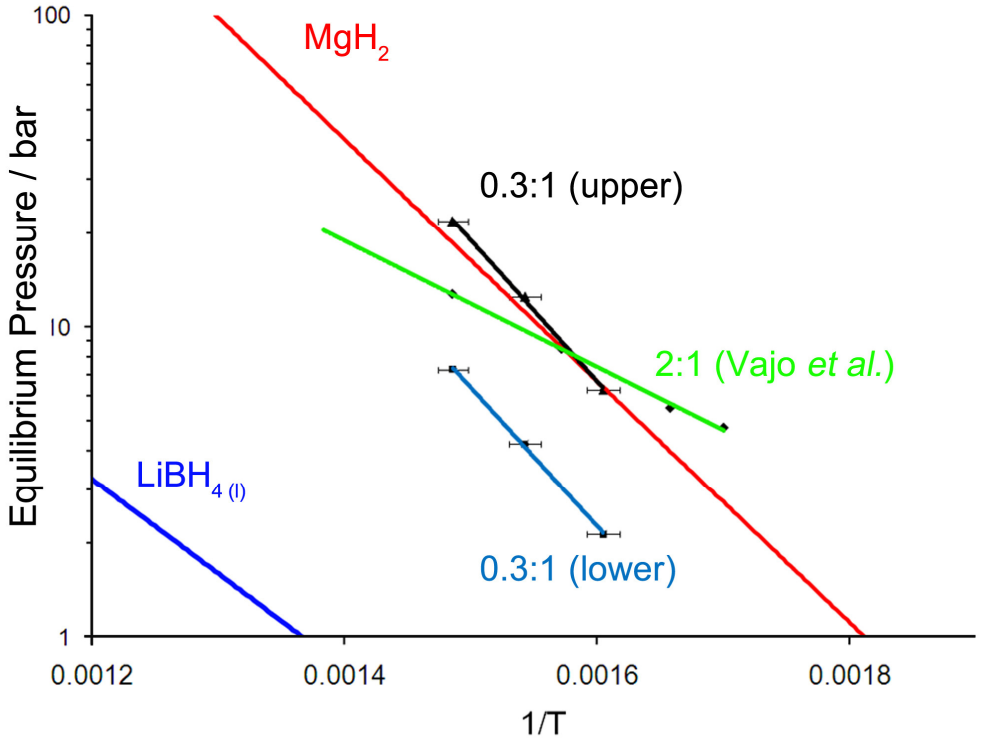

Figure 5.7. Van't Hoff plot constructed using experimental plateau values from figure 4.25 for a 0.3$LiBH_4$: MgH_2 sample, experimental values for 2$LiBH_4$: MgH_2 from Vajo *et al*. (Vajo *et al*., 2005), and literature data for $LiBH_4$ and MgH_2 (IEA/DOE/SNL; Lide 2007).

The calculated enthalpy and entropy for the upper plateau pressures are ΔH= 90.2 kJ mol^{-1} H_2 and ΔS= 160 J mol^{-1} H_2 which are higher than the literature values, *cf*. ΔH= 75.3 kJ mol^{-1} H_2 and ΔS= 132 J mol^{-1} H_2 for MgH_2. Using the associated experimental error for the van't Hoff data points, one can calculate the error range for the thermodynamic values, this gives a lower values of ΔH= 71.2 kJ mol^{-1} H_2 and ΔS= 131 J mol^{-1} H_2 which shows that the literature values are within experimental error for the PCI experiment. The lower plateau gave values of ΔH= 85.5 kJ mol^{-1} H_2 and ΔS= 144 J mol^{-1} H_2, and lower values within experimental error of ΔH= 74.7 kJ mol^{-1} H_2 and ΔS= 127 J mol^{-1} H_2: significantly higher than the theoretical $LiBH_{4(l)}$ values ΔH= 58.6 kJ mol^{-1} H_2 and ΔS= 80 J mol^{-1} H_2. In contrast to the general assumption that thermodynamic

destabilisation is via reducing the ΔH of reaction, destabilisation has occurred here because ΔS has been greatly increased.

These results suggest that through the decomposition isotherm the upper plateau was due to the MgH_2 component (equation 5.13) and that the lower plateau was due to destabilised $LiBH_4$, however, the lower plateau was not found to be reversible. If the directly formed end products through the decomposition isotherm were MgB_2 and LiH (as in equation 5.7), then on hydrogenation one would expect the reverse reaction to occur, forming $LiBH_4$ and Mg going through the same lower pressure plateau. However, the presence of B within MgB_2 appears to be limiting the $LiBH_4$ formation until a pressure is reached which enables the formation of MgH_2, releasing B which can then react with LiH. It is therefore likely that the lower plateau relates to an alternative destabilisation reaction, which subsequently progresses to form LiH and MgB_2.

It is possible that the lower plateau from PCI experiments relates to decomposition of $LiBH_4$ at the Mg surface forming highly dispersed B on the Mg, equation 5.14. Subsequent reaction with Mg could form a more stable MgB_2, equation 5.15, which does not release the boron for hydrogenation until MgH_2 forms.

$$0.3\ LiBH_4 + MgH_2 \rightarrow 0.3\ LiBH_4 + Mg + H_2 \qquad \textbf{Equation 5.13}$$

$$0.3\ LiBH_4 + Mg \rightarrow 0.3\ LiH + Mg + B_{(surface)} + 0.45\ H_2 \qquad \textbf{Equation 5.14}$$

$$0.3\ LiBH + Mg \rightarrow 0.15\ MgB_2 + 0.85\ Mg + 0.15\ H_2 \qquad \textbf{Equation 5.15}$$

It is interesting to consider the formation of a surface boron in systems under vacuum, as the form of boron in these systems has not been identified after

decomposition of $LiBH_4$. One would expect an analogous formation of B in this more active form to occur during dehydrogenation, however the slow reaction of the B with Mg <450 °C (Vajo *et al.*, 2005; Yu *et al.*, 2006b) allows the LiMg alloys to form first, apparently inhibiting the formation of MgB_2 (NPD results showed no MgB_2 by 560 °C) and presumably retaining the B at the alloy surface. This more dispersed form of B may provide the improved cycling kinetics shown for the 0.3:1 samples under vacuum.

The PCI results by Vajo *et al.* for the stoichiometric 2:1 system presented only one plateau during the decomposition isotherm, but this had a sloping plateau covering a range of 10 bar. This suggests equilibrium had not been reached for each data point, and potentially masked the dual plateau behaviour. The calculated thermodynamics for hydrogenation isotherms were ΔH= 40.5 kJ mol^{-1} H_2 and ΔS= 81.3 J K^{-1} mol^{-1} H_2 (Vajo *et al.*, 2005), however the slope of the reported plateaus, and lack of error bars makes comparison with values calculated here difficult. Further investigation of the 2:1 system under equivalent cycling conditions would be needed to compare the sample thermodynamics.

Investigation of the 0.3:1 system through PCI experiments (and the thermodynamic data extracted) shows that the presence of Mg during decomposition of $LiBH_4$ has thermodynamically destabilised the $LiBH_4$, and whilst the van't Hoff plot does not yield experimental thermodynamic data which supports the traditional view of destabilisation (ie. a lower enthalpy of reaction), it does yield a lower T(1bar) of 322 °C (*cf.* 459 °C for $LiBH_{4(l)}$) and on hydriding, the reaction of end products is inhibited by the formation of MgH_2,

thus the whole system follows the upper plateau, i.e. $LiBH_4$ formation conditions are the same as those for MgH_2.

5.7. Practical application

Investigation of mulit-component destabilised systems allows discussion of these materials within a broader context of application. The DOE targets for automotive application include capacity of 5.5 wt.% and 40 g H_2 L^{-1} by 2015, rising to 7.5 wt.% and 70 g H_2 L^{-1} as ultimate targets, with the aim of storing 5 kg H_2 (enough for 200 miles of vehicle range). For the materials investigated all compositions meet both of these targets, 0.3:1 for example contains 9.8 wt.% with a volumetric capacity of 83.8 g H_2 L^{-1}, however these comparisons ignore the total system capacity, which will be dramatically reduced by the storage tank and heat management systems. Car manufacturer guidelines suggest 3 wt.% system capacity is achievable for a 4 wt.% material (2009), for 5 kg H_2 this equates to a 40 kg tank system. This extra weight applied to 5 kg H_2 stored within 0.3:1 (9.8 wt.%) is approximately half the weight of the hydride *ca.* 51 kg, and yields a system capacity of only 5.4 wt.% (below DOE targets even for 2015) research into weight reduction for system tank and heat transfer systems is therefore required in order to meet DOE targets, for all compositions investigated.

Other key DOE targets relate to charging time, these are currently set at 3.3 minutes by 2015 and an ultimate target of 2.5 minutes (Dilich 2009). Of the investigated systems, 0.3:1 decomposed under both vacuum and D_2 showed the fastest deuteriding, with un-catalysed samples showing 90% deuteriding in less than 20 minutes. These kinetics, although significantly faster than the 2:1 system investigated (*ca.* 50 % after 4 h deuteriding) do not meet the DOE

targets. It is also important to consider the heat management requirements for a scaled up system, for a system with an enthalpy of formation ΔH_f = 39.8 kJ mol^{-1} H_2 hydrogenation would require 15800 kWh of energy dissipation, or 0.66 MW within 2.5 min. Chaise *et al*. have shown thermal conductivity improvements for Ti-V-Cr catalysed MgH_2 by pressing powders (under 1000 MPa) and by addition of 10 wt.% expanded natural graphite (Chaise *et al.,* 2009), however, such large quantities of heat generation are unlikely to be acceptable for onboard regeneration of stores. Complex hydride systems may therefore be best utilised for automotive application with off-board regeneration, this could be achieved by using exchangeable tanks, allowing slower hydrogenation of the store external to the vehicle.

Material costs must also be as low as possible, a target of 67 $ kg^{-1} H_2 was set by the DOE, but has not been updated for new guidelines. Economies of scale suggest material prices would reduce dramatically were a complex hydride store taken to mass production, purchasing at laboratory grade material prices would require £2500 for the 50 kg of 0.3:1 a 5 kg H_2 store would require (Sigma-Aldrich 2009).

The major technical target remaining is that of temperature, PEM fuel cells operate at 100 °C, stores operating above this temperature sacrifice their efficiency due to the wasted energy required to keep them at operating temperature. Further investigation of catalysts and destabilising additions would be required to approach these temperatures, even for systems operating at their T(1bar) which is generally kinetically limited. The other alternative application is as a store for hotter operating temperature fuel cells, such as solid oxide type.

Certainly, whilst automotive targets currently require further development for systems, there are niche applications for which current complex hydride storage systems could find application. Stationary power source requiring high stability would favour complex hydrides over liquid stores as they would not have the dormancy of liquid H_2 systems. High volumetric capacity, also makes complex hydrides suitable for space restricted storage without the weight constraint, such in naval application (Güther *et al.*, 1999).

Comparison of the investigated system therefore comes down to kinetics and capacity. The Mg-rich systems of 0.23:1, 0.3:1 and 0.44:1 appear to provide significant kinetic advantage over the Li-rich stoichiometric composition 2:1, whilst still maintaining high capacity (and being less expensive for their lower Li content). This capacity advantage is due to the destabilisation effect of Mg on LiH, allowing hydrogen from this hydride to be decomposed significantly below its T(1bar) under vacuum conditions. However it is important to consider the potential decomposition environment of an operating hydride bed, this is most likely to be a low partial pressure of hydrogen unless an inert carrier gas were employed (which would require subsequent separation stage).

Decomposition under hydrogen has shown MgB_2 formation in all systems discussed so far, suggesting this is the favoured decomposition pathway under H_2. Development of destabilising additions may enable the progression through alloy end products under H_2, this is discussed in relation to further destabilising additions in section 5.9. The alternative would be investigation of systems with sufficient capacity through the LiH/MgB_2 end products, whilst maintaining the kinetic advantages of Mg-rich systems. The advantages which may be inferred by the presence of MgH_2, may be morphological, as discussed with reference to

hydrogenation kinetics in section 5.6.1. Development of stoichiometric system reported in the literature has focused on improvement of heat transfer and reduction in sintering of end products, carbon nanostructures have been investigated as host structures for the $LiBH_4$ in order to improve these issues (Yu *et al.,* 2007; Fang *et al.,* 2008a; Fang *et al.,* 2008b; Gross *et al.,* 2008; Wellons *et al.,* 2009), it is possible that the presence of a larger component MgH_2/Mg matrix acts in a similar way.

Development of Mg-rich systems can take one of two paths, with optimisation of the system for decomposition under either H_2 or under inert conditions. Improvements of the Mg-rich system under H_2 would be best made through a range of kinetic experiments into varying stoichiometry, and a detailed morphological investigation of the system allowing refinement of the system to yield the largest $LiBH_4$ component whilst retaining the catalytic advantage of larger Mg content. However, many studies have investigated this reaction pathway for the 2:1 system, and whilst the system shows potential, more valuable investigation relates to the system decomposing under inert conditions.

Investigation of Mg-rich samples 0.22:1 and 0.44:1 samples showed progression of alloys reaching their theoretical alloy composition of α-alloy, and β-alloy respectively, the results also show the facile reaction of the α-alloy, and the slower kinetics of β-alloy formation. Further investigation of these Mg-rich systems is therefore two fold; firstly improvement of kinetics is required to improve β-alloy formation, thus allowing higher Li systems to be investigated. Secondarily development of the system to include further destabilising additions, in order to increase plateau pressures at a given temperature,

potentially allowing alloy formation under partial pressures of H_2. The first of these routes was investigated through addition of various catalysts highlighted from the literature for MgH_2 and $LiBH_4$, these results are discussed in section 5.8. The second route, into further destabilising additions is discussed with reference to Al addition through $LiAlH_4$ in section 5.9.

5.8. Catalysts

Work presented thus far has been into systems milled for 1h, containing no catalyst. Investigated catalysts were characterised through XRD of milled material, followed by DSC decomposition and subsequent *ex-situ* XRD of decomposition products (*cf.* Section 4.4). Figure 5.8 shows the key DSC temperatures for investigated catalysts to the 0.3:1 system, MgH_2 decomposition was taken from peak temperature, the $LiBH_4$ decomposition is taken as the maximum temperature of the largest peak.

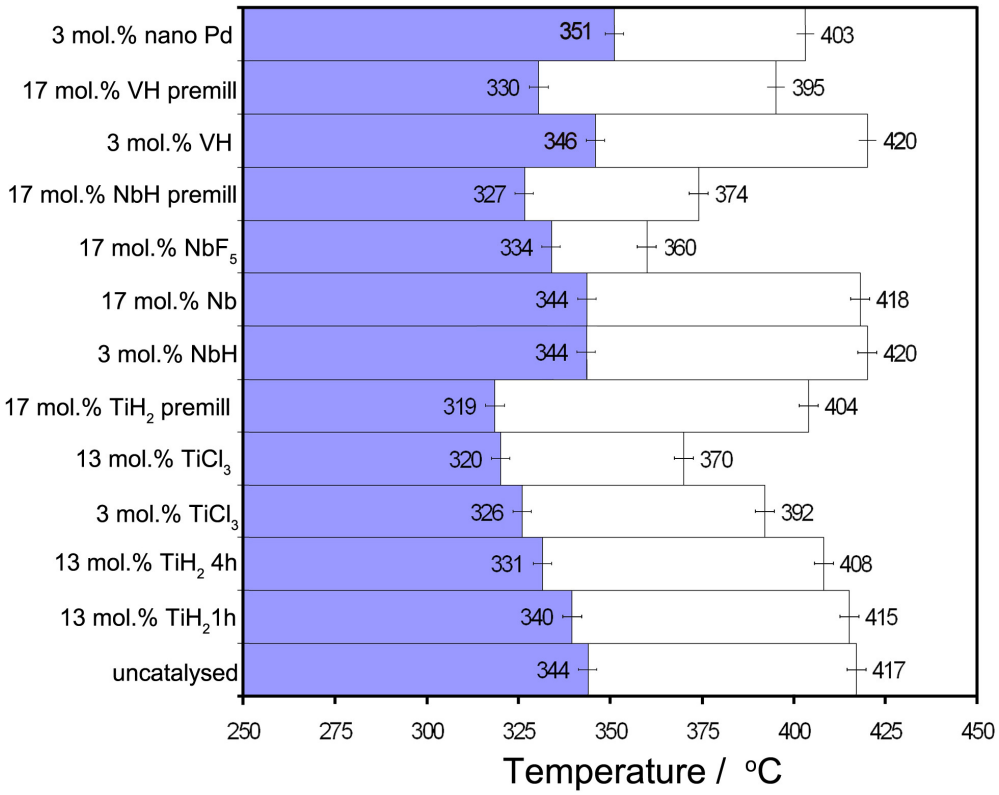

Figure 5.8. DSC peak temperatures for components of catalysed 0.3$LiBH_4$: MgH_2 samples, MgH_2 (blue) and $LiBH_4$ (white).

5.8.1. Milling

Addition of hydride catalysts TiH_2, NbH, VH and metallic Nb through a standard 1h mill provided no significant reduction in decomposition temperature in either $LiBH_4$ or MgH_2 phases. Longer milling of 4h for the TiH_2 addition provided a small improvement in both MgH_2 (*ca.* 13 °C*)* and $LiBH_4$ (*ca.* 9 °C) phases. However, a more drastic effect was noted for the pre-milled samples, which gave large reductions in $LiBH_4$ and MgH_2 for TiH_2 additions (*ca.* 25 °C and 13 °C), NbH (*ca.* 17 °C and 43 °C) and VH (*ca.* 14 °C and 18 °C). TiH_2 shows the largest effect on MgH_2 temperature but the smallest effect on $LiBH_4$ temperature, whilst NbH provides the largest effect on $LiBH_4$ reducing temperature by *ca.* 43 °C, these results suggest pre-milling for 30h with MgH_2 allows a fine dispersion

of catalyst. Improved dispersal was also investigated through Pd additions, dispersed on carbon cones, the addition provided a strong effect on $LiBH_4$ reducing the event to one peak and reduced temperature (*ca.* 14 °C), however MgH_2 decomposition temperature was higher than for the uncatalysed sample, this was most likely due to reduced milling efficiency from the carbon structures.

These results compare well with reported catalytic improvements in the literature, Fan *et al* showed decomposition of $0.3LiBH_4$: MgH_2 catalysed by 16 wt.% Nb_2O_5 (15 h milled) under Ar at 10 °C min^{-1} to reduce MgH_2 decomposition to 321 °C (*cf.* 344 °C for their uncatalysed sample) and $LiBH_4$ decomposition to 372 °C (*cf.* 430 °C for their uncatalysed sample) (Fan *et al.,* 2008). They report that Nb_2O_5 reacts to form a stable NbH catalyst. This suggests Nb_2O_5 reacts to disperse NbH similarly to the dispersion caused by long pre-milling. However, Fan *et al.* show large MgO patterns in their decomposition products, which would act to reduce system capacity. This suggests pre-milled NbH additions offer a better catalyst.

Bosenberg *et al.* investigated a range of catalysts for 2:1 systems decomposing under 5 bar H_2, including VCl_3 and SiO_2, the greatest effect was shown for 5 at.% titanium isopropoxide additions, reducing MgH_2 and $LiBH_4$ decomposition from 370 °C to 350 °C and >470 °C to 420 °C respectively (Bosenberg *et al.,* 2007). The decomposition environment used does not allow direct comparison with results presented here, however the reductions in temperature of 20 °C for MgH_2 and 50 °C for $LiBH_4$ are similar to those shown for pre-milled NbH, and halide additions of NbF_5 and $TiCl_3$.

Whilst investigated hydride and metal catalysts do show kinetic improvements, results do not provide evidence of a final catalytic phase. However, they do suggest processing conditions are the most important factor when making hydride or metal additions to these systems, pre-milling being an important tool to dispersal of hydride phases. This agrees with investigation by Au *et al.* who showed TiH_2 additions milled for short periods (5h) produced minimal effect on $LiBH_4$ decomposition temperature (Au *et al.*, 2008); it is likely that without long milling times dispersion of the active phase is not achieved.

5.8.2. Catalyst halide additions

Whilst pre-milling for long periods of time can improve the dispersion of hydride catalysts, similar catalytic improvements were achieved through 1h milling with metal-halide additions. This appears to be due to the reactivity of the halide phase, causing formation of either chloride, or fluoride species with the Li from $LiBH_4$. This effect can be seen on milling of 13 mol.% $TiCl_3$ with 0.3:1, as milled products showed a LiCl and $TiH_{1.924}$ pattern, which suggests reaction of these $TiCl_3$ addition during milling to form LiCl and consequent hydrogenation of Ti (from H_2 evolved from partially decomposed $LiBH_4$) yielding a dispersion of $TiH_{1.924}$ and LiCl. The reactivity of $TiCl_3$ additions has been reported in the literature, with Au *et al.* showing full reaction of additions, forming LiCl in milled products (Au *et al.*, 2008). This reaction is likely to have occurred in 3 mol.% additions of $TiCl_3$ but below detection limits for characterisation parameters. This effect however, contrasts with the 17 mol.% additions of NbF_5, which showed no LiF on milling, these results again agree with reports in the literature suggesting fluoride additions are less reactive, Au *et al.* finding only partial reaction of $LiBH_4$ and TiF_3 under the same parameters as $TiCl_3$ additions. Decomposition of halide catalysed samples showed dramatic

reductions in both $LiBH_4$ and MgH_2 phases, for 3 mol.% $TiCl_3$ this provided 18 °C and 25 °C reductions, whilst for 13 mol.% reductions were 24 °C and 47 °C, NbF_5 addition of 17 mol.% yielded a 10 °C and 43 °C drop in MgH_2 and $LiBH_4$ respectively. The improved effects of the halide catalysts over hydride additions on $LiBH_4$, suggest an increased role of the halide species on this phase.

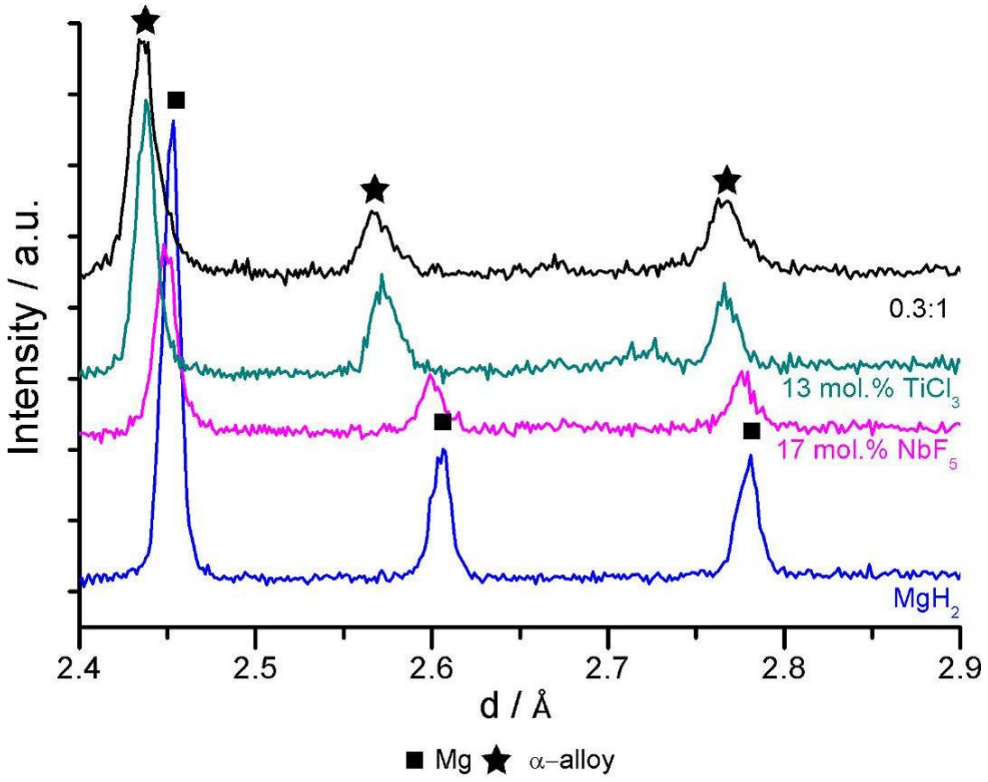

Figure 5.9. XRD data for end products after DSC for NbF_5 and $TiCl_3$ catalysed $0.3LiBH_4 : MgH_2$ compared to uncatalysed $0.3LiBH_4 : MgH_2$ and MgH_2.

End products of NbF_5 showed significantly less alloying in end products and large LiF lines. Figure 5.9 shows the decomposition product Mg/α-alloy peaks for NbF_5 catalysed sample compared to 0.3:1 and MgH_2 samples. The d spacing for (002) plane shows a shift of 0.0074 Å from Mg spacing, compared to 0.0391 Å for the 0.3:1 sample. Assuming a linear relationship this would equate to an

alloy composition of $Mg_{0.965}Li_{0.035}$, this agrees with the theoretical calculation for the system forming LiF; where the ratio 0.3Li:0.25F suggests 83% LiF formation to 17% LiMg would form (*i.e.* an alloy of $Mg_{0.952}Li_{0.048}$). The 13 mol.% $TiCl_3$ showed a similar reduction in alloying for end products, the Mg/α-alloy lines for these products are also shown in figure 5.9. The shift in d-spacing (*ca.* 0.0348 Å for $TiCl_3$ 0.0391 Å for 0.3:1) corresponds to an alloy of $Mg_{0.834}Li_{0.166}$, which agrees with theoretical calculations for Li:Cl ratio (*ca.* 0.3Li:0.117Cl) would leave an alloy of $Mg_{0.845}Li_{0.155}$. The stability of the LiF/LiCl phases are likely to be very high, therefore representing dead phases in terms of reversibility, with consequent reduction in system capacity. This draws comparison with other work into catalysts forming stable end products, such as work into TiO_2 (Yu *et al.,* 2008) and SiO_2 (Mosegaard *et al.,* 2008) which form stable lithium titianate and orthosilicate phases respectively.

Discussion of the literature in section 2.7, highlighted cation exchange and $M(BH_4)_3$ formation as a possible result of metal-halide catalysts (Au *et al.,* 2008). This phase was not observed experimentally and without *in-situ* structural analysis, or use of spectroscopy techniques the possibility of these phases still remains. It seems more likely that TiH_2, or NbH phases form alongside LiCl and LiF with hydrides aiding H_2 disassociation and providing a spillover effect for hydrogen. The generated LiCl or LiF may interact with the remaining $LiBH_4$ with consequent alteration of melting point and potentially thermodynamics, this effect has been shown experimentally by several groups, with fluoride additions shown to reduce melting point (Wang *et al.,* 2009) and chloride additions to increase it (Au *et al.,* 2008). Whether this effect is due to dissolution of the lithium halide species within $LiBH_4$ or substitution of halide with hydrogen is not known. Observed melting points presented here do not

show significant alteration due to halide addition; for fluoride additions this is due to the large addition yielding no detectable $LiBH_4$ events through DSC decomposition. Chloride additions yield no significant shifts in melting point, however this may be due to the $LiBH_4$ starting materials; discussion in section 5.2 into as received and milled $LiBH_4$ noted the shifted $LiBH_4$ melting points to higher temperatures (*ca.* 289 °C compared to literature 268–286 °C) observed through DSC. XRD analysis of as received $LiBH_4$ showed evidence of some chloride impurities, it is therefore possible that these impurities had the effect of increasing $LiBH_4$ melting temperature by forming solid solution with $LiBH_4$ above >100 °C as shown by Moesgaard *et al.* and discussed in section 2.7.2 (Mosegaard *et al.*, 2008).

Investigation of catalysts showed the greatest effects due to additions of halide precursor catalysts; however, large additions of these phases seem to form highly stable end products, reducing capacity. Therefore greatest catalytic advantage is likely to come from the NbH pre-milled addition, providing reduction of 17 °C for the MgH_2 component and 43 °C for the $LiBH_4$ component.

5.9. Al additions

Destabilised multi-component systems discussed so far have shown exciting reaction pathways through alloy formation. Further work was therefore undertaken into expansion of the system to include further alloying additions of Al. Additions of $LiAlH_4$ were made rather than Al metal, due to its ability to disperse a fine Al content through the sample on decomposition (Zhang *et al.*, 2008). $LiAlH_4$ has not been shown to be reversible without the use of a THF adduct (Wang *et al.*, 2006), therefore the inclusion of this phase can be considered merely as a means to deposit a fine dispersion of Al (and LiH) in the sample.

Characterising the behaviour of $LiAlH_4$ is important when elucidating its effects in multi-component systems. Decomposition of $LiAlH_4$ through DSC is shown in figure 4.41. The first exotherm (*ca.* 153 °C) has been reported to relate to a reaction between $LiAlH_4$ and hydroxide traces (Ares *et al.*, 2008) and precedes a larger endotherm (*ca.* 171 °C) which was due to the sample melting before partial decomposition into a solid phase Li_3AlH_6 and Al through equation 2.10 at 197 °C. Finally this solid phase decomposed through equation 2.11 to form LiH and Al, resulting in an endotherm at 246 °C. At higher temperatures the LiH component of the sample goes through decomposition at 436 °C and 461 °C which agrees with temperatures reported in the literature (Block *et al.*, 1965) and in itself represents a self destabilising reaction, forming LiAl through equation 2.12 (Blanchard *et al.*, 2004).

Investigation of binary phase systems was made in order to simplify the reaction pathways, which can then lead to further understanding of ternary phase systems. Binary systems were therefore based on a ternary phase

composition; figure 5.10 shows the ternary phase diagram for Li-Mg-Al, a simple single α-alloy forming system of $3LiBH_4$: $15MgH_2$: $LiAlH_4$ was chosen. Equivalent binary systems $3LiBH_4$: $LiAlH_4$ and $15MgH_2$: $LiAlH_4$ were investigated.

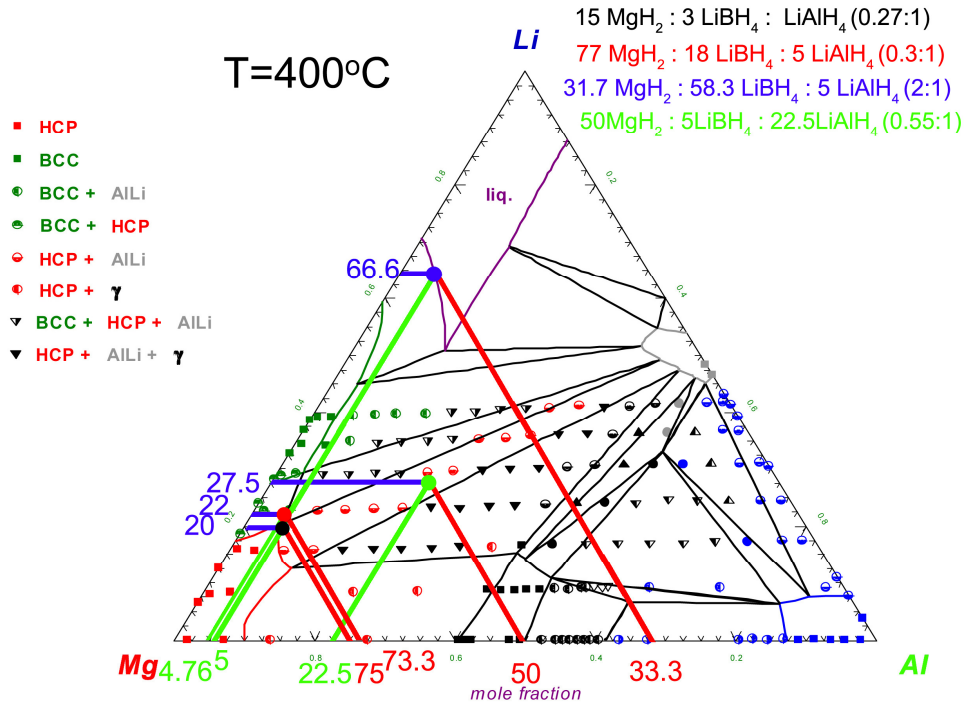

Figure 5.10. Ternary Li-Mg-Al phase diagram from thermodynamic calculations *(Harvey et al., 2007; Kang et al., 2009)* adapted to include chosen ternary compositions.

The $LiAlH_4$: $3LiBH_4$ binary system decomposition through DSC (figure 4.43) showed no significant shifts from single component temperatures, with *ex-situ* XRD (figure 4.44) showing only Al detected. These results suggest little effect of $LiAlH_4$ on $LiBH_4$ through the investigated experimental parameters.

In contrast, $15MgH_2$: $LiAlH_4$ showed MgH_2 decomposition at 347 °C (cf. 366 °C for 1h milled MgH_2) suggesting either a destabilising or catalytic effect of Al/LiH, reduced MgH_2 decomposition. A shoulder at 375 °C also suggests the LiH evolved from $LiAlH_4$ may have decomposed, which would be significantly lower

than shown for the single component $LiAlH_4$ (*ca.* >430 °C). The decomposition products for this experiment (figure 4.44) show formation of an alloy of Mg, however it matches neither α-alloy nor a Mg-rich $Al_{0.2}Mg_{1.8}$ (Frebel *et al.*, 1976), most likely this alloy is a solid solution of Mg-Li-Al, as predicted by the ternary phase diagram (*cf.* figure 5.10). Further investigation through *in-situ* techniques would be required to follow the reaction between these components; whatever the role of Al it seems to improve the thermodynamic destabilisation of LiH, allowing dehydrogenation to proceed at lower temperatures. Data from experiments by Yu *et al.* into the decomposition of MgH_2 : LiH is reproduced in figure 5.11 (Yu *et al.*, 2006a), they show significantly higher LiH decomposition (*ca.* >450 °C) for the MgH_2 : LiH ratios, than shown for $LiAlH_4$: $9MgH_2$ system presented here (*ca.* 375 °C).

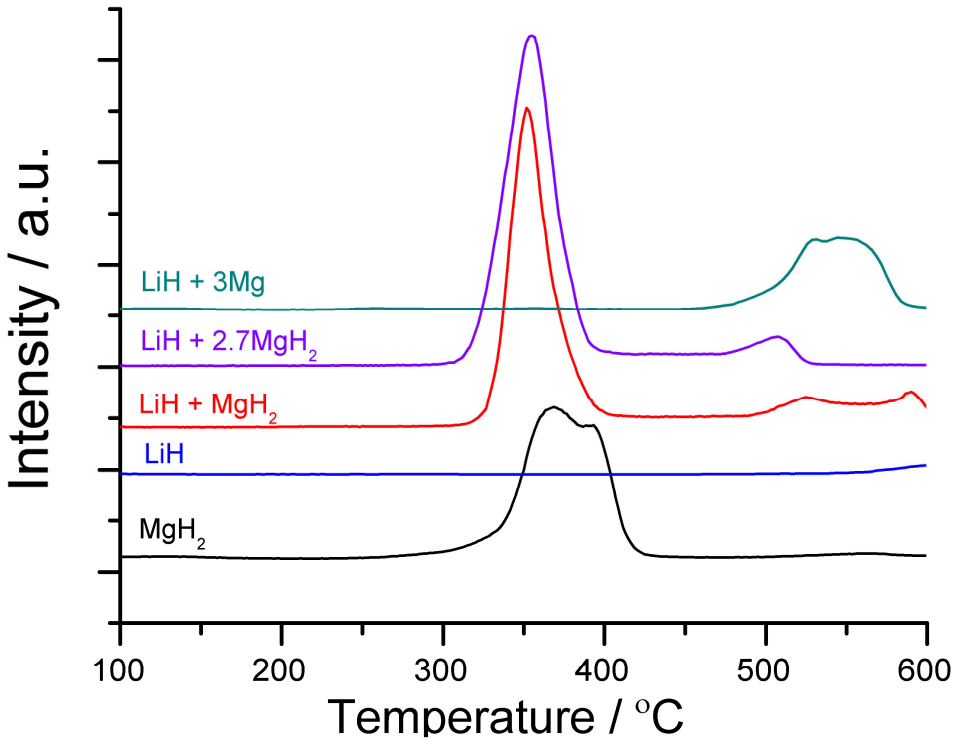

Figure 5.11. Mass spectrometry results for H_2 evolution from MgH_2 : LiH systems adapted from work by Yu *et al.* (Yu *et al.*, 2006a).

5.9.1. Ternary phase system

Section 4.5.3 presents investigation into ternary phase systems of $LiBH_4$: MgH_2 : $LiAlH_4$. Experiments were undertaken into 0.3:1 and 2:1 systems including 5 mol.% $LiAlH_4$ (4.75 mol.% for the 0.3:1 system to stay within the dual phase region, figure 5.10), the compositions were such that systems retain the same Li:Mg ratio of their $LiBH_4$: MgH_2 equivalents. These systems can therefore be compared to those presented in section 4.3.1 into $LiBH_4$: MgH_2.

Milled materials (figure 4.45) characterised through XRD, show similar materials to 0.3:1 and 2:1 systems, with some Al detected. This suggests partial decomposition of $LiAlH_4$ during milling, this has been observed during milling in the literature (Ares *et al.,* 2008) however, no formation of Li_3AlH_6 is observed, probably due to it only being in a small proportion in the sample.

Figure 4.46 shows decomposition behaviour characterised through DSC and compared to $LiBH_4$: MgH_2 equivalents for both ratios under both H_2 and Ar. All samples showed $LiBH_4$ phase change and melting, the latter of which was shifted to lower temperatures in every case. This is likely to be due to the improved thermal conductivity of samples containing Al (*ca.* 218 W m^{-1} K^{-1} at 100 °C (Butts *et al.,* 2004b)). Most significantly MgH_2 decomposition temperature was reduced in all samples, suggesting Al presence caused a destabilisation effect similar to that shown for the binary system. For systems decomposed under Ar the reaction may proceed to form LiAlMg alloys, as confirmed by *ex-situ* XRD in figure 4.47 and more clearly in figure 5.12.

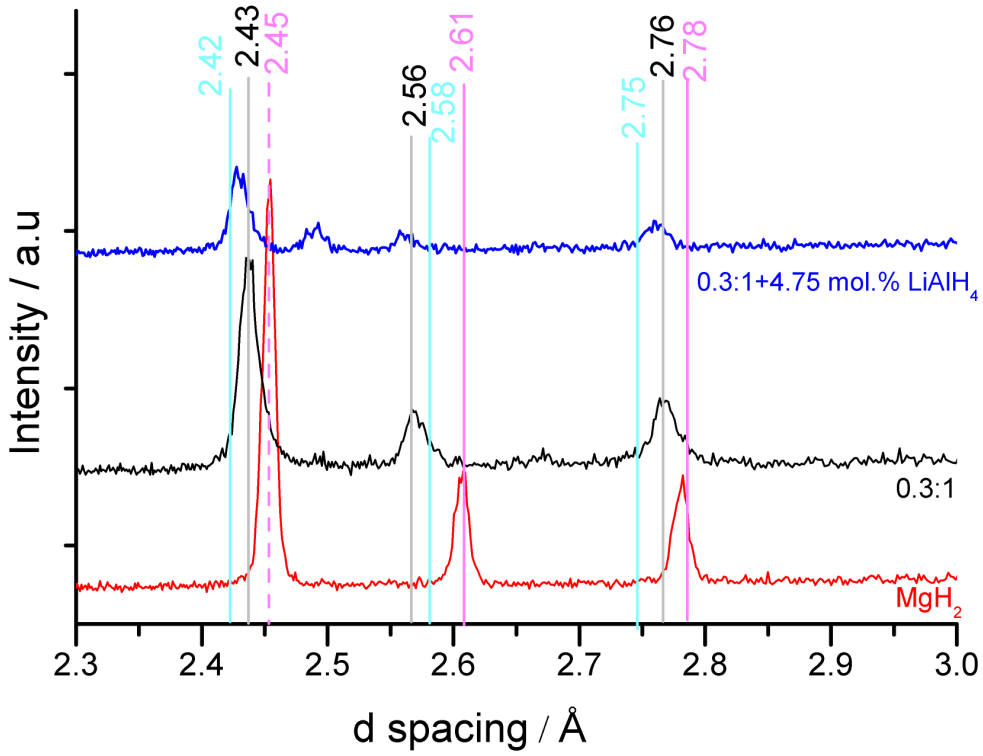

Figure 5.12. XRD data for DSC decomposition products for $LiAlH_4$ additions, compared to the $0.3LiBH_4$: MgH_2 and MgH_2 samples, reference d-spacing for Mg (pink), α-alloy (black) and $Al_{0.2}Mg_{1.8}$ (blue) are displayed.

Figure 5.12 shows 0.3:1+4.75 mol.% $LiAlH_4$ decomposition products alongside the decomposition products of 0.3:1 (*viz.* α-alloy) and MgH_2 (*viz.* Mg). The ternary phase system shows shifted to lower d-spacing than α-alloy, toward those of $Al_{0.2}Mg_{1.8}$ (Frebel *et al.*, 1976). This suggests a ternary LiAlMg alloy forms (002), as predicted from the ternary phase diagram figure 5.10.

In contrast to samples without $LiAlH_4$, alloying was also observed for decomposition under H_2. *Ex-situ* XRD of the decomposition products shows a Mg-type alloy, however the d-spacing does not allow conclusions to be made about the specific composition. This formation would explain the thermal events displayed in DSC for both ratios under H_2, which could be due to a simultaneous MgH_2 decomposition (endothermic) and Mg-Al alloying (exothermic). The temperature for this potential alloying was below the theoretical T(4 bar) for MgH_2 (*ca.* 330 °C at 4 bar H_2) therefore representing a destabilisation reaction. The main MgH_2 decomposition occurred at >345 °C (and below those shown for standard 0.3:1 and 2:1 samples), which suggests this reaction was not due to destabilisation but catalysed by Al presence. It is unlikely that the alloy contained any Li, as the LiH would be very stable under experimental pressures, requiring temperatures above 1000 °C for decomposition (a reduction enthalpy of 80 kJ mol^{-1} H_2 would be required to give a 4 bar H_2 plateau at 450 °C).

The only system to show a significant reduction in $LiBH_4$ decomposition temperature was the 2:1 + 5 mol.% $LiAlH_4$ decomposed under H_2, with decomposition beginning approximately 80 °C lower than for standard the 2:1 sample. Unfortunately decomposition products do not show any evidence for Li or Al containing species, it is therefore not clear whether an alternative destabilisation reaction occurred for this sample. Further investigation would be required to elucidate the reaction pathway for this system.

5.9.2. Al rich ternary phase system

In order to more clearly understand the role of Al in the system, an Al-rich compositions placing the Al, Li, Mg ratio at 50 : 27.5 : 22.5 was prepared (see figure 5.10). XRD for the as milled Al-rich sample (figure 4.48) shows Al and Li_3AlH_6 phases which would suggest the $LiAlH_4$ component partially decomposed through equation 2.10.

Decomposition of these systems are compared in figure 4.49, the Mg-rich sample is almost identical to the 0.3:1 + 4.75 mol.% $LiAlH_4$ sample presented in figure 4.46. The Al-rich sample showed MgH_2 decomposition 23 °C lower than the Mg-rich sample, suggesting the larger Al content may destabilise the MgH_2 more effectively than for smaller additions. At higher temperatures the Al-rich sample showed a sharp peak at 428 °C which is likely due to an alloy melting reaction before $LiBH_4$ decomposition at *ca.* 490 °C. The LiAl alloy shown in sample decomposition products (figure 4.50) is unlikely to be the cause of the event in DSC, as its melting point is much higher, *ca.* 695 °C, however it may be due to a preliminary alloy to LiAl. The phase diagram shown in figure 2.10 suggests melting of a Mg-rich Mg-Al alloy could occur at 437 °C (the Li content would cause reduction of melting point), at higher temperatures β-alloy formation and extra LiH from $LiBH_4$ decomposition would deplete the Mg content of the alloy with excess Li and Al forming LiAl. However without *in-situ* analysis this reaction pathway can only be postulated. Similar eutectics were shown by Leon *et al.* who showed a sharp endothermic event at 460 °C for MgH_2 : $LiAlH_4$ sample, the differing stoichiometry is likely to have yielded a different alloy (and hence melting point) for this system (Léon *et al.*, 2009).

5.9.3. Cycling of ternary phase systems

The stability of Mg_2Al_3 phases shown by Zhang *et al.* was a postulated cause of poor cycling of MgH_2 in systems containing Al and Mg (Zhang *et al.,* 2008). Cycling experiments were therefore performed on the Mg-rich $3LiBH_4 : 15MgH_2 : LiAlH_4$ sample through four dehydrogenation/hydrogenation cycles, shown in figure 4.51. The $LiBH_4$ melting endotherm can be clearly seen on each decomposition cycle, indicating cycling of this phase. The third cycle did not show $LiBH_4$, due to an incomplete hydriding stage however after full hydrogenation the following cycle showed the $LiBH_4$ component had reformed. It is possible that the low Al content allows a Mg type alloy to form which does not exhibit the same stability as Mg_2Al_3 phases suggested by other groups (Zaluska *et al.,* 2001; Zhang *et al.,* 2008) allowing the catalysis of the $LiBH_4 : MgH_2$ cycling. These results suggest the system cycles well, however PCI experiments are needed to fully understand the system capacity and behaviour.

6. Conclusions

The principle objective of this thesis was the elucidation of reaction pathways for the multi-component hydride system $LiBH_4$: MgH_2, investigating the effects of stoichiometry and reaction environment.

The overall reaction was shown to be not independent of stoichiometry, but the partial pressure of H_2 was found to have a significant effect. *In-situ* NPD showed decomposition under D_2 of both 2:1 and 0.3:1 ratios forming MgB_2 and LiD, with excess Mg for non-stoichiometric 0.3:1. In contrast, decomposition of both samples under vacuum showed formation of Mg-alloys, with some LiD retained in the 2:1 sample. These findings represent the first investigation to show the role of reaction environment on these destabilised systems. Further exploration of stoichiometry showed Mg-alloy formation under vacuum was dependent on Li:Mg ratio within the system, with 0.23:1, 0.3:1 and 0.44:1 forming α-alloy, α/β-alloy and β-alloy decomposition products, respectively.

Even low partial pressures of hydrogen can alter the reaction pathway, as found during the cooling of reaction products under a dynamic vacuum generated by different pumps. Cooling samples using pumps with a poor H_2 pumping efficiency, i.e. leaving the sample under a higher H_2 partial pressure, showed instability of the alloys with the Li reacting out of the alloy forming to LiH and Mg. This explains why many groups did not find formation of the α- or β-alloys in their decomposition products, evidently the pump being used was insufficient to produce a low enough partial pressure of H_2 to prevent Li from hydriding during cooling.

The formation of alloys at temperatures of 400 °C during decomposition under dynamic vacuum represents a destabilisation reaction of LiH as the thermodynamics would suggest that at pumping pressures of H_2 (*ca.* $>10^{-3}$ bar H_2) the LiH should not decompose until temperatures above 600 °C. PCI isotherms of the 0.3:1 system showed that the decomposition stage of these isotherms went through two plateaus, the upper plateau was similar to that expected for MgH_2. The lower plateau was at a higher pressure than expected for $LiBH_4$ yielding a calculated T(1bar) for the lower plateau of 322 °C (*cf.* 459 °C for $LiBH_{4(l)}$) therefore showing the $LiBH_4$ component had been thermodynamically destabilised. However the degree of destabilisation was lower than expected for MgB_2 formation, which raises the possibility of an intermediate destabilisation reaction with subsequent facile reaction of these products to form more stable MgB_2.

Stoichiometry was shown to play a significant role in the kinetics of the systems. For decomposition through DSC experiments, all investigated Mg-rich ratios showed a reduction in decomposition temperature in comparison with that for the 2:1 ratio of up to 50 °C. These results were supported by *in-situ* experiments, but in addition showed for 0.3:1 samples that loss of the $LiBH_{4(l)}$ component resulted in a concomitant formation of reaction products at low temperature, whilst for 2:1 samples the reaction progressed through an amorphous intermediate phase, with decomposition products forming at the end of, rather than during the loss of the amorphous $LiBH_4$ component. This resulted in a reduction in the decomposition product formation in 0.3:1 samples of 80 °C under vacuum, and 40 °C under D_2.

The Mg-rich system, 0.3:1, was shown to have significantly faster hydrogenation kinetics than the 2:1 system. The 0.3:1 samples decomposed under both reaction environments showed, on application of 100 bar D_2 at 400 °C, very fast kinetics, reaching 90 % conversion within 20 minutes. In contrast 2:1 samples showed kinetics an order of magnitude slower; with vacuum decomposition products only achieving 10 % $LiBD_4$ and 30 % MgD_2 conversion over 4h, whilst deuteriding from D_2 decomposition products yielded only 50 % $LiBD_4$ and 43 % MgD_2 over 4h.

Investigation of catalytic additions showed improved decomposition kinetics over uncatalysed samples. One of the greatest effects on catalyst activity is likely to be the dispersion of the catalyst, the greatest catalytic effects were achieved either by pre-milling hydride additions with MgH_2 or through metal halide catalyst precursors, where reaction with $LiBH_4$ forms LiCl, or LiF and highly dispersed metal catalyst. NbH pre-milled samples offered the best catalytic addition of those investigated, an advantage of using the hydride rather than a metal salt precursor is that there is less reduction in hydrogen capacity for the milled materials through formation of a stable Li-halide species.

Through addition of $LiAlH_4$ to $LiBH_4$: MgH_2 a ternary phase hydride system was developed. Evidence for a ternary Mg-type alloy of Mg-Li-Al suggests the observed lower decomposition temperature of MgH_2 component was due to both a catalytic and destabilisation effect. Destabilisation of the MgH_2 was also shown under H_2, with MgAl alloy formation. Cycling showed the $LiBH_4$: MgH_2 components could be taken through 4 cycles, hydrogenating under 50 bar H_2 at 400 °C.

These results present the first broad investigation of the $LiBH_4$: MgH_2 system, investigating phase progression, stoichiometry, reaction environment, cycling, catalysis and further destabilising additions. The results have shown improvement in cycling, kinetics and operating temperature, offering potential for the system as a mobile hydrogen storage material.

7. Future work

Investigation of the $2LiBH_4$: MgH_2 system provided evidence of reaction pathways through intermediate phases. Investigation through *in*-situ NPD was limited by the amorphous nature of these phases. Future investigations could be made through spectroscopic analysis, allowing the chemical bonding, rather than the structural form of the material to be probed.

Ex-situ neutron scattering techniques such as quasi-elastic, inelastic and deep inelastic neutron scattering could be combined to investigate samples of $2LiBH_4$: MgH_2 quenched during $LiBH_4$ decomposition. This should reveal how the intermolecular interactions in the intermediate phases affect the vibrational spectra and allow a direct comparison between the observed mean proton kinetic energies and available experimental values for known intermediates of $LiBH_4$. Optical techniques such as Raman spectroscopy are complementary to the neutron work and could be used to cover intermediate neutron energy transfer regions. Finally magic angle spinning nuclear magnetic resonance (MAS-NMR) spectroscopy could be employed to follow B species within $LiBH_4$ during decomposition. Further understanding of H mobility within this phase could be probed through use of tri-deuterided borohydride $LiBD_3H$ investigated through this technique.

Valuable knowledge of thermodynamics of the investigated systems could be made through further PCI experiments into 2:1 and 0.3:1 systems. Interesting comparison could be made by decomposing systems under either dynamic vacuum or H_2 prior to the hydrogenation isotherm, which may show varying thermodynamics for hydrogenation from different end products. Most interesting would be investigation into these samples through *in-situ* NPD

experiments during isotherms, in order to characterise the phase progressions for each plateau.

It would also be interesting to investigate cycling of catalysed samples through kinetic isothermal decomposition experiments at low temperature, observing the dehydrogenation and hydrogenation kinetics for the highlighted catalysed systems. Investigation could also be made into other catalysts with the objective of high dispersion, either through decomposition of a precursor addition or through nano-scale particles of metal deposited on carbon structures. Investigation into infiltration (chemical or melt) of carbon structures proposed by various groups (Fang *et al.,* 2008a; Gross *et al.,* 2008), could be combined with dispersed catalysts to allow both encapsulation and catalysis of the system, whilst minimising segregation and sintering.

The investigated ternary phase system incorporating $LiAlH_4$ could be further probed through *in-situ* NPD, to follow formation of Mg-Al-Li alloys, and characterise their influence on reaction pathway. Additions of MgB_2 could also be made to the system, which should allow the LiH evolved from $LiAlH_4$ to form $LiBH_4$ on cycling, thus reducing the capacity loss through addition of this phase. Further investigation into metal additions to multi-component destabilised systems could be made to promote alloy formation. The improved kinetics of β-alloy in the liquid state suggests the potential for low melting point Mg-alloys. Possible additions include Zn, which shows melting of 342 °C for a 48 at.% Mg eutectic composition (Butts *et al.,* 2004a) or Ga, for which 20 at.% additions reduce melting point from 650 °C to 425 °C (Predel 1996), through addition of these metals, the system may operate in the liquid state.

8. References

Aceves, S. M., G. D. Berry, J. Martinez-Frias and F. Espinosa-Loza (2006a). "Vehicular storage of hydrogen in insulated pressure vessels." International Journal of Hydrogen Energy **31**(15): 2274-2283.

Aceves, S. M., G. D. Berry, A. H. Weisberg, F. Espinosa-Loza and S. A. Perfect (2006b). Advanced Concepts for Vehicular Containment of Compressed and Cryogenic Hydrogen. WHEC, Lyon, France.

Agnew, S. R., M. H. Yoo and C. N. Tome (2001). "Application of texture simulation to understanding mechanical behavior of Mg and solid solution alloys containing Li or Y." Acta Materialia **49**(20): 4277-4289.

Aiello, R., M. A. Matthews, D. L. Reger and J. E. Collins (1998). "Production of hydrogen gas from novel chemical hydrides." International Journal of Hydrogen Energy **23**(12): 1103-1108.

Amendola, S. C., S. L. Sharp-Goldman, M. S. Janjua, M. T. Kelly, P. J. Petillo and M. Binder (2000). "An ultrasafe hydrogen generator: aqueous, alkaline borohydride solutions and Ru catalyst." Journal of Power Sources **85**(2): 186-189.

Andreasen, A. (2004). Predicting formation enthalpies of metal hydrides. Risø National Laboratory Report. **6:** 33.

Ares, J. R., K. F. Aguey-Zinsou, T. Klassen and R. Bormann (2007). "Influence of impurities on the milling process of MgH_2." Journal of Alloys and Compounds **434-435**: 729-733.

Ares, J. R., K. F. Aguey-Zinsou, M. Porcu, J. M. Sykes, M. Dornheim, T. Klassen and R. Bormann (2008). "Thermal and mechanically activated decomposition of $LiAlH_4$." Materials Research Bulletin **43**(5): 1263-1275.

Attard, G. and C. Barnes (1998). Surfaces, Oxford University Press Oxford.

Au, M. and A. Jurgensen (2006). "Modified Lithium Borohydrides for Reversible Hydrogen Storage." Journal of Physical Chemistry B **110**(13): 7062-7067.

Au, M., A. R. Jurgensen, W. A. Spencer, D. L. Anton, F. E. Pinkerton, S. J. Hwang, C. Kim and R. C. Bowman Jr (2008). "Stability and Reversibility of Lithium Borohydrides Doped by Metal Halides and Hydrides." Journal of Physical Chemistry C **112**(47): 18661-18671.

Barkhordarian, G., T. Klassen and R. Bormann (2003). "Fast hydrogen sorption kinetics of nanocrystalline Mg using Nb2O5 as catalyst." Scripta Materialia **49**(3): 213-217.

Barkhordarian, G., T. Klassen, M. Dornheim and R. Bormann (2007). "Unexpected kinetic effect of MgB_2 in reactive hydride composites containing complex borohydrides." Journal of Alloys and Compounds **440**(1-2): 18-21.

Benard, P. and R. Chahine (2008). Carbon nanostructures for hydrogen storage. Solid state hydrogen storage : materials and chemistry. G. Walker, Woodhead Publishing**:** 261-284.

Blanchard, D., H. W. Brinks, B. C. Hauback and P. Norby (2004). "Desorption of $LiAlH_4$ with Ti- and V-based additives." Materials Science and Engineering B **108**(1-2): 54-59.

Block, J. and A. P. Gray (1965). "The Thermal Decomposition of Lithium Aluminum Hydride." Inorganic Chemistry **4**(3): 304-305.

Bogdanovic, B. and M. Schwickardi (1997). "Ti-doped alkali metal aluminium hydrides as potential novel reversible hydrogen storage materials." Journal of Alloys and Compounds **253-254**: 1-9.

Borgschulte, A., M. Bielmann, A. Züttel, G. Barkhordarian, M. Dornheim and R. Bormann (2008). "Hydrogen dissociation on oxide covered MgH_2 by catalytically active vacancies." Applied Surface Science **254**(8): 2377-2384.

Bosenberg, U., S. Doppiu, L. Mosegaard, G. Barkhordarian, N. Eigen, A. Borgschulte, T. R. Jensen, Y. Cerenius, O. Gutfleisch, T. Klassen, M. Dornheim and R. Bormann (2007). "Hydrogen sorption properties of MgH_2-$LiBH_4$ composites." Acta Materialia **55**(11): 3951-3958.

Bowman, R. C., S. Hwang, C. C. Ahn and J. J. Vajo (2005). NMR and X-ray Diffraction Studies of Phases in the Destabilized LiH-Si System. Mater. Res. Soc. Symp. Proc., Warrendale, Pa.; Materials Research Society; 1999.

Busk, R. S. (1952). Effect of temperature on the lattice parameters of magnesium alloys. **4:** 207-209.

Butts, D. A., W. F. Gale and T. C. Totemeier (2004a). Equilibrium diagrams. Smithells Metals Reference Book (Eighth Edition). Oxford, Butterworth-Heinemann**:** 1-534.

Butts, D. A., W. F. Gale and T. C. Totemeier (2004b). The physical properties of aluminium and aluminium alloys. Smithells Metals Reference Book (Eighth Edition). Oxford, Butterworth-Heinemann**:** 14-14.

Chaise, A., P. de Rango, P. Marty, D. Fruchart, S. Miraglia, R. Olivès and S. Garrier (2009). "Enhancement of hydrogen sorption in magnesium hydride using expanded natural graphite." International Journal of Hydrogen Energy **34**(20): 8589-8596.

Chandra, D. (2008). Intermetallics for hydrogen storage. Solid state hydrogen storage : materials and chemistry. G. Walker, Woodhead Publishing**:** 315-348.

Chase, M. W. (1998). NIST-JANAF Thermochemical Tables. New York, American Institute of Physics.

Chen, J., N. Kuriyama, Q. Xu, H. T. Takeshita and T. Sakai (2001). "Reversible Hydrogen Storage via Titanium-Catalyzed $LiAlH_4$ and Li_3AlH_6." Journal of Physical Chemistry B **105**(45): 11214-11220.

Cho, Y. W., J.-H. Shim and B.-J. Lee (2006). "Thermal destabilization of binary and complex metal hydrides by chemical reaction: A thermodynamic analysis." Calphad **30**(1): 65-69.

Communication, P. (2009). IEA Task 22, Korea.

Corbo, P., F. Migliardini and O. Veneri (2009). "Hydrogen release properties of lithium alanate for application to fuel cell propulsion systems." Journal of Power Sources **In Press, Corrected Proof**.

Danaie, M. and D. Mitlin (2009). "TEM analysis and sorption properties of high-energy milled MgH_2 powders." Journal of Alloys and Compounds **476**(1-2): 590-598.

Dilich, S. (2009). Hydrogen Program and Vehicle Technologies Program Annual Merit Review and Peer Evaluation Meeting. Annual Merit Review and Peer Evaluation Meeting, Arlington, Virginia, USA.

Fan, M.-Q., L.-X. Sun, Y. Zhang, F. Xu, J. Zhang and H.-l. Chu (2008). "The catalytic effect of additive Nb_2O_5 on the reversible hydrogen storage performances of $LiBH_4$-MgH_2 composite." International Journal of Hydrogen Energy **33**(1): 74-80.

Fang, Z.-Z., X.-D. Kang, P. Wang, H.-W. Li and S.-I. Orimo (2009). "Unexpected dehydrogenation behavior of $LiBH_4/Mg(BH_4)_2$ mixture associated with the in situ formation of dual-cation borohydride." Journal of Alloys and Compounds **In Press, Accepted Manuscript**.

Fang, Z. Z., X. D. Kang, H. B. Dai, M. J. Zhang, P. Wang and H. M. Cheng (2008a). "Reversible dehydrogenation of $LiBH_4$ catalyzed by as-prepared single-walled carbon nanotubes." Scripta Materialia **58**(10): 922-925

Fang, Z. Z., P. Wang, T. E. Rufford, X. D. Kang, G. Q. Lu and H. M. Cheng (2008b). "Kinetic- and thermodynamic-based improvements of lithium borohydride incorporated into activated carbon." Acta Materialia **56**(20): 6257-6263

Farmer, R. (2009). Hydrogen Production. Annual Merit Review and Peer Evaluation Meeting, Arlington, Virginia, USA.

Filinchuk, Y., D. Chernyshov, A. Nevidomskyy and V. Dmitriev (2008). "High-Pressure Polymorphism as a Step towards Destabilization of LiBH4 The authors are grateful to SNBL for the provision of in-house beam time and to P. Pattison for critical reading of the manuscript." Angewandte Chemie, International Edition **47**(3).

Fleisch, T. and R. Abermann (1977). "On the reduction of Ag2S films by hydrogen spillover under ultra high vacuum conditions." Journal of Catalysis **50**(2): 268-278.

Fluck, E. (1996). "Inorganic Crystal Structure Database (ICSD) and Standardized Data and Crystal Chemical Characterization of Inorganic Structure Types (TYPIX)-Two Tools for Inorganic Chemists and Crystallographers." Journal of Research of the National Institute of Standards and Technology **101**: 217-220.

Frebel, M., K. Behler and B. Predel (1976). "Beitrag zur kenntnis des ausscheidungsverhaltens einiger magnesium-mischkristalle." Materials Science and Engineering **22**: 201-212.

Friedrichs, O., F. Buchter, A. Borgschulte, A. Remhof, C. N. Zwicky, P. Mauron, M. Bielmann and A. Zuttel (2008). "Direct synthesis of $LiBH_4$ and $LiBD_4$ from the elements." Acta Materialia **56**(5): 949-954

Friedrichs, O., J. W. Kim, A. Remhof, F. Buchter, A. Borgschulte, D. Wallacher, Y. W. Cho, M. Fichtner, K. H. Oh and A. Züttel (2009). "The effect of Al on the hydrogen sorption mechanism of $LiBH_4$." Physical Chemistry Chemical Physics **11**(10): 1515-1520.

Gennari, F. C., F. J. Castro and G. Urretavizcaya (2001). "Hydrogen desorption behavior from magnesium hydrides synthesized by

reactive mechanical alloying." Journal of Alloys and Compounds **321**(1): 46-53.

Glage, A., R. Ceccato, I. Lonardelli, F. Girardi, F. Agresti, G. Principi, A. Molinari and S. Gialanella (2009). "A powder metallurgy approach for the production of a MgH2-Al composite material." Journal of Alloys and Compounds **478**(1-2): 273-280.

Gomes, S., H. Hagemann and K. Yvon (2002). "Lithium boro-hydride LiBH4: II. Raman spectroscopy." Journal of Alloys and Compounds **346**(1-2): 206-210.

Grant, D. M. (2008). Magnesium hydride for hydrogen storage. Solid state hydrogen storage : materials and chemistry. G. Walker, Woodhead Publishing**:** 357-376.

Grobner, J., R. Schmid-Fetzer, A. Pisch, C. Colinet, V. V. Pavlyuk, G. S. Dmytriv, D. G. Kevorkov and O. I. Bodak (2002). "Phase equilibria, calorimetric study and thermodynamic modeling of Mg-Li-Ca alloys." Thermochimica Acta **389**(1-2): 85-94.

Gross, A. F., J. J. Vajo, S. L. Van Atta and G. L. Olson (2008). "Enhanced Hydrogen Storage Kinetics of $LiBH_4$ in Nanoporous Carbon Scaffolds." Journal of Physical Chemistry C **112**(14): 5651-5657.

Güther, V. and A. Otto (1999). "Recent developments in hydrogen storage applications based on metal hydrides." Journal of Alloys and Compounds **293-295**: 889-892.

Hansen, T. C., P. F. Henry, H. E. Fischer, J. Torregrossa and P. Convert (2008). "The D20 instrument at the ILL: a versatile high-intensity two-axis neutron diffractometer." Measurement Science and Technology(3): 034001.

Harris, P. M. and E. P. Meibohm (1947). "The crystal structure of lithium borohydride $LiBH_4$." Journal of the American Chemical Society **69**(5): 1231-1232.

Harvey, J.-P. and P. Chartrand (2007). Thermodynamic Modeling of the Mg-Li-Al-Si System. Montréal, École Polytechnique de Montréal.

Herbstein, F. H. and B. L. Averbach (1956). "The structure of lithium-magnesium solid solutions--I : Measurements on the Bragg reflections." Acta Metallurgica **4**(4): 407-413.

Holzkamp, U., H. Haferkamp and M. Niemeyer (2000). Magnesium Alloys and their Applications. Weinheim, DGM.

Huot, J., G. Liang, S. Boily, A. Van Neste and R. Schulz (1999). "Structural study and hydrogen sorption kinetics of ball-milled magnesium hydride." Journal of Alloys and Compounds **293-295**: 495-500.

Huot, J., G. Liang and R. Schulz (2001). "Mechanically alloyed metal hydride systems." Applied Physics A: Materials Science & Processing **72**(2): 187-195.

Huot, J., J. F. Pelletier, L. B. Lurio, M. Sutton and R. Schulz (2003). "Investigation of dehydrogenation mechanism of MgH2-Nb nanocomposites." Journal of Alloys and Compounds **348**(1-2): 319-324.

Ibikunle, A., A. J. Goudy and H. Yang (2009). "Hydrogen storage in a $CaH_2/LiBH_4$ destabilized metal hydride system " Journal of Alloys and Compounds **475**(1-2): 110-115.

IEA/DOE/SNL Hypark: Hydride databases available at Hydride Information
Center, Sandia National Laboratories.
In, S. R. (2009). "Hydrogen pumping characteristics of dry pumps." Vacuum **In Press, Corrected Proof**.
InfoMine (2009). www.infomine.com.
J. T. Houghton, Y. D., D. J. Griggs (2001). IPCC Third Assessment Report: Climate Change 2001 (Cambridge University Press, Cambridge)**:** 944.
Jcpds-Icdd, I. (1996). Reference Pattern Database. **46**.
Johnson, S. R., P. A. Anderson, P. P. Edwards, I. Gameson, J. W. Prendergast, M. Al-Mamouri, D. Book, I. R. Harris, J. D. Speight and A. Walton (2005). "Chemical activation of MgH_2; a new route to superior hydrogen storage materials." Chemical Communications(22): 2823-2825.
Kang, J. K., S. Y. Kim, Y. S. Han, R. P. Muller, W. A. Goddard and III (2005). "A candidate $LiBH_4$ for hydrogen storage: Crystal structures and reaction mechanisms of intermediate phases." Applied Physics Letters **87**(11): 111904-3.
Kang, X.-D., P. Wang and H.-M. Cheng (2007a). "Advantage of TiF_3 over $TiCl_3$ as a dopant precursor to improve the thermodynamic property of Na3AlH6." Scripta Materialia **56**(5): 361-364.
Kang, X.-D., P. Wang, L.-P. Ma and H.-M. Cheng (2007b). "Reversible hydrogen storage in $LiBH_4$ destabilized by milling with Al." Applied Physics A: Materials Science & Processing **89**(4): 963-966.
Kang, Y.-B., C. Aliravci, P. Spencer, G. Eriksson, C. Fuerst, P. Chartrand and A. Pelton (2009). "Thermodynamic and volumetric databases and software for magnesium alloys." Journal of the Minerals, Metals and Materials Society **61**(5): 75-82.
Kapischke, J. and J. Hapke (1998). "Measurement of the effective thermal conductivity of a Mg-MgH_2 packed bed with oscillating heating." Experimental Thermal and Fluid Science **17**(4): 347-355.
Kellington, S. H., D. Loveridge and J. M. Titman (1969). "The lattice parameters of some alloys of lithium." Journal of Physics D: Applied Physics **2**(8): 1162-1163.
Kevorkov, D., J. Gröbner, R. Schmid-Fetzer, V. Pavlyuk, G. Dmytriv and O. Bodak (2001). "The ternary Gd-Li-Mg system: Phase diagram study and computational evaluation." Journal of Phase Equilibria and Diffusion **22**(1): 34-42.
Kim, J. W., O. Friedrichs, J.-P. Ahn, D. H. Kim, S. C. Kim, A. Remhof, H.-S. Chung, J. Lee, J.-H. Shim, Y. W. Cho, A. Züttel and K. H. Oh (2009). "Microstructural Change of $2LiBH_4$/Al with Hydrogen Sorption Cycling: Separation of Al and B." Scripta Materialia **60**(12): 1089-1092.
Krozer, A. and B. Kasemo (1989). "Equilibrium hydrogen uptake and associated kinetics for the Mg-H2 system at low pressures." Journal of Physics: Condensed Matter(8): 1533.
Lee, B.-M., J.-W. Jang, J.-H. Shim, Y. W. Cho and B.-J. Lee (2006). "Thermodynamic assessment of the NaH Na_3AlH_6 $NaAlH_4$ hydride system." Journal of Alloys and Compounds **424**(1-2): 370-375.

Léon, A., O. Zabara, S. Sartori, N. Eigen, M. Dornheim, T. Klassen, J. Muller, B. Hauback and M. Fichtner (2009). "Investigation of (Mg, Al, Li, H)-based hydride and alanate mixtures produced by reactive ball milling." Journal of Alloys and Compounds **476**(1-2): 425-428.

Liang, G., J. Huot, S. Boily, A. Van Neste and R. Schulz (1999a). "Catalytic effect of transition metals on hydrogen sorption in nanocrystalline ball milled MgH_2-Tm (Tm=Ti, V, Mn, Fe and Ni) systems." Journal of Alloys and Compounds **292**(1-2): 247-252.

Liang, G., J. Huot, S. Boily, A. Van Neste and R. Schulz (1999b). "Hydrogen storage properties of the mechanically milled MgH_2-V nanocomposite." Journal of Alloys and Compounds **291**(1-2): 295-299.

Liang, G. and R. Schulz (2004). "The reaction of hydrogen with Mg-Cd alloys prepared by mechanical alloying." Journal of Materials Science **39**(5): 1557-1562.

Lide, D. (2007). CRC Handbook of Chemistry and Physics, 88th Edition (CRC Handbook of Chemistry and Physics), CRC.

Lim, J.-H., J.-H. Shim, Y.-S. Lee, Y. W. Cho and J. Lee (2008). "Dehydrogenation behavior of $LiBH_4/CaH_2$ composite with NbF_5." Scripta Materialia **59**(12): 1251-1254.

Lin, X., J. Jia, N. R. Champness, P. Hubberstey and M. Schröder (2008). Metal-organic framework materials for hydrogen storage. Solid state hydrogen storage : materials and chemistry. G. Walker, Woodhead Publishing**:** 288-308.

Liu, X., G. S. McGrady, H. W. Langmi and C. M. Jensen (2009). "Facile Cycling of Ti-Doped $LiAlH_4$ for High Performance Hydrogen Storage." Journal of the American Chemical Society **131**(14): 5032-5033.

Lodziana, Z. and T. Vegge (2004). "Structural Stability of Complex Hydrides: $LiBH_4$ Revisited." Physical Review Letters **93**(14): 145501-4.

Lopez, N., T. V. W. Janssens, B. S. Clausen, Y. Xu, M. Mavrikakis, T. Bligaard and J. K. Nørskov (2004). "On the origin of the catalytic activity of gold nanoparticles for low-temperature CO oxidation." Journal of Catalysis **223**(1): 232-235.

Ma, L.-P., P. Wang and H.-M. Cheng (2007). "Improving hydrogen sorption kinetics of MgH2 by mechanical milling with TiF3." Journal of Alloys and Compounds **432**(1-2): L1-L4.

Mao, J. F., Z. Wu, T. J. Chen, B. C. Weng, N. X. Xu, T. S. Huang, Z. P. Guo, H. K. Liu, D. M. Grant, G. S. Walker and X. B. Yu (2007). "Improved Hydrogen Storage of $LiBH_4$ Catalyzed Magnesium." Journal of Physical Chemistry C **111**(33): 12495-12498.

Meisner, G. P., M. L. Scullin, M. P. Balogh, F. E. Pinkerton and M. S. Meyer (2006). "Hydrogen Release from Mixtures of Lithium Borohydride and Lithium Amide: A Phase Diagram Study." Journal of Physical Chemistry B **110**(9): 4186-4192.

Miwa, K., N. Ohba, S.-i. Towata, Y. Nakamori and S.-i. Orimo (2004). "First-principles study on lithium borohydride $LiBH_4$." Physical

Review B: Condensed Matter and Materials Physics **69**(24): 245120-8.

Moriwaki, T., Y. Akahama, H. Kawamura, S. Nakano and K. Takemura (2006). "Structural Phase Transition of Rutile-Type MgH_2 at High Pressures." Journal of the Physical Society of Japan **75**(7): 074603-074603.

Mosegaard, L., B. Moller, J.-E. Jorgensen, U. Bosenberg, M. Dornheim, J. C. Hanson, Y. Cerenius, G. Walker, H. J. Jakobsen, F. Besenbacher and T. R. Jensen (2007). "Intermediate phases observed during decomposition of $LiBH_4$." Journal of Alloys and Compounds **446-447**: 301-305.

Mosegaard, L., B. Moller, J. E. Jorgensen, Y. Filinchuk, Y. Cerenius, J. C. Hanson, E. Dimasi, F. Besenbacher and T. R. Jensen (2008). "Reactivity of $LiBH_4$: In Situ Synchrotron Radiation Powder X-ray Diffraction Study." Journal of Physical Chemistry C **112**(4): 1299-1303.

Motoaki, M., T. Hitoshi, M. Hideki, L. Hai-Wen and O. Shin-ichi (2009). "Stabilization of lithium superionic conduction phase and enhancement of conductivity of $LiBH_4$ by LiCl addition." Applied Physics Letters **94**(8): 084103.

Muller, A., F. Mathey and J. Bensoam (1980). Production of hydrogen, Google Patents.

Nakagawa, T., T. Ichikawa, N. Hanada, Y. Kojima and H. Fujii (2007). "Thermal analysis on the Li-Mg-B-H systems." Journal of Alloys and Compounds **446-447**: 306-309.

Nations, U. (1997). Kyoto protocol to the United Nations framework convention on climate change.

Ohba, N., K. Miwa, M. Aoki, T. Noritake, S.-i. Towata, Y. Nakamori, S.-i. Orimo and A. Zuttel (2006). "First-principles study on the stability of intermediate compounds of $LiBH_4$." Physical Review B: Condensed Matter and Materials Physics **74**(7): 075110-7.

Ohlrogge, K., J. Wind and D. Hassel (2001). New technology for emission reduction at petrol stations, American Chemical Society; 1999. **46:** 145-149.

Orimo, S.-I., Y. Nakamori, N. Ohba, K. Miwa, M. Aoki, S.-i. Towata and A. Zuttel (2006). "Experimental studies on intermediate compound of $LiBH_4$." Applied Physics Letters **89**(2): 021920-3.

Orimo, S., Y. Nakamori, G. Kitahara, K. Miwa, N. Ohba, S. Towata and A. Zuttel (2005). "Dehydriding and rehydriding reactions of $LiBH_4$." Journal of Alloys and Compounds **404-406**: 427-430.

Panella, B., M. Hirscher and S. Roth (2005). "Hydrogen adsorption in different carbon nanostructures." Carbon **43**(10): 2209-2214.

Pinkerton, F. E. and M. S. Meyer (2008). "Reversible hydrogen storage in the lithium borohydride--calcium hydride coupled system." Journal of Alloys and Compounds **464**(1-2): L1-L4.

Pinkerton, F. E., M. S. Meyer, G. P. Meisner, M. P. Balogh and J. J. Vajo (2007). "Phase Boundaries and Reversibility of $LiBH_4/MgH_2$ Hydrogen Storage Material." Journal of Physical Chemistry C **111**(35): 12881-12885.

Pistorius, C. (1974). "Melting and polymorphism of $LiBH_4$ to 45 kbar." Phys. Chem. Neue Folge. **88**: 253-263.

Predel, B. (1996). Ga-Mg (Gallium-Magnesium). Ga-Gd – Hf-Zr, Springer-Verlag**:** 1-5.

Protocol, K. (1990). United Nations Framework Convention on Climate Change. **11**.

Puszkiel, J. A. and F. C. Gennari (2009). "Reversible hydrogen storage in metal-doped Mg-$LiBH_4$ composites." Scripta Materialia **60**(8): 667-670.

Quadrelli, R. and S. Peterson (2007). "The energy-climate challenge: Recent trends in CO_2 emissions from fuel combustion." Energy Policy **35**(11): 5938-5952

Reilly, J. J. and R. H. Wiswall (1967). "Reaction of hydrogen with alloys of magnesium and copper." Inorganic Chemistry **6**(12): 2220-2223.

Reilly, J. J. and R. H. Wiswall (1968). "Reaction of hydrogen with alloys of magnesium and nickel and the formation of Mg_2NiH_4." Inorganic Chemistry **7**(11): 2254-2256.

Remhof, A., O. Friedrichs, F. Buchter, P. Mauron, J. W. Kim, K. H. Oh, A. Buchsteiner, D. Wallacher and A. Züttel (2009). "Hydrogen cycling behavior of $LiBD_4$/Al studied by in situ neutron diffraction." Journal of Alloys and Compounds **484**(1-2): 654-659

Sandrock, G. (1999). "A panoramic overview of hydrogen storage alloys from a gas reaction point of view." Journal of Alloys and Compounds **293-295**: 877-888.

Schimmel, H. G., J. Huot, L. C. Chapon, F. D. Tichelaar and F. M. Mulder (2005). "Hydrogen Cycling of Niobium and Vanadium Catalyzed Nanostructured Magnesium." Journal of the American Chemical Society **127**(41): 14348-14354.

Schlapbach, L. and A. Zuttel (2001). "Hydrogen-storage materials for mobile applications." Nature **414**(6861): 353-358.

Schlesinger, H. I. and H. C. Brown (1940). "Metallo Borohydrides. III. Lithium Borohydride." Journal of the American Chemical Society **62**(12): 3429-3435.

Schlesinger, H. I., H. C. Brown, H. R. Hoekstra and L. R. Rapp (1953). "Reactions of Diborane with Alkali Metal Hydrides and Their Addition Compounds. New Syntheses of Borohydrides. Sodium and Potassium Borohydrides." Journal of the American Chemical Society **75**(1): 199-204.

Schulz, R., J. Huot, G. Liang, S. Boily, G. Lalande, M. C. Denis and J. P. Dodelet (1999). "Recent developments in the applications of nanocrystalline materials to hydrogen technologies." Materials Science and Engineering A **267**(2): 240-245.

Schuth, F., B. Bogdanovic and M. Felderhoff (2004). "Light metal hydrides and complex hydrides for hydrogen storage." Chemical Communications(20): 2249-2258.

Sigma-Aldrich. (2009). "http://www.sigmaaldrich.com."

Sklar, N. and B. Post (1967). "Crystal structure of lithium aluminum hydride." Inorganic Chemistry **6**(4): 669-671.

Song, G. S. and M. V. Kral (2005). "Characterization of cast Mg-Li-Ca alloys." Materials Characterization **54**(4-5): 279-286.

Soulie, J.-P., G. Renaudin, R. Cerny and K. Yvon (2002). "Lithium boro-hydride $LiBH_4$: I. Crystal structure." Journal of Alloys and Compounds **346**(1-2): 200-205.

Stojic, D. L., M. P. Marceta, S. P. Sovilj and S. S. Miljanic (2003). "Hydrogen generation from water electrolysis--possibilities of energy saving." Journal of Power Sources **118**(1-2): 315-319.

Sundqvist, B. and O. Andersson (2009). "Thermal Conductivity and Phase Diagrams of Some Potential Hydrogen Storage Materials Under Pressure." International Journal of Thermophysics: 1-12.

Takacs, L. and J. McHenry (2006). "Temperature of the milling balls in shaker and planetary mills." Journal of Materials Science **41**(16): 5246-5249.

Talyzin, A. V., O. Andersson, B. Sundqvist, A. Kurnosov and L. Dubrovinsky (2007). "High-pressure phase transition in $LiBH_4$." Journal of Solid State Chemistry **180**(2): 510-517.

Tight, M. R., A. L. Bristow, A. Pridmore and A. D. May (2005). "What is a sustainable level of CO_2 emissions from transport activity in the UK in 2050?" Transport Policy **12**(3): 235-244.

Vajo, J. J., F. Mertens, C. C. Ahn, R. C. Bowman and B. Fultz (2004). "Altering Hydrogen Storage Properties by Hydride Destabilization through Alloy Formation; LiH and MgH_2 Destabilized with Si." Journal Of Physical Chemistry B **108**(37): 13977-13983.

Vajo, J. J. and G. L. Olson (2007a). "Hydrogen storage in destabilized chemical systems." Scripta Materialia **56**(10): 829-834.

Vajo, J. J., T. T. Salguero, A. F. Gross, S. L. Skeith and G. L. Olson (2007b). "Thermodynamic destabilization and reaction kinetics in light metal hydride systems." Journal of Alloys and Compounds **446-447**: 409-414.

Vajo, J. J., S. L. Skeith and F. Mertens (2005). "Reversible Storage of Hydrogen in Destabilized $LiBH_4$." Journal of Physical Chemistry B **109**(9): 3719-3722.

van Setten, M. J. and M. Fichtner (2009). "On the enthalpy of formation of aluminum diboride, AlB_2." Journal of Alloys and Compounds **477**(1-2): L11-L12.

Walker, G. S. (2008). Hydrogen Storage Technologies. Solid state hydrogen storage : materials and chemistry. G. Walker, Woodhead Publishing**:** 3-15.

Walker, G. S., D. M. Grant, T. E. C. Price, V. Legrand and X. Yu (2009). "High capacity multicomponent hydrogen storage materials investigation of the effect of stoichiometry and decomposition conditions on the cycling behaviour of $LiBH_4$ - MgH_2." Journal of Power Sources **189**(2): 902-908.

Wan, X., T. Markmaitree, W. Osborn and L. L. Shaw (2008). "Nanoengineering-Enabled Solid-State Hydrogen Uptake and Release in the $LiBH_4$ Plus MgH_2 System." Journal of Physical Chemistry C **112**(46): 18232-18243.

Wang, J., A. D. Ebner and J. A. Ritter (2006). "Physiochemical Pathway for Cyclic Dehydrogenation and Rehydrogenation of $LiAlH_4$." Journal of the American Chemical Society **128**(17): 5949-5954.

Wang, P., X.-D. Kang and H.-M. Cheng (2005a). "Exploration of the Nature of Active Ti Species in Metallic Ti-Doped $NaAlH_4$." Journal of Physical Chemistry B **109**(43): 20131-20136.

Wang, P., X. D. Kang and H. M. Cheng (2005b). "Improved Hydrogen Storage of TiF_3 Doped $NaAlH_4$." ChemPhysChem **6**(12): 2488-2491.

Wang, P., L. Ma, Z. Fang, X. Kang and P. Wang (2009). "Improved hydrogen storage property of Li–Mg–B–H system by milling with titanium trifluoride." Energy & Environmental Science **2**(1): 120-123.

Weeber, A. W. and H. Bakker (1988). "Amorphization by ball milling. A review." Physica B Condensed Matter **153**: 93-135.

Weitkamp, J., M. Fritz and S. Ernst (1995). "Zeolites as media for hydrogen storage." International Journal of Hydrogen Energy **20**(12): 967-970.

Wellons, M. S., P. A. Berseth and R. Zidan (2009). "Novel catalytic effects of fullerene for $LiBH_4$ hydrogen uptake and release." Nanotechnology **20**(20): 204022.

Wolverton, C., J. S. Donald, A. R. Akbarzadeh and V. Ozolins (2008). "Discovery of novel hydrogen storage materials: an atomic scale computational approach." Journal of Physics: Condensed Matter(6): 064228.

Xia, G. L., Y. H. Guo, Z. Wu and X. B. Yu (2008). "Enhanced hydrogen storage performance of $LiBH_4$-Ni composite." Journal of Alloys and Compounds **In Press, Accepted Manuscript**.

Yan, Y., X. Lin, S. Yang, A. J. Blake, A. Dailly, N. R. Champness, P. Hubberstey and M. Schroder (2009). "Exceptionally high H_2 storage by a metal-organic polyhedral framework." Chemical Communications(9): 1025-1027.

Yang, J., A. Sudik and C. Wolverton (2007). "Destabilizing $LiBH_4$ with a Metal (M = Mg, Al, Ti, V, Cr, or Sc) or Metal Hydride (MH_2 = MgH_2, TiH_2, or CaH_2)." Journal of Physical Chemistry C **111**(51): 19134-19140.

Yu, X., D. M. Grant and G. S. Walker (2006a). Dehydrogenation in MgH_2/LiH system, MH2006.

Yu, X., Z. Wu, F. Li, B. Xia and N. Xu (2004). "Body-centered-cubic phase hydrogen storage alloy with improved capacity and fast activation." Applied Physics Letters **84**(16): 3199-3201.

Yu, X. B., D. M. Grant and G. S. Walker (2006b). "A new dehydrogenation mechanism for reversible multicomponent borohydride systems: The role of Li-Mg alloys." Chemical Communications (Cambridge)(37): 3906-3908.

Yu, X. B., D. M. Grant and G. S. Walker (2008). "Low-Temperature Dehydrogenation of $LiBH_4$ through Destabilization with TiO_2." Journal of Physical Chemistry C **112**(29): 11059-11062.

Yu, X. B., Y. H. Guo, H. Yang, Z. Wu, D. M. Grant and G. S. Walker (2009a). "Improved Hydrogen Storage in Magnesium Hydride Catalyzed by Nanosized $Ti_{0.4}Cr_{0.15}Mn_{0.15}V_{0.3}$ Alloy." Journal of Physical Chemistry C **113**(13): 5324-5328.

Yu, X. B., Y. H. Guo, Z. X. Yang, Z. P. Guo, H. K. Liu and S. X. Dou (2009b). "Synthesis of catalyzed magnesium hydride with low

absorption/desorption temperature." Scripta Materialia **In Press, Accepted Manuscript**.

Yu, X. B., Q. Shi, T. Vegge, D. M. Grant and G. S. Walker (2009c). "Dehydrogenation in lithium borohydride/conventional metal hydride composite based on a mutual catalysis." Scripta Materialia **In Press, Accepted Manuscript**.

Yu, X. B., Z. Wu, Q. R. Chen, Z. L. Li, B. C. Weng and T. S. Huang (2007). "Improved hydrogen storage properties of $LiBH_4$ destabilized by carbon." Applied Physics Letters **90**(3): 034106-3.

Zaluska, A., L. Zaluski and J. O. Ström-Olsen (1999). "Nanocrystalline magnesium for hydrogen storage." Journal of Alloys and Compounds **288**(1-2): 217-225.

Zaluska, A., L. Zaluski and J. O. Ström-Olsen (2001). "Structure, catalysis and atomic reactions on the nano-scale: a systematic approach to metal hydrides for hydrogen storage." Applied Physics A: Materials Science & Processing **72**(2): 157-165.

Zhang, Y., Q.-F. Tian, S.-S. Liu and L.-X. Sun (2008). "The destabilization mechanism and de/re-hydrogenation kinetics of MgH_2-$LiAlH_4$ hydrogen storage system." Journal of Power Sources **185**(2): 1514-1518.

Zlotea, C., J. Lu and Y. Andersson (2006). "Formation of one-dimensional MgH_2 nano-structures by hydrogen induced disproportionation." Journal of Alloys and Compounds **426**(1-2): 357-362.

Züttel, A. (2004). "Hydrogen storage methods." Naturwissenschaften **91**(4): 157-172.

Züttel, A., A. Borgschulte and S.-I. Orimo (2007). "Tetrahydroborates as new hydrogen storage materials." Scripta Materialia **56**(10): 823-828.

Züttel, A., S. Rentsch, P. Fischer, P. Wenger, P. Sudan, P. Mauron and C. Emmenegger (2003a). "Hydrogen storage properties of $LiBH_4$." Journal of Alloys and Compounds **356-357**: 515-520.

Züttel, A., P. Wenger, S. Rentsch, P. Sudan, P. Mauron and C. Emmenegger (2003b). "$LiBH_4$ a new hydrogen storage material." Journal of Power Sources **118**(1-2): 1-7.